Silicic caldera volcanism and the 1883 eruption of Krakatau Volcano, Indonesia

Amber L. Madden-Nadeau

University College

Supervised by Dr. Michael Cassidy, Professor David Pyle and Professor Tamsin Mather

Thesis submitted to the University of Oxford for the degree of Doctor of Philosophy (DPhil)

Trinity 2021

Declaration

I declare that the work presented in this thesis is wholly my own, except where otherwise stated. The views and interpretations expressed herein are mine, and do not represent those of any other person or group except where this is cited to be the case.

Abstract

Silicic caldera-forming eruptions are major geohazards. The largest eruption with detailed written accounts occurred in 1883 at Krakatau; this allows information on the eruptive progression to be integrated with the chemostratigraphy. Freshly exposed sequences of the 1883 stratigraphy allow for its reassessment. Matrix glass from the base of the stratigraphy is more evolved than the overlying sequence, indicating a more silicic melt-rich region was evacuated during the precursory activity in May 1883. Phase equilibria experiments suggest that this precursory magma was stored deeper than the paroxysmal (August 1883) magma. These results challenge the hypothesis that the 1883 eruption emanated from a single, zoned magma reservoir. Thermodynamic models simulating fractional crystallisation show it is possible to evolve to 1883 rhyodacite from an Anak Krakatau basaltic andesite. Modelled melt chemistry for the paroxysm, using trace elements in plagioclase and partition coefficients, shows melt evolution trends for plagioclase of $An_{<67}$, which overlap with experimental matrix glasses generated under shallow crustal conditions (<6 km). Modelled melt chemistry using higher anorthite contents does not overlap with these experimental glasses, or show simple trends of melt evolution, instead indicating greater thermochemical diversity within the deeper system.

This study also investigates other pre- and post-1883 explosive records at Krakatau. More distal deposits originally attributed to the 1883 Krakatau eruption are found to require further geochemical analysis to place them within the context of Krakatau's eruptive history. The sequence of 2018-2019 ash deposits, associated with tsunamigenic flank collapse on Anak Krakatau, overlies a likely tsunami deposit and is consistent with observed post-collapse pulsatory Surtseyan activity. Thus, these deposits provide no evidence for a direct magmatic trigger for the collapse of Anak Krakatau in 2018. This work suggests that the structure of Krakatau's magmatic system is not dissimilar to other volcanoes in areas undergoing active extension.

Extended Abstract

Silicic, explosive caldera-forming eruptions are hazardous volcanic phenomena. The 1883 eruption of Krakatau is the largest volcanic event for which there are detailed contemporary written accounts, allowing information on the eruptive progression to be integrated with the stratigraphy and geochemistry of its products. Freshly exposed sequences of the 1883 eruptive deposits of Krakatau, stripped of vegetation by a tsunami generated by the flank collapse of Anak Krakatau in 2018, provides a novel opportunity to reassess the eruptive sequence. Matrix glass from the base of the stratigraphy is chemically distinct and more evolved than the overlying sequence indicating the presence of a more silicic melt-rich region that was evacuated during the early eruptive activity from May 1883 onwards. Results from phase equilibria experiments suggest that the material erupted during this precursory activity was stored at 100 - 150 MPa (~4 - 6 km) and 850 +/- 25 °C, whereas the bulk of the paroxysmal (August 1883) tephra was likely stored at lower pressures of 100 - 50 MPa (~ 2 - 4 km), and temperatures of 850 - 900 °C. Therefore, the products of precursory activity may have originated deeper within the magmatic system than the bulk of the 1883 pyroclastic sequence. The eruption of material in May potentially led to disruption of the stress fields associated with the magma reservoir, which culminated in the onset of the climactic phase of the eruption on 26th August 1883. Pyroclastic density currents (PDCs) emplaced during this phase of the eruption show a change in transport direction from north east to south west, coinciding with the deposition of a lithic lag breccia unit. This lag breccia may therefore be attributed to partial collapse of an elevated portion of the island, resulting in the removal of a topographic barrier. Partial collapse potentially further reduced the overburden on the underlying magmatic system, leading to the most explosive phase of the eruption in the morning of 27th August 1883. This phase of the eruption culminated in a final stage of caldera collapse, which is recorded in the stratigraphy as a second lithic lag breccia. The massive PDC deposits emplaced during this final phase contain glassy blocks up to 8 m in size, observed for the first time in 2019, which are chemically similar to the pyroclastic sequence, and show evidence of ductile deformation during hot emplacement and thus are likely juvenile products of the 1883 eruption.

Thermodynamic models, simulating fractional crystallisation of an Anak Krakatau basaltic andesite starting composition, show that it is possible to evolve to 1883 rhyodacitic compositions without invoking other processes (e.g., crustal assimilation). In addition, melt chemistry is modelled using trace elements in plagioclase and partitioning models for the paroxysmal phase of the eruption. Strong positive correlations between modelled melt TiO_2, and to a lesser extent MgO contents, with both anorthite content of plagioclase ($An_{<67}$) and modelled Sr content of the melt, are consistent with melt evolution. Furthermore, these modelled melt compositions also overlap with experimental matrix glass data generated under shallow crustal conditions. For plagioclase with higher anorthite contents ($An_{>67}$), modelled melt compositions do not show simple trends of melt evolution, and instead indicate greater melt diversity. The melt compositions modelled from plagioclase of higher anorthite contents are not replicated by experiments at shallow crustal conditions, suggesting that these melt compositions derive from deeper within the magmatic system. Melt evolution by fractional crystallisation of a chemically homogenous melt is therefore likely to be the dominant process in the shallow magmatic system, but deeper in the system, greater melt diversity accounts for the more complex plagioclase crystallisation histories.

Matrix glass chemistry from the proximal 1883 stratigraphy at Krakatau is consistent with explosive eruptions prior to 1883. In addition, at least one other volcano within the region has an overlapping liquid line of decent with Krakatau. The deposits originally attributed to the 1883 Krakatau eruption on islands Sebesi and Sebuku (16 and 25 km away, respectively) have matrix glass chemistry consistent with having been erupted from Krakatau volcano, however it cannot on this basis alone be definitively ascribed to this eruption. At least one volcanic unit, observed on Sebuku, Kecil, has matrix glass chemistry distinct from the 1883 tephra. The likely tsunami deposit below this unit contained a fragment of pottery, however, which means it was potentially deposited in historical times. These deposits need to be assessed in more detail to be placed within the context of Krakatau's eruptive history. If these deposits are from older Krakatau eruptions, this highlights the possibility that events that can generate PDCs which travel >25 km over the sea surface, are not uncommon for this volcano. The fact that these

eruptive deposits may not pertain to the 1883 eruption of Krakatau has important implications for modelling the 1883 pyroclastic density currents, and subsequent tsunamis.

The sequence of 2018-2019 ash deposits associated with flank collapse on Anak Krakatau overlies a likely tsunami deposit. This sequence of thin, fine ash units is consistent with observed pulsatory Surtseyan activity after the tsunamigenic flank collapse of Anak Krakatau on 22nd December 2018. The phreatomagmatic activity is likely to have occurred as a result of the vent being truncated below sea level as a result of the collapse. The first unit erupted immediately post-collapse has lower Al_2O_3 and higher TiO_2 and FeO than the overlying sequence, likely reflecting less Fe/Ti oxide microlite formation, which may be as a result of high decompression rates in the immediate aftermath of the flank collapse, which then decreased over time. The 2018-2019 ash found on the Krakatau islands is thus representative of post-collapse volcanic activity that appears decompression driven, and thus provide no evidence for a direct magmatic trigger for the collapse of Anak Krakatau in 2018.

This study provides new evidence for the role that precursory eruptions potentially play in the months leading up to caldera-forming eruptions, and highlights the fact that caldera collapse in silicic systems may occur in stages. In addition, it highlights melt evolution through fractional crystallisation alone is the dominant process in the shallow system. This study also shows it is possible that high magnitude explosive volcanism on Krakatau may be more common than previously thought, as observed by Krakatau's explosive records on more distal islands, which highlights important areas for further study.

Acknowledgements

Firstly, I would like to profusely thank my supervisors Dr. Mike Cassidy, Prof. David Pyle and Prof. Tamsin Mather for their experience, knowledge, mentorship, guidance, and seemingly endless patience. Without their support, I would have been unable to undertake and finish this DPhil project. I would also like to thank all my collaborators, but in particular Dr.Eng. Mirzam Abdurrachman, who has provided invaluable expertise, enabled the procurement of samples, and was an excellent host whilst we were on fieldwork. I am also very appreciative of Dr. Sebastian Watt and Dr. Samantha Engwell for sharing their extensive knowledge in the field and aiding the interpretation of the data thereafter. Additionally, I would like to acknowledge the help that I have had from Prof. Victoria Smith, Dr. Phil Gopon, Prof. Jon Wade and Dr. Erin Johnson using electron imaging facilities, and Owen Green and Jon Wells for help with sample preparation.

It would be remiss of me to forget the moral support I received from all of my friends during this process, but in particular from (the soon to be Drs) Diana Avadanii and Grace Manley, as well as Dr. James King, Dr. Thomas Caton Harrison and Dr. Ricky Sengupta. I would also like to thank Dr. Jean Christopher Mittelstaedt, who provided much needed respite during the writing process, and who patiently shrouded me with encouragement when I needed it most. Saving the most important until last, I must thank my parents, Sharon and Terry Madden-Nadeau for their enduring love, for facilitating, but never pushing, and for providing all of the opportunities and privileges I have enjoyed that have culminated in the writing of this thesis. A special thanks must also be said to my little brother, best friend and cheerleader, Jordan Madden-Nadeau, who first taught me the meaning of collaboration, as well as to the rest of my extended family.

Funding and other support

This work has been made possible through the funding of the Natural Environment Research Council (NERC), predominantly through NERC Studentship NE/L202612/1. Subsidiary financial support was provided by University College, Oxford. Thank you to the British Geological Survey for the loan of historical samples.

List of contents

List of Figures

List of Tables

List of abbreviations

Ab..... Albite

Ac.....Accessory minerals

AD.....Anno Domini (the year of our lord)

am..... Ante meridiem (before midday)

An.....Anorthite

Ap..... Apatite

Approx. .....Approximate

BSE .....Back scatter electron

BGS.....British Geological Survey

Cpx..... Clinopyroxene

cm.....Centimetres

C-S .....Clast-supported

D.....Diffusion coefficient

D_x ..... Partition coefficient of particular element

EDS.....Energy dispersive spectroscopy

e.g..... exempli gratia (for example)

EPMA .....Electron Probe Microanalysis

etc..... et cetera (and other things)

FEG.....Field emission gun

fO_2.....Fugacity of oxygen

Gl ..... Glass

GPa..... Gigapascals

ka..... thousand years ago

km ..... Kilometres

kV..... Kilovolt

LOI..... Loss on ignition

Lq..... Liquid

L-R..... Lithic-rich

m ..... Metres

MG..... Matrix glass

Mg#..... Magnesium number

mm ..... Millimetres

MPa..... Mega pascals

M-S ..... Matrix-supported

n ..... Number

NA..... Not applicable

nA..... Nanoamp

NNO..... Nickel-nickel-oxide buffer

Ol ..... Olivine

Opx..... Orthopyroxene

Or ..... Orthoclase

Ox ..... Fe-Ti oxide

P ..... Pressure

P_{H2O} ..... Partial pressure of water

PDC ..... Pyroclastic density current

Plg ..... Plagioclase

pm ..... Post meridiem (after midday)

Px ..... Pyroxene

Qtz/Qz ..... Quartz

R ..... Gas constant

R^2 ..... Least squares regression

s ..... Second

SEM ..... Scanning electron microscope

T ..... Temperature

t ..... Time

VEI ..... Volcanic explosivity index

VF ..... Vesicle-free

vol% ..... Volume percent

WR ..... Whole-rock

wt% ..... Weight percent

X_{An} ..... Molar concentration of anorthite

x ..... Length

XRF.....X-ray fluorescence

x-strat .....Cross-stratified

~ ..... Approximately equal to

°C ..... Degrees Celsius

> ..... Greater than

< .....Less than

σ ..... Standard deviation

1. Introduction

1.1 Explosive, silicic caldera volcanism

More than 800 million people on Earth live within 100 km range of a known active volcano, and are exposed to the direct effects of an eruption, such as health complications, loss of life and socioeconomic damage (United Nations Office for Disaster and Risk Reduction, 2015). Risk mitigation is thus of great importance to the livelihoods of this global community, and currently depends on the identification and rapid evacuation of endangered populations. This in turn is reliant on early recognition of the signs of an impending eruption, which can be achieved by increasingly more sophisticated volcano monitoring networks. Volcano monitoring is achieved using a range of geophysical techniques, including measuring ground displacement via InSAR, earthquakes using seismology, gas fluxes and chemistry, and more recently local gravitational acceleration and subterranean magnetic fields (e.g., Saccorotti et al., 2015). However, despite this progress, the non-linear dynamics that control volcanic eruptions mean that more work needs to be done if volcanologists are to achieve the goal of being able to forecast the timing, the style (e.g., explosive vs. effusive; Cassidy et al., 2018) and the size of an impending eruption (Papale, 2018). Therefore, present day risk assessment is achieved within the context of the eruptive history of the volcano, complimented by data from analogous systems (Newhall and Pallister, 2015).

However, assessing the probability and risk associated with eruptions of VEI (Volcanic explosivity index; Newhall and Self, 1982) 6 and above is more complicated, as these eruptions occur less frequently, and there is unlikely to be geophysical monitoring data for previous eruptions of a similar magnitude, or background monitoring data prior to such an eruption. One quarter of the major explosive eruptions that have occurred since 1979 (satellite era) have come from volcanoes that had no prior activity within the last century (Pyle and Barclay, 2020). Therefore, the volcanoes that produce the most explosive eruptions in the future may lack prior instrumental records. This lack of historical geophysical data poses challenges for the assessment of contemporary geophysical monitoring data (e.g., Newhall and Dzurisin, 1988; Gottsmann and Marti, 2008; Druitt et al., 2012).

These large, explosive eruptions often form calderas, and are especially dangerous and deadly natural hazards, as a result of large volumes of tephra being ejected during the collapse, forming pyroclastic density currents (PDCs), or high speed, hot dispersions of ash and gas. Calderas also produce some of the most scenic landscapes on earth, attracting tourists, and can also be associated with economic deposits, and thus play an important role in many economies worldwide. However, this generates further risk, impacting not only those who live there, but also people who visit and work near the volcano.

Explosive, silicic, caldera-forming systems are usually associated with high fluxes of mantle-derived basaltic magmas, and are found in convergent, rifting and intra-plate settings (Hildreth, 1981; de Silva and Gosnold, 2007; Barker et al., 2020; Wilson et al., 2021). Some systems have produced multiple caldera-forming eruptions throughout their histories, which makes it likely that some of these systems which are still active today have the potential to produce a caldera-forming eruption in the future. This has led to the hypothesis that these systems undergo caldera cycles, comprising pre-collapse activity, followed by caldera formation and post collapse resurgence and recovery (Smith and Bailey, 1968; Lipman, 1984; 2000; Cole et al., 2005; Maisonneuve et al., 2021). There is a growing consensus that magmas within silicic caldera systems are stored in vertically extensive mushy state, which is largely crystalline (Marsh, 1981; Huber et al., 2009; Cooper and Kent, 2014; Cashman et al., 2017). Magma mush zones are generally considered to be long lived (on the order of 10 – 100 ka). Melts are then extracted from this mush into shallow melt bodies prior to, and perhaps during, large silicic eruptions. This is corroborated by the fact that geophysical techniques so far have only found evidence of partially molten reservoirs, rather than melt-dominant bodies (e.g., Heise et al., 2010; Huang et al., 2015; Koulakov et al., 2016; Flinders et al., 2018). However, there appears to be no ubiquitous model for the subterranean architecture of these magmatic systems, with end members including multiple compositionally distinct melt-dominant bodies, a single compositionally stratified magma reservoir, or a single unzoned reservoir, whereby compositional variation introduced by rejuvenation is homogenised through mixing (Wilson et al., 2021).

The present is the key to the past (Lyell, 1830), and thus gaining a better understanding of the architecture of magmatic systems, and conditions therein, for past silicic caldera-forming eruptions, provides the context for contemporary geophysical monitoring of these volcanoes. This is particularly important for silicic caldera-forming eruptions, as mentioned before, because of the infrequency of their occurrence. It is therefore important to combine detailed field-based study, with petrological data, for past silicic caldera-forming eruptions, so that they might be linked to contemporary geophysical studies in the monitoring of currently active systems (Wilson et al., 2021). In addition, the use of written historical records of these transitions between different eruptive behaviour are also important for understanding eruptive progression (Pyle and Barclay, 2020). Study of volcanic tephra, including whole-rock, matrix glass and mineral chemistry, particularly when placed in the context of the volcanic stratigraphy, can provide a unique insight into the thermochemical structure of the subterranean magmatic system prior to these explosive eruptions. This petrological data also allows pre-eruptive magma storage conditions, such as pressure, temperature and volatile content, to be estimated. These variables can then be constrained further using experimental petrology, through which it is possible to replicate the conditions under which the pre-eruptive magma was stored by comparing the chemistry of magmatic products generated under a range of temperatures and pressures with natural volcanic material. In addition, petrological modelling of magma evolution and of trace element partitioning between the melt and particular phases can shed light on magmatic processes, such as fractional crystallisation.

Physical and chemical properties of a magma also influence its ability to outgas and, in turn, its ascent rate, both of which are strongly linked with eruptive style (Cassidy et al., 2018). Pressure is an important variable to constrain, as it controls water solubility, and thus viscosity, both of which may affect the explosive potential of the magma. Pressure estimates can also be used to broadly constrain the depths of magma storage regions. The location of magma storage regions is important for the interpretation of seismology data in volcano monitoring. Temperature is a key parameter when estimating timescales of magmatic processes based on diffusion models (e.g., Costa et al., 2020), which are likely to play an important role in forecasting the timing of future eruptions. In

addition, petrological data can shed light on important magmatic processes like mafic recharge, magma mixing, assimilation and fractional crystallisation, all of which have the potential to contribute to triggering volcanic eruptions (e.g., Knesel et al., 1999; Ruprecht et al., 2012; Cassidy et al., 2015; 2016). The relative importance of these processes within the magmatic system needs to be assessed so that they can be monitored in the present-day system. Petrological investigation of silicic caldera-forming eruptions can thus provide extensive groundwork for the monitoring of these volcanoes.

The very largest silicic, caldera-forming volcanic eruptions (VEI 8, 1000 km^3 Dense rock equivalent; DRE) occur very infrequently, with estimates of recurrence of 1 in 17,000 - 100,000 years (Sparks et al., 2005; Self, 2006; Miller and Wark, 2008; Rougier et al., 2018) with the most recent taking place 27,000 years ago at Taupo volcano (Wilson and Walker, 1985; Hogg et al., 2019). However, globally there have been 11 occurrences of silicic caldera-forming eruptions of VEI 6 and 7 in historical times (the last 5,000 years), and so these are more frequent than VEI 8 eruptions, while still having substantial local and global impacts. The most recent silicic, caldera-forming eruption occurred from Mt. Pinatubo, Philippines in 1991, a VEI 6 eruption that caused global surface cooling in excess of 0.5 °C in the subsequent year (Dutton and Christy, 1992). The climatic changes associated with caldera volcanism has been hypothesised to impact global socioeconomics on several occasions, including but not limited to the eruption of Tambora in 1815, which created "the year without a summer" in Europe, generating famine, starvation, and mass migrations (Papale and Marzocchi, 2019). In addition, Newhall et al. (2018) argue that a VEI 7 eruption from Gunung Salmalas (Rinjani), Indonesia in the 13th century was a major contributing factor to the Little Ice Age. The devastating local and global impacts of these eruptions, along with a lack of geophysical monitoring data in the run up to, and during these eruptions, therefore, make them a priority for study.

1.2 Krakatau Volcano

1.2.1 1883 eruption

Krakatau Volcano is located in the straits of Sunda between Java and Sumatra, Indonesia (Figure 1.1). The 1883 eruption of Krakatau is the largest known eruption for which there are detailed documented observations in contemporary accounts (Figure 1.2). This is partly because the eruption occurred shortly after the invention of the telegraph, and the construction of transatlantic telegraph cables, and thus became global news in a relatively short period of time. The Royal Society, London, set up the "Krakatoa" committee to investigate the eruption, and put out adverts in newspapers to request information on this and subsequent phenomena, such as vivid sunsets, in the first concerted global scientific effort to understand a natural phenomenon, and one of the first and most famous occurrences of citizen science and crowd sourcing data. In addition, a Dutch geologist R.D.M Verbeek was in the region at the time of the eruption, and took it upon himself to record details of the event from people in the area in the immediate aftermath. These detailed observations allow the temporal progression of an explosive, silicic, caldera-forming eruption to be integrated with other datasets (e.g., stratigraphy, petrology and geochemistry) similar to studies of the 79 AD eruption of Vesuvius (e.g. Sigurdsson et al., 1982; Cioni et al., 2000).

The eruption on 26th and 27th August 1883 was the culmination of months of unrest. The VEI 6 eruption produced 18 – 21 km^3 of ejecta (9 – 10 km^3 dense rock equivalent; Self and Rampino, 1981) in a sequence of pyroclastic density currents (PDCs). The majority of the~36,000 fatalities were as a result of subsequent tsunamis (Self, 1992), however the precise source of these tsunamis are debated. Many of the smaller waves are thought to be air/sea coupled waves, as a result of the shockwaves produced, rather than true tsunamis. Of the larger waves produced, at least one is thought to be as a result of a pyroclastic flow (e.g, Maeno and Imamura, 2011). The origin of the largest wave, generated on 27th August and over 40 m in height when it reached mainland Java, is still debated. Francis (1985) proposes that the largest tsunami was likely generated as a result of caldera collapse, however modelling studies by Nomanbhoy & Satake (1995) suggest instead that a submarine explosion is more likely. Caldera collapse resulted in the destruction of two-thirds of the

main island of Krakatau. The soundwaves produced by the eruption were the greatest ever recorded in the audible range, and the atmospheric effects were seen around the world, with vivid sunsets observed up to a year after the eruption (Symons et al., 1888).

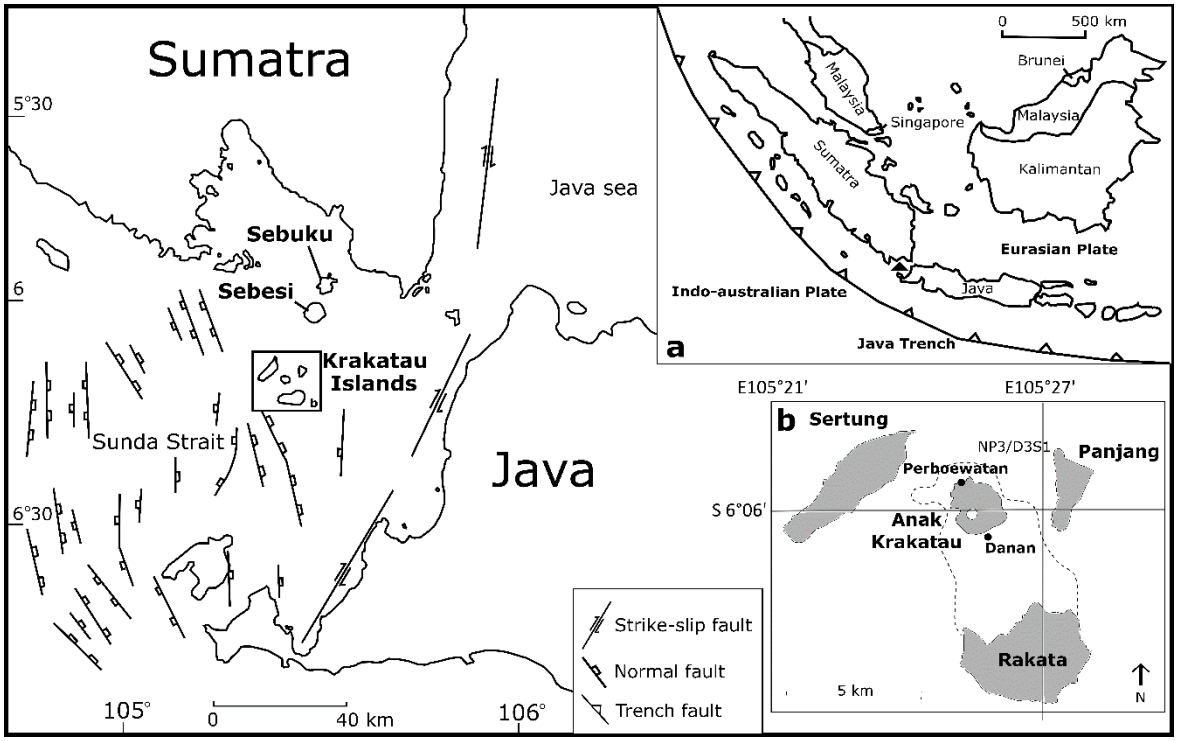

Figure 1.1: Tectonic map showing the location of the Krakatau islands, in the Sunda Strait between the islands of Java and Sumatra, Indonesia. Insert (a) is a zoomed-out map showing Krakatau's location (black triangle) and the Java trench. Insert (b) shows the proximal Krakatau islands, with the dashed line representing the extent of volcanic island destroyed in the 1883 caldera collapse. Perboewatan, Danan and Rakata were all active cones prior to the 1883 eruption. Figure based on Mandeville et al. (1996b), Schlüter et al. (2002), Lunt et al. (2009), Susilohadi et al. (2009) and Dahren et al. (2012).

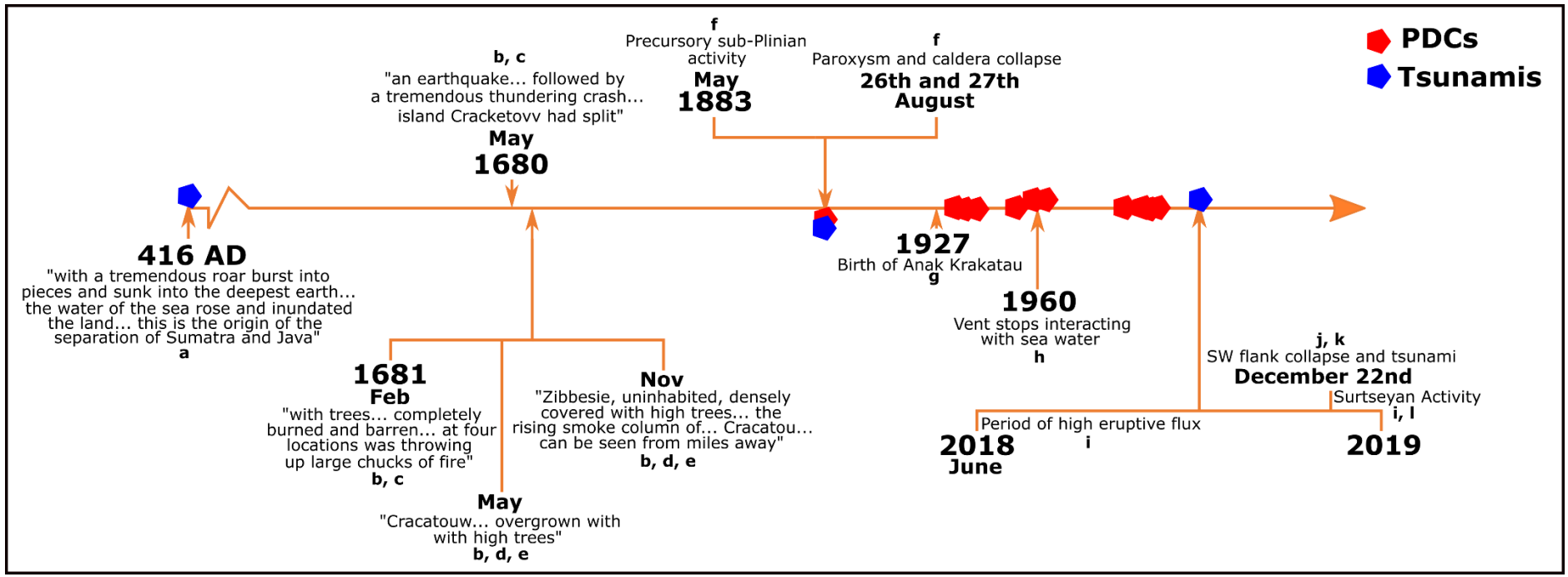

Figure 1.2: Timeline from 416 AD to 2019, showing Krakatau's eruptive history. Each arrow gives a year on the timeline for which we have written records. Letters represent the following references: (a) Judd (1889), (b) Van den Berg (1884), (c) Vogel (1690), (d) Hesse (1690), (e) Hesse (1694), (f) Madden-Nadeau et al., (2021), (g) Stehn (1929), (h) Abdurrachman et al. (2018), (i) Walter et al. (2019), (j) EM – DAT (2018) (k) Novellino et al. (2020) and (l) Prata et al. (2020). Extracts from (a) – (e) can be found in Simkin and Fiske (1983).

1.2.2 1883 stratigraphy

The stratigraphy of the 1883 eruptive deposits has been investigated previously through analysis of subaerial deposits on the proximal islands of Panjang, Sertung and Rakata (Figure 1.1). Self and Rampino (1981) reported that the proximal stratigraphy comprised sub-Plinian fall deposits interbedded with surge deposits up to 20 m thick, overlain by up to 55 m of massive ignimbrite. Mandeville et al. (1996b) reported a soil horizon, followed by a layer of olive- to bluish-grey, fine-ash fall deposit up to 4 cm, 5 - 20 cm of pumice fall deposit, followed by 4 to 6 m of fall deposits interbedded with surge deposits. At the top of the stratigraphy, Mandeville et al. (1996b) report thick accumulations of massive pyroclastic flow deposits. The thickness of the fall deposit layer is therefore disputed, with Self and Rampino (1981) observing fall deposits interbedded with surges up to 20 m thick, and Mandeville et al. (1996b) observing up to 6.2 m of fall deposit interbedded with surge deposits. In addition, Self and Rampino (1981) and subsequently Self (1992) do not note the basal olive fine ash fall detailed by Mandeville et al. (1996b).

As well as land-based stratigraphic columns, there are 51 hand-held cores that were taken in the area. Twenty-one of these, selected as the least reworked, were analysed by Mandeville et al. (1996b) for grain-size distributions, and showed that the submarine and subaerial deposits are similar in this respect, and are interpreted to have been deposited by pyroclastic flows. Carey et al. (1996) suggest that the pyroclastic flows produced by the 1883 eruption are likely to have segregated, travelling both above and below sea level.

Volcanic deposits on the islands of Sebesi and Sebuku, 16 and 25 km distance respectively from Krakatau (Figure 1.1), were originally attributed to the 1883 eruption by Carey et al. (1996), who interpreted their deposition to be as a result of pyroclastic density currents. Verbeek (1885) notes that 1 - 1.5 m of volcanic ash covered Sebesi in September 1883, one month after the eruption, and that vegetation had been destroyed. The inhabitants of Sebesi are also reported to have lost their lives as a result of pyroclastic density currents.

1.2.3 1883 magma reservoir

As discussed before, understanding the conditions and processes ongoing within the magma reservoir prior to the 1883 eruption of Krakatau is important because this provides context for contemporary geophysical monitoring of systems with the potential to produce large silicic, explosive eruptions. Most estimates of pre-eruption temperatures via mineral-mineral or mineral-melt equilibria are within the range of 870 – 950 °C (Camus et al., 1987; Mandeville et al., 1996a). Mandeville et al. (1996a) proposed that the magma reservoir responsible for the 1883 eruption was a chemically and thermally zoned magma reservoir at 5 to 8 km depth (Figure 1.3). Mandeville et al. (1996a) inferred that a rhyodacite magma (880-890°C), which would account for the vast majority of erupted products, overlay progressively hotter dacites (890-913ºC), and andesites (980-1000°C) from Fe-Ti oxide thermometry. Pressures are poorly constrained, but are estimated within the region of 100 – 200 MPa (Mandeville et al., 1996a). Constraints on pre-eruptive magmatic water contents come from analysis of volatiles by difference of glass inclusions, at 4 +/- 0.5 wt% (Mandeville et al., 1996a).

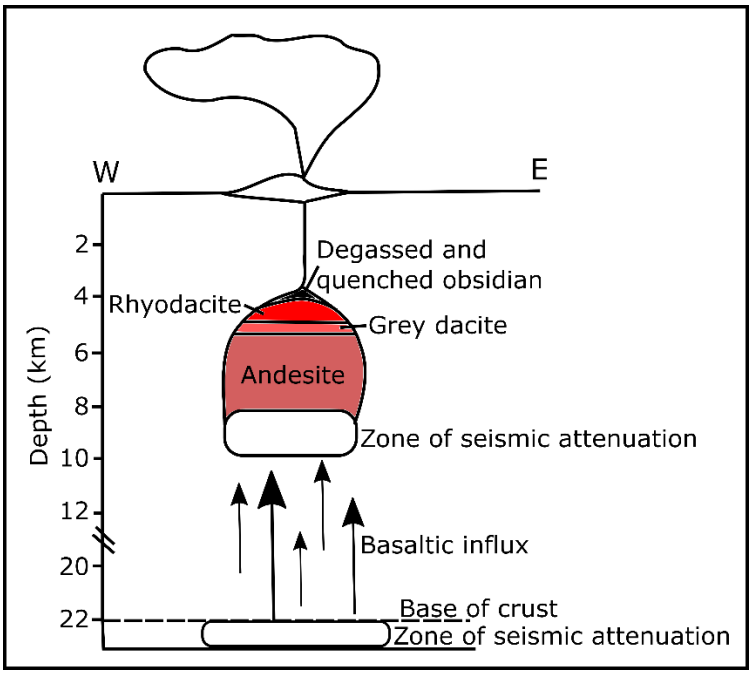

Figure 1.3: Schematic model proposed by Mandeville et al. (1996a) for a chemically and thermally zoned magma reservoir prior to Krakatau's 1883 eruption.

Dahren et al. (2012) used petrological and seismic techniques to analyse the structure of the plumbing system beneath Anak Krakatau, the post-caldera volcano that in 1927 emerged above sea-level within the 1883 Krakatau caldera. They concluded that the contemporary and 1883 plumbing systems were likely to have been subject to comparable structural controls, based on compositionally similar phenocrysts. From mineral data, they inferred that magmas stalled in three lithologically controlled zones: 23 – 28 km (plagioclase cores), 7 – 12 km (clinopyroxene) and 3 - 7 km (plagioclase rims).

There is still debate regarding the relative importance of different magmatic processes involved at various stages of the 1883 eruption. Potentially important processes include (i) fractional crystallisation, leading to "second boiling" (Camus et al., 1987; Mandeville et al., 1996a), (ii) magma mixing (Francis and Self, 1983; Self and Wohletz, 1983) and (iii) phreatomagmatism, which has been proposed as a trigger for the main explosions on the morning of 27th August, with magma interacting with sea water in the vent during caldera collapse (Verbeek, 1884). Self and Rampino (1981) ruled out phreatomagmatism, as they found no textural evidence for magma-water interaction. Verbeek (1884) reported two distinct compositions of ash erupted during May 1883: dacite and a high-alumina basalt (Stehn, 1929). This led Francis and Self (1983) and Self and Wohletz (1983) to suggest that magma mixing triggered the 1883 eruption of Krakatau. Several studies have noted the presence of rare, banded pumice clasts from the main phase of the eruption (e.g., Self and Rampino 1981), which is often used as an indicator for magma mixing (Sparks et al., 1977; Andrews and Manga, 2014; Rossi et al., 2019), however, the two visually distinct glasses were found to be chemically similar (Self, 1992). Camus et al. (1987) and Mandeville et al. (1996a) suggested fractional crystallisation as the most important process prior to the 1883 eruption, citing the limited amount of reverse zoning in phenocrysts. Fractional crystallisation increases the SiO_2 content of the residual melt whilst enriching it in volatiles, making an eruption more likely and potentially more explosive (Blake, 1984). Both products of the 1883 and contemporary Krakatau system show evidence for assimilation of crustal material in the form of crustal xenoliths (Gardner

et al., 2012). Using mineral and whole rock Sr isotope data, Gardner et al. (2012) showed that evolving a basaltic andesite starting compositions from the contemporary edifice Anak Krakatau to 1883 rhyodacitic compositions required 45% crystallisation, accompanied by assimilation of 5-23% carbonate or quartzo-feldspathic siltstone.

1.2.4 Pre-1883 volcanism

The ages of pre-1883 eruptions are poorly constrained, with little published data relating to the pre-1883 volcanic stratigraphy (Self, 1992). Ash from a ca. 60 ka eruption in the Sunda Straits was identified in drill cores, however this cannot be definitively attributed to Krakatau (Ninkovich, 1979). The Javanese chronicle Pararaton, or the Book of Kings, describes an explosive eruption in 416 AD originating in the Sunda Straits, with "heavy rains of stone" and that the main volcanic centre of Krakatau at the time "with a tremendous roar burst into pieces and sunk into the deepest earth" (Figure 1.2; Symons et al., 1888; Judd 1889). This eruption is also described to have generated a tsunami that was said to be "the origin of the separation between Java and Sumatra". However, no geological evidence presented to date substantiates this eruption. In May 1680, and February and November of 1681, observations of earthquakes and pumice were made in the diaries of Johann Wilhelm Vogel and Elias Hesse, likely pertaining to eruptions of Krakatau (Figure 1.2; Verbeek, 1884).

1.2.5 Anak Krakatau

It was not until 1927 that Anak Krakatau, or "child of Krakatau", emerged above the sea surface, forming a new subaerial volcanic cone (Stehn, 1929). This soon became a permanent island, which has since grown rapidly (~8 cm a year; Gardner et al., 2012). Anak Krakatau has predominantly erupted effusively, punctuated with Vulcanian and Strombolian explosions since the active vent stopped interacting with seawater in 1960 (Figure 1.2; Abdurrachman et al., 2018). Magmatism in

this region is a function of subduction, but also of rifting and extension (Harjono et al., 1989), and is associated with slab-thinning and mantle upwelling (Abdurrachman et al., 2018).

After 15 months of quiescence, Anak Krakatau began erupting on 21st June 2018, characterised by Strombolian activity with low-level ash plumes and lava flows, typical in eruptive style to previous activity (Global Volcanism Programme Bulletin Report, 2018). However, the magmatic flux is thought to have been higher during this eruptive period than had been previously recorded (Walter et al., 2019). On 22nd December 2018, a lateral collapse of the southwestern flank of Anak Krakatau, where half of the island failed (Hunt et al., 2021) and its height was reduced from 320 to 120 m, generated a tsunami >50 m high in the proximal islands (Grilli et al., 2021) that killed 453 people (EP-DAT, 2018). The collapse truncated the vent below sea level, and after 22nd December 2018, Anak Krakatau made the transition to pulsatory phreatomagmatic activity. This activity was particularly intense in the days immediately after the flank collapse, which caused a rapid regrowth of the island (Novellino et al., 2020).

1.3 Aims and objectives

The primary aim of this study, which are discussed primarily in Chapters 2 and 3 (with some relevant information also presented in Chapter 4) is to investigate how the 1883 silicic caldera-forming eruption of Krakatau progressed through time, both in terms of eruptive behaviour and magma reservoir conditions and processes. Achieving this aim is hoped to lead to a better understanding of magmatic systems prior to caldera-forming eruptions more generally, so that the information can be used for future monitoring of similar systems with the potential to produce large explosive eruptions. This information is also relevant to present day Anak Krakatau, which is still an active system. A parallel aim of this thesis is, therefore, to investigate explosive activity produced by Anak Krakatau, to improve the understanding of this system as a whole through time; this is discussed in Chapter 4. To achieve these aims, five objectives must be realised:

(1) Sample and constrain the proximal eruptive stratigraphy of the 1883 eruption

Although the stratigraphy of the 1883 eruption of Krakatau has been investigated previously (Self and Rampino, 1981; Mandeville et al., 1996a), the tsunami generated by flank collapse of Anak Krakatau in 2018 eroded the proximal coastal cliff sections, which has led to far superior exposure than has previously been observed and documented. This has provided the opportunity to reassess the deposits with the goal of further constraining the eruptive stratigraphy. In particular, the increased exposure allows us to investigate the vertical extent of the fall deposits recorded at the base of the stratigraphy, and to identify the basal ash detailed by Mandeville et al., (1996a). The reassessment of the stratigraphic sequence also allows for systematic sampling throughout the stratigraphy, which will be crucial for achieving Objective (3), to investigate the thermochemical structure of the magma reservoir. In addition, the thicknesses of the pyroclastic density current (PDC) deposits throughout the stratigraphy are assessed to ascertain changes in PDC directionality as the eruption progressed. The proximal 1883 stratigraphy is presented as part of Chapter 2.

(2) Integrate the stratigraphy with the eruptive timeline

The eruptive timeline of the 1883 eruption is reassessed from historical records to establish the sequence of events, for integration with the data ascertained in Objective (1), to link the eruptive dynamics observed at the time with the stratigraphic sequence. The integration of historical records with the stratigraphic sequence is presented predominantly in Chapter 2, and isrevisited in Chapter 3 to consider how the experimental and modelling results fits into the model proposed for the magmatic system.

(3) Investigate the architecture of, and conditions and processes within, the pre-eruptive 1883 subterranean system

The newly constrained 1883 eruptive stratigraphy and systematic sampling throughout achieved in objective (1) will permit the assessment of how the chemistry of the deposits changed as the eruption progressed, for the first time. This is done by looking at whole-rock, matrix glass and phenocryst chemistry throughout the stratigraphy. In addition, mineral and matrix glass chemistry is used in

conjunction with the most up-to-date thermometers and hygrometers (e.g., Ghiorso and Evans, 2008; Waters and Lange, 2015) to estimate pre-eruptive temperature and H_2O contents. Assessing chemical changes through the stratigraphy will help us to investigate the thermochemical structure of the pre-eruptive magma reservoir and test whether the magma reservoir was thermochemically zoned, as suggested by Mandeville et al. (1996a). Fractional crystallisation is modelled using Rhyolite-MELTS (Gualda et al., 2012) to investigate whether 1883 eruptive chemistry can be recreated from an Anak Krakatau, basaltic andesite starting material. If this is possible, these models may be able to provide some constraints on magmatic conditions such as H_2O content and pressure. Assessment of the pre-eruptive conditions within the magma reservoir, and the processes ongoing therein, is presented in Chapter 2, in conjunction with the stratigraphy, and will be linked to the eruptive dynamics, as derived from historical records. In addition, trace element chemistry of phenocryst phases is used to investigate magma chemistry throughout plagioclase crystallisation histories prior to the 1883 eruption. Experimental petrology is also used to further constrain pressure and temperature estimates. Assessment of the pre-eruptive conditions and magmatic processes is therefore revisited in Chapter 3 in the context of the modelling of melt chemistry using trace elements in plagioclase, and experimental results. These chemical and physical characteristics pertaining to magma storage are important for understanding eruptive style changes, and may also help with future seismic and deformation monitoring of Krakatau, and other similar systems.

(4) Correlate 1883 deposits further afield

The deposits found at more distal locations by Carey et al. (1996) are reassessed in the context of the proximal chemostratigraphy, to identify whether they can be unequivocally attributed to the 1883 eruption of Krakatau. Further assessment of the nature of these deposits and a better understanding of the extent of the 1883 volcanic stratigraphy will aid those attempting to model pyroclastic density current (PDC) generation and propagation (e.g., Marti et al., 2016). The 1883 eruption also produced large tsunamis, the generation of which has been the subject of extensive debate (e.g., Nomanbhoy and Satake, 1995; Choi et al., 2003). One hypothesis is that PDCs were the source of the tsunamis, which is also hypothesised for similar volcanogenic tsunamis, such as the Late Bronze Age eruption,

Santorini (Nomikou et al., 2016). Assessing the stratigraphy of these deposits in more detail will thus also help provide better constraints on tsunami models for the 1883 event (e.g., Nomanbhoy and Satake, 1995; Choi et al., 2003). To achieve this, the stratigraphy of the exposures identified by Carey at al. (1996) needs reassessment and sampling, along with the analysis of matrix glass chemistry through these sequences. In order to assess how effective matrix glass chemistry is in determining whether or not these deposits pertain to the 1883 eruption of Krakatau, pre-1883 explosive deposits requires analysis, to determine whether Krakatau has erupted similar compositions throughout its accessible explosive record. Assessment of deposits at more distal locations to Krakatau are presented in Chapter 4, which explores further records of explosive volcanism at Krakatau.

(5) Establishing the 2018/2019 eruptive stratigraphy of deposits associated with tsunamigenic flank collapse of Anak Krakatau

Anak Krakatau has erupted predominantly basaltic andesite products since the island become subaerial in 1927. The tsunamigenic flank collapse on December 2018 was the largest disaster at Krakatau since then. It is thus important to assess whether or not there is evidence for a direct magmatic trigger for the flank collapse, or whether it occurred as a result of other processes e.g., rapid growth and oversteepening of the vent over time (Watt, 2019). To do this, the stratigraphy of the 2018/2019 eruptive products is established via fieldwork, and the matrix glass chemistry of these deposits are assessed in the context of this stratigraphy. This will allow us to assess whether the stratigraphy was deposited pre- or post-collapse, and whether there is any evidence for a chemical change in these eruptive products, relative to previous activity. Understanding whether there is a direct magmatic trigger for the 2018 flank collapse will help identifyprecursors to volcanic collapse events, and will aid in the assessment of hazards produced by Anak Krakatau in the present day. In addition, improved understanding of intra-caldera eruptions is important for identifying common trends in how these systems evolve between caldera-forming eruptions, which will be key in hazard assessment of future volcanic activity of these systems (Maisonneuve et al., 2021). The 2018/2019

stratigraphic sequence ispresented in Chapter 4, as part of further explosive records of Krakatau volcano.

In summary, Chapter 2 explores the magmatic and eruptive evolution of the 1883 eruption of Krakatau, through integration of historical accounts with the stratigraphy and geochemistry. This chapter presents new field observations as a result of erosion by the 2018 tsunami generated by flank collapse of Anak Krakatau, in order to further constrain the stratigraphy, which fulfils the first aim of this thesis. Whole-rock, phenocryst and matrix glass chemistry are then explored, as well as modelling fractional crystallisation of an Anak Krakatau basaltic andesite starting composition to ascertain whether this can produce the same chemistry as the 1883 rhyodacite. Estimates for magmatic conditions are also presented, using mineral-mineral, and mineral-melt, equilibria. These results will aid the exploration of the third aim, which is to establish the thermochemical architecture of the magmatic system. These datasets are then discussed in tandem with detailed historical records to assess how the subterranean system evolved as the eruption progressed, which addresses the second aim of this thesis.

Chapter 3 then uses experimental petrology to further constrain conditions within the magmatic system. These results are discussed alongside modelled melt chemistry using trace element chemistry in plagioclase and partition coefficients to further explore the chemical structure of the magmatic system, and the processes therein. This chapter tests some hypotheses presented in Chapter 2, and further contributes to the exploration of the third aim, to investigate the architecture of, and conditions and processes within, the pre-eruptive 1883 subterranean system, as well as the second aim when this is integrated into the eruption timeline.

Chapter 4 presents field observations of further explosive deposits associated with Krakatau volcano. Stratigraphy assessed from more distal localities, thought to be related to the 1883 eruption, are reassessed, along with definitively pre-1883 successions, and explosive deposits related to Anak Krakatau. These stratigraphic constraints are then discussed alongside matrix glass chemistry to assess how similar the chemistry of the explosive record at Krakatau is over time, and whether this is similar to other volcanoes in the region. These datasets address the fourth objective in attempting

to correlate the 1883 volcanic deposits further afield. The 2018/2019 eruptive deposits associated with flank collapse of Anak Krakatau are targeted, to look at whether these deposits were eruptive pre- syn- and/or post-collapse and whether their chemistry is similar to other products of Anak Krakatau. This fulfils the fifth and final aim, in investigating the 2018/2019 activity and establishing its stratigraphy. Lastly, Chapter, 5 assesses the final conclusions, implications and future research avenues resulting from this body of work.

2. The magmatic and eruptive evolution of the 1883 caldera-forming eruption of Krakatau: integrating field- to crystal-scale observations

A very similar version of this chapter was published in the *Journal of Volcanology and Geothermal Research*, with the following author list:

Madden-Nadeau, A.L.[1*], Cassidy, M.[1], Pyle, D.M.[1], Mather, T.A.[1], Watt, S.F.L.[2], Engwell, S.L.[3], Abdurrachman, M.[4], Nurshal, M.E.M.[4], Tappin, D.R.[5,6] & Ismail, T.[7]

[1]Department of Earth Sciences, University of Oxford, South Parks Road, Oxford OX1 3AN UK

[2]School of Geography, Earth and Environmental Sciences, University of Birmingham, Edgbaston, Birmingham B15 2TT UK

[3]British Geological Survey, The Lyell Centre, Research Avenue South, Edinburgh, EH14 4AP UK

[4]Faculty of Earth Sciences and Technology, Institut Teknologi Bandung, Jalan Ganesa No. 10 Bandung 40132, West Java, Indonesia

[5]British Geological Survey, Nicker Hill, Keyworth, Nottingham NG12 5GG, UK

[6]Dept. of Earth Sciences, University College, London, WC1E 6BT, UK

[7]Department of Geology, Sekolah Tinggi Teknologi Mineral Indonesia, Bandung 40263, West Java, Indonesia

Abstract

Explosive, caldera-forming eruptions are exceptional and hazardous volcanic phenomena. The 1883 eruption of Krakatau is the largest such event for which there are detailed contemporary written accounts, allowing information on the eruptive progression to be integrated with the stratigraphy and geochemistry of its products. Freshly exposed sequences of the 1883 eruptive deposits of Krakatau, stripped of vegetation by a tsunami generated by the flank collapse of Anak Krakatau in 2018, shed new light on the eruptive sequence. Matrix glass from the base of the stratigraphy is chemically distinct and more evolved than the overlying sequence indicating the presence of a shallow, silicic melt-rich region that was evacuated during the early eruptive activity from May 1883 onwards. Disruption of the shallow, silicic magma may have led to the coalescence and mixing of chemically similar melts representative of a range of magmatic conditions, as evidenced by complex and varied plagioclase phenocryst zoning profiles. This mixing, over a period of two to three months, culminated in the onset of the climactic phase of the eruption on 26th August 1883. Pyroclastic density currents (PDCs) emplaced during this phase of the eruption show a change in transport direction from north east to south west, coinciding with the deposition of a lithic lag breccia unit. This may be attributed to partial collapse of an elevated portion of the island, resulting in the removal of a topographic barrier. Edifice destruction potentially further reduced the overburden on the underlying magmatic system, leading to the most explosive and energetic phase of the eruption in the morning of 27th August 1883. This phase of the eruption culminated in a final period of caldera collapse, which is recorded in the stratigraphy as a second lithic lag breccia. The massive PDC deposits emplaced during this final phase contain glassy blocks up to 8 m in size, observed for the first time in 2019, which are chemically similar to the pyroclastic sequence. These blocks are interpreted as representing stagnant, shallow portions of the magma reservoir disrupted during the final stages of caldera formation. This study provides new evidence for the role that precursory eruptions and amalgamation of shallow crustal magma bodies potentially play in the months leading up to caldera-forming eruptions.

2.1 Introduction

The 1883 eruption of Krakatau (or Krakatoa) is one of the most infamous volcanic disasters, and the first caldera-forming eruption in history to make headline news around the world (Symons et al., 1888). The eruption demonstrated that violent, caldera-forming eruptions can have not only devastating local effects, but also global impacts (Verbeek, 1884; Symons et al., 1888; Simkin and Fiske, 1983). Subsequent work on other caldera-forming systems shows that these high-magnitude, low-frequency events may have very long build-up phases, characterised by both effusive and weakly explosive activity (e.g., Forni et al., 2018; Druitt et al., 2019). Long-term shifts in eruptive style are poorly understood in general, but this is particularly the case for caldera systems, as there has not yet been the opportunity to monitor any volcano during the long run-up through to a caldera-forming eruption; this poses challenges for the interpretation of contemporary geophysical data in volcano monitoring (e.g., Newhall and Dzurisin, 1988; Gottsmann and Marti, 2008; Druitt et al., 2012). Petrological tools offer a unique insight into the architecture of pre-eruptive magma plumbing systems, and the conditions leading up to eruption. The 1883 eruption of Krakatau is particularly useful in this regard, as it is the largest known eruption for which there are multiple documented observations in contemporary accounts, which allow the eruption progression to be integrated with other datasets, analogous to studies of the 79 AD eruption of Vesuvius (e.g. Sigurdsson et al., 1982; Cioni et al., 2000).

Physical and chemical properties of a magma influence its ascent rate and ability to outgas, and are in turn strongly linked with eruptive style (Cassidy et al., 2018). Petrological data allow pre-eruptive magma storage conditions, such as pressure, temperature and volatile content, to be constrained. Pressure is an important constraint, as it controls water solubility, and thus viscosity, and pressure estimates can also be used to infer magma storage depths. Temperature is a key parameter when estimating timescales of magmatic processes based on diffusion models (e.g., Costa et al., 2020). In addition, petrological data can provide information on magmatic processes like mafic recharge, magma mixing, assimilation and fractional crystallisation (e.g., Knesel et al., 1999; Ruprecht et al., 2012; Cassidy et al., 2015; 2016).

Past studies place some constraints on the structure of the upper-crustal magma storage system at Krakatau. Mandeville et al. (1996a) proposed that the 1883 eruption was fed from a chemically and thermally zoned magma reservoir at 5 to 8 km depth. From the analysis of co-existing iron-titanium oxides, Mandeville et al. (1996a) inferred that a rhyodacite magma (880-890°C) overlay progressively hotter dacites (890-913ºC), and andesites (980-1000°C). Fugacity of oxygen was estimated by the same method for rhyodacitic pumice at -10.79 to -11.07 log fO_2 (or approximately 0.96 to 1.43 above nickel-nickel-oxide (NNO) buffer; assuming pressure at 100 MPa). Dahren et al. (2012) used petrological and seismic techniques to analyse the structure of the plumbing system beneath Anak Krakatau, the post-caldera volcano that in 1927 emerged above sea-level within the 1883 Krakatau caldera. They concluded that the contemporary and 1883 plumbing systems were likely to have been subject to comparable structural controls, based on compositionally similar phenocrysts. From mineral data, they inferred that magmas stalled in three lithologically controlled zones: 23 – 28 km (plagioclase cores), 7 – 12 km (clinopyroxene) and 3 - 7 km (plagioclase rims). The only constraints on pre-eruptive magmatic water contents come from analysis of volatiles by difference of glass inclusions, at 4 +/- 0.5 wt% (Mandeville et al., 1996a). In this study, we provide further constraints on critical magmatic storage conditions (temperature, pressure, H_2O content, fO_2) prior to the 1883 eruption.

There is still debate regarding the main triggers involved at various stages of the 1883 eruption. Potentially important processes include (i) fractional crystallisation, potentially leading to "second boiling" (Camus et al., 1987; Mandeville et al., 1996a), (ii) magma mixing (Francis and Self, 1983; Self and Wohletz, 1983) and (iii) phreatomagmatism, which has been proposed as a trigger for the main explosions on the morning of 27th August (Verbeek, 1884). Self and Rampino (1981) ruled out phreatomagmatism as they found no textural evidence for interaction of the magma with water during fragmentation. Verbeek (1884) reported two distinct ash compositions that were erupted during May 1883: dacite and a high-alumina basalt (Stehn 1929). This led Francis and Self (1983) and Self and Wohletz (1983) to suggest that magma mixing triggered the initial stage of the Krakatau 1883 eruption. Several studies have noted the presence of rare, banded pumice clasts from the main phase

of the eruption (e.g., Self and Rampino 1981), which is often used as an indicator for magma mixing (Sparks et al., 1977; Andrews and Manga, 2014; Rossi et al., 2019). However, the two visually distinct glasses are of very similar chemical compositions (Self, 1992). Camus et al. (1987) and Mandeville et al. (1996a) suggested that fractional crystallisation was the most important process prior to the 1883 eruption, increasing the SiO_2 content of the residual melt and enriching it in volatiles. Both factors make an eruption more likely and potentially more explosive (Blake, 1984). A final process recognised for the 1883 and contemporary Krakatau system is assimilation of crustal material (Gardner et al., 2012). Using mineral and whole rock Sr isotope data, Gardner et al. (2013) showed that evolving basaltic andesite (Anak Krakatau) to rhyodacite (1883 compositions), required 45% crystallisation, accompanied by assimilation of 5-23% carbonate or quartzo-feldspathic siltstone.

This study aims to integrate the known eruptive progression at Krakatau in 1883 – based on historical accounts – with new studies of the stratigraphy, crystal zoning and glass geochemistry. The new exposure of pyroclastic sequences from the 1883 eruption by the tsunami generated by the flank collapse of Anak Krakatau in December 2018 (Grilli et al., 2019; Novellino et al., 2020), means that it is possible to build significantly on prior work (e.g., Self, 1992; Mandeville et al., 1996a). Whole-rock and matrix glass data were collected and analysed in the context of this sequence and help to constrain the chemical structure of the plumbing system, allowing the magma reservoir zonation hypothesis to be tested. Thermodynamic modelling using Rhyolite-MELTS (Gualda et al., 2012), provides further insight into the role of fractional crystallisation prior to the 1883 eruptions. Chemical analyses of both plagioclase and pyroxene phenocrysts at higher spatial resolution than previous studies (e.g., Mandeville et al., 1996a) allow the crystal growth history to be constrained in more detail. Furthermore, thermobarometric and hygrometric models provide improved constraints on magmatic conditions. These field observations, geochemical and petrological data shed new light on this highly active caldera system, and provide new context for the monitoring of the present-day activity of Anak Krakatau, as well as providing broader lessons applicable to other similar systems globally.

2.2 Geological Context

2.2.1 Tectonic setting

The Krakatau complex comprises four islands: Panjang, Sertung, Rakata, and Anak Krakatau (Figure 2.1). Panjang and Sertung are remnant islands left behind after a caldera-forming eruption prior to that in 1883; Rakata is the southern remnant of a pre-existing larger island that lay between Panjang and Sertung, the northern two thirds of which was destroyed in 1883 (dashed line, Figure 2.1). Prior to the 1883 caldera collapse, this main island of Krakatau consisted of three volcanic centres aligned NNW: Perboewatan, in the north, Danan, in the centre, and Rakata forming a higher peak to the south (Figure 2.1). Anak Krakatau is the current subaerial volcanic cone, which first emerged above sea-level in 1927 on the same alignment as the 1883 vents, and lies between the positions of Perboewatan and Danan.

The Krakatau archipelago is part of the Sunda Arc; volcanism in this region is caused by subduction of the Indo-Australian Plate beneath the Eurasian Plate (Figure 2.1). Krakatau lies in the Sunda Strait, between Java and Sumatra, at the intersection of a NNE trending lineament of Quaternary volcanic edifices roughly perpendicular to the Java trench (Nishimura et al., 1992) and a fault connecting Krakatau with the Sunda Graben (e.g. Harjono et al., 1989). The Sunda Strait is extending, as Sumatra rotates relative to Java (Ninkovich, 1976; Hall and Spakman, 2002; Hall, 2012). Therefore, magmatism in the Sunda Strait is not only a function of subduction, but also of rifting and extension (Harjono et al., 1989) associated with slab-thinning and mantle upwelling beneath Krakatau (Abdurrachman et al., 2018).

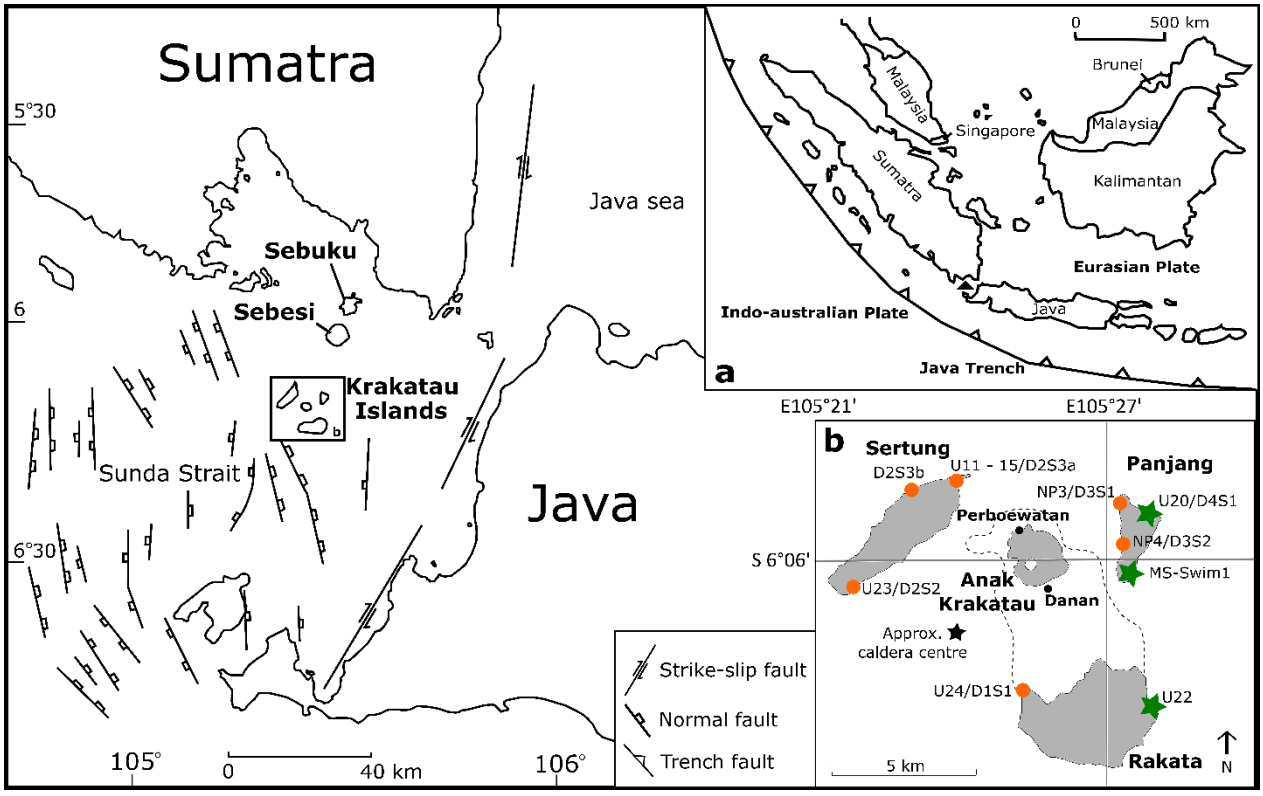

Figure 2.1: Tectonic map showing the Sunda Straits, with insert (a) showing the Java trench and (b) showing the Krakatau islands and field sites visited. The green stars in insert (b) are new field sites, presented here for the first time, whereas localities matching, or very close to, the orange circles were also visited by Self and Rampino (1986) and/or Mandeville et al. (1996b). Localities with two names were visited in both field campaigns (2017 and 2019). All sites visited in 2019 had considerably more exposure than observed and/or presented previously, due to erosion by the 2018 tsunami associated with a flank collapse on Anak Krakatau. The black star labelled approx. caldera centre marks the deepest part of the caldera structure, estimated from bathymetric data from Deplus et al. (1995). The dotted line represents the island prior to collapse in 1883, with Perboewatan and Danan, the 1883 active cones, marked as black circles. Figure based on Mandeville et al. (1996b), Schlüter et al. (2002), Lunt et al. (2009), Susilohadi et al. (2009) and Dahren et al. (2012).

2.2.2 Pre-1883 eruptive history

The ages of pre-1883 eruptions are uncertain. Drill core data suggests an eruption in the Sunda Straits at ca. 60 ka, however this cannot be definitively attributed to Krakatau (Ninkovich, 1979). The Javanese chronicle Pararaton, or the Book of Kings, describes a very large eruption, with "heavy rains of stone" in 416 AD originating from the straits of Sunda (Symons et al., 1888). However, no geological evidence presented to date substantiates this eruption. In May 1681, observations of earthquakes and pumice were made in the diaries of Johann Wilhelm Vogel and Elias Hesse, likely pertaining to an eruption of Krakatau (Vogel, 1690; Hesse, 1690; Hesse, 1694; Verbeek, 1884).

2.2.3 1883 Eruption

The eruption of Krakatau volcano on 26th and 27th August 1883 was the culmination of at least four months of unrest (Figure 2.2). The climactic eruption ejected 18 – 21 km^3 of dominantly rhyodacite ejecta (9 – 10 km^3 dense rock equivalent; Self and Rampino, 1981) in a sequence of pyroclastic density currents (PDCs) that swept across the straits of Sunda, causing volcanogenic tsunamis. In total there were approximately 36,000 fatalities (Self, 1992). This eruption resulted in the destruction of two-thirds of the main island of Krakatau, forming a submarine caldera, which manifests today as a 250 m deep depression in the seafloor (Deplus et al., 1995). The soundwaves produced from the eruption were the greatest ever recorded in the audible range , and the atmospheric effects were seen around the world, with vivid sunsets observed up to a year after the eruption (Symons et al., 1888).

The first record of the 1883 eruption of Krakatau is for 20th May, with contemporary descriptions suggesting Vulcanian to Sub-Plinian activity from Perboewatan (Verbeek, 1885), which declined after 22nd May (Symons et al., 1888). Self (1992) suggested that this precursory eruption column reached 20 km, with ash fall up to ~375 km away. There are no records of activity between 23rd and 26th May (Symons et al., 1888). On 27th May a party visited the island and observed explosions every 10 minutes (Verbeek, 1885). While there are no specific records from 28th May to 19th June, Krakatau was reported to have continuously expelled "smoke" throughout June according to the newspaper

Javasche Courant, and Symons et al. (1888) report no interruption in activity "according to reports from lighthouses… and vessels". Krakatau began to "smoke heavily" again on 19th June (Simkin and Fiske, 1983) (Figure 2.2).

On 24th June, a second column of "smoke" was observed from Java for the first time, likely emanating from Danan. This coincided with the reported disappearance of the summit of Perboewatan (Symons et al., 1888). However, Ferzenaar, who was the last person to set foot on the island on 11th August prior to the climactic phase of the eruption, instead reported that Danan had partially collapsed (Verbeek, 1885). The few records that exist suggest that activity continued to fluctuate. Verbeek (1885) observed "no ash" but "a hazy red glimmer" on 3rd July, interpreted to be lava extrusion, and Symons et al. (1888) reported "continued eruptions, earthquakes and occasional violent explosions" throughout July.

Plinian activity began on 26th August (Figure 2.2). At 2pm local time, a black eruption column rose ~ 26 km into the atmosphere, with explosions every 10 minutes (Sturdy, 1884). By 3pm, explosions were heard ~ 670 km away (Symons et al., 1888), and the first abnormal sea wave was recorded in Batavia (modern-day Jakarta; Latter, 1981). By 5pm explosions were heard all over Java (Symons et al., 1888). There was intense volcanic lightning through the night and a strong sulphurous smell was reported on nearby ships, such as the Charles Bal (Sturdy, 1884).

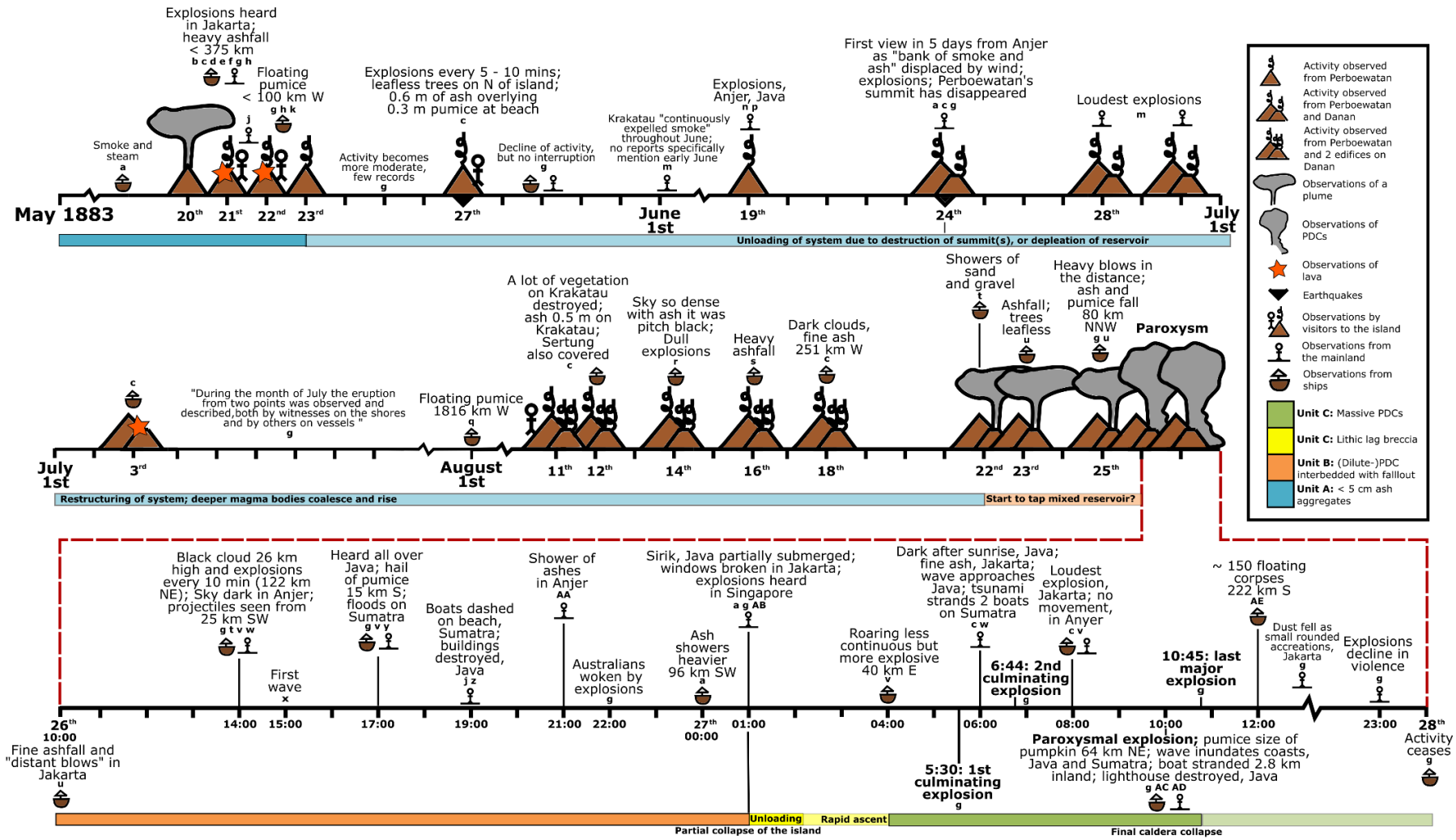

Figure 2.2: Schematic diagram showing the timeline of the eruption as given by various eye witness accounts. The accounts from which the information is taken is represented by letters, as follows: (a) Tenison-Woods (1884), (b) Times of London 03/06/1883, (c) Verbeek (1885), (d) Captain Walker 16/06/1883, (e) MacKenzie, Java Bode 30/05/1883, (f) Tagliche Rundchau (1883), (g) Symons et al. (1888), (h) Grainger, Algmeen Dagblad 23/05/1883, (j) Furneaux (1964), (k) Sulzer, Java Bode 30/05/1883, (m) Javasche Courant, 20/07/1883, (n) Algemeen Dagblad, 20/06/1883, (p) Algemeen Dagblad, 26/06/1883, (q) Ashdown (1883), (r) Bataviaasch Handelsblad, 16/08/1883, (s) Algemeen Dagblad, 17/08/1883, (t) Joly (1885), (u) van Heerdt, report in Royal Society archives, (v) Sturdy (1884), (w) Metzger (1884), (x) Latter (1981), (y) Algemeen Dagblad, 11/09/1883, (z) Algemeen Dagblad, 05/09/1883, (AA) Bataviaasch Handelsblad, 09/09/1883, (AB) Algemeen Dagblad, 27/08/1883, (AC) Ceylon Observer 06/09/1883, (AD) Algemeen Dagblad, 03/09/1883, (AE) Times of London, 08/10/1883. Interpretations regarding the eruptive progression have been made from this, and then has been combined with information of the 4 units in the 1883 eruptive deposits. Page numbers for more accessible sources for historical references (Macleod, 1884; Joly, 1885; Verbeek, 1885; Symons et al., 1888; Furneaux, 1964; Simkin and Fiske, 1983) can be found in Supplementary Table A, Appendix 1. Note that not all tsunami timings have been included, due to limited space.

The most powerful explosions, based on pressure deviations recorded on the Batavia gasometer record (Latter, 1981), occurred at 5.30 am, 6.44 am, ~10:00 am and 10.45 am on 27th August (Symons et al., 1888); the third of these was the most violent, and was heard 850 km away in Singapore (Strachey 1888). Multiple tsunami waves traversed the Sunda Straits from the 26th to 27th August and caused the majority of casualties (Symons et al., 1888). The largest of these waves originated at approximately 10 am on 27th August (Verbeek, 1885; Latter, 1981), broadly coinciding with the most powerful recorded explosion. The whole of the northern portion of the island disappeared into the sea during caldera formation (Lindemann, 1884). However, the precise timing of caldera collapse has not yet been determined (Self, 1992). Details of historical sources are summarised in Supplementary Table A in Appendix 1.

2.2.4 Anak Krakatau

In 1927 Anak Krakatau, or "child of Krakatau", emerged above the sea surface, forming a new subaerial volcanic cone (Stehn, 1929). This soon became a permanent island, which has grown rapidly. Since the 1960s, when the active vent stopped interacting with seawater, Anak Krakatau has predominantly erupted effusively, punctuated with Vulcanian and Strombolian explosions (Abdurrachman et al., 2018).

A period of elevated activity from July to October 2018 culminated in the collapse of the southwestern portion of Anak Krakatau on December 22nd 2018. This created a volcanogenic tsunami which greatly impacted the coast along the straits of Sunda, killing 437 people (Grilli et al., 2019; Novellino et al., 2020).

2.3 Methods and material

2.3.1 1883 Stratigraphy and samples

Field campaigns to the Krakatau islands were undertaken in September 2017 and August 2019. Some field locations, originally described by Self and Rampino (1981) and Mandeville et al. (1996b), were revisited (Figure 2.1b). The 2019 field campaign provided new constraints on the stratigraphic sequence, as erosion associated with the December 2018 tsunami increased exposure of the 1883 sequence considerably at all localities. Stratigraphic logs were created from field observations, and cross correlated using lithological and stratigraphic characteristics, as well as glass chemistry.

In addition to samples collected on both field campaigns, three archived samples from the British Geological Survey (BGS) were analysed: two from the mail steamer Norham Castle (08 and 72), which was 92 km from Krakatau in the Sunda Straits on 26th and 27th August 1883, and one sample of ash from "Districts of java opposite Krakatau and on volcanic island itself" (07). Field locations and sample details are presented in Analytical Data 1 in the published dataset Madden-Nadeau (2020).

2.3.2 X-ray fluorescence (XRF)

Whole-rock chemistry, when placed in the context of the eruption stratigraphy, can allow for a better understanding of the structure of the magma reservoir and, in particular, will allow us to test whether it was chemically zoned. A selection of samples collected through the 1883 stratigraphy were analysed for whole-rock major and minor element chemistry by X-Ray Fluorescence (XRF) at the Department of Geology, University of Leicester on a PANalytical Axios Advanced XRF spectrometer. Most of these samples were powdered pumice clasts, except for one sample comprising fine ash aggregates (U22.2), and four samples of bulk tephra, containing both ash and pumice. For the pumice analyses, multiple clasts were powdered from a single sample and analysed in a single aliquot.

Major and minor elements (SiO_2, TiO_2, Al_2O_3, Fe_2O_3, MnO, MgO, CaO, NaO_2, K_2O, P_2O_5 and SO_2) and Loss on Ignition (LOI) were determined on fused glass beads prepared from ignited powders, while trace elements (As, Ba, Ce, Co, Cr, Cs, Cu, Ga, La, Mo, Nb, Nd, Ni, Pb, Rb, Sb, Sc, Se, Sn, Sr, Th, U, V, W, Y, Zn, Zr) were determined on pressed pellets.

2.3.3 Scanning electron microscope (SEM)

Obtaining back-scatter electron (BSE) images of plagioclase and pyroxene phenocrysts allows us to investigate of crystal zoning. BSE images of plagioclase, pyroxene and matrix glass picked from crushed pumice samples and mounted in resin blocks, were obtained with an FEI Quanta 650 field emission gun (FEG) scanning electron microscope (SEM) in the Department of Earth Sciences, University of Oxford, and a Zeiss Merlin Compact FEG-SEM at the Sir William Dunn School of Pathology, University of Oxford. Operating conditions were 20 KeV with a 15-micron aperture.

2.3.4 Electron Probe Microanalysis (EPMA)

Chemical changes across phenocryst phases record pre-eruptive processes and conditions. Phenocryst phases were analysed on a FEG CAMECA SX-5 electron microprobe at the Department of Earth Sciences, University of Oxford. Sodium was always analysed first with a 10 s peak count time, to prevent Na migration.

Compositional profiles (n = 56) for Al, Si, Na, Ca, K, Fe, Ti, Mn and Mg were collected by Electron Probe Microanalysis (EPMA) for plagioclase phenocrysts at a 15 kV acceleration voltage and 20 nA beam current, with a 5-micron defocussed beam size. Point spacings in line analyses were approximately 10 microns. Points were also analysed for BSE image calibration for anorthite content with the same operating conditions. Plagioclase phenocrysts were picked from archived ash collected at the time of the eruption (BGS samples), as well as samples collected in the field. Phenocrysts

were picked from samples of multiple crushed, cm-scale pumices, one ash sample, one sample of ash aggregates and two bulk tephra samples containing both pumice and ash.

Compositional profiles for pyroxene phenocrysts picked from archived ash collected at the time of the eruption (BGS samples; n = 46) were obtained at 15 kV, with a focused beam of 20 nA for Al, Si, Na, Ca, Fe, Ti, Mn, Cr and Mg. Fe/Ti oxides (n = 419) partially included into the rim of pyroxene phenocrysts and in contact with the melt from both archive and field samples, were also analysed as points under the same conditions.

Any changes in glass chemistry through the stratigraphy may illuminate the chemical structure of the magma reservoir. Point analyses of matrix glass, mounted in resin, were analysed on a Jeol JXA-8200 electron Microprobe in the School of Archaeology, University of Oxford. Glass analyses were conducted at 15 kV with a 5-micron defocussed beam of 6 nA for Al, Si, Na, Ca, K, Fe, Ti, Mn, Mg, P and Cl. Secondary standards of a similar composition to the target glass were analysed to check the accuracy of the calibration (see Supplementary excel file for Chapter 2, Supplementary Data 1). Most matrix glass analyses were obtained from grains picked from multiple crushed, cm-scale pumices, however two samples contain only ash, one ash-aggregates, and one is a bulk tephra sample, containing both pumice and ash. Multiple pumices were crushed per sample, and glass clasts were picked and mounted from crushed material. We also analysed a sample of crushed obsidian, and three samples taken from large glassy blocks at D2S2/U23. For each sample, analyses are based on at least two clasts, except for D1S1.2 and U23.7 where the only viable analyses came from the same clast.

2.3.5 Vesicularity and crystallinity

Investigating changes in crystallinity throughout the stratigraphy may aid in illuminating the structure of the subterranean magmatic system. Thin sections of pumice were used to estimate the phenocryst content of the 1883 samples through the stratigraphy. Five images per sample were photographed through a transmitted light microscope, and crystals were traced by hand using image

processing software to provide an average estimate of crystallinity reported on a vesicle-free (VF) basis. An example of a pictomicrograph used is in Supplementary Figure A, Appendix 1. Vesicularity is formed on magma ascent and thus represents conduit processes; changes in vesicularity throughout the stratigraphic sequence therefore reflect changes in conduit processes as the eruption progressed. The average vesicularity of the 1883 samples was estimated from BSE images (five to nine grains imaged per sample), picked from crushed samples, and thresholded using image processing software (e.g., Burgisser et. al., 2010). Estimates for vesicularity are likely to be slightly underestimated, as a result of plane of section effects.

Error will also be incurred as a result of the degree of user-defined thresholding chosen for each BSE image, and differences in how phenocrysts are traced by hand. Repeat measurements of thresholding and crystal tracing was carried out 10 times on a single image, averaged over 5 images, to give a 1 σ error in crystallinity estimates of +/- 0.1 %, and in vesicularity of +/- 2.5 %.

2.3.6 BSE image calibration for Plagioclase

Back scatter electron (BSE) intensity profiles of plagioclase phenocrysts were calibrated for anorthite content using quantitative point analyses obtained by EPMA following the approach outlined by Ginibre et al. (2002). Most phenocrysts were calibrated individually where enough EMPA data were available, whilst a global calibration was used for other crystals where brightness and contrast settings on the BSE images made the images comparable. Global calibrations were only used where $R^2 > 0.8$ for the correlation between anorthite and grey scale, determined using imageJ.

2.4 Results

2.4.1 Fieldwork and stratigraphy

The stratigraphic sequence of the 1883 eruptive deposits has previously been established by Self and Rampino (1981) and Mandeville et al. (1996b), however, the significantly increased exposure of

deposits in coastal cliffs following the 2018 tsunami made this worth revisiting. The stratigraphy as presented by Self (1992) (after Self and Rampino, 1981) and Mandeville et al. (1996b), is shown in Figure 2.3. Terminology for deposits pertaining to pyroclastic density currents (PDCs), and particularly dilute-PDCs, has been subject to some ambiguity. Here, we use the terms PDC deposit to refer to any unit with characteristics consistent with flow-driven transport and sedimentation; and we use the term dilute-PDC deposit specifically for those PDC units which show cross stratification and are generally finer-grained and better sorted, following Branney and Kokelaar (2002). Previous authors have used the terms ignimbrite to refer to PDC deposits with more massive or poorly sorted characteristics, and surge deposits for those with dilute-PDC deposit characteristics. However, when discussing stratigraphic descriptions of previous authors, we use their original terminology.

2.4.1.1. Previous work

Self and Rampino (1981) reported that the proximal stratigraphy comprised sub-Plinian fall deposits interbedded with surge (i.e., dilute-PDC) deposits up to 20 m thick, overlain by up to 55 m of massive ignimbrite (i.e., PDC deposit). Mandeville et al. (1996b) reported a layer of olive- to bluish-grey, fine-ash fall deposit up to 4 cm thick at the base of the 1883 deposit, which overlies a soil horizon on West Rakata and West Panjang (equivalent to our localities U24/D1S1 and NP3/D3S1, respectively). They attributed this to phreatomagmatic activity in May to August 1883. Next in the sequence, Mandeville et al., (1996b) reported 5 - 20 cm of coarse, light-grey pumice fall deposit, followed by 4 to 6 m of fall deposits interbedded with surge deposits. At the top of the stratigraphy, Mandeville et al. (1996b) report thick accumulations of massive pyroclastic flow (i.e., PDC) deposits. The thickness of the fall deposit layer is therefore disputed, with Self and Rampino (1981) observing fall deposits interbedded with surges up to 20 m thick, and Mandeville et al. (1996b) observing up to 6.2 m of fall deposit interbedded with surge deposits.

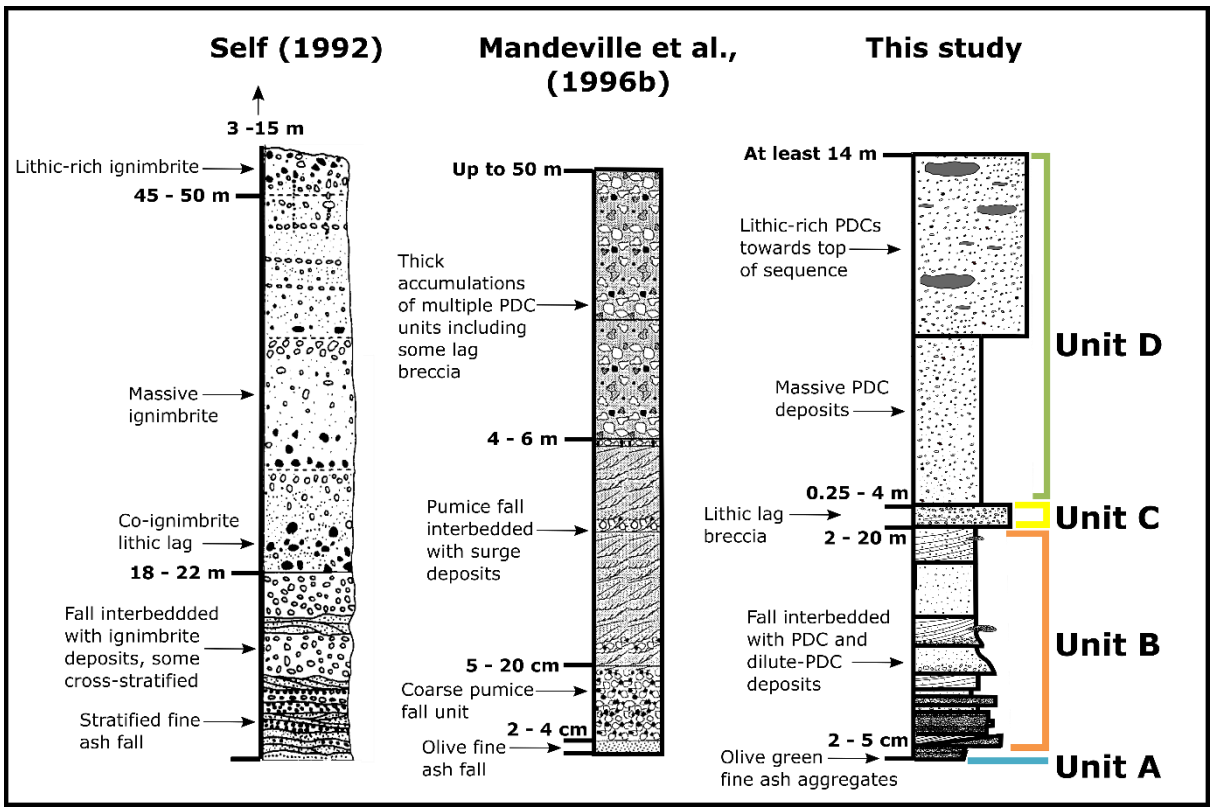

Figure 2.3: Composite logs of stratigraphy derived by Self (1992), Mandeville et al., (1996b) and this study. Thicknesses are for individual units, and are not cumulative.

2.4.1.2. This study

We present our new composite stratigraphy in Figure 2.3; field logs, stratigraphic correlations and field photographs for each locality are shown in Appendix 2. Like Mandeville et al. (1996b), we found a distinctive olive-green ash fall deposit at the base of the sequence (Figure 2.3), which we term Unit A (Figure 2.3; 2.4a). Unit A is between 2 and 5 cm thick and was only found exposed on West Rakata and South Panjang. This layer overlies a red paleosol, and is composed of fine-ash aggregates. A back-scatter electron image of the ash aggregates can be found in Supplementary Figure B, Appendix 1.

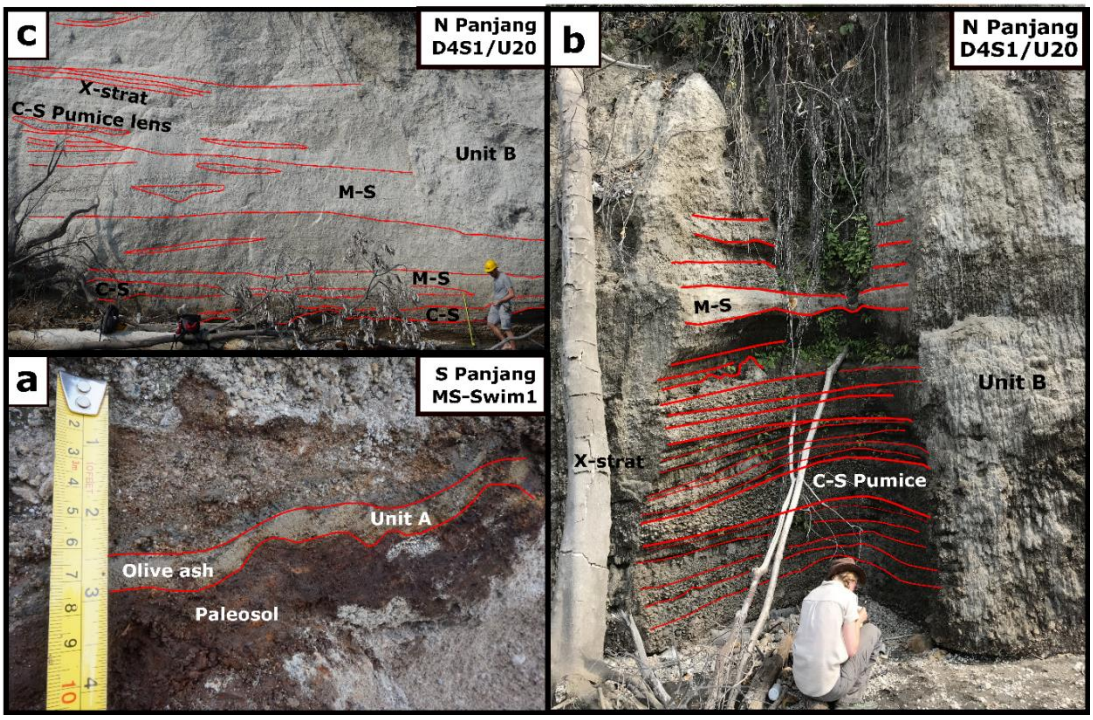

Figure 2.4: Panel (a) shows Unit A, as observed from locality MS-Swim1 on South Panjang, which is a thin layer of olive-green ash aggregates, overlying a red paleosol. Panel (b) shows the base of Unit B at locality D4S1/U20 on North Panjang, which is composed of clast-supported (C-S) fallout layers, interbedded with dilute-PDC deposits that show cross-stratification (X-strat). Panel (c) shows the units overlying those in panel (b), at the same locality (D4S1/U20). These are also part of Unit B, and show matrix-supported (M-S) dilute-PDC deposits interbedded with pumice-supported lenses. All locations are shown in Figure 2.1. People (b) or measuring tape (a and c) for scale; measuring tape is 1 m in (c).

Unit B is characterised by well-sorted beds of angular lapilli, interbedded with poorly sorted layers which are matrix-supported (Figure 2.4b; 2.4c; 2.5a). Clasts within the well-sorted layers are predominantly juvenile pumice (>80%), the remainder being dense, angular, and visibly altered volcanic lithics; Mandeville et al. (1996b) determined that the majority of these lithics are basalt and basaltic andesite. Of the juvenile clasts, ~90% are white pumice, although pink, grey and yellow pumice are also observed. Clasts within the poorly sorted units show similar proportions. Some of the poorly sorted beds are cross-bedded, and interpreted as dilute-PDC deposits (after Branney and

Kokelaar, 2002). These dilute-PDC deposits also contain laterally restricted, discontinuous lenses of well-sorted, sub-rounded, pumiceous lapilli. Unit B is interpreted to comprise fall deposits interbedded with PDC and dilute-PDC deposits. We find that Unit B is up to 20 m thick, in agreement with observations made by Self and Rampino (1981) (Figure 2.3). Charcoal and tree moulds were found towards the base of Unit B at two localities. Carbonised logs were also reported by Mandeville et al. (1996b), but not attributed to a specific unit within the stratigraphy.

Next in the sequence is Unit C, which is characterised by lithic blocks (up to 50 cm) in a poorly sorted, juvenile matrix (Figure 2.5a; 2.5b). This section of the sequence is interpreted to be a lithic lag breccia (Druitt and Sparks, 1982; Branney and Kokelaar, 2002). Both Self and Rampino (1981) and Mandeville et al. (1996b) identify lithic lag breccias in the sequence (Figure 2.3), however only Self and Rampino (1981) used them as a correlating horizon. The lag breccia is variable in stratigraphic thickness (0.3 to 4 m), and bifurcates in some outcrops (Figure 2.4a). The proportion of lithic blocks within this unit also varies between localities.

Unit D is a massive, poorly sorted, matrix-supported unit containing predominantly pumice clasts (80-90% of clasts) in an ash-rich matrix (Figure 2.5b). Both Self and Rampino (1981) and Mandeville et al. (1996b) identify a similar unit towards the top of the sequence (Figure 2.3). The structureless nature of Unit D suggests it was likely deposited by large volume, high-concentration PDCs. Another characteristic feature of Unit D is the presence of obsidian clasts. Frothy, glassy, and banded obsidian clasts are present (e.g., Shields et al., 2016), making it likely that the obsidian is juvenile (Self and Rampino, 1981). Rare black and white banded pumices, as reported by Self and Rampino (1981), were also observed.

A second lithic lag breccia horizon is observed at the top of Unit D on North Panjang (Figure 2.4b), which concurs with an updated stratigraphic log presented by Self (1992) (Figure 2.3). New exposure on South Sertung (D2S2/U23, Figure 2.1), observed for the first time in the August 2019 field campaign, contains large glassy blocks up to 8 m in length within the massive PDC unit (Figure 2.5c). Although the blocks are intact, they are intensely fractured and have sub-rounded irregular shapes, aligned broadly horizontally, but not confined to a single horizon within the deposit (Figure

2.4c). Some of these fractured blocks are black in colour and vitreous, and look similar to the smaller obsidian clasts already identified by Self and Rampino (1981), with a low phenocryst content, whereas other blocks are dull grey in colour, with a higher phenocryst content (comparable to pitchstone). Their geochemistry will be discussed further in section 2.4.5. This section of Unit D also contains clasts of mudstone. We also noted crude horizontal stratification of the PDCs delineated by subtle colour changes; this was also observed in massive PDC units described by Mandeville et al. (1996b).

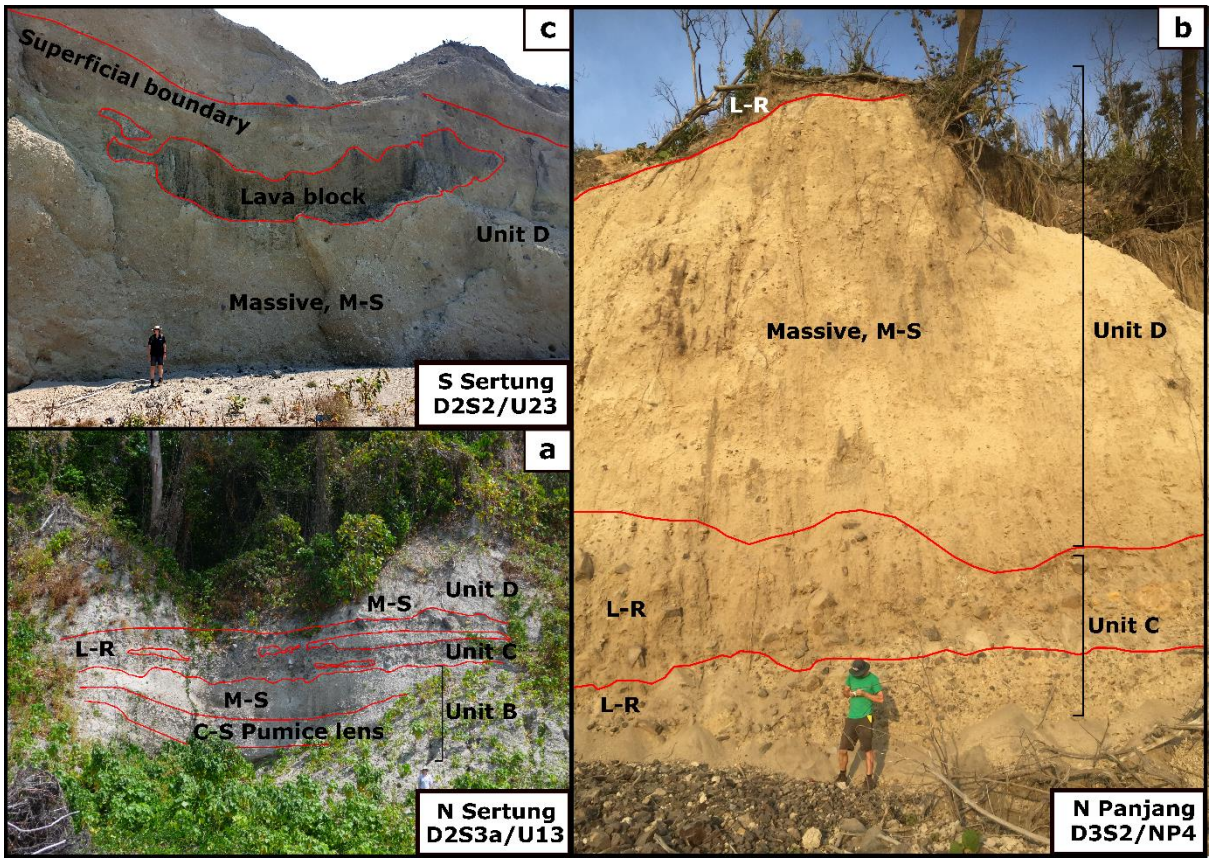

Figure 2.5: Panel (a) shows Units B, C and part of Unit D, as observed from locality D2S3a/U13, North Sertung. Unit B comprises clast-supported (C-S) pumice layers interbedded with matrix-supported (M-S) layers. Panel (b) shows Units C and D at locality D3S2/NP4, North Panjang. Unit C in both panels (a) and (b) show lithic-rich (L-R) layers. Panel (c) shows the top of Unit D at locality D2S2/U23, South Sertung. Unit D is comprised of massive PDC deposits in both panels (b) and (c). In panel (b), there is a second lithic-rich layer at the very top of the sequence. In panel (c) there are large, glassy blocks up to 8 m in size. All locations are shown in Figure 2.1. People for scale.

Locality U22 (Figure 2.6) is the only outcrop where the entire sequence (Units A to D) can be observed. The sequence appears to be condensed (2.8 m), and we use this as a type locality. Key marker beds in the 1883 stratigraphic sequence include: a thin, green, ash-aggregate layer overlying a red paleosol at the very base of the sequence, delineating Unit A (Mandeville et al., 1996b; Figure 2.3; 2.6a); Pumice fallout units interbedded with PDC and dilute-PDC deposits (Self and Rampino, 1981; Figure 2.3), some of which contain charcoal aligned east-west (Unit B; Figure 2.6b); the lithic lag breccia overlying Unit B (Unit C; Figure 2.6c); and Unit D, consisting of massive PDC deposits containing obsidian (Self and Rampino, 1981; Mandeville et al., 1996b; Figure 2.3) (Figure 2.6c). Figure 2.7 shows the logs from each locality cross-correlated by unit.

The spatial distribution and thicknesses of PDC (including dilute-PDC) deposits change through the stratigraphic sequence (Figure 2.8). Unit B is thickest to the north east, with approximately 20 m of vertical exposure (Figure 2.8a). Unit C appears to be more evenly distributed around the main island (Figure 2.8b), whereas Unit D is thickest in the south west (14 m; Figure 2.8c), rather than north as reported by Self and Rampino (1981). These thicknesses are based on only limited exposures, and there are only two localities where it was possible to observe the base of the sequence (MS-Swim1; south Panjang and U22; east Rakata); this will lead to underestimates of unit thickness. Self and Rampino (1981) noted a lack of fall deposits in the south west, which we confirmed.

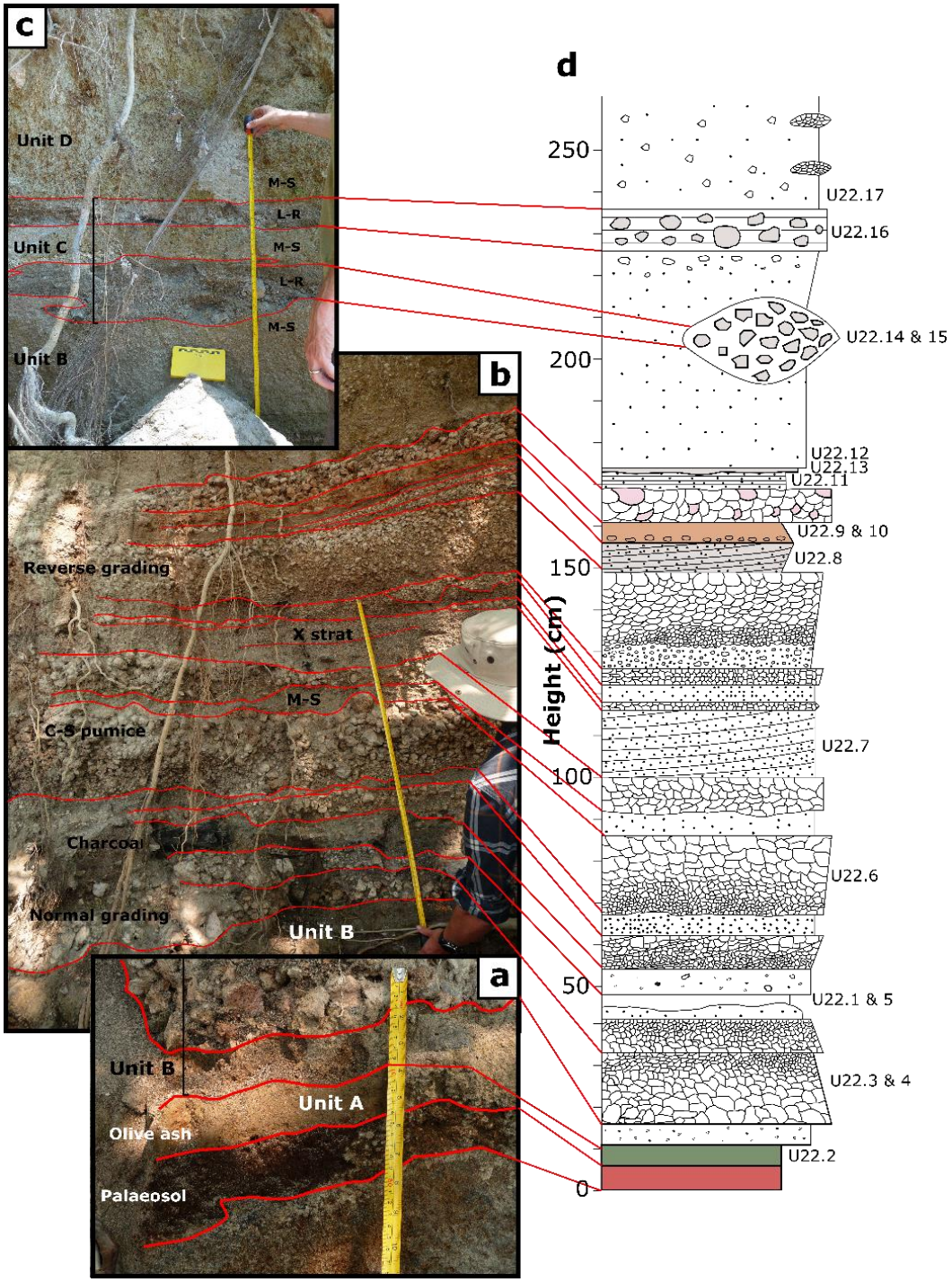

Figure 2.6: Photographs and log of deposit at locality U22 to show the entire sequence (E. Rakata; location shown in Figure 2.1). Panel (a) shows Unit A at the base of the sequence, (b) shows Unit B, (c) shows Units C and D, and (d) shows the cross correlated stratigraphic log, with sample numbers down the right-hand side. C-S stands for clast-supported, X-strat for cross-stratification, M-S for matrix-supported and L-R for lithic-rich. Measuring tape for scale (a-c); measureing tape is 27 cm in (a) and 1 m in (b) and (c) .

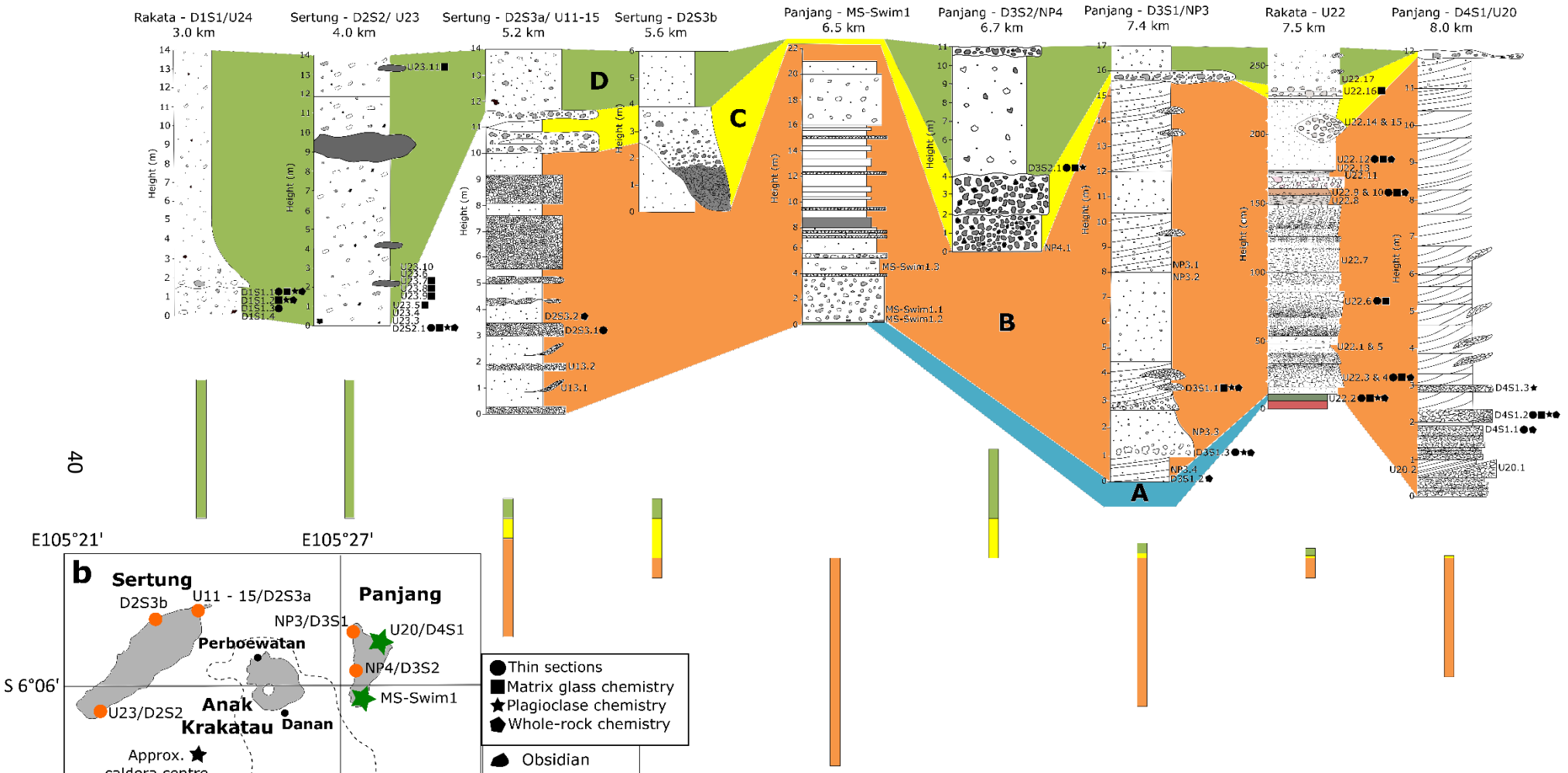

Figure 2.7: Cross correlated stratigraphic logs from all localities visited. It should be noted that the scale varies between logs. Insert map (a) shows the location of each locality, with the locations visited by Mandeville et al. (1996) and Self and Rampino (1986) shown in orange, and fieldsites new to this study indicated by a green star. Letters represent the discussed units, with A corresponding to blue, B to orange, C to yellow and D to green. Bars below logs represent the relative thicknesses of each unit. Symbols by sample numbers represent thin sections and chemical analyses. Distance above log is from the assumed caldera centre, taken from Deplus et al. (1995).

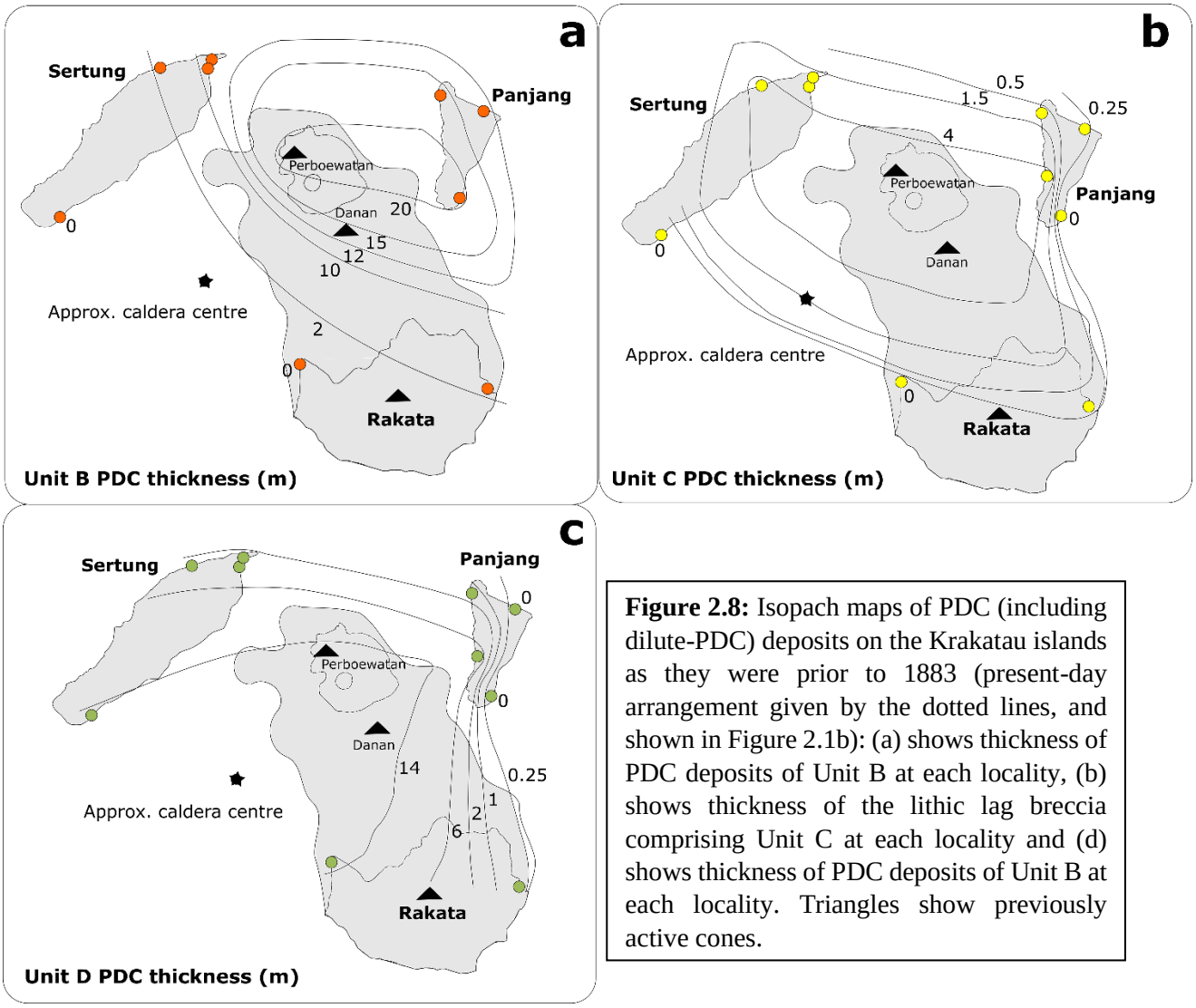

Figure 2.8: Isopach maps of PDC (including dilute-PDC) deposits on the Krakatau islands as they were prior to 1883 (present-day arrangement given by the dotted lines, and shown in Figure 2.1b): (a) shows thickness of PDC deposits of Unit B at each locality, (b) shows thickness of the lithic lag breccia comprising Unit C at each locality and (d) shows thickness of PDC deposits of Unit B at each locality. Triangles show previously active cones.

2.4.2 Vesicularity and crystallinity

Crystallinity of juvenile clasts increase up the stratigraphic sequence. Unit A (n = 1) is comprised of poorly vesicular ash aggregates, with crystallinity (on a vesicle-free (VF)/porosity-free basis) at 5 %. In Unit B (n = 7), crystallinity (VF) ranges from 10 – 20 % and Unit D (n = 3) has a crystallinity (VF) of 30 %. Vesciularity in both Units B and D ranges from 70 – 80 %.

2.4.3 XRF whole-rock chemistry

XRF whole-rock data are presented in Analytical Data 2 in the dataset Madden-Nadeau (2020). The 1883 whole-rock samples have anomalous major element compositions compared with previously reported values (Oba et al., 1982; Self 1992; Mandeville et al., 1996a; Turner and Foden 2001; and Gardner et al., 2013). These samples also have high LOI (3.1 – 8 wt%). We suspect these samples have experienced seawater alteration, based on the positive correlation between LOI and Na_2O (Figure 2.9a), and negative correlation with SiO_2 (Figure 2.9b). The values for major elements are anomalous, even after correcting for LOI, in all but two of the samples, and thus cannot be used to assess the chemostratigraphy.

Trace element compositions show no evidence for alteration, when plotted against Zr, which is a high field-strength element, assumed to be immobile (Figure 2.9 c-f). Correlations between Zr and other incompatible elements provide no evidence for loss or gain of these elements during alteration, as the ratios between them remain constant. Zr vs Y (Figure 2.9e) has the strongest positive correlation, with an R^2 value of 0.87. Once normalised to LOI to correct for the dilution effect (Figure 2.9d and f), there is no discernible systematic correlation with stratigraphic height for Ba and Y with Zr.

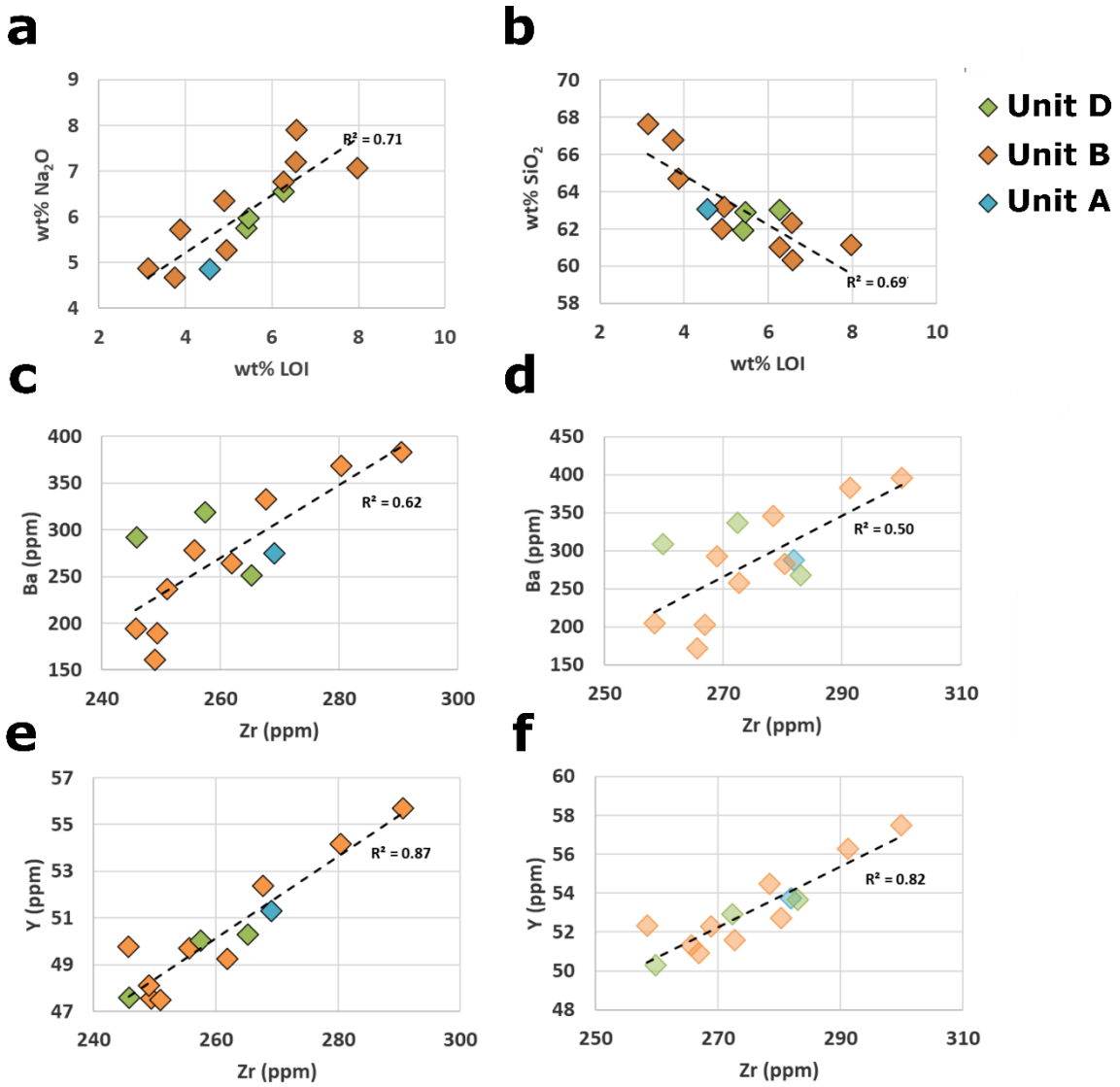

Figure 2.9: (a) a plot showing a positive correlation between LOI vs Na_2O and (b) the negative correlation between LOI and SiO_2, indicating that the samples are likely to have undergone seawater alteration. (c) and (d) show Ba plotted against Zr, which is assumed to be immobile, with (d) showing the data corrected for LOI (transparent symbols). (e) and (f) show Y against Zr, with (f) being corrected for LOI (transparent symbols). The dashed lines are the least squares linear regression, and in (c) and (e) represent the constant ratio between the two trace elements, and thus no losses or gains during alteration. The higher the R^2 value, the less those elements have been lost or gained during alteration. (e) Y vs Zr has the highest R^2 value of 0.87, thus being the elements least affected by alteration, and (f) shows that there is no correlation in chemistry of Y and Zr with stratigraphic height.

2.4.4 Phenocryst textures and chemistry

2.4.4.1 Plagioclase

Plagioclase is the dominant phenocryst phase in pumice clasts throughout the 1883 eruption stratigraphy and, as is typical of subduction settings, most plagioclase crystals are zoned. When discussed here, cores and rims refer to the centre and edge of euhedral, unbroken crystals. Zoning profiles vary between crystals from very complex to unzoned (Figure 2.10). Anorthite (An = molar Ca/(Ca+Na)) compositions present across all sampled plagioclase phenocryst cores, ranges from An_{29} to An_{90} (mean An_{54}; 95 analysed crystals), bearing in mind that the 'core' may be subject to section effects. Phenocrysts also have a wide range in rim compositions: An_{26} to An_{65} (mean An_{48}; 77 analysed crystals) (Figure 2.11). There is no discernible inter-unit variation in crystal textures, or the core and rim anorthite contents. There is also no correlation between anorthite content of the rims and cores. Resorption textures are common (e.g., Figure 2.10a), with some crystals having patchy cores and/or zones (~ 30 %; e.g., Figure 2.10c). Both normal (~ 35 % of rims) and reverse zoning (~ 60 % of rims) are also common at various stages in plagioclase crystallisation histories, with ~ 5 % of crystals showing no zoning at all (Figure 2.10e). The anorthite content of crystals does not converge on a single value at the rims. A high anorthite (>An_{70}) core is observed in ~ 20 % of phenocrysts (e.g., Figure 2.10a). Due to the complexity in the plagioclase phenocryst zoning profiles, it is not possible to identify discrete typologies, or common phases of growth, as has been achieved in previous studies (e.g., Druitt et al., 2012). All whole plagioclase anorthite traverses, from euhedral rim to core, are shown on a single plot in Supplementary Figure C, Appendix 1.

Analytical data for plagioclase phenocrysts, with accompanying BSE images, from Units B to D and archived BGS samples, can be found in Analytical Data 3 – 11 in the dataset Madden-Nadeau (2020). Analytical data for Unit A, and one Unit B sample (U22.3) can be found in the Supplementary excel file for Chapter 2, Supplementary Data 2.

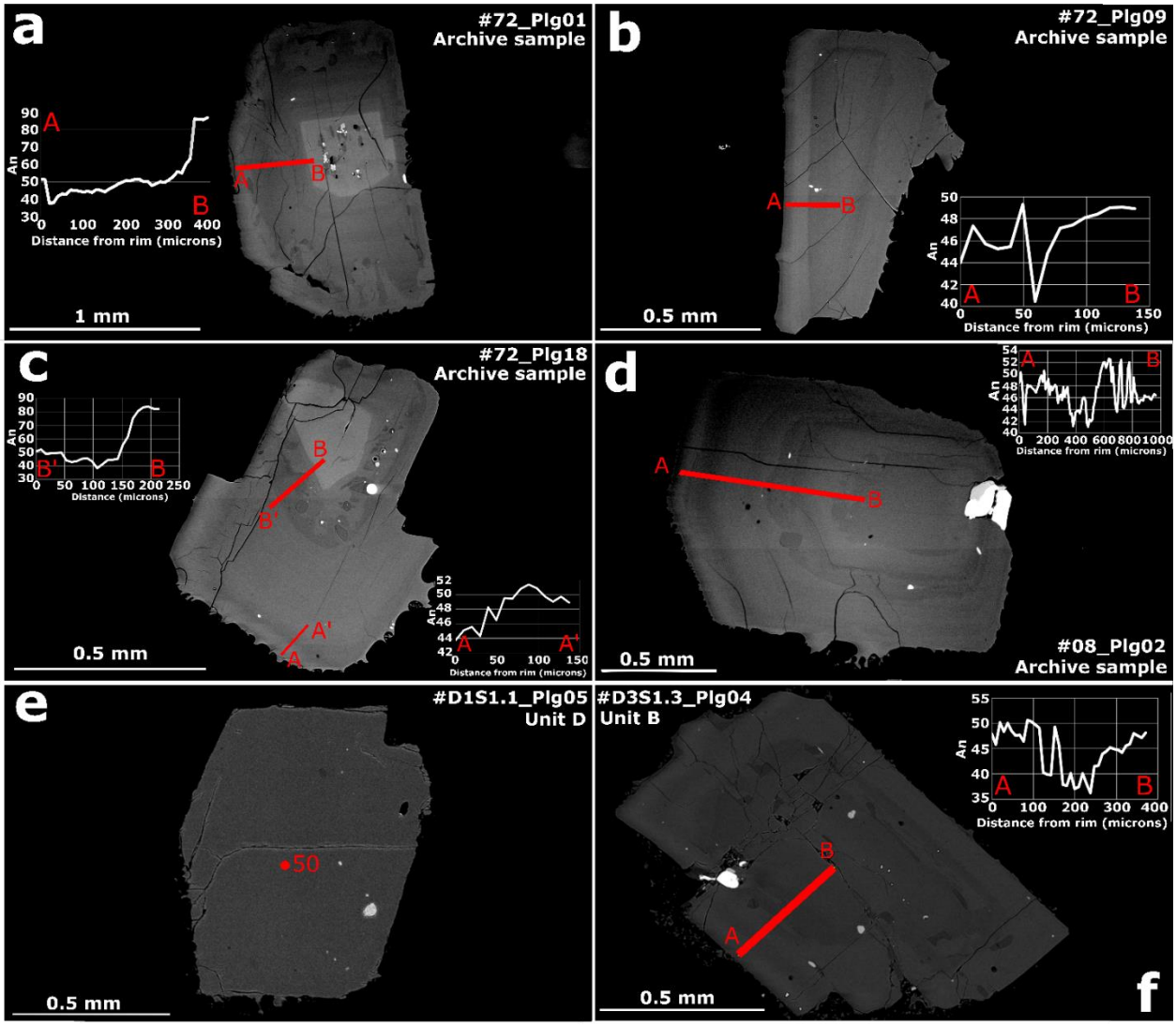

Figure 2.10: BSE images of a selection of plagioclase phenocrysts, with anorthite traverses shown in red. Note that the BSE grey scale differs between each image. Plagioclase (a) has a high anorthite core, followed by oscillatory zoning, resorption textures and a reverse zone at the rim; (b) has a single reverse zone between core and mantle, with normal zoning at the rim; (c) has a high An core, followed by a patchy, resorbed zone, then oscillatory zoning, with normal zoning at the rim; (d) has an An_{46} core with resorption textures, followed by oscillatory zoning, with the rim being reverse zoned; (e) appears largely unzoned with consistent composition of ~An_{50} and (f) has an An_{47} core with resorption textures, followed by two reverse zones.

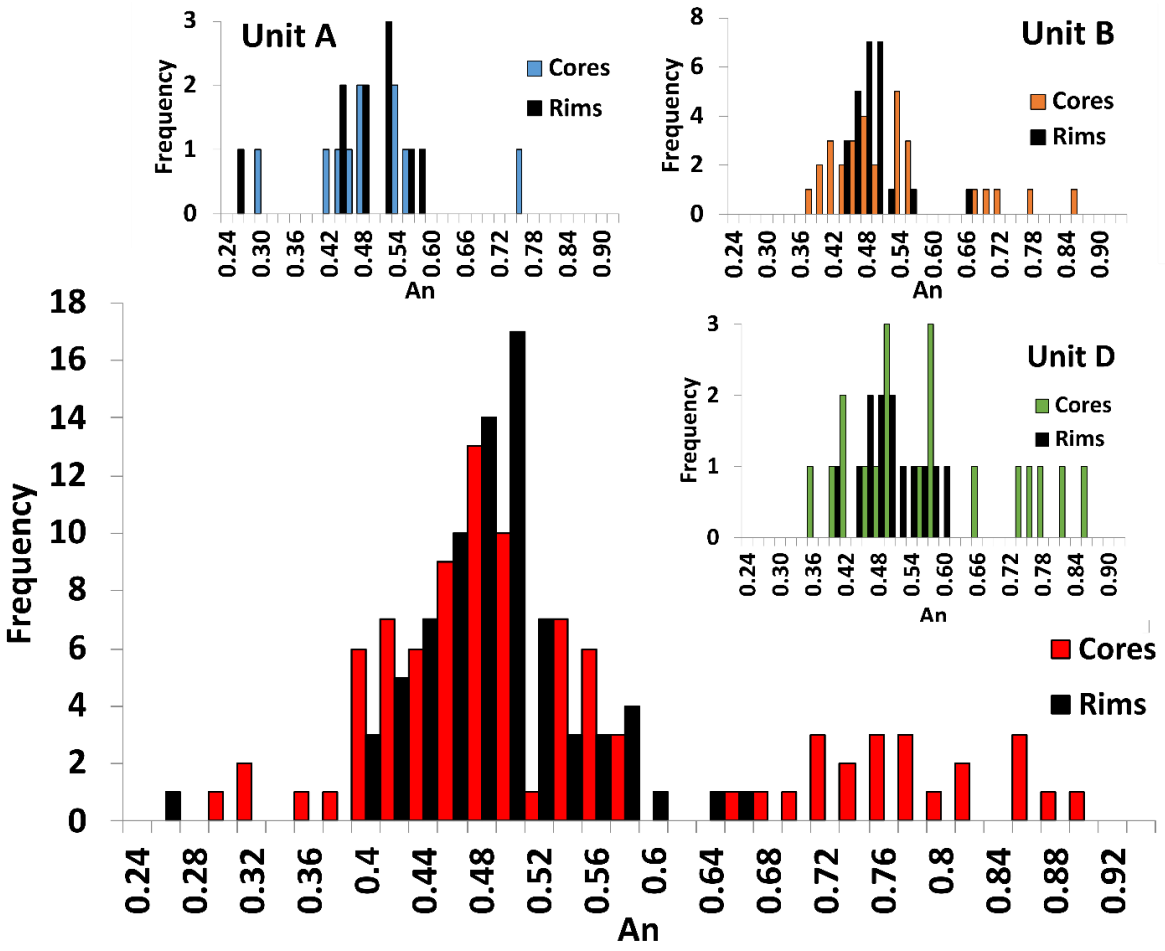

Figure 2.11: Histogram showing the frequency of core and rim compositions in anorthite for plagioclase phenocrysts; 97 individual crystals were used to create this histogram, taken from the 3 archive samples, as well as 4 samples from Units B, 3 samples from Unit D, and one sample from Unit A. The three inserted histograms show distributions of anorthite compositions for Unit A, B and D individually. It should be noted that there will be some error in crystal core compositions as a result of plane of section effects. Not all crystals had both viable core and rim analyses, as rim analyses were only included for euhedral, unbroken phenocrysts.

2.4.4.2 Pyroxene and Fe-Ti oxides

Pyroxene phenocrysts were picked from archived BGS ash samples, collected at the time of the eruption. When discussed here, cores and rims refer to the centre and edge of euhedral, unbroken crystals, and cores may be subject to plane of section effects. Orthopyroxene rims and cores range

in Mg# (Mg# = molar Mg/(Mg+Fe)) from 0.67 to 0.72 (n = 22, σ = 0.01), whilst the range for clinopyroxene is 0.73 to 0.77 (n = 23, σ = 0.01). Pyroxene phenocrysts are largely unzoned in major elements. All data for pyroxene phenocrysts can be found in Analytical Data 12 – 14 in the dataset Madden-Nadeau (2020), and a plot showing all whole pyroxene traverses from euhedral rim to core, is shown in Supplementary Figure D, Appendix 1.

Fe-Ti oxides (n = 419) partially included in pyroxene rims, and in contact with the melt, were analysed from Units B to D in the stratigraphy; they are magnetite and ilmenite. All chemical data for Fe-Ti oxides can be found in Analytical Data 15 in the dataset Madden-Nadeau (2020).

2.4.5 Matrix glass

Matrix glass data for the 1883 pyroclastic sequence normalised to 100 % anhydrous compositions are plotted in Figure 2.12, with full data table in Analytical Data 16 in the dataset Madden-Nadeau (2020). Totals range from 96.0 to 101.2 wt % prior to normalisation. Matrix glasses from Unit A are distinct, and more evolved than the rest of the proximal 1883 sequence, with SiO_2 ranging from 72.6 to 74.7 wt%. Data for Units B, C and D overlap, with a broad trend towards marginally less evolved compositions, showing a slight decrease in both SiO_2 and total alkalis, moving up the sequence (Figure 2.12). SiO_2 for Unit B glasses range from 71.4 to 72.7 wt%, Unit C from 70.9 to 72.3 wt%, with Unit D ranging from 70.6 to 72.3 wt%.

Matrix glass of an obsidian clast and samples from three of the large glassy blocks on the south of Sertung (U23/D2S2.2) within Unit D were also analysed. Matrix glass from the blocks and smaller obsidian fragments are broadly similar to the matrix glass of pumice and ash ejected in the 1883 eruption, extending to more evolved compositions, with SiO_2 ranging from 71.8 to 77.6 wt% (Figure 2.12). Full chemical data for the matrix glass of the blocks can be found in Supplementary excel file for Chapter 2, Supplementary Data 3.

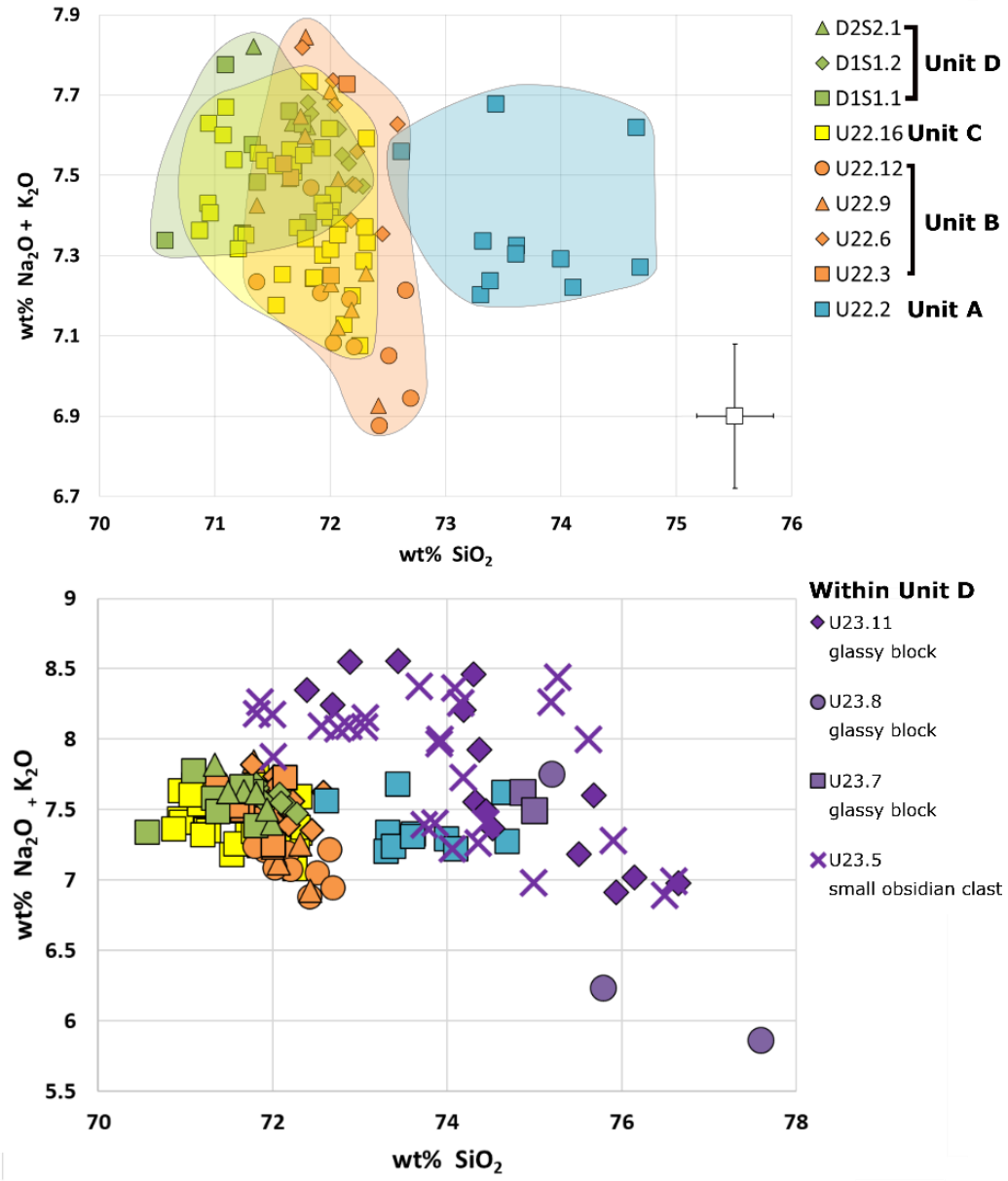

Figure 2.12: (a) Matrix glass data on a total alkali and silica diagram (Le Bas et al., 1986). Colours of symbols and transparent areas correspond to stratigraphic units: A = blue, B = orange, C = yellow and D = green, as in Figure 2.7. Each symbol represents a separate sample, with the key in stratigraphic order. Unit A is more evolved than, and distinct from, Units B to D. Average error is given to 1 σ. (b) shows the same data, overlain with data from the glassy blocks and obsidian found within Unit D at U23/D2S2 on south of Sertung.

2.4.6 Thermometry and hygrometry

2.4.6.1 Fe-Ti oxides

Pre-eruptive temperatures and oxygen fugacities of the 1883 magmas were estimated from the compositions of titanomagnetite and hemoilmenite crystals, using the Fe^{2+}-Mg exchange model of Ghiorso and Evans (2008). Fe-Ti oxide pairs were tested for equilibrium using the Mg-Mn equilibrium line (Bacon and Hirchsmann, 1988). Fe-Ti oxides are likely to yield the last equilibration temperature before quenching (Rutherford and Devine, 1988; Geschwind and Rutherford, 1992; Lindsley and Frost, 1992).

The temperature range for all Fe-Ti oxide pairs (n = 64; 24 touching, 47 partially included within the same pyroxene phenocryst and in contact with the melt; chemical data in Analytical Data 15; dataset Madden-Nadeau 2020) was 890 to 935 ^{o}C, with a mean value of 914 +/- 50 ^{o}C. The range of temperatures generated for the 24 touching Fe/Ti oxide pairs is between 891 and 935 ^{o}C, with an average of 913 ^{o}C. The oxygen fugacity (fO_2) range for all Fe-Ti oxide pairs is 0.6 to 0.85 log units above the nickel-nickel-oxide (NNO) buffer, with the mean being NNO + 0.76. The same range of values for fO_2 is seen within the data set for the 24 touching pairs (average of NNO + 0.74). The temperatures and fO_2 of Units B, C and D all show considerable overlap. A temperature fO_2 plot can be found in Supplementary Figure E, Appendix 1. These temperatures are interpreted as the final pre-eruption equilibration temperature.

2.4.6.2 Plagioclase hygrometer

Pre-eruptive dissolved water content of the melt for samples from Units A, B and D are estimated using a plagioclase-melt hygrometer (Waters and Lange, 2015) which is based on the crystal-liquid exchange reaction between the anorthite and albite components. From the anorthite contents of plagioclase rims and matrix glass data (n = 59), and the mean Fe/Ti oxide temperature (914 ^{o}C), we infer a mean H_2O content of 3.4 wt% for Unit A, 3.6 wt % for Unit B, and 3.5 wt% for Unit D. Allowing for uncertainty in Fe/Ti oxide temperatures (890 to 935 ^{o}C), gives a range of water contents

from 2.6 to 4.3 wt% for all three units. These results are consistent over pressure inputs of 100 to 250 MPa. It should be noted that these are estimates of the final pre-eruptive H_2O contents, and will not reflect the entire range of conditions experienced by plagioclase phenocrysts throughout their crystallisation histories.

Equilibrium in plagioclase is difficult to test, owing to composition being a function of both temperature and H_2O content, however only anorthite compositions for plagioclase with paired liquid anorthite compositions that overlap with the compositional data for which the hygrometer was calibrated have been used to generate these estimates of water content (Supplementary Figure F, Appendix 1).

2.4.7 Rhyolite-MELTS modelling

Melt evolution was modelled using Rhyolite-MELTs (Gualda et al., 2012) (Figure 2.13). The starting composition is the most primitive composition (4.63 wt% MgO) from Anak Krakatau analysed by Dahren et al. (2012). Initial H_2O contents of 1 – 3.5 wt% (steps of 0.5 wt%; varied between runs) were modelled isobarically. Pressure was varied between runs from 50 - 300 MPa (steps of 50 MPa). In all runs, temperature was dropped from 1200 to 700 °C in increments of 2 °C. The lines of descent that fit the best with whole-rock and matrix glass compositions for the 1883 pyroclastic sequence were modelled at an initial H_2O content of 1.5 wt%, and lie between 125 and 250 MPa (Figure 2.13; dashed lines). The evolution of H_2O within the melt indicates that it is water-undersaturated prior to eruption under these conditions, as otherwise the H_2O content would have plateaued on the H_2O vs SiO_2 plot in Figure 2.13(f). Varying the initial water content has a much larger effect on the liquid line of descent than varying the pressure.

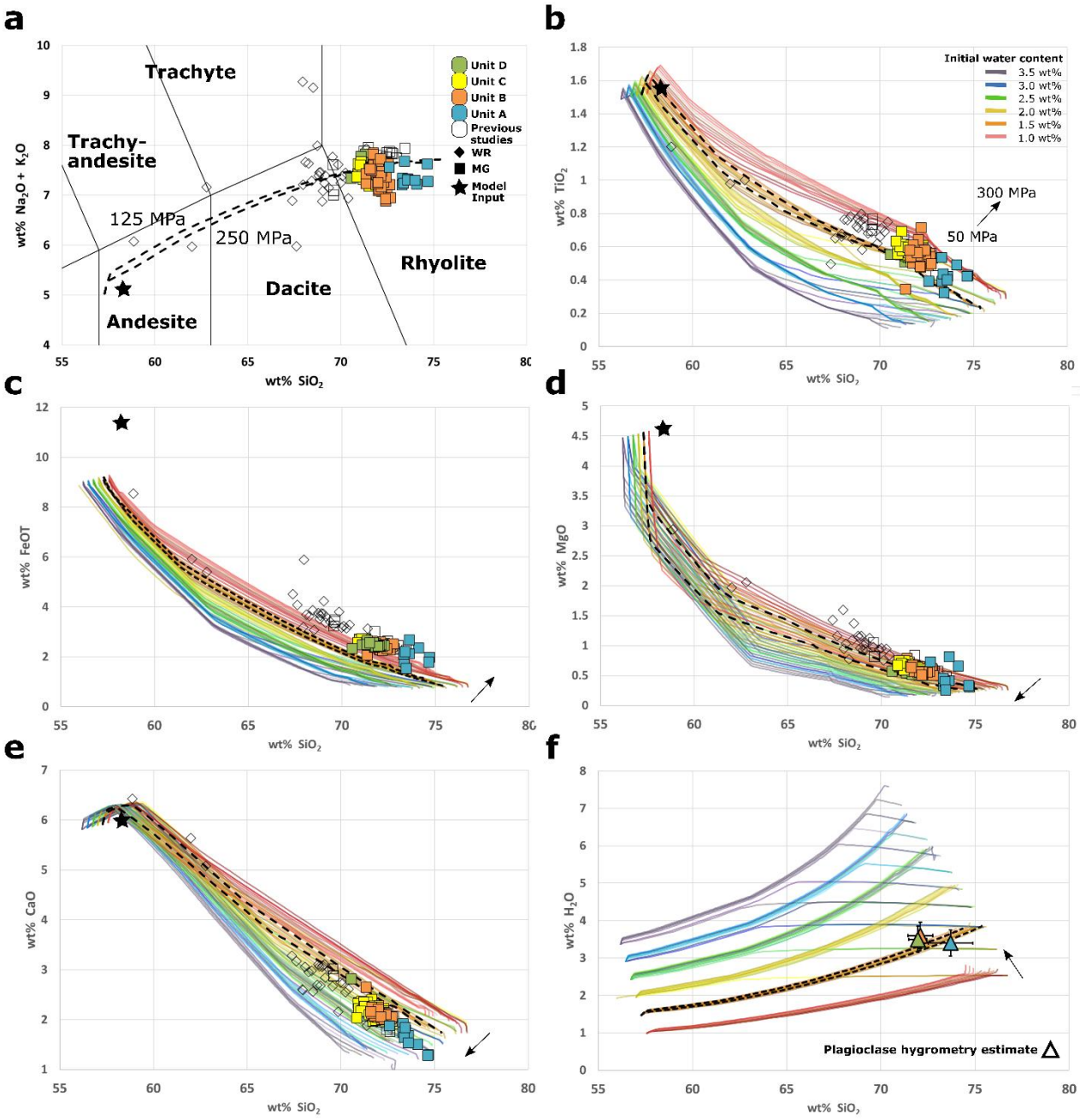

Figure 2.13: (a) shows a total alkali and silica diagram (Le Bas et al., 1986), and (b) to (e) show Harker diagrams containing matrix glass analyses from 1883 samples analysed in this study (MG, coloured squares), as well as matrix glass and whole rock analyses from previous studies (Colourless squares and diamonds, respectively; Oba et al., 1982; Self 1992; Mandeville et al., 1996a; Turner and Foden 2001; and Gardner et al., 2013). Colours denote the different stratigraphic units, as presented in Figure 2.7. Matrix glass data are all normalised to 100 % anhydrous. Liquid lines of descent are shown, modelled isobarically in Rhyolite-MELTS (Gualda et al., 2012), with (f) showing how H_2O content varies with SiO_2 in these models. Red lines were modelled with an initial H_2O

content of 1 wt%, orange 1.5 wt%, yellow 2 wt%, green 2.5 wt%, blue 3 wt% and purple 3.5 wt%. Arrows indicate direction of increasing pressure (steps of 50 MPa from 50 to 300 MPa) between liquid lines of descent modelled at the same initial water content (same colour). The effect of varying the initial H_2O content in these models is much greater than that of pressure. The dashed lines were modelled at 125 MPa and 250 MPa, with an initial H_2O content of 1.5 wt%, and liquid lines of descent that fall between these lines provide best estimates of the conditions under which the 1883 melt evolved. The input composition is indicated by the star and is from Anak Krakatau (Darhen et al., 2012). The triangles in (f) indicate H_2O contents of the average melt composition for Units A, B and D, as modelled using plagioclase hygrometry (Waters and Lange, 2015) using the average temperature generated by Fe/Ti oxide thermometry (914 ^oC; Ghiorso and Evans, 2008). Standard error of 0.35 wt% is indicated by the error bars, along with 2 σ of the average SiO_2 content. Where the lines flatten in (f) represents water saturation of the melt at the corresponding pressure.

2.5 Discussion

2.5.1 Structure of plumbing system

The structure of the pre-eruption magma plumbing system remains a key unknown, and yet an understanding of the reservoir architecture is critical to assessing long-term volcanic hazards (Edmonds, 2008). The lack of systematic change in trace element chemistry with stratigraphic height (Figure 2.9) is not consistent with the postulated existence of a single chemically zoned, and sequentially tapped, magma reservoir at shallow depths, as suggested previously for the 1883 system (Mandeville et al., 1996a; Gardner et al., 2013), and contrasts with the prominent chemical zonations recognised in the deposits of some other large magnitude explosive eruptions, such as the Green Tuff, Pantelleria and the Bishop Tuff, California (Williams et al., 2014; Hildreth and Wilson, 2007).

Fe-Ti oxide temperatures reported by Mandeville et al., (1996a), based on the Anderson and Lindsley (1988) model, were interpreted as evidence for a stratified magma reservoir, with homogenous rhyodacite (880-890 °C) overlying dacite (890-913 °C), and andesite (980-1000 °C). However, the

more mafic components form only a minor constituent of the erupted volume (~ 6 %), and there is no evidence that their frequency varies with stratigraphic height. We also found no evidence for these lower silica compositions as a juvenile melt component in the samples analysed in this study. Our Fe-Ti oxide temperature estimates, outlined in section 2.4.6.1 and based on the Ghiorso and Evans (2008) model, show no variation with stratigraphic height from Units B to D, with an average final equilibration temperature of 914 °C and a narrower range than previously reported (890 to 935 °C). The lack of systematic variation in temperature with stratigraphic height is not consistent with the existence of a simply zoned magma reservoir.

The diverse and heterogeneous populations of plagioclase phenocrysts, which display a large range of crystallisation histories over the entire stratigraphic sequence (Figure 2.10 and 2.11), is not easy to reconcile with a zoned magma reservoir. Patchy cores/zones are observed in 30% of crystals, however some have higher anorthite compositions and show resorption (e.g., Figure 2.10c), while others show the reverse (e.g., Figure 2.10a). Plagioclase rim compositions vary between An_{26} to An_{65}, with no clear modality, indicating a spectrum of different crystallisation conditions, and requiring crystals to have been mixed only shortly prior to eruption to prevent their rims from equilibrating (Figure 2.11). Normal zoning of rims accounts for 35 % of crystals, with 60 % being reverse zoned; there is no convergence towards a single anorthite content, as might be expected from simple homogenisation of two or more discrete magma compositions. Unzoned phenocrysts account for 5% of the population (e.g., Figure 2.10e). This variability in the phenocryst population is inconsistent with a simple zoned magma reservoir, and instead suggests that these phenocrysts grew under a range of different conditions until shortly before eruption.

The matrix glass in Unit A is chemically distinct and more evolved than the rest of the sequence (Figure 2.12; with the exception of the Unit D glassy blocks, discussed below), indicating the presence of a more silica-rich, and likely shallower melt-rich region that was erupted first. The matrix glass SiO_2 contents for Units B to D (Figure 2.12) show subtle compositional differences with stratigraphic height, with B presenting slightly more evolved compositions and spanning a wider range of total alkali contents than Units C and D. The broad compositional consistency means that

the melt present throughout the shallow system was likely of similar bulk compositions, with the variations in total alkali content (Figure 2.14a) within the 2 σ error. The subtle trend towards a slightly more homogenous and less evolved melt is more consistent with syn-eruptive mixing of chemically similar melts, than a large-scale zoned reservoir.

Our rhyolite-MELTS modelling suggest that the shallow magma system lies at 125 – 250 MPa (Figure 2.13), equivalent to approximately 5 to 10 km within the crust, consistent with the 5 – 8 km depths estimated by Mandeville et al. (1996a) from plagioclase melt barometry (Housh and Luhr, 1991). At present-day Anak Krakatau, Dahren et al. (2012) inferred that crystallisation of plagioclase and two pyroxenes takes place at 4 to 8 km, suggesting that the depth range of the pre-2018 magma plumbing system is little different from that of 1883, due to lithological controls on reservoir formation; these depths are corroborated by seismic tomography data (Jaxybulatov et al., 2011; Harajono et al., 1989).

In contrast to the complex and varied zoning profiles observed in the plagioclase phenocryst population (Figures 2.10 and 2.11), which suggests that they grew under a variety of conditions, pyroxene phenocrysts lack strong zoning. Muted zoning in pyroxene phenocrysts would therefore either suggest consistent magmatic conditions for growth, or that the crystals were resident in hot magma long enough for diffusion to smooth out their zoning profiles.

To determine whether the zoning in pyroxene phenocrysts was smoothed out via time-dependant diffusion, we can estimate diffusion timescales for pyroxene and plagioclase from the 1-dimensional diffusion equation:

$$x = \sqrt{(Dt)}$$

where *x* is the mean diffusion length, D is the diffusion coefficient and *t* is time. We have chosen to investigate Mg diffusion, as Mg zoning is present in plagioclase but is considerably muted in pyroxene. Given a diffusion coefficient for Mg in clinopyroxene ($5x10^{-21}$ m^2s^{-1}; Schwandt et al., 1998), it would take centuries for diffusion to homogenise a length scale of order 10 microns. When the above diffusion equation is applied to plagioclase, for the same temperature, over the same

distance, using the Mg diffusion coefficient given by LaTourrette and Wasserburg (1998) of 7.19×10^{-18} m^2/s, the timescales are in the order of months to years. Therefore, both plagioclase and pyroxene phenocrysts could not have been resident in a hot magma for sufficient time to smooth the Mg profiles in the pyroxene population, as significant Mg variations in plagioclase are retained. This implies that diffusion is unlikely to be the cause of the discrepancy in zoning complexity between the two crystal populations.

The compositional consistency in matrix glass (Figure 2.12) and pyroxene phenocryst chemistry means that the complex crystallisation histories recorded by plagioclase are therefore likely to reflect variations in magmatic conditions e.g., P_{H2O}, temperature, fO_2, rather than melt composition. Plagioclase crystallisation is more sensitive to these changes in magmatic conditions than other phenocryst phases (e.g., Mollo et al., 2011), meaning that, in a system where the melt composition was similar but other conditions varied, plagioclase could record complex crystallisation histories, whilst pyroxene remain largely unzoned. One hypothesis for generating varied magmatic conditions would be the existence of multiple, discrete, melt-rich regions of similar composition. To investigate the crystallisation histories in more detail, and test this hypothesis, automated processing of a much larger sample of phenocrysts could be used to identify common growth zones, and events within plagioclase zoning profiles (e.g., Cheng et al., 2017; Probst et al., 2018).

The presence of anorthite-rich (An_{70} to An_{92}) plagioclase cores in 20 % of plagioclase phenocrysts (e.g., Figure 2.10a) likely indicates the existence of a deeper, more mafic reservoir feeding the shallow system, as suggested by Mandeville et al. (1996a) for the 1883 eruption, and Dahren et al. (2012) for the Anak Krakatau system. Highly anorthitic plagioclase may reflect growth in a deeper, more mafic melt at earlier stages in the development of the reservoir. The relatively homogeneous glass chemistry suggests these more mafic compositions were largely erased by the time the reservoir had matured to its pre-eruptive state, as the alternative would require very efficient mixing of the melt phase. The range of high-anorthite plagioclase core compositions (An_{70} to An_{91}; Figure 2.11) indicates that they grew under differing conditions (e.g., fO_2, T, P, H_2O content) within the deeper system. Sieve textures in high anorthite cores, as well as strong resorption textures, followed by

lower anorthite mantles (e.g., Figure 2.11a), are most consistent with decompression (e.g., Nelson and Montana, 1992; Viccaro et al., 2010), potentially during extraction from this deeper reservoir, and subsequent mixing with magmas in the shallow system. The presence of a large range of different crystal textures in significant proportions is also consistent with accumulation of the magma body through many different episodes of mixing (e.g., El Chichón; Andrews et al., 2008). The lack of significant variation in matrix glass data (Figure 2.12) can be explained if the 1883 melt is sourced from a similar host composition.

2.5.2 Role of pre-eruptive fractional crystallisation

The importance of fractional crystallisation processes in both the compositional evolution of the magma, and in concentrating volatiles, varies greatly between volcanoes, with other processes such as magma mixing often cited as eruption triggers (e.g., Sparks et al., 1977). It is thus important to discuss the role of fractional crystallisation in the magmatic system prior to the 1883 eruption of Krakatau.

Mandeville et al. (1996a) conclude that fractional crystallisation is likely to have been the dominant process in the plumbing system beneath Krakatau prior to its 1883 eruption. They found limited evidence for magma mixing, and an abundance of normal zoning in phenocrysts. Normal zoning is a common feature in plagioclase within this dataset, and accounts for ~35 % of all rims, supporting an interpretation that a proportion of phenocrysts were growing under stable conditions not long before eruption.

Our Rhyolite-MELTS modelling (Figure 2.13) shows that it is possible to evolve from an Anak Krakatau composition (basaltic andesite) to the 1883 melt composition by simple fractional crystallisation, with a starting H_2O content of 1.5 wt%, and final water content of 3.4 - 3.6 wt%. Thus, no other internal processes need to be invoked to reach the composition of the 1883 magmas from an Anak Krakatau basaltic andesite starting composition. Small discrepancies between the model and natural samples may be as a result of the system not being entirely isobaric.

Eruptions of silica-rich magma bodies at < 300 MPa can be internally triggered by volatile saturation resulting from fractional crystallisation, without efficient degassing (Tramontano et al., 2017). The modelled evolution of H_2O using Rhyolite MELTS (Gualda et al., 2014; Figure 2.13f) suggests that it is likely that the pre-1883 reservoir did not reach water saturation prior to eruption, because the water content does not plateau under the best-fit pressure and temperature conditions. Using VolatileCalc (Newman and Lowenstern, 2002) we model H_2O saturation at a shallower crustal pressure of ~95 MPa (compared with best-estimates of 125-250 MPa for the 1883 reservoir), for a rhyodacite magma with 3.6 wt% H_2O at a temperature of 914 ^oC. However, over the pressure range of 125 – 250 MPa, an estimated, additional 175 – 925 ppm of CO_2 would be sufficient for the system to reach volatile saturation. These values are certainly within the range expected for arc magmas (e.g., Blundy et al., 2010), lending credence to the idea that the shallow magma system was volatile saturated prior to eruption, and that fractional crystallisation is likely to have primed the magmatic system for eruption, and is a potential trigger, if degassing was inefficient.

2.5.3 Role of pre-eruptive magma mixing

Recharge of magma reservoirs and magma mixing are often cited to be eruptive triggers (Sparks et al., 1977). Mandeville et al., (1996a) rule out magma mixing as a trigger for the 1883 eruption, based on a lack of reverse zoning in phenocrysts, and a low abundance of mixed pumices. However, ~60% of plagioclase phenocrysts in this study show reverse zoning at the rim, a result likely obtained by investigating crystal zoning transects at a spatial resolution of 10 microns, rather than just core and rim point analyses. It is important therefore to discuss the role that magma mixing had prior to the 1883 eruption of Krakatau.

As discussed in section 2.5.1, it is likely that the compositional variations in plagioclase crystals (Figures 2.10 and 2.11) represent different P, T and/or H_2O conditions, rather than differing melt composition, because the matrix glass and pyroxene phenocryst chemistry are broadly consistent. Therefore, the high proportion of reverse zoning at plagioclase rims is likely to indicate changes in

magmatic conditions, rather than mixing of compositionally distinct magmas. The volume of visually mingled pumice is also small (Mandeville et al., 1996a), and not observed in Units A – C of the stratigraphy. Furthermore, the visually mingled pumices do not show compositional differences between the dark and light matrix glasses (Self 1992). Mafic enclaves are also entirely absent within the stratigraphy. Stehn (1929) reports some mafic ash collected during the precursory eruptive phase, however evidence of this ash was not observed on either field campaign, suggesting it may not have been preserved, possibly because it is volumetrically minor component similar to the andesite glass (~1 %) reported by Mandeville et al., (1996a).

However, syn-eruptive mixing of chemically similar magmas (rather than pre- or syn-eruptive mixing of chemically distinct magmas) crystallising under different magmatic conditions, could account for the wide range in plagioclase rim compositions (Figure 2.10 and 2.11), as they would not have had time to equilibrate with the new host melt. The matrix glass compositions also support this, as they are broadly consistent, but become slightly more homogenous as the eruption progresses through Units B to D (Figure 2.12), which could result from mixing of chemically similar melts syn-eruption. One hypothesis might be that different melt-rich regions within the shallow system coalesced and mixed syn-eruptively as a result of magma withdrawal and system restructuring. In this case, magma mixing would be considered a consequence of magma body destabilisation during eruption, rather than an eruptive trigger (e.g., Christopher et al., 2015); this has been invoked as an explanation for homogeneity in pyroclasts coexisting with complex phenocryst zoning for similar crystal-poor caldera systems (Cashman and Giordano, 2014).

2.5.4 Eruptive progression

A schematic diagram illustrating the proposed evolution of the magmatic system and how this links with the eruptive progression is shown in Figure 2.14. Unit A (Figure 2.4a; 2.6a; 2.7) is comprised of a green ash aggregate fall deposit at the base of stratigraphy, which is distinct in its chemistry, being more evolved than the eruptive material that follows (Figure 2.12). Unit A is also

volumetrically minor when compared with the overlying sequence. We concur with Mandeville et al. (1996b) that Unit A likely represents the sub-Plinian May phase of the 1883 eruption of Krakatau. This is supported by reported observations of a maximum of 50 cm of green ash at the coast in June 1883 (Symons et al., 1888). We also suggest that Unit A erupted from a more-evolved, shallower melt-rich region.

The observation that Unit A is composed of aggregates of fine ash could indicate that the May 1883 activity was phreatomagmatic (Mandeville et al., 1996b). This interpretation is consistent with historical accounts made by inhabitants of the nearby island of Sebesi, who visited the main island of the Krakatau complex on 21st of May: "the earth burst open at their feet" on the beach. European officials who travelled from Anjer the following day also reported: "near the beach, the earth was belching fire and smoke" (Furneaux 1964). According to these accounts, Krakatau was erupting close to the coast in May, making magmatic interaction with seawater possible. This is corroborated by reports from the ship Prins Hendrick, which passed close to Krakatau on 12th August: "I passed the island on the north side… the new opening of the crater... appeared to be a small hole, maybe 100 ft in diameter, only a few meters above sea level" (Macleod 1884). However, Ferzenaar, a visitor to the island the day before, noted only subaerial vents. Brown et al., (2010) note that ash aggregates can also form in a moist atmosphere, so interaction of the magma with seawater during fragmentation is not required to account for the Unit A deposits. Therefore, there is ambiguity in both the evidence from deposits and the historical accounts regarding the degree of phreatomagmatic character of the 1883 May phase.

There are periods in both early June and late July 1883 which have sparse historical records (Figure 2.2), and it is not known whether the activity was continuous. The volcano was attracting much less attention, and therefore it is at least likely that the eruptions were smaller, if not less frequent. It is thus difficult to know whether any activity after 27th May contributed significantly to the deposition of Unit A or not.

As discussed in section 2.5.3, the wide range in plagioclase rim compositions (Figures 2.10 and 2.11), and subtle changes in matrix glass chemistry throughout the stratigraphy towards a more

homogenous melt (Figure 2.12), suggest that after the initiation of the eruption in May 1883 there was a continuing process of coalescence and syn-eruptive mixing of shallow-stored melt-rich regions. The emptying of the shallow silicic reservoir from May onwards may have promoted the restructuring and mixing of the shallow system. Partial collapse of the summits of Perboewatan or Danan from June to August (Verbeek 1885; Symons et al. 1888; Figure 2.2) may also have led to downward propagating stress changes in the magmatic system, aiding reorganisation of the magmatic system (e.g., Tarasewicz et al., 2012).

Our hypothesis is that magma body destabilisation occurred over the ~ 2-3 months leading up to the onset of the paroxysmal phase of the eruption. Unit B represents the onset of this climactic eruptive phase, comprising interbedded PDC and fall units (Figure 2.4b; 2.5a; 2.7), and tree remains (Figure 2.6b). The deposition of Unit B may have started as early as 22nd August (Figure 2.2). The increase in deposit thickness from Unit A (<5 cm) to B (up to 20 m) is likely as a result of increased eruptive flux, assuming no significant topographic changes. The increase in eruptive flux is likely to be due to vent widening, however stress changes related to the reduction in overburden on the shallow magmatic system, may have contributed (e.g., Watt, 2019).

The PDC deposits of Unit B appear to be thicker in the north east (Figure 2.8a), suggesting that this was the dominant direction of travel. Accounts from 23rd August corroborate this, with ash reported in the north east in the straits of Sunda by ships such as the Princess Wihelmina (Macleod 1884), and heavy rains of pumice in the north in Lampong Bay on 26th August. The north east direction of travel may indicate that the summit of Danan (> 400 m) to the south, acted as a topographic barrier to PDC transport.

The massive PDC deposits of Unit D (Figures 2.5b; 2.5c; 2.7) emanate from the inferred caldera centre, with a dominant direction of travel towards the south west (Figure 2.8c). The change in PDC transport direction could indicate that the topographic barrier formed by Danan had been diminished by this stage, perhaps due to collapse associated with the emplacement of the lithic lag breccias comprising Unit C (Figures 2.4c; 2.5a; 2.5b).

The thick, structureless PDC deposits emplaced as part of Unit D may correspond to the paroxysmal explosions in the morning of 27th August 1883. At the top of Unit D, a lithic lag breccia is observed at locality D3S2/NP4 (Figure 2.5b), and at D2S2/U23 there are intensely fractured metre-scale glassy blocks (Figure 2.5c). These blocks are reminiscent of the large lava blocks found in phase 3 of 4 of the Late Bronze Age (Minoan) eruptive sequence in Santorini (Druitt and Francaviglia 1992; Sparks and Wilson 1990). By analogy, lava blocks originating from the volcanic island may have been entrained by PDCs. However, matrix glass analyses of the blocks, and smaller obsidian clasts, in Unit D of the 1883 stratigraphy, show that their chemistry is similar to the 1883 pyroclastic sequence, but extend to more evolved compositions (Figure 2.12). This chemistry is distinct from the range of 1883 lithic compositions noted by Mandeville et al. (1996b), which are predominantly basalt and basaltic andesite. The broadly consistent matrix glass chemistry of these block means it is likely that they are derived from the same source. Given the broad compositional similarities, they may be directly related to the magma that fed the 1883 eruption. In addition, the rounded, irregular "tear-drop" shapes of these blocks (Figure 2.5c) suggest ductile deformation during hot emplacement, making it likely that they erupted concurrently with the pyroclastic material. Given that the blocks are found in Unit D, at the top of the stratigraphic sequence (Figure 2.7), and the fact that they have not undergone fragmentation, one hypothesis for their formation is that they were small, stagnant, pockets of highly evolved melt in the shallow crust that were excavated and incorporated with the pyroclastic material during the final stages of caldera formation. This section of the stratigraphy potentially corresponds to the largest explosion, and most devastating tsunami, at 10 am on 27th August 1883.

No textural evidence for phreatomagmatic activity was found in Unit D. This is contrary to what might be expected if the caldera collapse promoted significant magma-water interaction. However, there are records of ash falling as "rounded accretions" in Java after the main paroxysm (equated to Unit D; Figure 2.2), which may provide evidence for some magma interacting with water during or after caldera collapse. However, the lack of fine-grained, highly fragmented ash in Unit D is quite

striking, particularly when compared with a "wet" ignimbrite such as Oruanui (Allan et al., 2012), making it unlikely that water entered the vent in significant amounts.

The deposits from the 1883 Krakatau eruption are consistent with those observed in many caldera-forming eruptions, e.g., Bishop Tuff (Hildreth and Wilson, 2007), Crater Lake (Bacon, 1983; Kamata et al., 1993) and Santorini (Druitt et al., 2019). These eruptions commonly start with a Plinian plume, with the single vent widening through time and PDCs contributing to an increasing proportion of the erupted products. Caldera collapse then occurs when a critical volume of magma has been removed from the plumbing system beneath. The tapping of multiple melt batches has been documented for many crystal-poor, caldera-forming eruptions, particularly in systems undergoing active extension, similar to Krakatau, e.g., the Snake River Plain (Ellis et al., 2010; Ellis and Wolff, 2012) and the Taupo Volcanic Zone (Brown et al., 1998; Charlier et al., 2003; Gravley et al., 2007; Wilson and Charlier, 2009; Bégué et al., 2014). In these cases, melt was stored in laterally (rather than vertically) extensive systems, with a consistent bulk chemistry between melt lenses (Cashman and Giordano 2014). Many caldera-forming eruptions are preceded by some form of precursory eruption, however the period of time between this and the climactic eruption is often poorly constrained (e.g., Allan et al., 2012; Cashman and Giordano 2014; Druitt et al., 2019). The 1883 eruption of Krakatau is unique in the sense that we know when this precursory activity began (Figure 2.2; 20th May 1883) from direct observations. This may be invaluable for monitoring volcanoes with a history of producing explosive, caldera-forming eruptions, because it highlights the potential for a large event to follow a relatively moderate explosive eruption, on a timescale of months. However, the identification of such events as precursory to an incipient larger eruption remains challenging. Although a precursory Plinian eruption might increase the risk of a larger eruption, one does not always follow on from the other. Top-down factors, such as the removal of mass from the volcano edifice (discussed in section 2.5.4), potentially have a role in triggering these devastating paroxysms. Therefore, it would also be useful to carefully monitor surface deformation and any significant losses of mass at Anak Krakatau, as well as other similar volcanic systems.

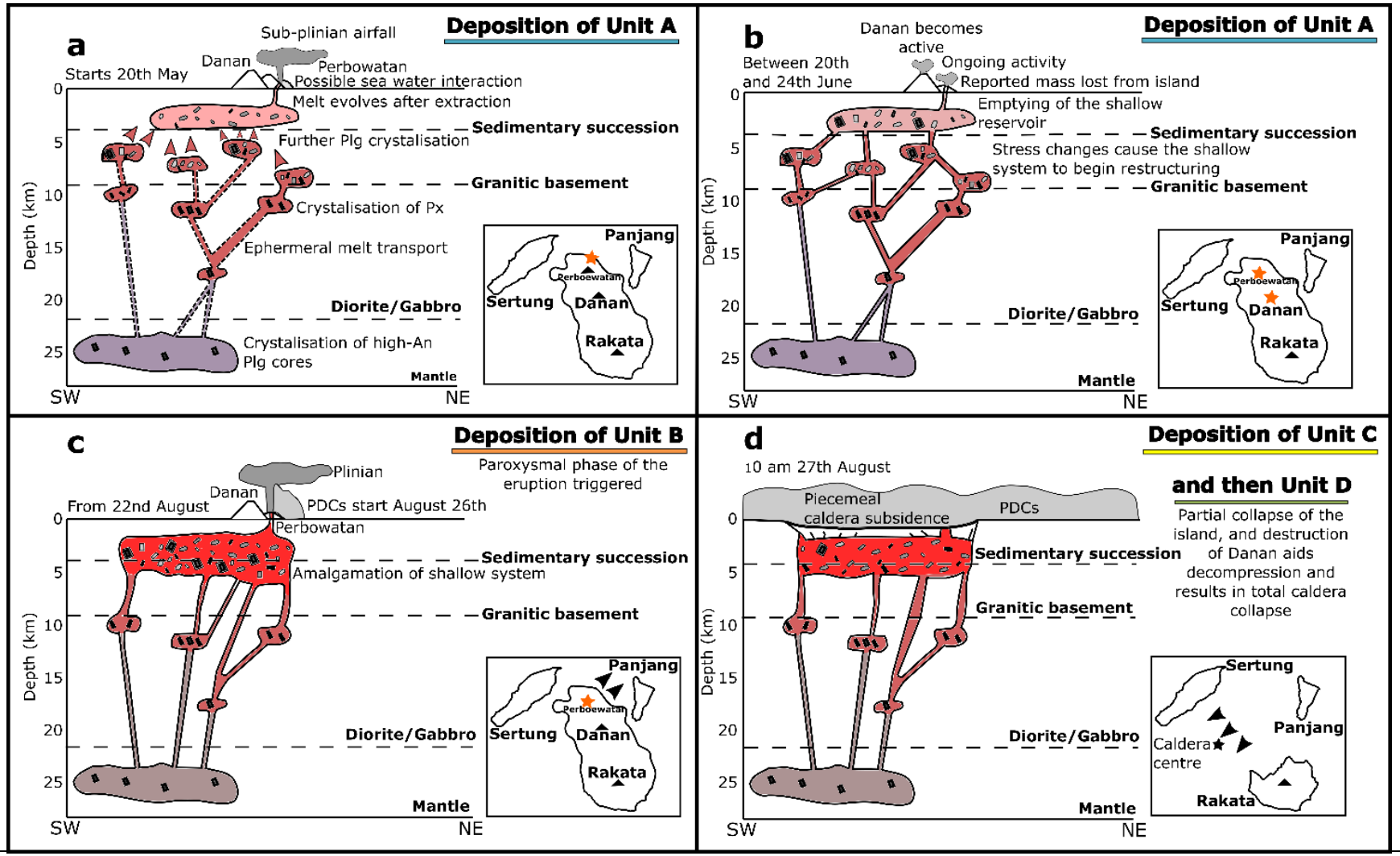

Figure 2.14: Series of schematic diagrams coupled with plan view maps illustrating one possible model for the magmatic and eruptive evolution of the 1883 eruption of Krakatau (lithological structure and crystallisation depths from Darhen et al., 2012). On maps orange stars indicate an active edifice, and black arrows represent the dominant direction of PDCs. Dashed lines on schematic cross sections indicate ephemeral transport pathways of magma. Red arrows indicate melt extraction. Colours of melt represent melt composition: Purple for the least evolved, followed by brown, bright red, with pink representing the most silicic melt. Panel (a) shows the deposition of Unit A (Figure 2.7), with evidence for a more silicic reservoir derived from matrix glass analyses (Figure 2.12), and the observed eruption dynamics (Figure 2.2). Panel (b) shows observed changes to the eruption dynamics (Figure 2.2), and proposed system restructuring. Panel (c) shows the deposition of Unit B (Figure 2.7), and the start of the paroxysmal phases of the eruption, as determined by observations (Figure 2.2), as well as syn-eruptive mixing of chemically similar melt batches hypothesised as a result of varied and complex plagioclase textures and chemistry (Figure 2.10; 2.11), and only minor variations in matrix glass chemistry (Figure 2.12). Panel (d) shows the deposition of Unit C and Unit D in a piecemeal caldera collapse, as there are two lithic lag breccias (Figure 2.7), and a substantial change in PDC and dilute-PDC directionality (Figure 2.8).

2.6 Conclusions

This study presents field observations from new exposures of the 1883 eruptive deposits of Krakatau, revealed as a result of the removal of vegetation by the 2018 tsunami generated by flank collapse of Anak Krakatau. This has allowed for the stratigraphy of the eruption to be considerably better constrained (Figure 2.3; Figure 2.7). Examination of the geochemistry in the context of this refined eruptive stratigraphy does not support previous studies (e.g., Mandeville et al., 1996a) that have proposed that the eruption emanated from a chemically zoned magma reservoir. An updated model for the magmatic system is proposed, accounting for the chemical variations in context with the stratigraphic sequence.

The existence of a distinct, green, basal ashfall (Figure 2.4a) is consistent with written accounts of precursory activity in May (e.g., Symons et al., 1888; Figure 2.2), with the matrix glass chemistry indicating a shallow, more silicic melt-rich region was tapped during this preliminary eruptive phase (Figure 2.12). It is likely that restructuring of the magmatic system and syn-eruptive mixing of multiple chemically similar melt batches then occurred, to account for the chemical homogeneity in pyroclasts in Units B to D (Figure 2.12), and complex plagioclase phenocryst zoning profiles and textures (Figures 2.10 and 2.11). This restructuring may have occurred simply as a result of gradual emptying of the initial silicic reservoir, however the loss of mass reported from the summits of Perboewatan and/or Danan (Figure 2.2) may also have played a role. The stress changes and reservoir reconstruction may have contributed to the onset of the climactic phase of the eruption on 26th August.

There is a substantial change in the directionality of the PDCs throughout the climactic phase of the eruption (Figure 2.8), which coincides with the deposition of a lithic lag breccia occupying a distinct horizon within the stratigraphy (Figure 2.4c; 2.5a; 2.5b). The lithic lag breccia is thus attributed to partial collapse of the island, and the removal of the edifice Danan as a topographic barrier. The 1883 eruption culminated in total caldera collapse, which, together with the PDC production at this stage, was a potential cause of the largest tsunami at 10 am on 27th August. This final caldera collapse is recorded in the stratigraphy as a second lithic lag breccia (Figure 2.5b), and at one locality

(U23/D2S2) glassy blocks up to 8 m in size are present (Figure 2.5c), which are reported within this sequence for the first time here. The matrix glass chemistry of these blocks (Figure 2.12) suggests that they are derived from the same melt as the 1883 pyroclastic material, and their shapes suggest that they underwent ductile deformation during hot emplacement.

The identification of at least two lag breccias may indicate piecemeal caldera formation, where the first stage of collapse is the driving force behind the most energetic and explosive, climactic part of the eruption. Precursory Plinian eruptions are therefore very useful phenomena to be aware of for the future monitoring of volcanoes with a history of producing silicic caldera-forming eruptions. The 1883 eruption of Krakatau provides an example of an event where relatively moderate explosive eruptions may potentially have run-away effects culminating in cataclysmic caldera-collapse several months later.

3. A combined experimental and petrological modelling approach to investigating the magmatic storage conditions prior to the 1883 eruption of Krakatau Volcano

Abstract

Silicic, caldera-forming eruptions, such as the 1883 eruption of Krakatau volcano, are major geohazards. The architecture of the magmatic system, and of the conditions therein, exert a key control on eruptive style. Thus, gaining an understanding of the subterranean system prior to an explosive eruption aids the monitoring of volcanoes with the potential to produce large eruptions. This study provides experimental constraints on the magmatic storage conditions within Krakatau's plumbing prior to its eruption in 1883. Results from phase equilibria experiments suggest that the material erupted during the precursory activity in May 1883 was stored at 100 - 150 MPa (~4 - 6 km) and 850 +/- 25 °C. The bulk of the paroxysmal (August 1883) tephra was likely stored at lower pressures of 100 - 50 MPa (~ 2 - 4 km), and temperatures of 850 - 900 °C. Therefore, the products of precursory activity may have originated deeper within the magmatic system than the bulk of the 1883 pyroclastic sequence, rather than from shallower depths. Melt chemistry is also modelled using trace elements in plagioclase and partitioning models. Strong positive correlations between modelled melt TiO_2, and to a lesser extent MgO contents, with both anorthite content of plagioclase ($An_{<67}$) and modelled Sr content of the melt, are consistent with melt evolution. These modelled melt compositions also overlap with our experimental matrix glass data generated under shallow crustal conditions. For plagioclase with higher anorthite contents, modelled melt compositions do not show simple trends of melt evolution, and instead indicate greater melt diversity. The melt compositions modelled from plagioclase of higher anorthite contents are not replicated by experiments, suggesting that they are located deeper within the magmatic system. These supporting datasets have important implications for the structure of the magmatic system prior to large caldera-forming eruptions, and thus contemporary geophysical monitoring of analogous systems.

3.1 Introduction

Silicic, caldera-forming eruptions are major natural hazards. These eruptions may not only have a devastating effect on local communities, but can also have global impacts (Verbeek, 1884; Symons et al., 1888; Simkin and Fiske, 1983). Although few such eruptions have been directly observed, caldera-forming eruptions are often thought to be preceded by long periods of unrest, characterised by milder explosive and effusive activity (e.g., Newhall and Dzurisin, 1988; Forni et al., 2018; Druitt et al., 2019). These long-term shifts in activity and eruptive behaviour are poorly understood due to a lack of geophysical monitoring data in the run up to a large, silicic, caldera-forming eruptions, posing significant challenges for volcano monitoring (e.g., Gottsmann and Marti, 2008; Druitt et al., 2012). Many studies note that magma storage conditions, such as pressure (depth), temperature, volatile content, and primary melt composition, may exert some control on the efficiency of outgassing, and thus eruptive behaviour (e.g., Ruprecht & Bachmann, 2010; Andújar & Scaillet, 2012; Koleszar et al., 2012; Sides et al 2014; Cassidy et al., 2016; Di Genova et al., 2017; Cassidy et al., 2018). It is thus important to ascertain the degree of melt diversity within the subterranean volcanic system, both chemically, and in terms of magmatic conditions, and where in the system these differences arise.

The 1883 eruption of Krakatau was a silicic caldera-forming eruption that killed 36,000 people as a result of pyroclastic density currents and subsequent tsunamis. Petrological tools have provided valuable insights into the architecture of the magma plumbing system prior to the 1883 eruption, and the conditions leading up to it (Self and Rampino, 1981; Francis and Self, 1983; Self and Wohletz, 1983; Camus et al., 1987; Self 1991; Mandeville et al., 1996a; Madden-Nadeau et al., 2021). An integrated study of the historical accounts, eruptive sequence and geochemistry of the eruptive material showed that there was precursory sub-Plinian activity in May 1883, three months prior to the paroxysm. An important implication of these observations for monitoring of similar systems is that precursory sub-Plinian to Plinian activity can precede paroxsyms by several months. The depth of this precursory activity may also be important for the interpretation of volcano seismicity and deformation data. Madden-Nadeau et al. (2021) hypothesised, based on the relatively more evolved

composition of the precursory products than the overlying volcanic sequence (attributed to the paroxysmal eruption) that this earlier activity was derived from a shallower magma storage region (e.g., Cashman and Giordano, 2014). Madden-Nadeau et al. (2021) also hypothesised that diverse pre-eruption magma conditions were required to produce varied and complex plagioclase zoning profiles found within the paroxysmal tephra, whilst maintaining otherwise fairly homogenous magma compositions. This has implications for the triggering of the eruption; in this case, mixing would be a syn-eruptive process resulting from eruption, rather than being the primary cause (e.g., Christopher et al., 2015).

Estimates of pre-eruptive pressures and temperatures of Krakatau 1883 magmas based on mineral-melt equilibria are summarised in Table 3.1. Most estimates of pre-eruption temperatures are within the range of 870 – 950 °C. This agrees with the most recent estimates of temperature provided in Madden-Nadeau et al. (2021) using the Ghiorso and Evans (2008) Fe-Ti oxide thermometer, which yielded 890 – 935 °C (see Chapter 2 for details). Darhen et al. (2012) found that the 1883 clinopyroxene and plagioclase rims were not in equilibrium with the 1883 glass, and so thermobarometers for these phases were not explored. However, it is thought that Fe-Ti oxides are likely to yield the last equilibration temperature before quenching (Rutherford and Devine, 1988; Geschwind and Rutherford, 1992; Lindsley and Frost, 1992), and so are likely to best represent the pre-eruptive temperature of the magma. Pressures are poorly constrained, but are generally estimated within the region of 100 – 200 MPa.

In this study, we use phase equilibria experiments to constrain the storage conditions of Krakatau's 1883 magma, and to test whether the precursory activity was derived from a shallower storage region than the bulk of the pyroclastic sequence. Phase equilibria studies have been successfully used to replicate pre-eruptive storage conditions of magmas associated with similar eruptions, such as the Late Bronze Age (Minoan) eruption on Santorini, where rhyodacite magmas were stored in a long-lived reservoir at > 200 MPa, between 850 and 900 °C (Cadoux et al., 2014) until shortly before eruption, with melt inclusion barometry supporting these constraints (Druitt et al., 2016). In addition, we use trace element transects from natural plagioclase crystals to investigate melt chemistry and

conditions within the subterranean magma system. Combining these experimental and modelling approaches helps to further constrain the architecture of Krakatau prior to the 1883 eruption, and provides new context for the monitoring of the present-day activity of systems with a history of explosive, caldera-forming eruptions.

Table 3.1: Summary of pre-eruptive pressure and temperatures of Krakatau 1883 magmas

Krakatau magma	Temperature estimates (°C)	Pressure estimates (MPa)	Reference
1883 – Rhyodacite pumice	869 (Fe/Ti1) 955+/- 15 (Plg1) 876-897 (Fe/Ti2) 830 -950 (Chl1) 890-935 (Fe/Ti3)	 100-200 (Plg2)	1 2 3
1883 - Obsidian	900-953 (Plg1) 948 (Px1) 869 (Fe/Ti1)	N/A	1
1883 – Dacitic pumice	887 – 931 (Fe/Ti2) 976 +/- 10 (Px1)	N/A	2
1883 – Andesitic Pumice	1024 -1068 (Plg1) 984 (Fe/Ti1)	N/A	1

Thermobarometric models:

Plg1 – Kudo and Weill (1970), plagioclase-liquid

Plg2 - Housh and Luhr (1991), plagioclase-liquid

Px1 – Wood and Banno, two pyroxenes

Fe/Ti1 – Powell and Powell (1977), Fe/Ti Oxides

Fe/Ti2 – Anderson and Lindsley (1988), Fe/Ti Oxides

Fe/Ti3 – Ghiorso and Evans, Fe/Ti Oxides

Chl1 - Metrich and Rutherford (1992), Chlorine in melt inclusions

References: 1 – Camus et al., 1987; 2 – Mandeville et al., 1996; 3 – Madden-Nadeau et al., 2021

3.2 1883 Eruption

The eruptive progression and stratigraphy have been extensively investigated in Chapter 2 (Figure 2.2; Madden-Nadeau et al., 2021), however we will provide a summary here. The first record of activity for Krakatau is for 20th May 1883, suggesting Vulcanian to Sub-Plinian activity, which has

been correlated with a 2-5 cm, green, ash-aggregate layer, of more evolved composition than the overlying sequence, termed here Unit A (Figure 3.1).

Plinian activity began on 26th August, with explosions being heard all over Java by 5pm (Symons et al., 1888). The onset of this paroxysmal phase of the eruption is correlated with well sorted, pumice-supported fallout units interbedded with poorly sorted, matrix supported PDC deposits (Unit B). The volume of PDC deposits relative to fall deposits increases moving up through this unit. Overlying this is a lithic lag breccia, denoted as Unit C, which is interpreted to be indicative of partial collapse of the island at some point in the night of 26th/27th August. Unit D consists of massive PDC deposits containing obsidian. At one locality (D2S2/U23), there are glassy, degassed, coherent blocks up to 8 m in size contained within this unit. In addition, one locality has a second lithic lag breccia at the top of Unit D, thought to correlate with the final stages of caldera collapse. The most powerful explosions (confirmed by pressure deviations recorded on the Batavia gasometer record; Latter, 1981), occurred at 5.30 am, 6.44 am, ~10:00 am and 10.45 am on 27th August (Symons et al., 1888). The explosion at 10 am was the most violent, and was heard 850 km away in Singapore. Tsunami waves swept through the Sunda Straits from the 26th to 27th August causing the majority of casualties (Symons et al., 1888). The largest of these waves broadly coincided with the most powerful recorded explosion at 10 am on 27th August.

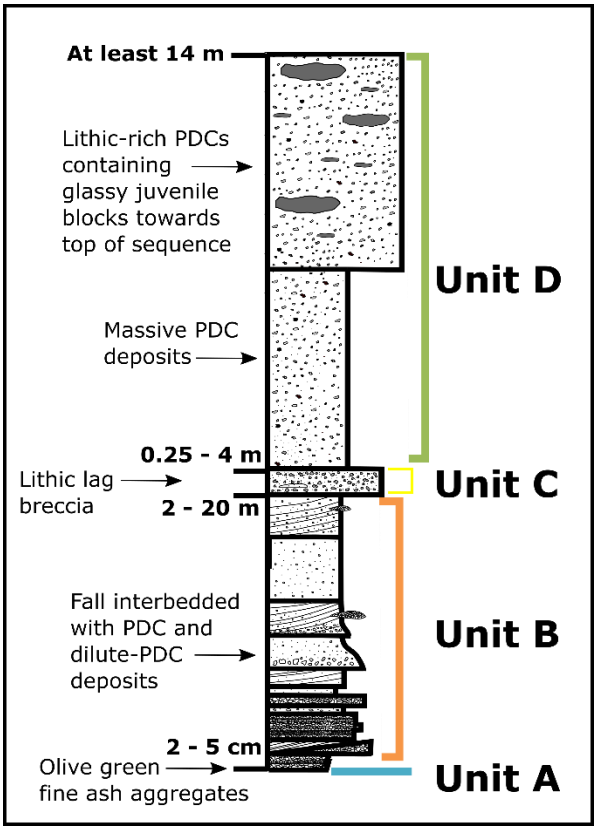

Figure 3.1: Composite log of the 1883 stratigraphic sequence, modified from Madden-Nadeau et al., (2021), Chapter 2.

3.3 Methods

3.3.1 Cold seal experiments

Experiments were undertaken to constrain the magma storage conditions prior to the 1883 eruption of Krakatau. A water-pressurized, cold-seal pressure vessel was used. Powdered aliquots of 1883 pumice from Unit B in the stratigraphy (sample D4S1.2; low crystallinity, ~10 – 15 %; dataset Madden-Nadeau, 2020; Madden-Nadeau et al., 2021) was used as starting material. The use of powdered whole-rock assumes total equilibrium, and this composition was selected because the whole rock likely represents the reactive magma in the system prior to the 1883 eruption (e.g., Martel et al., 1999; Scaillet & Evans, 1999; Costa et al., 2004; Pichavant et al., 2007). A coarsely crushed sample would instead achieve partial reactive equilibrium as this limits exposure of the reactive melt to phenocryst cores in disequilibrium (e.g., Cottrell et al., 1999; Coombs et al., 2000; Hammer &

Rutherford, 2002; Pichavant et al., 2007). A powdered sample was used because it was assumed that, as a result of the low crystallinity, the effect of the crystal cores on the chemistry of the sample would be negligible. Units B to D in the stratigraphy have almost indistinguishable matrix glass chemistries (Madden-Nadeau et al. 2021), and so these experiments are directly comparable to the bulk of the 1883 tephra. The experimental products will also be compared to the more evolved natural tephra sampled from Unit A. The matrix glass chemistry of Unit A marginally overlaps with the subsequent stratigraphy, however is chemically distinct from matrix glasses from Units B to D, and thus any comparisons drawn with experimental results should be treated with more caution (Madden-Nadeau et al., 2021). However, this chemical difference is not apparent in the whole rock data discussed in the previous chapter and therefore it is possible differences in the matrix glass compositions between the different units are a product of their variable crystallinity and crystal phases. It should be noted that the whole-rock major element data indicated that all samples had undergone alteration by seawater, however selected trace element concentrations showed no correlation with the stratigraphic sequence (Madden-Nadeau et al., 2021).

Approximately 0.1 g of sample was inserted into a $AgPd_{30}$ capsule previously welded at one end, together with sufficient distilled water using a micro syringe to saturate the magma in H_2O at the pressure and temperature of the experiments. The capsule was welded shut before being weighed again, to ensure no volatiles were lost during the welding process and then reheated and reweighed to check that the capsule is sealed. The capsules were inserted into an autoclave with a nickel rod to buffer fO_2 conditions close to nickel-nickel-oxide (NNO). A K-type thermocouple was inserted into a small hole in the end of the autoclave close to the capsule position to check for temperature offset between the furnace's internal thermocouple and autoclave. The samples were held at pressures and temperatures commensurate with upper crustal conditions (800–900 °C; 50–200 MPa) for between 4 and 8 days to equilibrate (see table 3.2), and then rapidly quenched using compressed air followed by lowering the sample into water to prevent further crystallisation and microlite formation. For experiments where there was microlite growth, repeat experiments were conducted and a rapid

quench system was used, whereby compressed air was aimed at the autoclave from multiple directions, to minimise the quench time.

Table 3.2: Experimental conditions for successful experiments without significant water loss.

	Pressure /MPa			
Temperature / °C	**50**	**100**	**150**	**200**
800	KK17 8 days	KK44 7 days	KK40 7 days	KK27 7 days
	-	KK13 8 days	KK14 8 days	-
850	KK18 8 days	KK21 7 days	KK42 7 days	KK38 7 days
	-	KK06 7 days	KK16 7 days	-
895	NA	NA	KK43 4 days	NA
900	KK32 7 days	KK04 8 days	KK34 7 days	NA

3.3.2 Scanning electron microscope (SEM)

Back-scatter electron (BSE) images of experimental glass mounted in resin blocks were obtained to identify phases and to qualitatively assess how microlitic the sample is. BSE images were also obtained for natural plagioclase phenocrysts, to assess chemical zoning in crystals. Plagioclase phenocrysts were picked from crushed pumice samples and mounted in resin blocks. All BSE images were obtained with an FEI Quanta 650 field emission gun (FEG) scanning electron microscope (SEM) and a FEG CAMECA SX-5 electron microprobe in the Department of Earth Sciences, University of Oxford. Operating conditions were 20 KeV with a 15-micron aperture. Energy dispersive spectroscopy (EDS) was also used to identify phases within the experimental glasses.

3.3.3 Electron Probe Microanalysis (EPMA)

Understanding chemical variations in natural plagioclase is important as these crystals provide a unique record of magma reservoir processes and conditions. Furthermore, trace element compositions for phenocrysts can provide detail not recorded in the major elements. Plagioclase phenocrysts were picked from ash samples archived at the British Geological Survey (BGS) that had been collected at the time of the eruption on ships within the Sunda Straits and on mainland Java, likely during the paroxysmal phase of the eruption (See dataset Madden-Nadeau 2020). In addition, experimental plagioclase phenocrysts were analysed to compare to natural data, which allows for the assessment of "best-fit" conditions for the 1883 magma reservoir. Plagioclase phenocrysts were analysed on a FEG CAMECA SX-5 electron microprobe at the Department of Earth Sciences, University of Oxford. Sodium was always analysed first with a 10 s peak count time, to prevent Na migration. Compositional profiles measured across natural plagioclase and point analyses of rims of experimental plagioclase for Al, Si, Na, Ca, K, Fe, Ti, Mn and Mg were measured at 15 kV acceleration voltage and 20 nA beam current, with 5-micron defocussed beam size (see Madden-Nadeau et al., 2020). Fe, Mg and Ti were acquired again, along with Sr, under a 40 nA beam with longer peak count times of 270 s, following parallel transects (n = 16) for natural plagioclases. Point spacing in these line analyses were approximately 10 microns.

Chemical analyses for experimental glass were also obtained to compare to natural glasses. Point analyses of experimental glass, mounted in resin, were analysed on a Jeol JXA-8200 electron Microprobe in the School of Archaeology, University of Oxford. Again, Na was always analysed first with a 10 s peak count time, to prevent Na migration. Glass analyses were conducted at 15 kV with a 5-micron defocussed beam of 6 nA for Al, Si, Na, Ca, K, Fe, Ti, Mn and Mg. Secondary standards of a similar composition to the target glass were analysed to check the accuracy of the calibration (see Supplementary excel file for Chapter 3, Supplementary Data 1).

3.3.4 Phase proportions

The proportions of glass and mineral phases of both natural and experimental products were estimated from BSE images (5 to 17 images per sample, covering a total area of 0.29 to 1.68 mm^2), for comparison to obtain "best-fit" conditions for the 1883 magma prior to eruption. Phases were digitally traced using image processing software, and thresholded to estimate vesicularity in order to report values on a vesicle-free basis (e.g., Burgisser et. al., 2010). Estimates for vesicularity are likely to be slightly underestimated, as a result of plane of section effects.

Error will also be incurred as a result of the degree of user-defined thresholding chosen for each BSE image, and differences in how phenocrysts are traced digitally. Repeat measurements of thresholding and crystal tracing were carried out 10 times on a single image, averaged over 5 images, to give an average 1 σ error: glass +/- 0.7 vol%; plagioclase and quartz +/- 0.6 vol%; pyroxenes +/- 0.3 vol%; and accessory phases +/- 0.2 vol%.

3.4 Results

3.4.1 Phase equilibria experiments

A phase diagram showing the proportions of glass and mineral phases crystallised during each experiment is shown in Figure 3.2 (for phase modalities, see Supplementary Table A, Appendix 3). Quartz is only present in the experiments conducted at 800 °C at both 150 and 200 MPa. Plagioclase is present in every experiment, except 150 MPa at 900 °C. Both pyroxenes are present in every experiment, however orthopyroxenes have clinopyroxene rims in experiments at 900 °C, at 100 and 150 MPa, 895 °C at 150 MPa and 800 °C at 200 MPa, suggesting they are no longer in equilibrium, and thus have only been included in the phase diagram as clinopyroxene. The experiments that most closely match the 1883 tephra in terms of phase proportions were conducted at 850 °C, at 50 to 150 MPa, and 900 °C at 50 MPa. Phase proportions of pumices from Unit D, representing the massive PDC deposits at the top of the stratigraphy emplaced during the paroxysmal phase of the eruption, are better replicated at 50 MPa and 850 °C, due to the overall increase in crystallinity. The obsidian

found within Unit D contains quartz, and this phase assemblage is best replicated at 800 °C, and pressures of >150 MPa, however it should be noted that experiments at < 800 °C might also yield matching phase assemblages (see section 3.5.1). Examples of back scatter electron images of experimental products are shown in Figure 3.3.

Figure 3.4 shows the major element chemical composition of experimental matrix glass and how it varies with pressure and temperature (for data, see Supplementary excel file for Chapter 3, Supplementary Data 2). Weight % Al_2O_3 is consistently higher in the experiments than in the natural matrix glasses, which might be as a result of the experimental starting material being powdered, rather than coarsely crushed, pumice which will include plagioclase core compositions not in equilibrium with the final melt. Mass balance calculations were completed after analysis to assess this affect further. If ~10 % of the starting powder is an average plagioclase core composition (An_{54}), the Al_2O_3 content of the starting material is elevated by ~ 2 wt% in comparison to natural matrix glass, in line with the elevation in analyses of experimental glass generated at temperatures of 850 – 900 °C. Na_2O is affected by >0.1 wt%, which does not affect comparison with natural glasses. The concentration of CaO is raised by ~1 wt% through mass balance (an increase of ~45 %), however this does not appear to have raised experimental values beyond natural concentrations. The dilution effect is negligible for other elements, particularly when using them for comparison to natural samples. It is therefore recommended that comparisons between natural and experimental matrix glass for Al_2O_3, and CaO are treated with caution.

SiO_2 overall shows a strong negative correlation with temperature. SiO_2 content has a small positive correlation with pressure, until 200 MPa, where SiO_2 decreases across the temperature range. Figure 3.5 shows a positive correlation between temperature and the proportion of plagioclase in experiments.

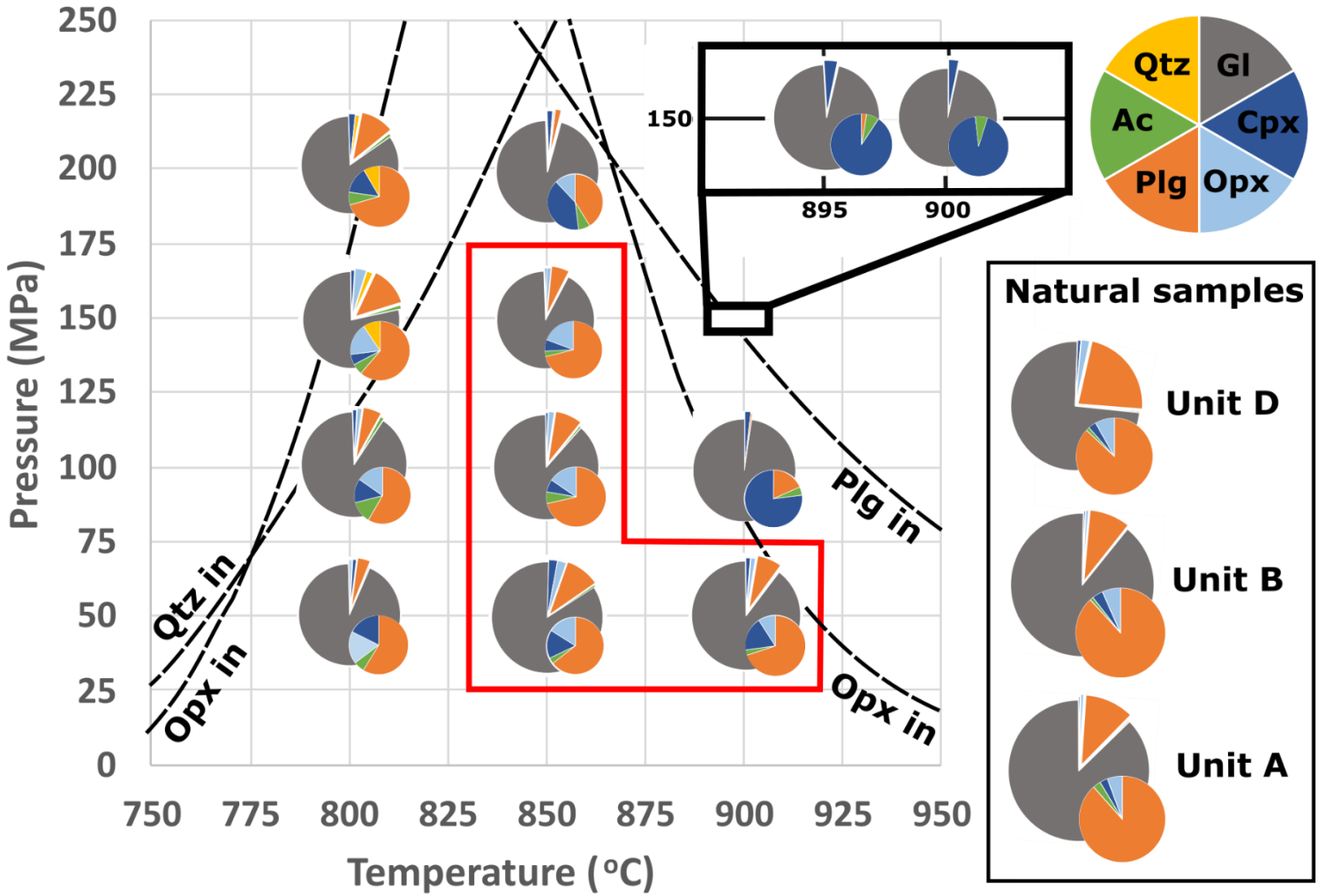

Figure 3.2: Phase diagram, showing proportions of glass and mineral phases present at experimental runs at a given temperature and pressure as large pie charts. Smaller pie charts show the relative proportions of phenocryst phases. On the right, the average proportions of phases are shown for natural samples through the stratigraphy, for comparison. Gl = glass (grey), Cpx = clinopyroxene, Opx = orthopyroxene Plg = plagioclase feldspar (orange), Ac = accessory phases (Fe-Ti oxides and apatite, both present in every experiment) and Qtz = quartz. Dashed lines show broadly where phases come in and out of equilibrium with the melt, constrained by the experiments shown. Red box indicates experimental products with similar phase proportions to natural 1883 tephra.

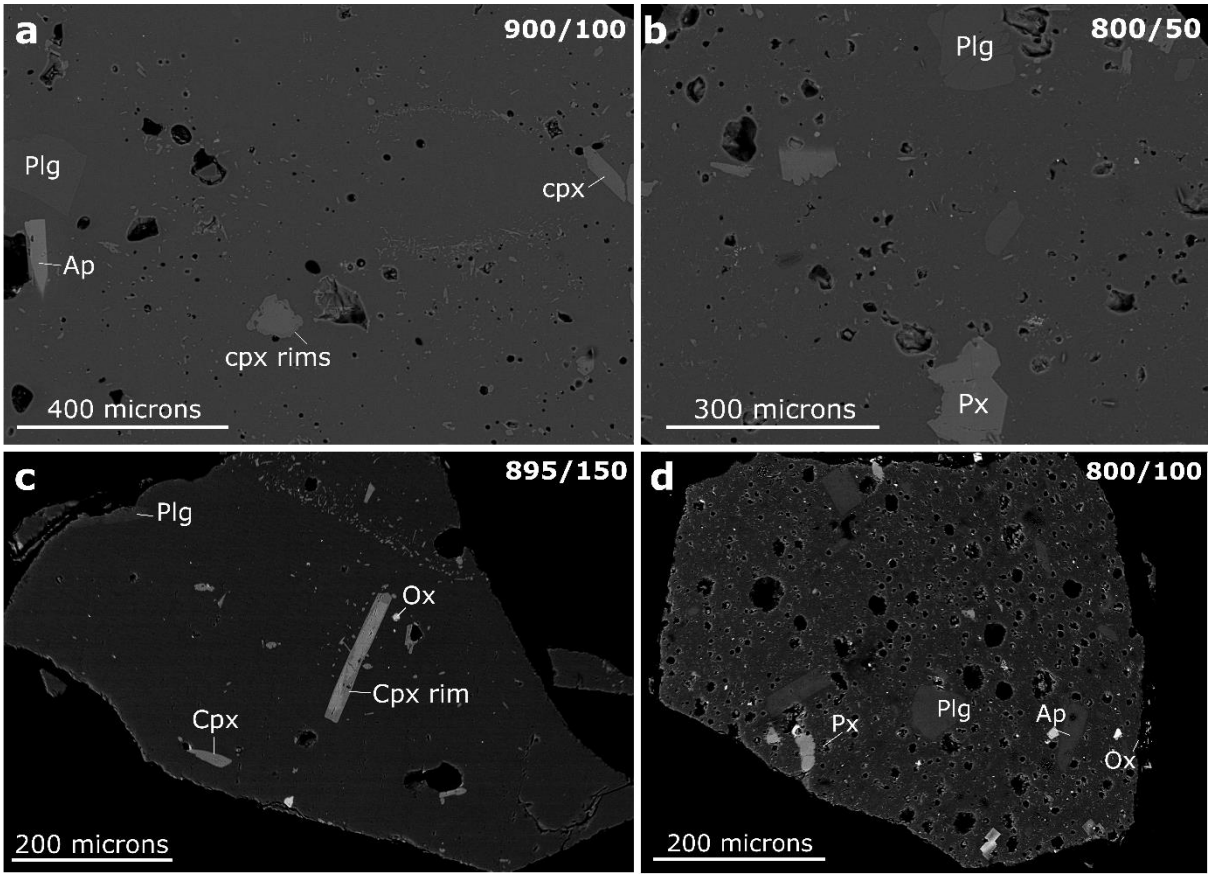

Figure 3.3: Back scatter electron images of experimental glasses and phases contained therein. (a) – (c) were used for glass chemistry, whereas (d) is an example of a microlitic glass that does not have equilibrium glass chemistry, even after a more rapid quench. The numbers show temperature (°C)/Pressure (MPa). Plg = plagioclase, Px = pyroxene, Cpx = clinopyroxene, Ox = oxide and Ap = apatite.

The matrix glass chemistry of Unit A in the stratigraphy most closely matches with experiments conducted at 850 °C at 150– 200 MPa (Figure 3.4). K_2O is marginally lower, and Na_2O marginally higher in the experiments than in the natural glass; these are the only oxides which do not overlap. When combined with the phase proportion data for these experiments, 150 MPa is the best match. However, Unit A has a more evolved matrix glass chemistry than the Unit B starting material, as so these comparisons should be treated with more caution (see section 4.3.1).

The chemical compositions of experiments at 100 - 150 MPa at 900 °C correlate most closely with the bulk of the 1883 pyroclastic sequence, comprising Units B to D in the stratigraphy (as in Madden-Nadeau et al., 2021; Figure 3.4). However, neither of these experiments have similar phase proportions to any component in the 1883 sequence (Figure 3.2). This is illustrated in Figure 3.5, which shows that ~88% of all crystals in natural pumice across all stratigraphic units are plagioclase. The experiments conducted at 100 – 150 MPa and 900 °C have, in contrast, between 0 and 20 % plagioclase. Glass chemistry measured for experiments conducted at 900 °C and 50 MPa was anomalous, with much lower SiO_2 contents than expected. These experimental glasses contained an abundance of microlites (Figure 3.3d), even after a more rapid quench, and thus analyses may have been affected by microlite contamination. In any case, the growth of microlites means that the matrix glass chemistry is unlikely to represent equilibrium conditions; this is also the case for experiments conducted at 850 °C and 800 °C at 100 MPa. However, the experiment at 900 °C and 50 MPa does have similar phase proportions to natural 1883 pumice (Figure 3.2; 3.5), and would likely have a similar matrix glass composition to other experiments at this temperature, given that pressure appears to have a minimal effect on matrix glass chemistry overall. To achieve the higher SiO_2 contents of the juvenile obsidian found in Unit D, lower temperatures of 800 °C are required across all pressures (50 - 200 MPa).

Figure 3.6 shows a ternary phase diagram for quartz-albite-orthoclase, with both natural and experimental glasses plotted. The only experiments saturated in quartz are those conducted at 800 °C. Some individual natural obsidian and Unit A glass analyses are saturated in quartz between 300 – 1000 MPa, at higher pressures than the 800 °C experiments (100 - 300 MPa). The projection shows clearly that the main field of overlap between experimental and natural samples is for temperatures in the region 850 – 895 °C, between 150 and 200 MPa.

Experimental plagioclase geochemistry shows no correlation with pressure or temperature (Figure 3.7; for data see Supplementary excel file, Supplementary Data 3). The total range of plagioclase rim compositions produced is An_{28} to An_{82} over all experiments, with the 1 σ range at An_{38} to $An_{65.}$ Mean anorthite compositions for experimental plagioclase rims range between An_{48} and $An_{52,}$ which

matches well with mean anorthite plagioclase rim compositions of natural samples (An_{48}; Madden-Nadeau et al., 2021). However, the range for natural plagioclase rims is An_{26} to An_{65}, which is narrower than that produced during our experiments. Experimental plagioclase rims also extend to higher anorthite contents; this may be as a result of the powdered starting material including some plagioclase cores of anorthite contents up to An_{92} (Pichivant et al., 2007). Four experiments (out of 11) had plagioclase of $An_{>70}$ (50 MPa at 900 °C, 100 MPa at 800 and 850 °C and 200 MPa at 850 °C), with them accounting for < 10 % of analyses, with six experiments (800 °C at both 50 and 200 MPa, in addition) with plagioclase of $An_{>60}$, accounting for < 15 % of analyses. Although all experiments are H_2O saturated, the wt% H_2O as a fluid phase may vary due to small losses during experimental runs, which may account for the lack of systematic correlation with pressure and temperature. Figure 3.7 also shows anorthite content of plagioclase crystallising at a given temperature as modelled using Rhyolite-MELTs (Gualda et al., 2012), for fractional crystallisation of an Anak Krakatau basaltic andesite starting composition (Darhen et al., 2012), at 125 MPa and an initial H_2O content of 1.5 wt%, which were determined to be best-fit conditions for 1883 whole-rock and matrix glass data (Madden-Nadeau et al., 2021). Anorthite contents modelled using Rhyolite-MELTS for any given temperature are consistently lower than any anorthite contents generated during experiments.

Experimental pyroxene analyses are shown in Figure 3.8 (See Supplementary excel file for Chapter 3, Supplementary Data 4). At >100 MPa, there is a positive correlation between Mg# and both pressure and temperature. The best match between experimental and 1883 clinopyroxene rims were experiments run at 150 – 200 MPa at 800 °C, and 50 - 150 MPa at 850 °C. All mean experimental orthopyroxene compositions overlap with the natural rim dataset.

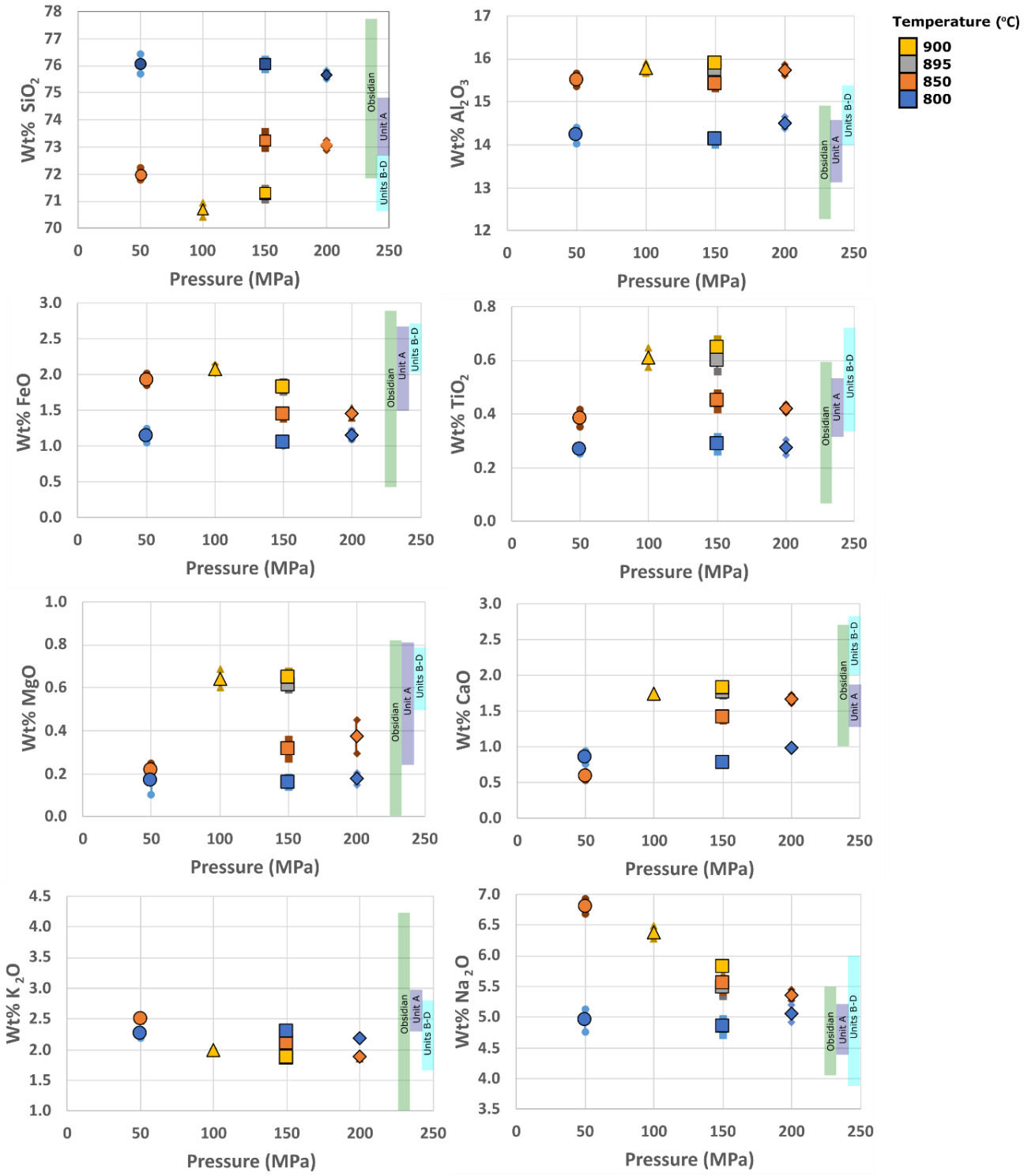

Figure 3.4: Graph showing how the measured compositions of experimental glasses, in wt% oxide, vary with pressure and temperature. Outlined symbols show the mean composition for a given pressure and temperature, with error bars representing 1 σ. Coloured boxes on the right hand side of each figure show the compositional range of matrix glass analyses for units within the stratigraphy (Figure 3.1), after Madden-Nadeau et al. (2021), for comparison.

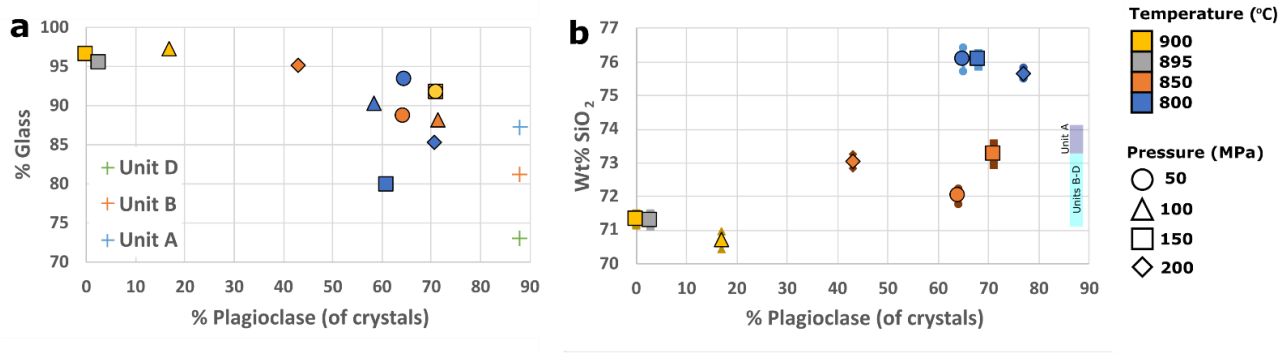

Figure 3.5: Graph (a) shows how mean % plagioclase of crystals in experimental products varies with the mean % glass, on a vesicle-free basis. Graph (b) shows how mean wt% SiO_2 of the experimental glasses vary with the mean % plagioclase of crystals (outlined symbols) for a given pressure and temperature, with error bars give to 1 σ. Compositions and percentage plagioclase of the natural 1883 stratigraphy provided for comparison in both plots (Units A, B and D).

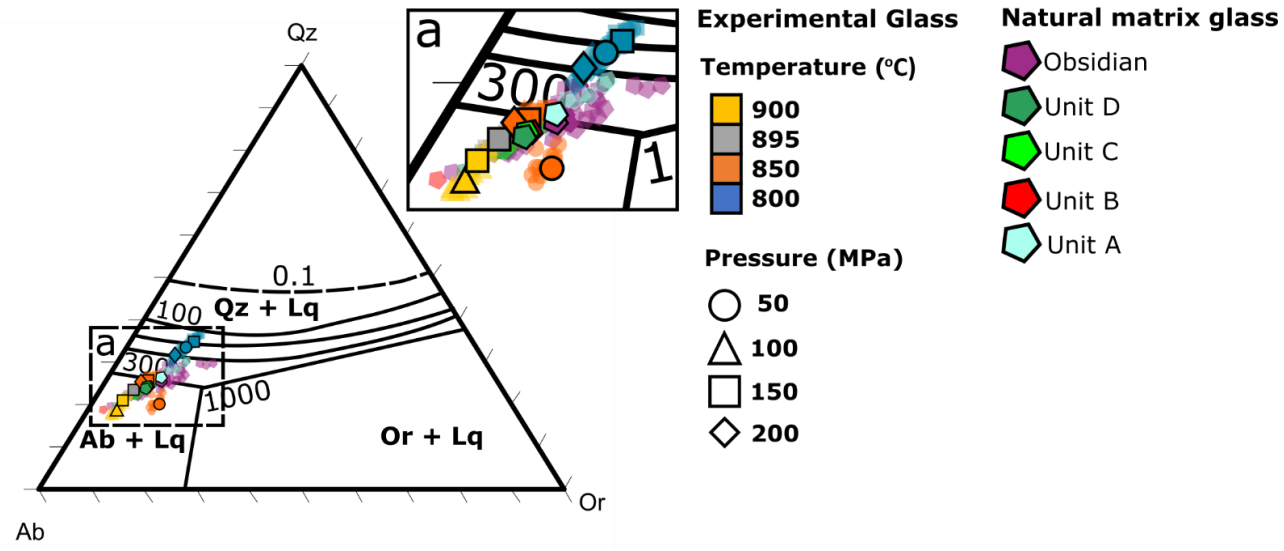

Figure 3.6: Ternary phase diagram for quartz-albite-orthoclase (Qz-Ab-Or) with both natural and experimental matrix glasses plotted (after Blundy and Cashman, 2001), with inset (a) zoomed in on the dataset. Numbers on phase boundaries show the pressure in MPa where a given melt/glass composition would be saturated in quartz. Outlined symbols represent the mean glass composition, whereas transparent symbols are individual analyses.

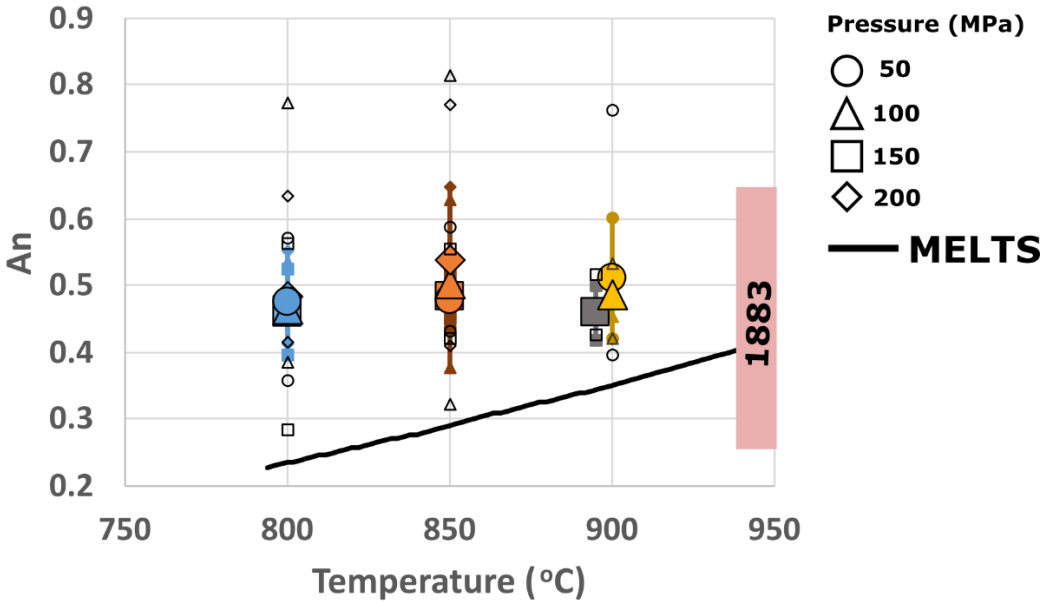

Figure 3.7: Graph showing how the measured anorthite content (An) of experimental plagioclase varies with pressure and temperature. Outlined symbols represent the mean anorthite content for a given pressure and temperature, with error bars given to 1 σ. Colourless symbols represent range extremities. Black line represents anorthite content of plagioclase crystallising at a given temperature as modelled using Rhyolite-MELTs (Gualda et al., 2012), for fractional crystallisation of an Anak Krakatau basaltic andesite starting composition (Darhen et al., 2012), at 125 MPa and an initial H_2O content of 1.5 wt%, which were determined to be best-fit conditions (Madden-Nadeau et al., 2021). Natural 1883 plagioclase rim compositions are shown for comparison on the right side of the graph.

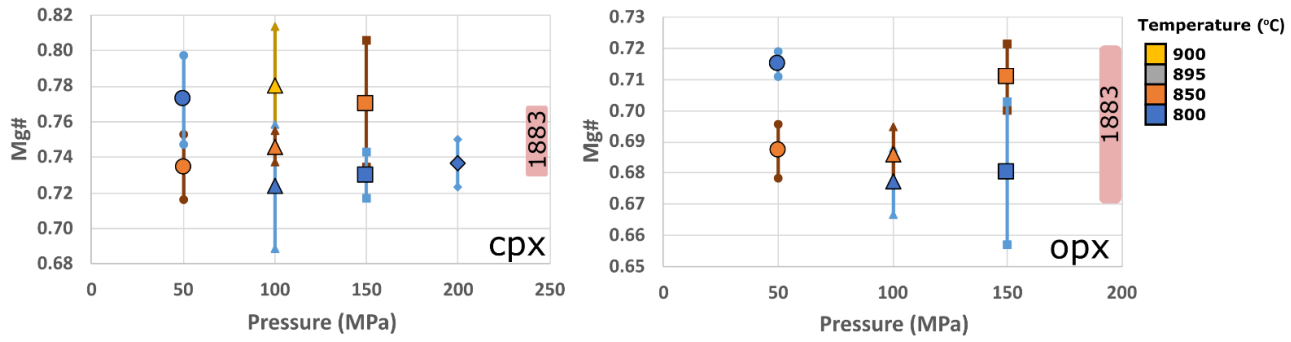

Figure 3.8: Graph showing how magnesium number (Mg#) of experimental clinopyroxene (cpx) and orthopyroxene (opx) varies with pressure and temperature. Outlined symbols represent the mean Mg# for a given pressure and temperature, with error bars to 1 σ standard deviation. Pink boxes represent natural pyroxene rim compositions as measured from archived BGS samples (Madden-Nadeau et al., 2021), collected during the paroxysmal phase of the eruption on 26th/27th August 1883 (Units B to D equivalent).

3.4.2 Plagioclase trace elements

Plagioclase phenocrysts in the natural Krakatau samples are diverse in their zoning profiles, with a broad range in rim compositions (Figure 3.9), as discussed previously by Madden-Nadeau et al. (2021), and cannot be placed into discrete typologies. In addition, phenocrysts from Units A, B and D cannot be distinguished from one another (Figure 3.9a). The trace elements Mg, Fe, Ti and Sr were analysed for 16 plagioclase crystals picked from BGS archive samples, which were collected during the paroxysmal phase of the eruption (Units B to D equivalent). Ten of these crystals are complete, with transects taken from core to euhedral rim, and are shown in Figure 3.9b. The trace element compositions of 13 of 16 crystals analysed show a consistent trend with anorthite content (Figure 3.10). There is a positive correlation between Ti and anorthite where $An_{<60}$ (R^2 = 0.48), whereas for $An_{>60}$ Ti has a negative correlation with anorthite (R^2 = 0.69; Figure 3.10a). Mg vs anorthite has a similar overall trend to Ti ($An_{<60}$, R^2 = 0.47; $An_{>60}$, R^2 = 0.50; Figure 3.9b). A positive correlation between Fe and anorthite can also be observed (R^2 = 0.75; Figure 3.10c). There is a strong negative correlation between Sr and anorthite (R^2 = 0.85; Figure 3.10d).

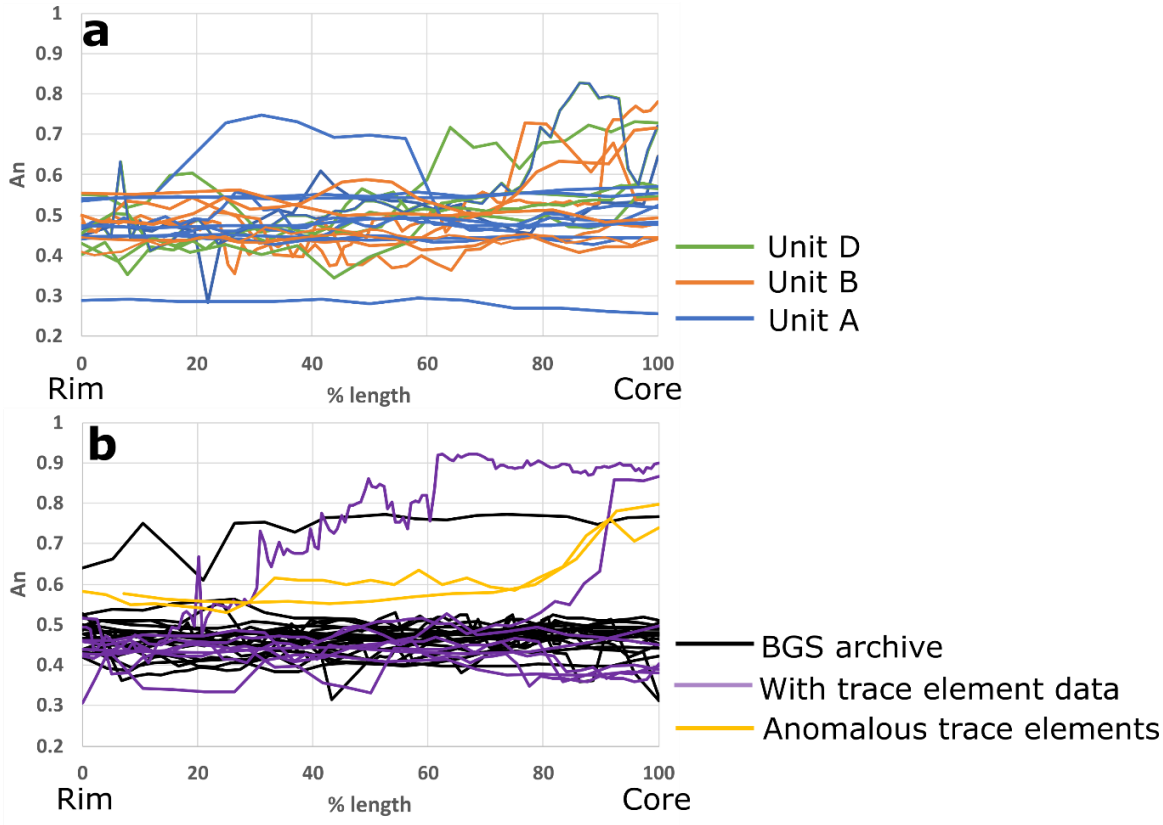

Figure 3.9: Complete anorthite transects (n = 51) across natural euhedral plagioclase phenocrysts, taken rim to core, and normalised to % length, for (a) Unit A (blue), B (orange) and D (green) in the stratigraphy, taken from Madden-Nadeau et al. (2021) and (b) BGS archive samples collected during the paroxysmal phase of the eruption (Units B-D equivalent), after Madden-Nadeau et al. (2021). Transects in purple are for unbroken crystals with trace element data (Mg, Fe, Ti, Sr), with the two yellow transects having anomalous trace element data. Not all anorthite transects for phenocrysts with trace element data are shown here, as not all were complete crystals with euhedral rims.

Three crystals have trace element chemistry that is distinct from these trends. Phenocryst #07_08, #72_04 and #72_05 have higher Fe and Mg (Figure 3.10b and c) than the other phenocrysts. Two of the three anomalous crystals are unbroken with transects from core to euhedral rim (#07_08 and #72_05; yellow lines in Figure 3.9b). These unbroken anomalous crystals have similar zoning patterns: they both have a high An patchy core (An_{80} and An_{76}, respectively), followed by a mantle that contains fine oscillatory zones (Figure 3.9b). The rim composition for both crystals is An_{58}. All

analytical data for plagioclase phenocrysts, and accompanying BSE images, can be found in Analytical Data 3 – 11 in the dataset Madden-Nadeau (2020), and in the Supplementary excel file for Chapter 2 (previous chapter), Supplementary Data 2.

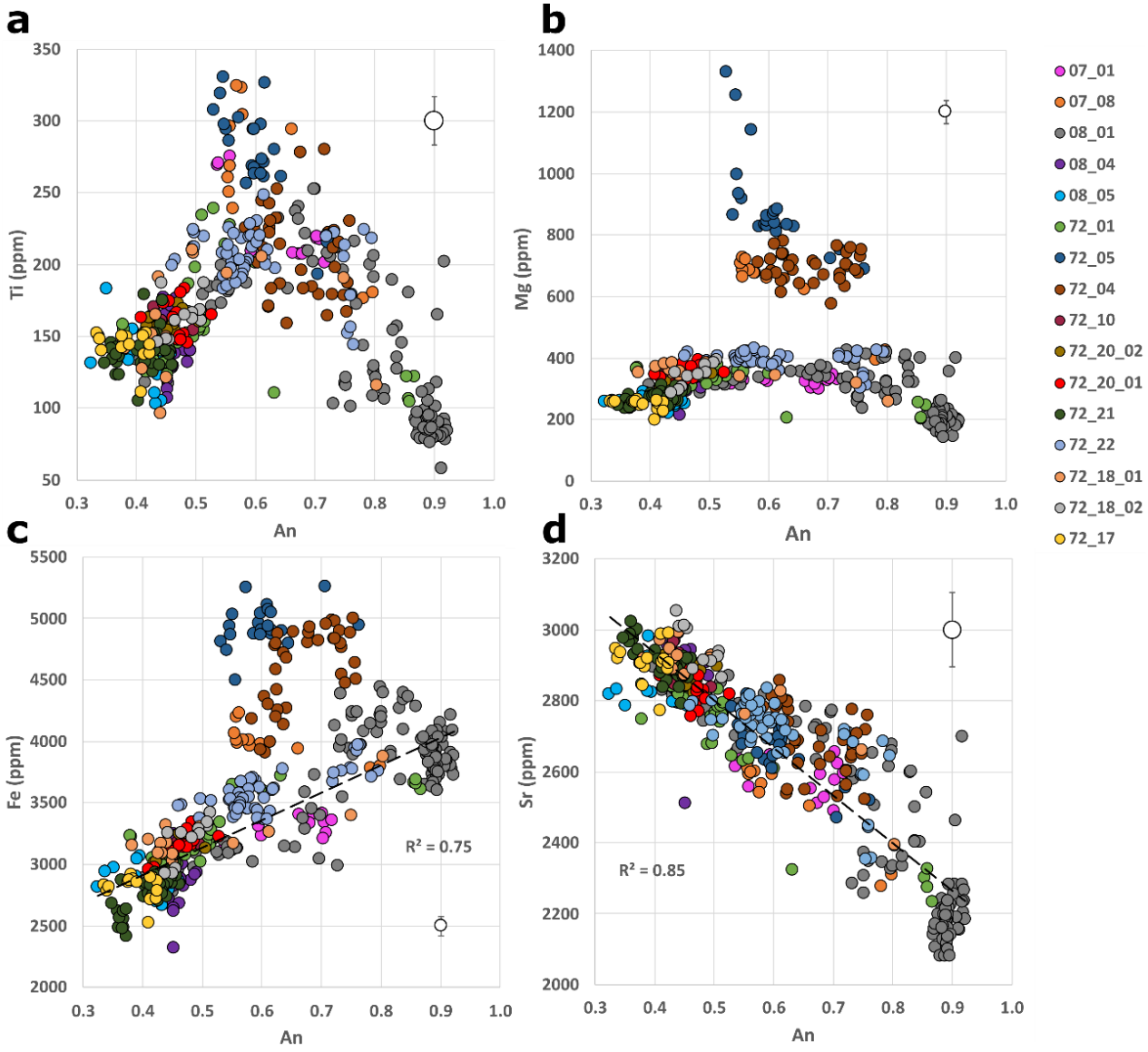

Figure 3.10: Trace elements plotted against anorthite content for plagioclase phenocryst traverses, picked from the archived BGS samples collected during the paroxysmal phase of the eruption on 26th and 27th August 1883 (equivalent to Units B –D in the stratigraphy). Data for each individual crystal traverse is denoted by a different colour, and can be found in Analytical Data 3(a) and (h); 4(a), (c) and (d); and 5(a) - (c), (h), (m) - (r) in the dataset Madden-Nadeau (2020). Trend line and

R^2 values are shown in (c) and (d) for Fe and Sr, excluding the three anomalous crystals. Error bars are shown on the colourless black circle in each plot, and represent 1 σ.

3.4.3 Trace element modelling

Melt chemistry can be modelled using empirically derived formulas for partition coefficients, estimates for melt temperature, and/or SiO_2 content, and trace element concentrations in phenocryst phases. This is useful as it not only provides chemical information about the pre-eruptive melt, but also information about the chemistry of the melt at all stages of the chosen phases' crystallisation history. Modelling melt chemistry this way will thus allow us to test the degree to which there is melt diversity within the magmatic system, both in terms of chemistry and magmatic conditions. Melt concentrations of Ti, Mg and Sr were modelled using measured concentrations in plagioclase phenocrysts (Figure 3.10) and partition coefficients. These elements were chosen because they are trace elements in plagioclase above the detection limit using EPMA, and have partitioning behaviour between plagioclase and the melt that has previously been experimentally investigated (e.g., Drake and Weill, 1975; Bindemann et al., 1998; Dohmen and Blundy, 2014; Neilsen et al., 2017).

Partition coefficients governing how Ti partitions between the melt and plagioclase were calculated using the model of Nielsen et al. (2017), which is expressed as a function of temperature and anorthite content:

$$RT\ln(D_{Ti}) = -32.5\ X_{An} - 15.1$$

where R is the gas constant (J Kg^{-1} Mol^{-1}), T is temperature (K), D_{Ti} is the partition coefficient between melt and plagioclase for Ti, and X_{An} is the molar concentration of anorthite. This model has been calibrated using experimental data over plagioclases of $An_{0\text{-}100}$, from 0.1 – 2700 MPa, and 750 – 1385 °C. However, it should be noted that there are gaps in this dataset, notably between 850 and 1086 °C, where there is only one experiment at 950 °C.

Partition coefficients for Mg were initially calculated in a similar fashion using the model of Bindemann et al. (1998):

$$RTln(D_{Mg}) = -26.1\ X_{An} - 25.7$$

where D_{Mg} is the partition coefficient between melt and plagioclase for Mg. This model is calibrated using experimental data, over plagioclase compositions of $An_{42\text{-}77}$ at 0.1 MPa, over a temperature range of 1153 – 1299 °C. Given that the range in anorthite compositions, pressures and temperatures over which this model was calibrated are not inclusive of measurements and estimates for 1883 products, partition coefficients for Mg were recalculated, along with partition coefficients for Sr, using a sophisticated model for partitioning between plagioclase and the melt as a function of temperature, anorthite content and melt composition, derived by Dohmen and Blundy (2014). This model is calibrated using experimental data, with plagioclase anorthite contents of $An_{0\text{-}100}$, under atmospheric pressure to 2.7 GPa. However, the temperature range this model was calibrated over is 1086 to 1410 °C, which does not include pre-eruptive temperature estimates for Krakatau 1883 of 890-935 °C. In addition, the highest SiO_2 content this model was calibrated for is 68 wt%, and the paroxysmal Krakatau 1883 tephra includes SiO_2 contents of in excess of 72 wt%.

To calculate partition coefficients for compositions of $An_{<59}$, the melt temperature and SiO_2 content were estimated from models of the fractional crystallisation of an Anak Krakatau basaltic andesite starting composition at 125 MPa (corresponding well to experimental range of 100 - 150 MPa) and 1.5 wt% initial H_2O content with Rhyolite-MELTS (Gualda et al., 2012; Figure 3.11) which were shown to be best estimates for the conditions that generated the 1883 rhyodacite (Madden-Nadeau et al., 2021; Chapter 2). A basaltic andesite starting composition was selected, as this is the most common composition erupted by Anak Krakatau.

Rhyolite-MELTS models of fractional crystallisation of an Anak Krakatau starting composition (the most primitive reported on Krakatau by Darhen et al., 2012) through cooling from 1200 °C could not crystallise plagioclase of composition $An_{>59}$ even at higher pressures (up to 1000 MPa) and higher water contents (up to 10 wt%). Erupted volcanic products may only represent a small

proportion of magmas present within a volcanic system, however. Understanding unerupted magmas is important, as they have implications for eruptive style, and for triggering eruptions through magma mixing (E.g., Di Genova et al., 2017). Plutonic xenoliths can therefore provide useful chemical information on magma stored beneath the volcano, that is not necessarily erupted. Unfortunately, plutonic xenoliths were not found in the Krakatau 1883 tephra, nor are they common in the erupted products of Anak Krakatau (Gardner et al., 2012). However, plutonic xenoliths are exceptionally common in the Lesser Antilles (Arculus and Wills 1980; Lewis 1973), providing the most comprehensive dataset for melts resident within an arc volcanic system that are not erupted. Thermometry of plutonic xenoliths with a broadly similar mineralogy to 1883 tephra (Table 3.3; plagioclase dominant phase, with pyroxenes) and containing plagioclase with high anorthite contents, has been completed on samples from Bequia (Camejo-Harry et al., 2018), Martinique (Cooper et al., 2016), St. Eustatius (Cooper et al., 2019) and St. Vincent (Tollan et al., 2012), as well as for Raoul Island in the Tonga-Karmadec arc (Hasse et al., 2014). The total range in temperatures calculated for these plutonic xenoliths is 910 – 1051 °C (Table 3.3). Given that the majority of these estimates are achieved using late equilibrating phases such as Fe-Ti oxides, and late crystalising phases, such as orthopyroxene, and that Rhyolite-MELTs estimates (Anak Krakatau starting composition, initial water content of 1.5 wt%; Gulda et al., 2012) of temperatures generating anorthite contents of An_{59} is ~ 1050 °C, a temperature estimate of 1050 °C is used to generate partition coefficients for plagioclase of $An_{>59}$. The melt SiO_2 contents used to generate partition coefficients for Mg and Sr (Dohmen and Blundy, 2014) are systematically decreased from 61 wt% at An_{58}, as estimated using Rhyolite-MELTs, to 40 wt% at An_{92}, in line with whole-rock compositions of plutonic xenoliths (Table 3.3).

Table 3.3: Thermometry estimates of plutonic xenoliths of a broadly similar mineralogy to the 1883 tephra found at different arc volcanoes, with corresponding anorthite compositions for plagioclase and SiO_2 contents.

Location	Study	Volcanic compositions	Mineralogy of plutonic xenoliths	Method	Temperature (°C)	Anorthite content	SiO_2 content (Wt%)
Bequia (LA)	Camejo-Harry et al. (2018)	Basalt to andesite	Plg + Cpx + Ol + Ox Plg + Cpx + Ol + Ox Plg + Cpx + Ol Plg + Cpx + Ol + Ox	Cpx-Ol-Plg (COIP) thermometry Ziberna et al., (2017)	982 – 1051 (+/- 20)	An_{87-90} An_{84} An_{70-93} An_{58-92}	42.4 46.2 51.5 53.7
Martinique Mt. Pelee and Mt. Concil (LA)	Cooper et al. (2016)	Basalt to rhyolite	Plg + Cpx + Opx + Ox	Fe/Ti oxide thermometry (Ghiorso and Evans, 2008)	900 – 920 (+/- 50)	An_{55-95}	48 - 49
St. Eustatius (LA)	Cooper et al. (2019)	Basalt to rhyolite	Plg + Cpx + Opx + Ol + Opx Plg + Ol + Opx + Cpx	Two pyroxene thermometry (Putirka, 2008)	910 945 (+/- 40)	An_{74-95} An_{52-94}	45 57
St. Vincent, near La Soufriere (LA)	Tollan et al. (2012)	Basalt and Basaltic Andesite	Plg + Ol + Cpx + Ox + Opx	Two pyroxene thermometry QUILF (Anderson et al., 1993)	970	An_{92-94}	38 - 46
Raoul Island, Tonga Arc	Haase et al. (2014)	Basalt to rhyolite	Plg + Cpx + Opx, + Ol + Ox	Two pyroxene thermometry (Putirka et al., 2003)	975-980 (+/- 40)	An_{90-97}	46.3

SiO_2 contents are whole-rock measured via x-ray fluorescence. Minerals given in order of abundance. Plg = plagioclase, Cpx = clinopyroxene, Opx = orthopyroxene, Ol = olivine and Ox = oxides. LA = Lesser Antilles. Xenoliths from the lesser Antilles were generally found ex situ.

There are very large uncertainties attached to the modelled melt compositions shown in Figures 3.12 and 3.13, and so it should be noted that the intention of this modelling is not to discuss absolute values, but instead to highlight general trends and to provide an internal comparison between melts at different stages of plagioclase crystallisation, prior to the 1883 eruption. Melt chemistry modelled using partition coefficients (calculated from Rhyolite-MELTs inputs for plagioclase $An_{<59}$, and from plutonic xenolith inputs for $An_{>59}$) shows that for $An_{<65,}$ there is a moderate positive correlation (R^2

= 0.53) between the crystallised anorthite content and the estimated wt% MgO in the melt (Dohmen and Blundy, 2014; Figure 3.12a, b). The modelled MgO content is consistently higher than experiments crystallising plagioclase of similar anorthite contents, with some overlap within error with higher temperature experiments (895 -900 °C). At compositions of $An_{>65,}$ modelled wt% MgO in the melt has a weak to moderate negative correlation with anorthite (R^2 = 0.34), with a greater diversity in MgO contents of melts crystallising plagioclase of these anorthite contents. Modelled MgO is <2 wt% over the entire range of anorthite contents, which is low for high anorthite plagioclase, most often associated with more primitive melts (discussed further in section 4.5.2). Modelled wt% MgO in the melt increases as both temperature and SiO_2 content decrease. The highest MgO contents modelled using Dohmen and Blundy (2014) partition coefficients and 1883 plagioclase Mg concentrations for plagioclase of An_{80} is still only 1.69 wt%, achieved for a melt with 45 wt% SiO_2 at 800 °C. The model presented by Bindemann et al. (1998) produces more realistic estimates of modelled MgO in the melt for high anorthite contents, ranging from 2 – 6 wt % for $An_{>80}$ under conditions informed by arc plutonic xenolith data (see Supplementary Figure A, Appendix 3). Three crystals with anomalous Mg and Fe contents (Figure 3.10), appear to have been crystallised from more Mg-rich melts. For the Dohmen and Blundy (2014) model, MgO content of the melt estimated by these crystals range between 2 and 4 wt%, and for the model of Bindemann et al. (1988) this ranges from 4.6 to 9.1 wt%.

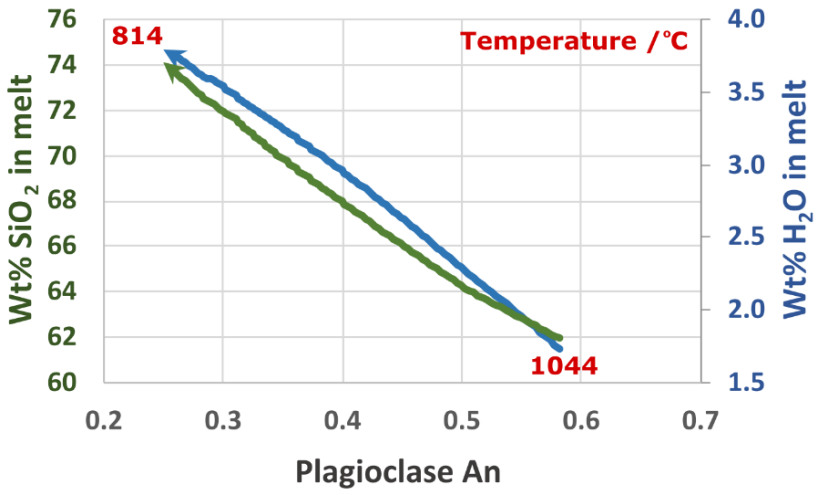

Figure 3.11: Graph showing how SiO_2 (green) and H_2O (blue) vary with plagioclase anorthite content during fractional crystallisation modelled isobarically by Rhyolite-MELTS at 125 MPa, with an initial water content of 1.5 wt% (Gualda et al., 2012). These fractional crystallisation trends best match trends in major elements for 1883 matrix glass and whole rock compositions (Madden-Nadeau et al., 2021). Temperature values are shown in red for the melt compositions where plagioclase begins to crystallise, and where the melt SiO_2 content is the same as the average glass composition of Unit A (most evolved; After Madden-Nadeau et al., 2021). These SiO_2 contents are used with their respective anorthite contents to model partition coefficients for Mg and Sr between plagioclase crystals and the 1883 melt using the model of Dohmen and Blundy (2014), for plagioclase of $An_{<59}$.

There is a strong positive correlation between the estimated TiO_2 composition of the melt and the corresponding plagioclase anorthite composition, for $An_{<75}$ (Figure 3.12c; $R^2 = 0.84$; excluding 3 anomalous crystals). The modelled TiO_2 compositions for $An_{<75}$ match well with the experimental glass chemistry at all conditions. There are three points (at An_{63}, An_{73} and An_{75}) which have significantly lower estimated TiO_2 concentrations than the prevailing trend. At $An_{>75}$ there is a very weak negative correlation ($R^2 = 0.12$) between the estimated TiO_2 of the melt and corresponding plagioclase anorthite composition. Estimated Sr concentration of the melt has a very strong positive

correlation with all corresponding anorthite compositions of all plagioclase crystals analysed (Figure 3.11d; $R^2 = 0.98$; including anomalous crystals).

Figure 3.13a and b show the estimated MgO and TiO_2 in the melt, against the estimated Sr concentration of the melt. At a modelled Sr content of the melt of <1200 ppm, ignoring the anomalous crystals, there is a positive correlation between Sr, and MgO ($R^2 = 0.49$) and TiO_2 ($R^2 = 0.77$) respectively. At modelled Sr contents of 1300 – 1800 ppm, there is a very weak positive correlation between TiO_2 ($R^2 = 0.12$), and MgO ($R^2 = 0.16$), and Sr. At modelled Sr contents of >2000 ppm, there is no correlation between either MgO ($R^2 = 0.002$) or TiO_2 ($R^2 = 0.07$) with Sr. Figure 3.13c shows how modelled TiO_2 varies with modelled MgO in the melt. The experiments produce glass along this trend at low MgO and TiO_2 contents, within error. In addition, this data matches well with Rhyolite-MELTS modelling of isobaric fractional crystallisation of a basaltic andesite Anak Krakatau starting composition at 125 MPa and an initial water content of 1.5 wt% (Gualda et al., 2012).

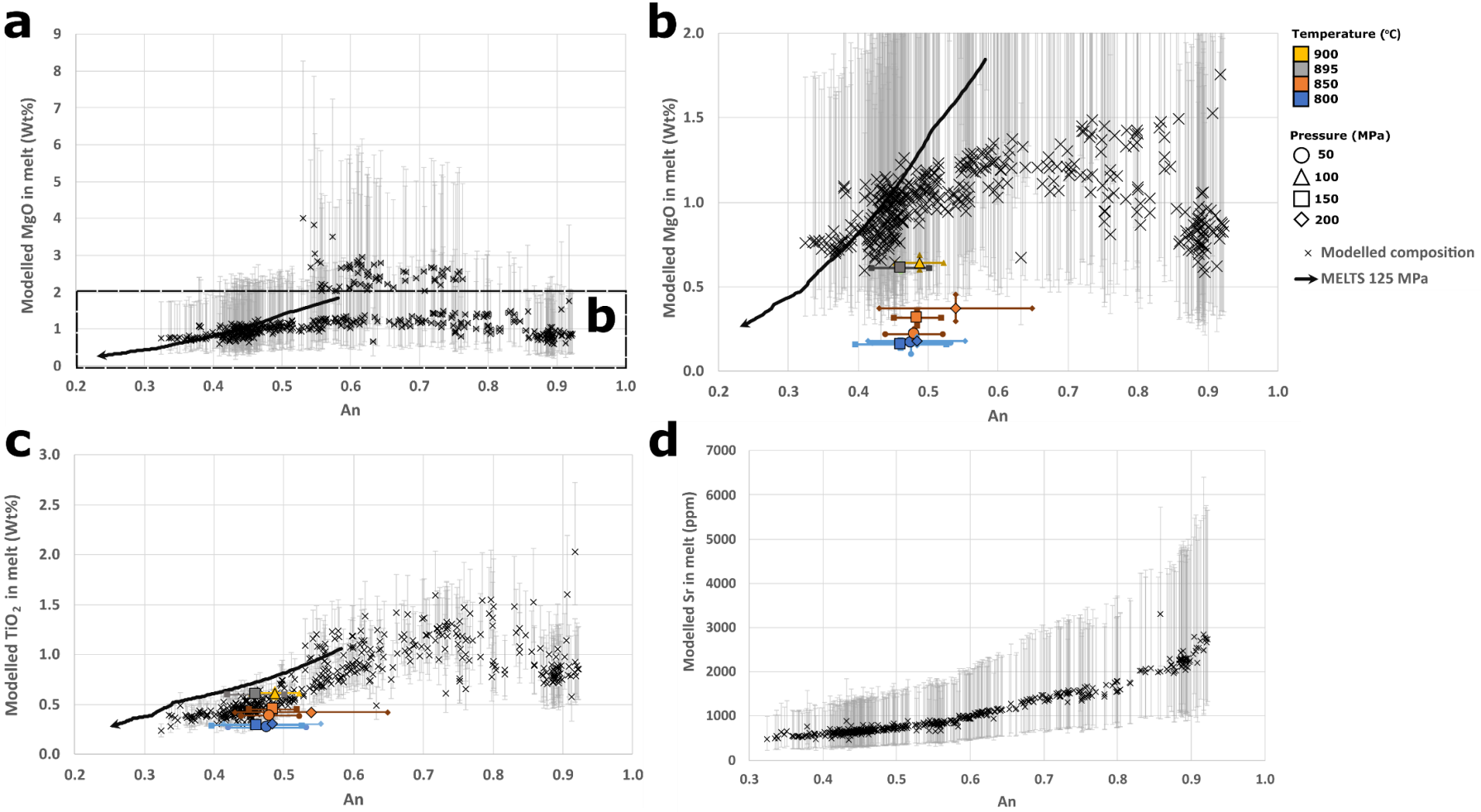

Figure 3.12: Estimated melt composition (black crosses) against the corresponding crystallised anorthite content, modelled using partition coefficients and plagioclase trace element data. (a) shows MgO variation, with melt chemistry evolution estimated via Rhyolite-MELTS models at 125 MPa (Figure 3.9; Gualda et al., 2012; Madden-Nadeau et al., 2021) for comparison, with (b) being zoomed in on the main trend, with experimental plagioclase anorthite and melt composition plotted as coloured symbols. (c) shows TiO_2 variation, with Rhyolite-MELTS trends and experimental analyses, and (d) shows how Sr (in ppm) varies against anorthite content. Error bars for modelled melt composition in (a), (b) and (d) represent the range in compositions produced when you vary the partition coefficient by a factor of 2, as Dohmen and Blundy (2013) state that 69 % of values are within this range. Error bars on modelled melt composition in (c) are derived from estimated errors on empirically derived coefficients used to estimate the partition coefficients used to model TiO_2 concentrations in the melt, given by Nielsen et al., (2017). This has then been added to the analytical error associated with the plagioclase analyses. Error bars on experimental data is given to 1 σ.

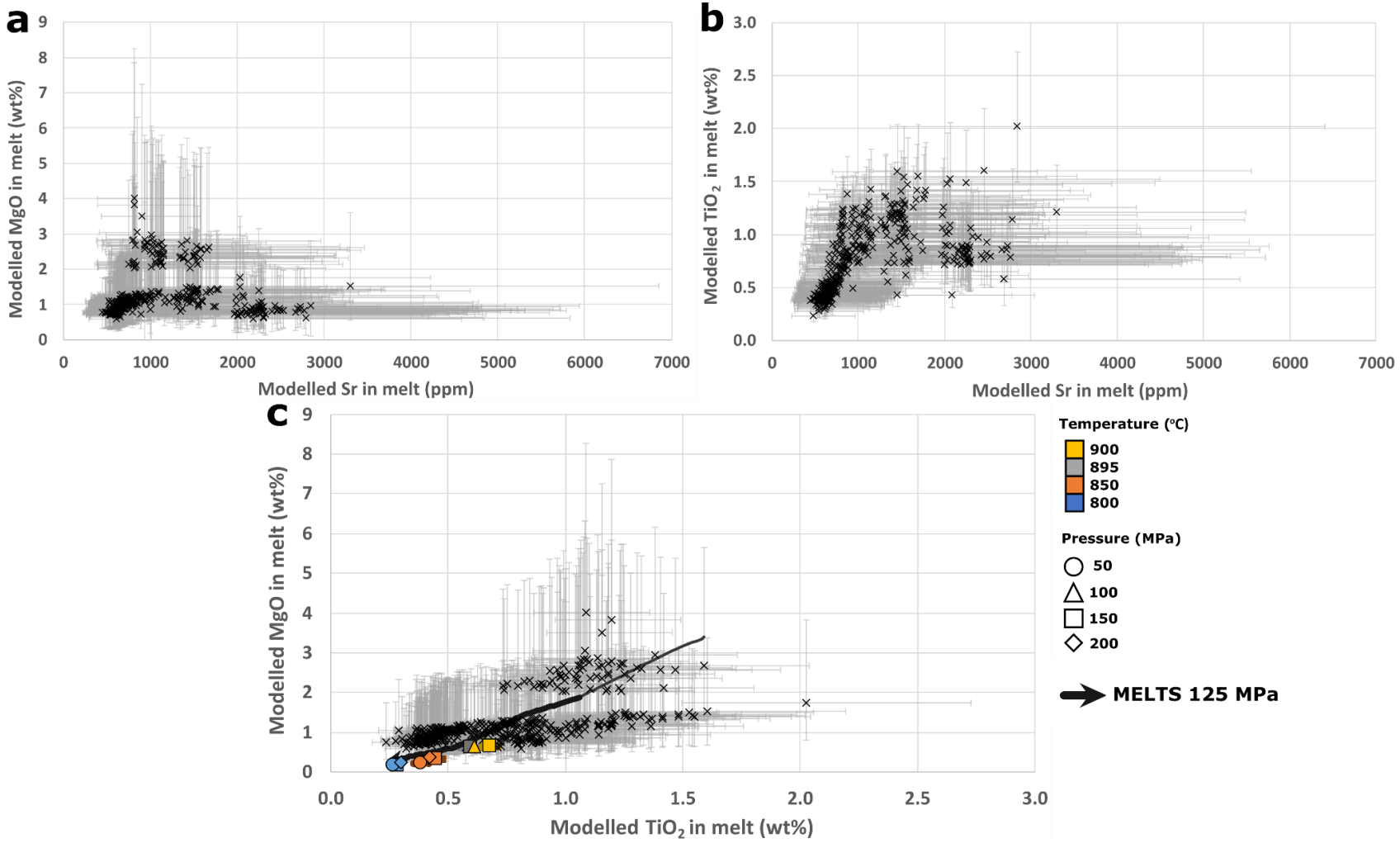

Figure 3.13: Graph showing modelled (a) MgO against Sr and (b) TiO_2 against Sr. Sr is taken to be an indicator of melt evolution (Figure 3.6d). Graph (c) shows modelled MgO against TiO_2, with experimental glasses plotted, as well as a Rhyolite-MELTs model of isobaric fractional crystallisation of an Anak Krakatau basaltic andesite starting composition, at 125 MPa and an initial H_2O content of 1.5 wt% (black line; Gualda et al., 2012). This run represents best fit conditions for fractional crystallisation generating the 1883 tephra (Madden-Nadeau et al., 2021). Where the black line thickens represents the onset of plagioclase crystallisation in this rhyolite-MELTs run. Error bars for MgO and Sr represent the range in compositions produced when you vary the partition coefficient by a factor of 2, as Dohmen and Blundy (2013) state that 69% of values are within this range. Error bars in for TiO_2 are derived from estimated errors on empirically derived coefficients used to estimate the partition coefficients used to model TiO_2 concentrations in the melt, given by Nielsen et al., (2017). This has then been added to the analytical error associated with the plagioclase analyses.

3.5 Discussion

3.5.1 Experimental constraints on pre-eruptive magmatic conditions

Aiming for an improved understanding of magma storage conditions, such as pressure and temperature, of explosive caldera forming eruptions, is useful in the interpretation of geophysical data in volcano monitoring. Previous studies have attempted to constrain the pre-eruptive pressure and temperature of the 1883 event petrologically (Table 4.1), however this is the first experimental attempt to investigate these conditions. Madden-Nadeau et al. (2021) provide the most up-to-date estimate of pre-eruptive temperature using Fe-Ti oxide thermometry (after Ghiorso and Evans, 2008) of 890 – 935 °C. Pressure is generally poorly constrained, but estimated at between 100 - 200 MPa (4 - 8 km depth; Mandeville et al., 1996a). Experiments may thus serve to further constrain pressure and temperature conditions for the pre-eruptive 1883 magma.

The experiments conducted all had the same starting composition: a sample taken from Unit B within the stratigraphy (D4S1.2). We compare experimental results with all units within the stratigraphy, as well as the obsidians found within Unit D, which assumes a similar starting composition. Powdered pumice was used as a starting material, and mass balance calculations show that the presence of plagioclase appears to have had some effect on the starting composition. Although this appears to have only affected Al_2O_3, to verify these results, further work should include completing experiments using coarsely crushed material, to obtain local equilibrium, and exclude crystal cores which would have been out of equilibrium with the pre-eruptive melt.

The ~2-5 cm layer of ash aggregates at the base of the 1883 pyroclastic sequence (Unit A) was likely erupted as part of the precursory sub-Plinian activity in May (Madden-Nadeau et al., 2021). Unit A contains phenocrysts of plagioclase and both pyroxenes, with accessory Fe/Ti oxides and apatite (Figure 3.2), with the SiO_2 content of the matrix glass ranging from 72.6 to 73.8 wt% higher in relative terms than Units B - D (Figure 3.4; Madden-Nadeau et al., 2021). Experimental glass produced at 150 - 200 MPa and temperatures of 850 °C most consistently matches the natural glass compositions, overlapping in SiO_2, TiO_2, FeO, MgO and CaO (Figure 3.4). However, ~50 % of the crystals grown in experiments at 200 MPa are pyroxene, which is inconsistent with natural

phenocryst proportions in Unit A, where pyroxene only accounts for ~9% of crystals (Figure 3.2). There is no chemical data available for matrix glass of the experiment at 850 °C and 100 MPa, or 900 °C and 50 MPa, but the phenocryst phase proportions match well with natural tephra (Figure 3.2 and 3.5a). The other experiments at 900 °C do not vary greatly from each other in composition, however, making it unlikely that the experiment at 900 °C and 50 MPa would replicate natural glass compositions. In addition, Na_2O increases significantly at lower pressures (50 -100 MPa) between 850 and 900 °C, taking values far out of range of the natural Unit A compositions (Figure 3.4). However, 850 °C and 100 MPa cannot be ruled out at this time, constraining the magmatic pre-eruptive conditions of Unit A to 100 - 150 MPa (~4 – 6 km depth; assuming crustal density of 2700 g/cm^3) and ~850 +/- 25 °C.

Units B to D of the pyroclastic sequence again contain only plagioclase and pyroxene phenocrysts with accessory Fe/Ti oxides and apatite, but have a lower SiO_2 content than Unit A, ranging from 70.5 to 72.6 wt% (Figure 3.4). Glass chemistry of Unit B – D natural tephra overlaps with glasses in experiments at 50 MPa and 850 °C (SiO_2, TiO_2, and K_2O), 100 MPa and 900 °C (SiO_2, TiO_2, FeO, MgO and K_2O) and 150 MPa at both 895 and 900 °C (SiO_2, TiO_2, MgO, Na_2O and K_2O; Figure 3.4). However, phase proportions are only similar for one of these experiments: 50 MPa and 850 °C (Figure 3.2; 3.5). Glass chemistry was not available for experiments conducted at 100 MPa and 850 °C, and 50 MPa and 900 °C, and, as they have similar phase proportions to natural tephra (Figure 3.2 and 3.5), these pre-eruptive conditions cannot be ruled out. In addition, clinopyroxene Mg# also overlaps for experiments conducted at 850 °C at both 50 and 100 MPa (Figure 3.8a). Conditions of 50 - 100 MPa (2 -4 km) and 850 – 900 °C are therefore most likely to represent the magma feeding the paroxysmal phase of the eruption on 26th and 27th August 1883. These estimates agree well with Fe-Ti oxide thermometry which provided an average melt temperature of 914 +/- 50 °C (Madden-Nadeau et al., 2021). The pressure estimates for the paroxysmal phase of the 1883 eruption of Krakatau are lower than for similar caldera forming eruptions with dacitic products (see Cassidy et al., 2019) e.g., Late Bronze Age eruption, Santorini (200 MPa; Cadoux et al., 2014), 1991 eruption of Mt. Pinatubo, Philippines (~ 200 MPa; Scalliet and Evans, 1999), Nevado de Toluca, Mexico (150

– 200 MPa; Arce et al., 2006; 2013) and to a lesser extent Mt. Aniakchak, Alaska (~ 100 – 150 MPa; Larsen, 2006). The experimentally derived temperatures are similar to all of these eruptions, except the 1991 eruption of Mt. Pinatubo, which is estimated to have cooler pre-eruptive storage conditions (750 – 800 °C; Scalliet and Evans, 1999).

Coherent juvenile obsidian blocks up to 8 m in length were observed in Unit D (Madden-Nadeau et al., 2021). Some of the obsidian was black and vitreous, with a low phenocryst content, whereas a proportion was grey and dull in colour, with a higher phenocryst content. Those obsidians with a higher phenocryst content were the most evolved, and contained quartz. All experiments conducted at 800 and 850 °C overlapped with obsidian glass compositions, however the highest SiO_2 contents require a cooler temperature to replicate the natural glass compositions. In addition, the experiments run at 800 °C and 150 and 200 MPa generated the only experimental products to contain quartz. Some obsidians are saturated in quartz on the Qz-Ab-Or phase diagram at pressures between 300 and 1000 MPa (Figure 3.6), although this was not the case for all obsidians, but analyses do not overlap significantly with experimental glass at 800 °C. It should be noted that experiments were not conducted below 800 °C, where SiO_2 can saturate in the melt at lower pressures, forming quartz. For example, quartz is stable during isobaric fractional crystallisation at 125 MPa (initial H_2O content of 1.5 wt%; best fit conditions with 1883 tephra; Madden-Nadeau et al., 2021) of an Anak Krakatau (basaltic andesite) starting composition modelled via Rhyolite-MELTS, below 794 °C (Gualda et al., 2012). The range of possible conditions to generate the obsidians in Unit D are therefore < 850 °C across all pressures (50 - 200 MPa).

The pressure estimates for Unit A puts its magma storage region deeper in the crust than Units B to D, which comprises the bulk of the 1883 pyroclastic sequence. This runs contrary to previous hypotheses that Unit A erupted from a shallower magma storage region (Madden-Nadeau et al., 2021), and also makes it unlikely that the magma reservoir was (vertically) zoned (e.g., Mandeville et al., 1996a). Other systems, such as Toba volcano, Sumatra, prior to the eruption of the 75 ka youngest Toba Tuff, are hypothesised to have a similar subterranean structure, containing melts of very similar major element chemistry, with the earliest material representing the smallest volume,

but deepest, magma body (Pearce et al., 2020). The fact that the sub-Plinian precursory activity in May was sourced from deeper than previously hypothesised (Madden-Nadeau et al., 2021) also has important implications of the interpretation of geophysical monitoring data for systems with the potential to produce explosive, caldera-forming eruptions.

The obsidians were likely stored at <850 °C between 2 and 8 km depth, with natural and experimental phase proportions and glass chemistry being similar at these conditions. However, the melts that produced some of the most evolved obsidians likely need cooler temperatures of <800 °C than the bulk of the 1883 tephra to account for their more evolved composition, as shown through Rhyolite-MELTS models of fractional crystallisation (Gualda et al., 2012). The obsidians may therefore have been incorporated into PDCs from small, cool, stagnant bodies of melt during final caldera collapse, as proposed by Madden-Nadeau et al. (2021). However, it should be noted that there are currently no thermobarometric estimates that support a cooler temperature for the obsidians (e.g., Camus et al., 1987). Another possible mode of formation for the obsidians is fragmented 1883 melt sticking and sintering to sides of the conduit walls, before being erupted (e.g., Rust et al., 2004; Gardner et al., 2017; Wadsworth et al., 2020). Although some obsidians are more evolved than 1883 tephra, and contain quartz, further crystallisation of sintered ash has been achieved in experiments (Wadsworth et al., in press). In this case, crystallisation of quartz and other SiO_2 polymorphs likely occurs due to the presence of gases, such as SO_2, during the sintering process, and so quartz can form even if it would not ordinarily crystallise during simple differentiation of the melt. This would account for the fact that the obsidian melt chemistry is not saturated in quartz at lower pressures. It should be noted, however, that these obsidian clasts are up to 8 m in length, and therefore considerably larger than obsidians that have been previously linked to the sintering mechanism. The new evidence derived from phase equilibria experiments is accounted for in an amended schematic of the magmatic system in Figure 3.14.

3.5.2 Fractional crystallisation in shallow magmatic system

A better understanding of the melt chemistry, combined with estimated magmatic conditions, shed further light on the architecture of the pre-1883 Krakatau system. Madden-Nadeau et al. (2021), amongst others, conclude that fractional crystallisation is likely an important process, but that this likely occurs within multiple melt-rich regions within the shallow magmatic system. Trace elements in plagioclase can provide invaluable insight into the melt composition within the magmatic system, and thus may be able to test this hypothesis. This section concerns itself with the paroxysmal phase of the eruption (Units B – D in the stratigraphy); trace element profiles were taken across plagioclase picked from archived ash samples collected on 26th and 27th August 1883. It should be noted that the error bars on the modelled melt compositions are large (Figures 3.12 and 3.13), and so absolute values of melt composition cannot be reliably extracted from this modelling. However, general trends can be assessed tentatively, and compared with models of fractional crystallisation via Rhyolite-MELTs (Gualda et al., 2012; Madden-Nadeau et al., 2021) and the glass and phase chemistry of experiments, to evaluate the melt diversity within the magmatic system prior to Krakatau's eruption in 1883.

Focusing on the main trends in Figure 3.10, the overall positive correlation between Fe and anorthite in plagioclase phenocrysts is consistent with experiments and petrological studies that show similar trends as a melt evolves (Figure 3.10c; Bindeman et al., 1998; Ginibre et al., 2002; Cassidy et al., 2015). Ti and Mg also have a positive correlation with anorthite for $An_{<60}$, indicating that partitioning of these elements is also likely to be controlled by evolution of the melt through crystallisation over this range of anorthite contents (Bindeman et al., 1998; Ginibre et al., 2002; Cassidy et al., 2015). The negative correlation between Sr content in plagioclase with anorthite means that Sr partitioning is instead likely to be controlled by the anorthite content of the crystal, with Sr entering albitic plagioclase more readily as a result of the greater elasticity of the structure of albite in comparison with anorthite (Figure 3.10d; Blundy and Wood, 1991; Ginibre et al., 2002).

The modelled Sr content of the melt appears to show a strong positive correlation with anorthite content (Figure 3.12d), consistent with the determination by Blundy and Wood (1991) that Sr

partitioning in plagioclase is predominantly controlled by anorthite content. At <1200 ppm Sr in the melt (which crystallises plagioclase of composition $An_{<67}$), there is a strong positive correlation between Sr and both TiO_2 and MgO (Figure 3.13), which is suggestive of a simple melt differentiation trend. Modelled TiO_2 and MgO contents also intersect with isobaric fractional crystallisation trends as modelled using Rhyolite-MELTS (Gualda et al., 2012) of an Anak Krakatau basaltic andesite starting material at 1.5 wt% H_2O and 125 - 250 MPa (Figure 3.12 a, c; Madden-Nadeau et al., 2021). There is also overlap between the modelled TiO_2 composition of the melt and all measured experimental matrix glasses, and modelled MgO of the melt and experimental matrix glasses generated at 895 -900 °C at 100 – 150 MPa (Figure 3.12 a, c); the overlap between modelled data and experiments conducted at upper crustal pressures suggests these cooling trends are likely representative of the shallow system. This also overlaps with our storage estimates from experiments of 50 – 100 MPa and 850 – 900 °C.

The hypothesis of multiple, chemically similar melt rich regions operating under differing magmatic conditions e.g., pressure, temperature, H_2O content etc., within the shallow system was originally invoked to explain relatively homogeneous melt compositions and pyroxene zoning profiles, juxtaposed with varied and complex plagioclase zoning profiles (Figure 3.9; Chapter 3; Madden-Nadeau et al., 2021). This is because plagioclase is more sensitive to changes in these conditions than other phases (Mollo et al., 2011). However, melt composition as modelled using partition coefficients shows a simple fractional crystallisation trend with cooling in the shallow system. Therefore, varying the temperature in these models in line with the crystallisation of varied plagioclase rim anorthite compositions, would also require greater chemical diversity within the pre-eruptive melt to produce the measured trace element concentrations in the plagioclase phenocryst population. Varied melt compositions within the shallow system are inconsistent with relatively homogenous glass compositions, and pyroxene phenocrysts, and the lack of widespread evidence for magma mixing (discussed in Chapter 2; Madden-Nadeau et al., 2021).

However, if plagioclase crystals settled and became isolated from the melt within a mush pile in the shallow system, and then were reincorporated syn-eruption, this could produce the observed range

in rim compositions discussed in Chapter 2 (Madden-Nadeau et al., 2021) within a melt of relatively homogenous composition and uniform conditions. This is also supported by the observation that the plagioclase rims being out of equilibrium with the 1883 matrix glass (Darhen et al., 2012). It is also possible that crystals recently transported from the deeper system did not have time to re-equilibrate their rims before being erupted. The fact that Unit D within the eruptive stratigraphy has a higher crystallinity than Unit B (Figure 3.2), but a very similar matrix glass chemistry (Figure 3.4; Madden-Nadeau et al., 2021), can also be explained by settled crystals being reincorporated syn-eruption, and with crystals being directly sourced from the deeper magmatic system. It should also be noted that these models do not consider the role of H_2O content in trace element partitioning within plagioclase; if this is because H_2O does not greatly affect trace element partitioning, then it is also possible that variations in H_2O contents within an otherwise homogenous melt might result in varied plagioclase rim compositions. Data from plagioclase rims of experiments are also varied, and extend to higher anorthite compositions than the 1883 tephra, despite homogenous starting composition, and temperature and pressure conditions (Figure 3.7). Variations in the amount of H_2O present may therefore be responsible for large ranges in anorthite composition in plagioclase.

There are deviations from the main trends outlined above. Three plagioclase phenocrysts out of 16 have significantly elevated measured Mg concentrations over their entire transects, for a given anorthite content, with smaller elevations in the Fe and Ti contents (Figure 3.10). All three crystals have Sr contents consistent with the rest of the crystal population; as discussed previously, Sr concentrations in plagioclase are predominantly crystal controlled, and thus less affected by melt composition, and so the elevation in the other elements can be explained if these phenocrysts crystallised in a melt with a different composition. It is possible that these crystals are xenocrystic, perhaps being incorporated from the conduit walls, however only small elevations in Fe and Ti suggest some relation to the main crystal cargo.

The overlap between modelled melt chemistry for $An_{<67}$ via partition coefficients, and experimental matrix glass compositions (Figure 3.12), along with the fact that experimentally grown plagioclases under pre-eruptive shallow conditions have a mean composition of An_{48-53}, means it is likely that

these plagioclase compositions crystallised in the pre-eruptive shallow system. Strong positive correlations between modelled TiO_2 concentrations in the melt with both anorthite content of plagioclase (R^2 = 0.84; Figure 3.12), and modelled Sr contents (R^2 = 0.77; Figure 3.13), along with positive correlations between MgO and both anorthite content of plagioclase and modelled Sr concentrations (R^2 = 0.53 and 0.49, respectively; Figures 3.12 and 3.13) are likely indicative that fractional crystallisation of a single melt is the dominant process in the shallow system, which is corroborated by modelling of melt evolution of a basaltic andesite Anak Krakatau starting composition using Rhyolite-MELTs (Madden-Nadeau et al., 2021).

3.5.3 Melt diversity in the deeper magmatic system

Madden-Nadeau et al. (2021) identify a wide range in plagioclase core compositions, extending to An_{92} (Figure 3.9). Similar high anorthite plagioclase cores (>An_{77}) found in Anak Krakatau lavas are in equilibrium with a basaltic composition, and are estimated to have equilibrated at pressures of 645 to 807 MPa; Darhen et al., 2012). In addition, experiments reproducing these high anorthite compositions have been conducted at 500 MPa (~ 20 km; Laumonier et al., 2017), therefore making it likely that the 1883 plagioclase cores crystallised in the deeper system. Trace elements in plagioclase can again be used to further investigate melt chemistry associated with high anorthite plagioclase within products the paroxysmal phase of the 1883 eruption of Krakatau.

At $An_{>60}$, Ti concentrations in plagioclase have a negative correlation with anorthite content (Figure 3.10a). However, the modelled TiO_2 in the melt instead has a positive correlation for $An_{<75}$, and a negative correlation thereafter (Figure 3.12c); this can be attributed to the onset of Fe-Ti oxide crystallisation. Partitioning of Ti between the melt and plagioclase is thus predominantly controlled by the anorthite content of the crystal at $An_{>60}$. (Bindeman et al. 1998; Ginibre et al. 2002; Cassidy et al. 2015).

The negative correlation of Mg with $An_{>60}$ does not seem to be controlled by the major element crystal chemistry, nor is it compatible with differentiation. The modelled MgO content of the melt

that crystallised the highest anorthite plagioclase is low (< 1 wt% for $An_{>80}$; Figure 3.12). This appears counterintuitive, as more primitive melts, usually associated with higher MgO contents, most often crystallise high anorthite contents in plagioclase. Therefore, a better understanding of how the crystal structure controls how Mg partitions between a melt phase and plagioclase may be required. It should also be noted that the input temperature used falls just below the range of temperatures for which the Dohmen and Blundy (2014) partitioning model was calibrated, which may affect results.

Modelled melt compositions crystallising plagioclase with compositions of $An_{>67}$ are not replicated by experiments at shallow conditions (Figure 3.12 and 3.13), indicating that they were likely crystallised deeper within the magmatic system. Where modelled Sr contents are between 1300 - 1800 ppm (crystallising plagioclase of An_{67} - An_{82}), there is only a very weak positive correlation between the modelled TiO_2 and Sr concentrations of the melt, compared with the strong positive correlations observed for lower Sr contents. This weak correlation between 1300 and 1800 ppm Sr is likely indicative of increased melt diversity crystallising plagioclase of these compositions. Increased diversity in the modelled TiO_2 contents for any given anorthite content could be as a result of the existence of multiple melt-rich regions deeper within the system, which may at least partially account for the diversity in plagioclase zoning profiles (discussed in more detail in Section 3.5.2; Figure 3.9). Trace element modelling was at a fixed temperature of 1050 °C for plagioclase of composition $>An_{59}$ (consistent with thermometry for analogous systems; see section 3.4.3), indicating that even with fixed magmatic conditions (e.g., temperature), there is likely to be a chemically diverse set of melts within this part of the magmatic system.

Where the melt has >1900 ppm Sr in the melt (crystallising plagioclase $An_{>84}$) there is a wider range of modelled TiO_2 contents for any given anorthite content, and no correlation with Sr (Figure 3.13). It is likely that melts producing plagioclase at $An_{>84}$ would occupy the deepest part of the system, with experiments reproducing these compositions at 500 MPa (~ 20 km; Laumonier et al., 2017). There is also no known natural Krakatau eruptive products that have the higher TiO_2 and Sr compositions - modelled via plagioclase trace elements – which characterise these deeper magmatic zones, at either Anak Krakatau or prior to the 1883 eruption, nor in our experiments, which suggests

that these potentially more mafic compositions are never erupted. The wider range in modelled TiO_2 for a given anorthite composition makes it likely that there are diverse melts in the deepest part of the magmatic system, in terms of melt chemistry, and possibly also magmatic conditions.

The shallow, middle and deeper crystallisation zones identified in this study may broadly correspond to those outlined by Mandeville et al. (1996a), and are shown in Figure 3.14. To summarise, the main difference between the model presented in Figure 3.14, and the model presented in Chapter 2 (Figure 2.14) is that the precursory activity in May 1883 emanates from a deeper reservoir than the paroxysm in August. This has been updated to reflect the results from phase equilibria experiments presented in this chapter, which show that the glass chemistry and phase proportions of experimental products generated at 100 – 150 MPa are most similar to Unit A (basal ash aggregates; precursory activity), whereas experimental products generated at 50 - 100 MPa are most similar to Units B – D, erupted during the paroxysm. In addition, the melt feeding the paroxysmal August activity is likely to have been subject to similar conditions prior to eruption, as evidenced by the plagioclase trace element chemistry which shows fractional crystallisation trends. In Figure 3.14 the paroxysmal magma is therefore shown as residing in a single magma reservoir, rather than the multiple reservoirs hypothesised in Chapter 2. Instead of having multiple reservoirs under different magmatic conditions, it is proposed that crystal settling and reincorporation, and incorporation of crystals from the deeper system, are two processes that could be responsible for the diversity in plagioclase zoning profiles, and more specifically in rim compositions, identified in Chapter 2.

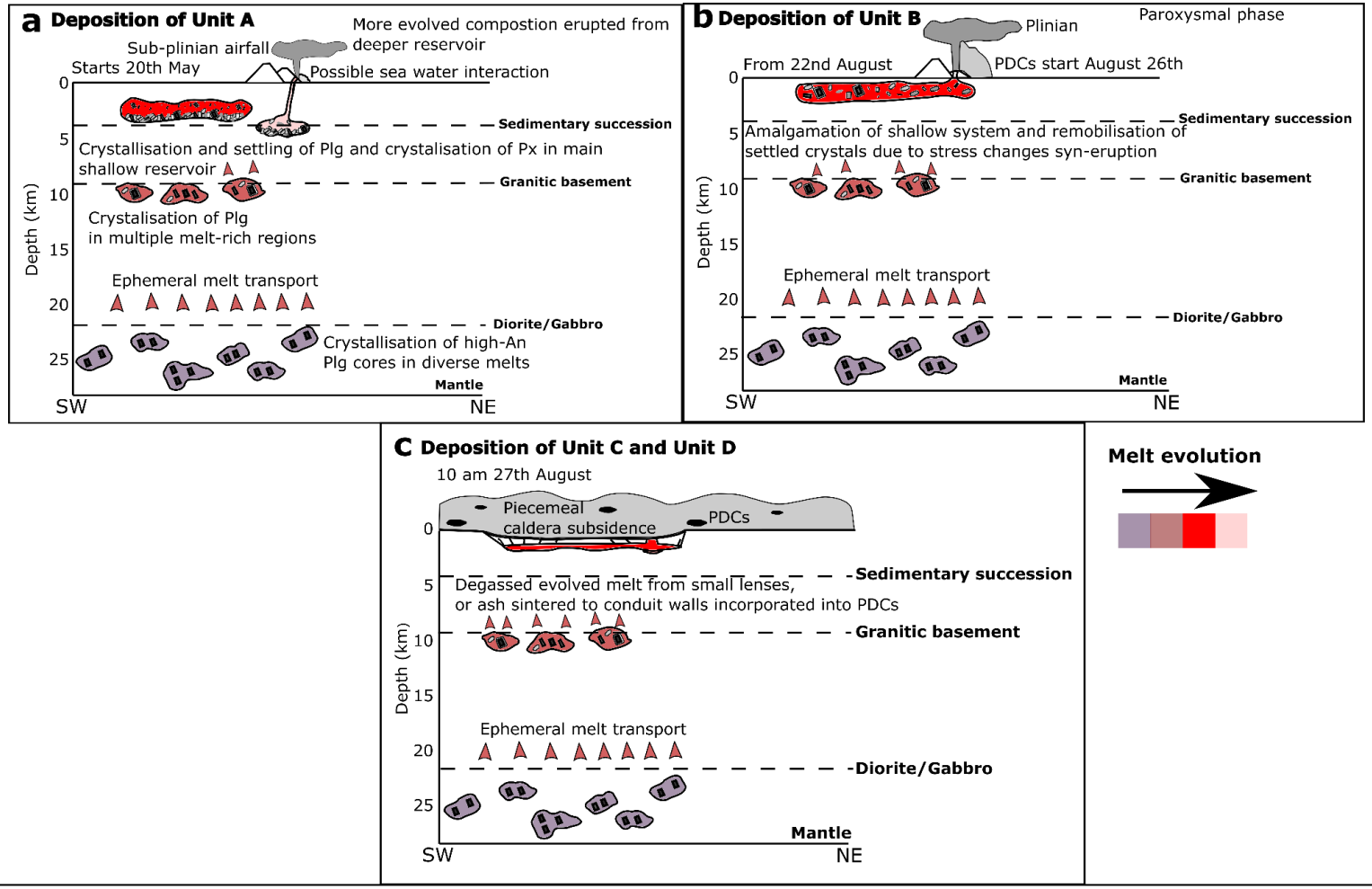

Figure 3.14: A series of schematics showing one possible hypothesis for the evolution of the magmatic system during the 1883 eruption of Krakatau (modified from Madden-Nadeau et al., 2021; lithological structure and crystallisation depths from Darhen et al., 2012; Mandeville et al., 1996a). Arrows indicate ephemeral melt transport between storage regions. Panel (a) shows the deposition of Unit A (Figure 3.1) evidenced from historical accounts and stratigraphic observations, with evidence for a more silicic reservoir derived from matrix glass analyses (Chapter 3; Madden-Nadeau et al., 2021). Phase equilibria experiments constrain the depth of this reservoir to 4 - 6 km (Figures 3.2 and 3.4). The reservoir at 2 – 4 km depth is evidenced by matrix glass chemistry and phase proportions of phase equilibria experiments (Figures 3.2 and 3.4), with ongoing fractional crystallisation and melt evolution as the dominant process, evidenced by plagioclase trace element modelling for $An_{<67}$ (Figure 3.12) and Rhyolite-MELTs modelling of a basaltic andesite Anak Krakatau starting composition (Chapter 2; Madden-Nadeau et al., 2021). Crystal settling, and isolation from the melt may also occur in this reservoir, to account for the wide range in plagioclase rim chemistry, disequilibria with the matrix glass, and diverse zoning profiles, all juxtaposed with homogenous matrix glass chemistry (Madden-Nadeau et al., 2021). Panel (b) shows the start of the paroxysmal phases of the eruption from this shallower reservoir, as determined by stratigraphic and historical observations (Chapter 2; Madden-Nadeau et al., 2021). Settled crystals are incorporated back into the melt syn-eruption, without time to reequilibrate. Panel (c) shows the deposition of Unit C and Unit D in a piecemeal caldera collapse, evidenced by two lithic lag breccias within the stratigraphy (Chapter 2; Madden-Nadeau et al., 2021). The massive PDCs erupted incorporated melts from evolved, small, stagnant melt-rich regions, or from ash sintered to the conduit walls, with similar evolved geochemistry to the 1883 tephra (Chapter 2; Madden-Nadeau et al., 2021).

3.6 Conclusions

This study presents constraints from plagioclase trace element modelling and phase equilibria experiments on the architecture of and storage conditions within the Krakatau 1883 magma reservoir prior to eruption. Conditions estimated by phase equilibria experiments (Figures 3.2 and 3.3) for the material erupted during the precursory activity in May 1883 are estimated at 100 - 150 MPa (~4 - 6 km) and 850 +/- 25 °C. The bulk of the paroxysmal tephra was likely stored at 50 - 100 MPa (~ 2 – 4 km) and 850 - 900 °C. The most evolved juvenile obsidian, incorporated into the PDCs during the final stages of the eruption was likely stored at cooler temperatures of >800 °C before being erupted, and may either have been small, stagnant degassed melt bodies, or were sintered to the conduit walls. The precursory activity was therefore likely derived from deeper within the magmatic system than the bulk of the 1883 pyroclastic sequence, rather than from shallower depths as previously suggested by Madden-Nadeau et al. (2021). The deeper location of the reservoir from which the precursory activity in May was derived has important implications for the interpretation of geophysical monitoring data, and in particular volcano seismicity data, for similar systems. Further experiments are recommended to see how using a coarsely crushed natural starting composition, rather than powdered, affect the outcome of the experiments, as mass balance calculations indicate the incorporation of plagioclase crystals not in equilibrium with the melt is at least affecting Al_2O_3 concentrations.

Melt chemistry modelled using partition coefficients and plagioclase trace element transects, compared with experimental glass compositions and Rhyolite-MELTS models of isobaric fractional crystallisation of an Anak Krakatau basaltic andesite starting composition, provides further evidence that fractional crystallisation was the dominant process within the shallow system, crystallising plagioclases of $An_{<67}$ (Figure 3.12). This makes it likely that plagioclase of $An_{<67}$ crystallised within chemically similar melts, under similar pressure and temperature conditions. Plagioclase of $An_{>67}$ show no evidence of melt evolution trends for modelled melt compositions, and are not replicated by experiments at shallow depths, indicating greater melt diversity within the deeper magmatic system.

4. Further records of explosive eruptions from Krakatau Volcano

Data on the stratigraphy and matrix glass chemistry of 2018-2019 Anak Krakatau ash, and subsequent discussion, is currently under review in the journal *Earth and Planetary Science Letters* as part of the larger manuscript *'Downward-propagating eruption following vent unloading implies no direct magmatic trigger for the 2018 lateral collapse of Anak Krakatau'* with the following author list:

Cutler, K.S.[1,2]*, Watt, S.F.L.[1], Cassidy, M.[2], **Madden-Nadeau, A.L.[2]**, Engwell, S.L.[3], Abdurrachman, M.[4], Nurshal, M.E.M.[4], Tappin, D.R.[5,9], Carey, S.N.[6], Novellino, A.[5], Hayer, C.[7], Hunt, J.E.[8], Day, S.J.[9], Grilli, S.T.[6,10], Kurniawan, I.A.[4] and Kartadinata, N.[11]

1 School of Geography, Earth and Environmental Sciences, University of Birmingham, Edgbaston, Birmingham, B15 2TT, UK

2 Department of Earth Sciences, University of Oxford, South Parks Road, Oxford OX1 3AN, UK

3 British Geological Survey, The Lyell Centre, Research Avenue South, Edinburgh EH14 4AP, UK

4 Faculty of Earth Sciences and Technology, Institut Teknologi Bandung, Jalan Ganesa No. 10 Bandung 40132, West Java, Indonesia

5 British Geological Survey, Nicker Hill, Keyworth, Nottingham NG12 5GG, UK

6 Graduate School of Oceanography, University of Rhode Island, Narragansett, R.I 02882, USA

7 Department of Earth and Environmental Sciences, The University of Manchester, Oxford Road, Manchester M13 9PL, UK

8 National Oceanography Centre, Waterfront Campus, University of Southampton, European Way, Southampton, SO14 3ZH, UK

9 Institute for Risk and Disaster Reduction, University College London, London, WC1E 6BT, UK

10 Department of Ocean Engineering, University of Rhode Island, Narragansett, R.I 02882, USA

11 Volcano Research and Monitoring Division, CVGHM - Geological Agency of Indonesia, Jl. Diponegoro No. 57, Bandung, 40228, Indonesia

Abstract

Constraining the explosive eruptive history of Krakatau is important in assessing the hazard this volcano poses. Deposits, originally attributed to the 1883 eruption, on the islands of Sebesi and Sebuku, and in Anjer, mainland Java (16, 25 and 40 km away, respectively) have matrix glass chemistry that falls on Krakatau's liquid line of descent. However, at least one other volcano in the region has tephra with major element compositions that overlap with Krakatau, meaning the most distal deposits were not necessarily erupted from this volcano. The majority of tephra analysed from Sebesi and Sebuku have matrix glass chemistry consistent with the 1883 eruption, however these rhyodacitic compositions have been erupted by Krakatau in the past, therefore these deposits cannot be definitively attributed to the 1883 eruption on this basis. These deposits require further chemical analysis (e.g., dating, trace element chemistry) to be placed within the context of Krakatau's eruptive history. At least one deposit on Kecil, Sebuku has matrix glass chemistry inconsistent with proximal 1883 tephra, and thus was likely deposited pre-1883. A plate fragment found within the likely tsunami deposit directly below this volcanic unit means it is possible that this tephra was erupted historically, which has important implications for the recurrence of these explosive events. The fact that these eruptive deposits may not pertain to the 1883 eruption of Krakatau has important implications for modelling the 1883 pyroclastic density currents, and subsequent tsunamis. In addition, the sequence of 2018-2019 ash deposits, associated with flank collapse of Anak Krakatau, overlies a likely tsunami deposit, and are consistent with observed pulsatory Surtseyan activity post-collapse. The first unit erupted immediately post-collapse has lower Al_2O_3 and higher TiO_2 and FeO than the overlying sequence, likely reflecting less Fe-Ti oxide microlite formation, which may be as a result of high decompression rates in the immediate aftermath of edifice failure, which then

decreased over time. The 2018-2019 ash found on the Krakatau islands is thus representative of post-collapse volcanic activity that appears decompression driven, and thus provides no evidence for a direct magmatic trigger for the collapse of Anak Krakatau in 2018.

4.1 Introduction

Gaining a better understanding of the deposits associated with Krakatau helps to resolve details of the eruptive history of a volcano with the potential to produce caldera-forming eruptions. In turn, this may shed light on how magma reservoir processes, and eruptive behaviour, evolve through time. A temporal understanding of the eruptive behaviour will allow for refined assessments of eruptive hazards associated with caldera systems, whilst understanding of the subterranean system aids in the interpretation of contemporary geophysical monitoring data. The volcanic deposits associated with Krakatau volcano comprise: (1) pre-1883 deposits which are poorly characterised, and have not yet been dated (Self, 1992; Beauregard, 2001), (2) the 1883 pyroclastic sequence (Self and Rampino, 1981; Self, 1992; Carey et al., 1996; Mandeville et al., 1996b; Madden-Nadeau et al., 2021) and (3) the post-1927 sequence of lavas and pyroclastic deposits erupted from Anak Krakatau, the current subaerial volcanic centre (Abdurrachman et al., 2018).

The ages of pre-1883 eruptions are poorly constrained, with little published data relating to the pre-1883 volcanic stratigraphy (Self, 1992). Deposits from an eruption in the Sunda Straits at ca. 60 ka were identified in drill cores, however this cannot be definitively attributed to Krakatau (Ninkovich, 1979). The Javanese chronicle Pararaton, or the Book of Kings, describes a very large eruption in 416 AD, with “heavy rains of stone” that “with a tremendous roar burst into pieces and sunk into the deepest earth” originating in this region (Symons et al., 1888; Judd 1889; Figure 4.1). This eruption is also described to have generated a tsunami that was said to be “the origin of the separation between Java and Sumatra”. However, no geological evidence presented to date substantiates this eruption. In May 1680, and February and November of 1681, observations of earthquakes and pumice were

made in the diaries of Johann Wilhelm Vogel and Elias Hesse, likely pertaining to an eruption of Krakatau (Verbeek, 1884).

Volcanic deposits on the islands of Sebesi and Sebuku, 16 and 25 km distance respectively from the island of Anak Krakatau (Figure 4.2), were originally attributed to the 1883 eruption of Krakatau by Carey et al. (1996). Further assessment of the nature of these deposits and a better understanding of the extent of the 1883 volcanic stratigraphy will aid those attempting to model pyroclastic density current (PDC) generation and propagation (e.g., Marti et al., 2016). The 1883 eruption also produced large tsunamis, the generation of which has been the subject of extensive debate (e.g., Nomanbhoy and Satake, 1995; Choi et al., 2003). One hypothesis is that PDCs were the source of the tsunamis, which is also hypothesised for similar volcanogenic tsunamis, such as the Late Bronze Age eruption, Santorini (Nomikou et al., 2016). Assessing the stratigraphy of these deposits in more detail will thus also help provide better constraints on tsunami models for the 1883 event (e.g., Nomanbhoy and Satake, 1995; Choi et al., 2003).

Since its emergence in 1927, Anak Krakatau has erupted periodically. Since the 1960s, when the active vent stopped interacting with seawater, Anak Krakatau has predominantly erupted effusively, punctuated with Vulcanian and Strombolian explosions (Abdurrachman et al., 2018). After 15 months of quiescence, Anak Krakatau began erupting on 21st June 2018, characterised by Strombolian activity with low-level ash plumes and lava flows, similar in eruptive style to previous activity (Global Volcanism Programme Bulletin Report, 2018). However, the magmatic flux was notably higher during this eruptive period than had been previously recorded at Anak Krakatau (Walter et al., 2019). On 22nd December 2018, a lateral collapse of the southwestern flank of Anak Krakatau reduced the height of the island from 320 to 120 m, generating a tsunami that killed 453 and injured 14059 people (EM-DAT 2018). The collapse is thought to have truncated the vent below sea level, and after 22nd December 2018, Anak Krakatau made the transition to phreatomagmatic activity. This activity was particularly intense in the days immediately after the flank collapse, which caused a rapid regrowth of the island (Novellino et al., 2020). Volcanic flank instability may develop as a result of a range of factors, including structural weaknesses, shallow magmatic intrusions and

hydrothermal alteration (e.g. McGuire, 2003; Reid, 2004). Establishing whether there was a direct volcanic link to the collapse, or whether it resulted from oversteepening of the edifice long-term, and in particular over the elevated period of activity earlier that year (Walter et al., 2019; Grilli et al., 2019) is critical to gain a better understanding of the factors that contributed to collapse, so that any precursors to such rapid-onset events can be identified. It is therefore important to establish if there was a link between Anak Krakatau's volcanism at the time, and the collapse that ensued.

Results from fieldwork on the islands of Sebesi and Sebuku, and at Anjer, on mainland Java, are presented here, along with matrix glass chemistry for cross correlation, to attempt to establish whether the deposits can be definitively attributed to the 1883 eruption of Krakatau. The stratigraphy and matrix glass chemistry of pre-1883 tephra is also assessed for direct comparison. This study will also present observations and matrix glass analyses of the 2018/19 Anak Krakatau ash to look at whether there is a chemical signature that might link the flank collapse to a direct eruptive trigger.

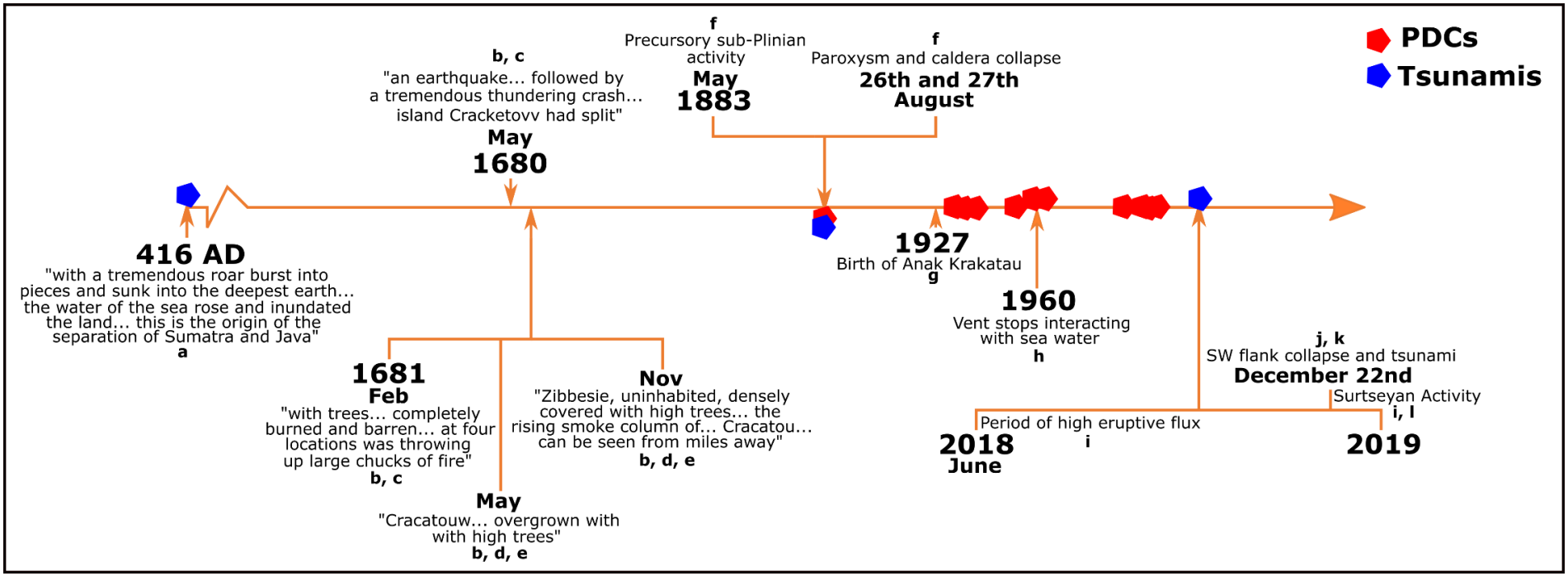

Figure 4.1: Timeline from 416 AD to 2019, showing Krakatau's eruptive history. Each arrow gives a year on the timeline for which we have written records. Letters represent the following references: (a) Judd (1889), (b) Van den Berg (1884), (c) Vogel (1690), (d) Hesse (1690), (e) Hesse (1694), (f) Madden-Nadeau et al., (2021), (g) Stehn (1929), (h) Abdurrachman et al. (2018), (i) Walter et al. (2019), (j) EM – DAT (2018) (k) Novellino et al. (2020) and (l) Prata et al. (2020). Extracts from (a) – (e) can be found in Simkin and Fiske (1983).

4.2 Methods

4.2.1 Fieldwork

Field campaigns to the Krakatau islands of Rakaka, Sertung and Panjang were undertaken in both September 2017 and August 2019. In addition, Anak Krakatau was visited in September 2017, and the islands of Sebuku and Sebesi, as well as a locality on mainland Java, were visited in August 2019 (Figure 4.2). The volcanic deposits on Sebuku and Sebesi were previously described by Carey et al., (1996), who associated them with the 1883 eruption of Krakatau. New stratigraphic logs were created from our field observations, and selected units cross correlated using lithological and stratigraphic characteristics, as well as glass chemistry.

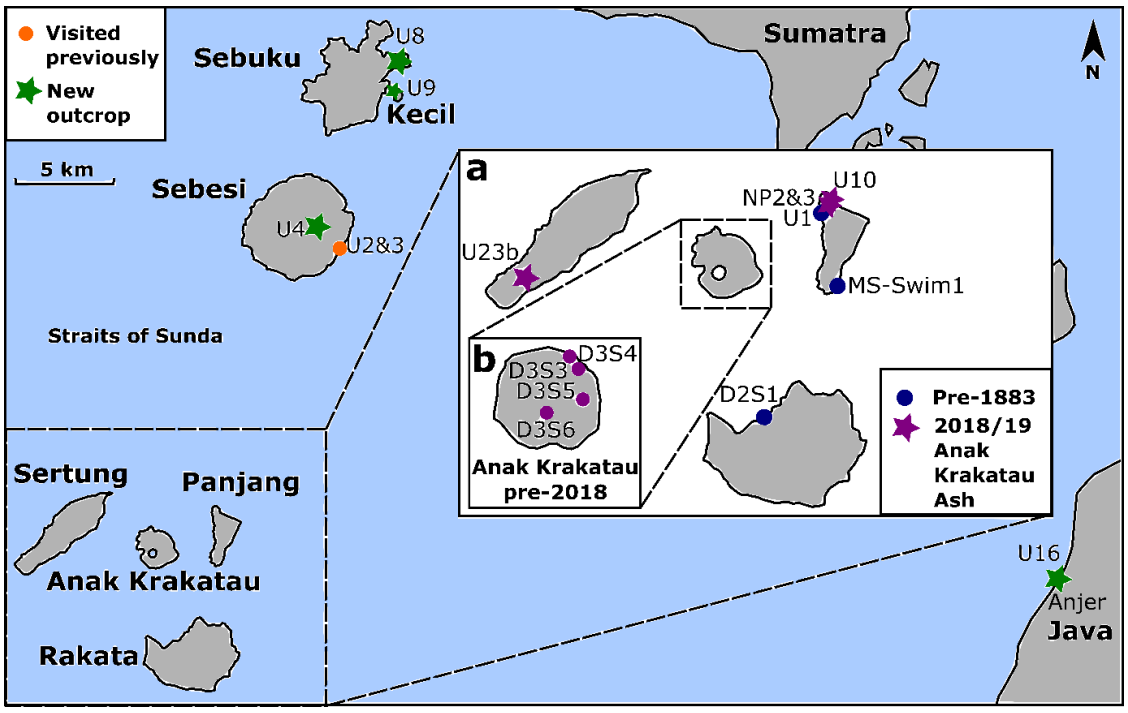

Figure 4.2: Map showing the Sunda Straits, and the field sites visited. The green stars are new field sites, presented here for the first time. Localities matching, or very close to, the orange circles were also visited by Carey et al. (1996). Insert (a) shows the contemporary Krakatau islands with locations with outcropping pre-1883 stratigraphy marked and field sites with 2018/2019 Anak Krakatau ash. Insert (b) shows field locations from Anak Krakatau in 2017, prior to its collapse in 2018.

4.2.2 Electron probe microanalysis (EPMA)

Point analyses of resin-mounted vesicular matrix glass were made on a Jeol JXA-8200 electron Microprobe in the School of Archaeology, University of Oxford. Glass analyses were conducted at 15 kV with a 5-micron defocussed beam of 6 nA for Al, Si, Na, Ca, K, Fe, Ti, Mn and Mg. Sodium was always analysed first, at a 10 s peak count time, and secondary standards of a similar composition to the target were analysed to check the accuracy of the calibration (See Supplementary excel file for Chapter 4, Supplementary Data 1).

Some matrix glass analyses were obtained from grains picked from multiple crushed, cm-scale pumices, with others picked directly from ash, or bulk tephra samples, containing both pumice and ash. For the nature of the samples analysed, see Table 4.1. Multiple pumices were crushed per sample, and glass clasts were picked and mounted from crushed material. For each sample, analyses are based on at least two clasts.

4.2.3 Mineral phase identification

Mineral phases were predominantly identified in hand specimen in the field, before being confirmed under a microscope, and then again using the back scatter on the electron probe. The exception to this is quartz, which was identified as present from analyses conducted via EPMA.

Table 4.1: List of field sites and samples discussed in this chapter

Island	Field site	Longitude	Latitude	Date visited	Sample numbers	Description
Sebesi	U2	5.95887	105.50939	05/08/19	NA	NA
	U3	5.95827	105.50961	05/08/19	U3.1	Ash from lower part of outcrop
					U3.2	Ash from middle of white unit
					U3.4	Pumice from top of outcrop, below road cutting
					U3.3	Pumice from above road cutting
	U4	5.94919	105.50207	06/08/19	NA	NA
Sebuku	U8	5.86521	105.53907	06/08/19	NA	NA
	U9	5.88037	105.53825	06/08/19	U9.2	Bulk dark green unit (mostly ash)
					U9.3	Bulk light green unit with laminations (mostly ash)
					U9.5	Bulk white unit (mostly ash)
Java	U16	6.12789	105.86324	09/08/19	U16.3	Ash from top of upper massive unit
Panjang	MS-Swim1	6.10646	105.45617	08/08/19	MS-Swim1.1	Pumice from massive unit (upper)
					MS-Swim1.4	Pumice from massive unit (lower)
	U10	6.08240	105.45481	07/08/19	U10.3	Purple fine ash
					U10.4	Bulk brown ash
					U10.6	Bulk brown bed with cross bedding
					U10.8	Bulk brown unit with coarse/fine alternations
					U10.10	Bulk ash towards top of sequence
	U1	6.05107	105.27157	04/08/19	NA	NA
Rakata	D2S1	6.08638	105.26084	16/09/17	NA	NA
Anak Krakatau	D3S4	6.05751	105.25775	17/09/17	D3S4.1	1995 lava flow
	D3S6	6.06262	105.25568	17/09/17	D3S6.1	2017 lava flow
					D3S6.2	2012 lava flow
	D3S5	6.06153	105.25868	17/09/17	D3S5.1	2012 volcanic bomb
	D3S3	6.05810	105.25812	17/09/17	NA	NA
Sertung	U23	6.01626	105.36577	10/08/19	U23.2	2018 ash with leaves

Localities in order of mention in chapter. Samples in stratigraphic order from lowest to highest.

4.3 Results

4.3.1 Fieldwork

4.3.1.1 Volcanic deposits on Sebesi, Sebuku and Anjer, Java

Volcanic deposits located between 15 and 25 km away from Krakatau volcano, on the islands of Sebesi, Sebuku and Kecil, as well as ~ 50 km away in Anjer on mainland Java (Figure 4.2) were visited to characterise and interpret the deposits and assess whether they are associated with the 1883 eruption of Krakatau. Volcanic deposits on Sebesi and Sebuku were originally described by Carey et al. (1996) and associated by them with the 1883 eruption of Krakatau. Verbeek (1885) notes that 1 - 1.5 m of volcanic ash covered Sebesi in September 1883, one month after the eruption, and that vegetation had been destroyed. Carey et al. (1996) did not detail why these deposits were attributed specifically to 1883, noting that "there is no consistent stratigraphic succession between outcrops". During fieldwork in 2019, we revisited one of these sites on the east coast of Sebesi (U2 and 3), and dug new holes further inland (U4) to ascertain the stratigraphy of these deposits. A new site on Sebuku (U8), as well as the island of Kecil off the east coast of Sebuku (U9), were also visited (Figure 4.2), along with a locality in Anjer, mainland Java (U16), which was thought to include some 1883 deposits.

Locality U2 is an outcrop on the eastern coast of Sebesi (Figure 4.3a), previously described by Carey et al., (1996). The volcanic deposits overlie a discontinuous, red mudstone lens above an orange coral packstone, with a mud matrix (Figure 4.3b). The lowermost volcanic unit is 1 m of poorly sorted, matrix-supported and green in colour, containing angular pumice up to 10 cm in size, while its ash matrix is comprises ~80% small pumices and glass shards. The other 20% is dark coloured, dense lava lithics. This unit contains rip-up clasts from the red mudstone below, and shells, as well as clast-supported lenses containing rounded pumices. Overlying this unit is a fine ash layer, above which is ~ 1 m of a matrix-supported, poorly sorted, white unit. The white unit is 80% ash matrix, containing pumice as well as a minor lithic component, and shows reverse grading, with larger average pumice sizes towards the top (maximum clast size 5 cm). It is also possible to observe

charcoal (Figure 4.3c) as well as fine, orange laminations (Figure 4.3d). Volcanic deposits at this locality all contained plagioclase and pyroxene phenocrysts.

Locality U3 is located 200 m NNE along the same beach as U2 (Figure 4.3a), with fairly continuous outcrop between the two. The poorly sorted, matrix supported green unit observed at U2 above the orange coral breccia has thinned to less than 20 cm (Figure 4.3). Above this is 37 cm of dark green ash containing laminations, bedding and cross stratification. Pumice-supported lenses, as well as lenses rich in dark, dense lava lithics (both cm-scale), are present in this unit. Overlying the dark green unit is white matrix-supported, poorly sorted unit containing sub-rounded yellow pumice, orange laminations and low angle cross bedding, with a larger maximum clast size. Quartz was identified in pumices in this lower part of the volcanic stratigraphy via EPMA, in addition to plagioclase and pyroxene phenocrysts. Above a road cutting is a white, poorly sorted, matrix-supported unit (U3.3) containing pumice-supported lenses. Pumices contain only pyroxene and plagioclase phenocrysts in the unit above the road cutting.

A 60 cm hole was dug at locality U4 inland on Sebesi (Figure 4.4a). At the base is ~ 10 cm of brown clay, with an undulating top surface contact with the layer above: a mm-scale unit containing mm scale pumices (Figure 4.4b). Overlying this is ~20 cm of reverse-graded ash containing lithics and lapilli sized pumices towards the top. Approximately 30% of clasts are lithics, and 70% are pumice. A clay clast, similar in character to the basal unit, was observed at the top of this unit. Overlying this is the second pyroclastic unit, lighter in colour, which is massive, poorly sorted and matrix-supported, overall finer than the unit below, but contains pumices of a larger maximum clast size. There is a minor lithic component, with lithics up to 5 mm in size. The boundary between the volcanic sequence and the top-soil is diffuse. Plagioclase and pyroxene phenocrysts were identified in all volcanic units at this locality.

The deposits at U2 and U3 were previously visited by Carey et al. (1996), with their stratigraphic log shown in Figure 4.5. They identify coral at the base, which correlates well with the orange coral packstone detailed here. Above this they report two major volcanic matrix-supported units, the first of which is described as a brown/grey massive, poorly sorted unit containing pumices and coral. The

second major volcanic unit is green/grey, similar in nature to the first, except containing crude cross stratification and charcoal. These units correspond well to the log presented here for localities U2 and U3 in Figure 4.3, which details similar observations. Although not observed at this particular locality, a pumice rich unit is noted at other localities on Sebesi towards the top of the sequence, which could be correlated with the increase in larger pumice clasts that we note towards the top of the white unit, shown in the photo in Figure 4.3e at localities U2 and 3. The deposits found in the hole dug further inland at locality U4 correspond approximately to a locality noted by Carey et al. (1996) in Leganda Coconut Grove, ~ 90 m above sea level. Carey et al. (1996) described a clay soil at the base, overlying which are two main poorly sorted volcanic units of brown/grey ash containing pumices, which correlates well with our log of U4 in Figure 4.4.

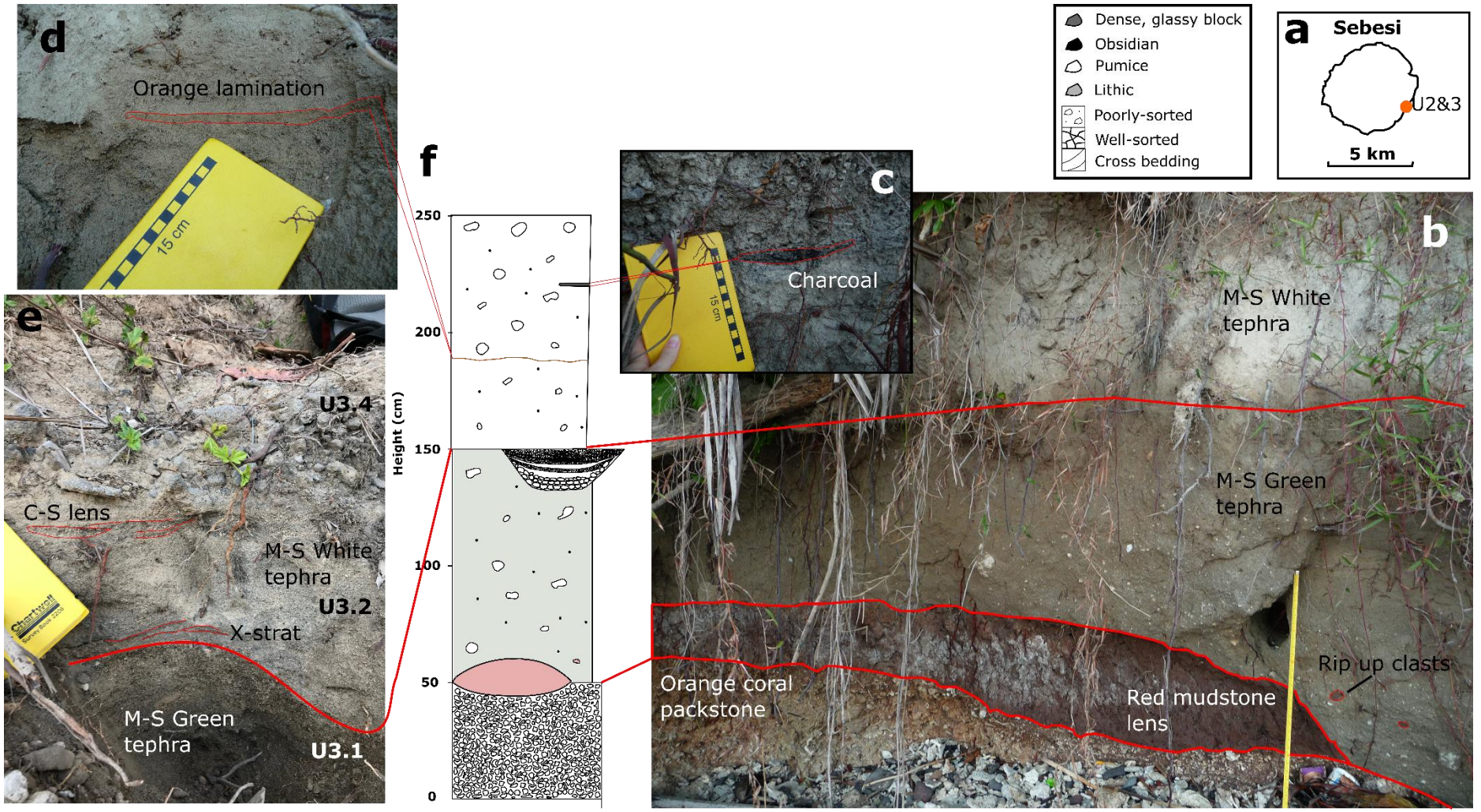

Figure 4.3: Insert (a) shows the location of the field sites U2 and U3 on the island of Sebesi (see figure 4.2 for location of Sebesi). Field photos (b), (c) and (d) were taken at locality U2, whilst (e) was taken 200 m NNE along the same beach, at locality U3. Revalevent sample numbers are labelled on photo (e), except U3.3 , which is located out of shot. M-S = matrix-supported, C-S = clast supported, x-strat = cross stratification. These photos are cross correlated in red with log (f).

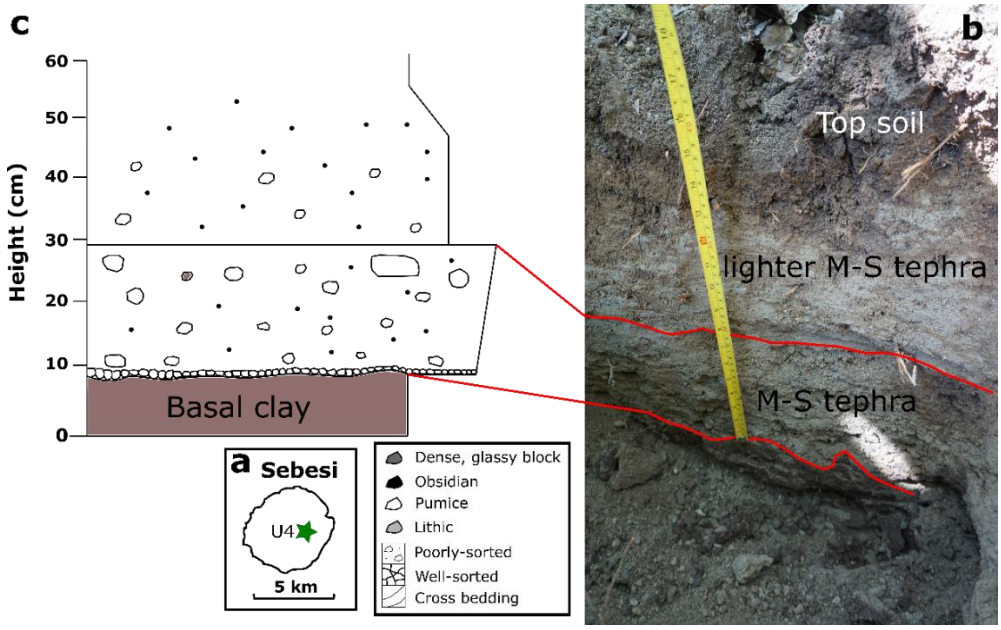

Figure 4.4: Insert (a) shows the location of locality U4 on the island of Sebesi (for the location of Sebesi, see figure 4.2). Field photograph (b) shows the hole dug revealing pyroclastic deposits at this locality, tape measure for scale. M-S = matrix supported. The field photograph is cross correlated in red with log (c).

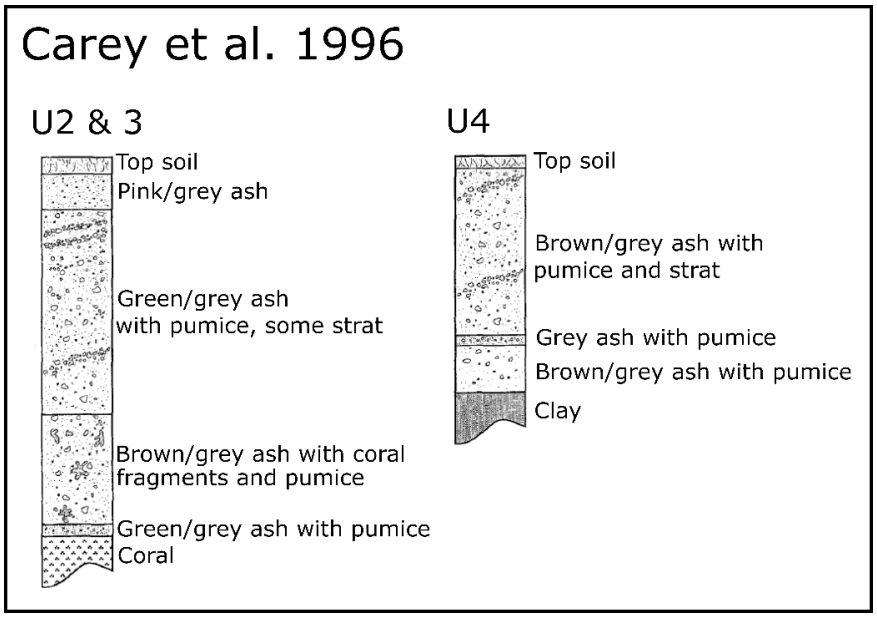

Figure 4.5: Two logs presented from localities on Sebesi, which correspond to our localities U2, U3 and U4, as presented by Carey et al. (1996). Strat = cross stratification.

Another 60 cm hole was dug on Sebuku at locality U8 (Figure 4.6a). At the base of the sequence is 12 cm of matrix-supported brown clay containing bivalve and clay fragments (Figure 4.6b). Above this is 7 cm of a poorly sorted, matrix-supported, lithic-rich ash containing sub-rounded pumices. The unit overlying this is similar in character, except with an overall finer grain size; the unit also contains pumice-supported lenses. The pumices (<5mm) within the lenses are subangular and elongate, with a fine ash matrix coating clasts. The top of this unit grades into the top soil. All volcanic units at this locality contain both plagioclase and pyroxene phenocrysts. Our observations agree well with logs presented by Carey et al. (1996) for Sebuku, which detail a clay rich soil, overlain by two major units of predominantly brown and grey ash, both containing pumice.

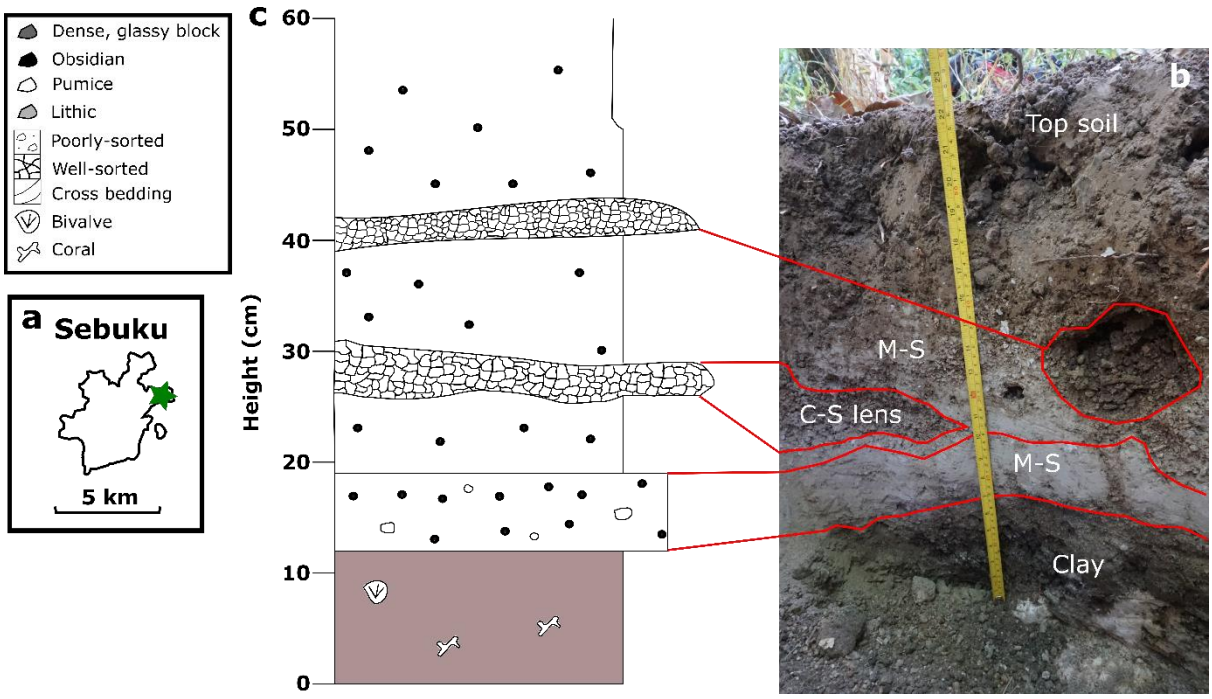

Figure 4.6: Insert (a) shows the location of locality U8 on the island of Sebuku (for the location of Sebuku, see Figure 4.2). Field photograph (b) shows the hole dug revealing pyroclastic deposits at this locality, tape measure for scale. M-S = matrix supported, C-S = clast-supported. The field photograph is cross correlated in red with log (c).

Locality U9 is located on Kecil, a small island off the east coast of Sebuku (Figure 4.7a). At the base of this outcrop is a poorly sorted conglomerate of variable thickness, with a fine silt matrix (Figure 4.7 b,c). A white pottery fragment (Figure 4.7d), which appears to be flatware (e.g., a plate), as well as coral fragments and bivalves were found within this unit. Conglomerate clasts range from rounded to angular, and were up to 5 cm in size. Overlying the conglomerate are volcanic deposits. The first volcanic unit is green in colour, ~ 10 cm thick, poorly sorted and matrix-supported, with some pumice and lithic lapilli (up to 3mm). At the top of this unit is a ~ 1cm thick clast-supported layer of mm-scale pumices, with well-sorted fine-ash layer on top. The pumices and ash within these units contain both plagioclase and pyroxene phenocrysts. Next in the sequence is 17 cm of a lighter-green, poorly sorted, matrix-supported unit, containing predominantly sparse cm-scale pumice lapilli, with some lithics (on average ~4 mm). This unit also contains dark sub-mm scale laminations where fine lithic components are concentrated. Towards the top of this unit is a thin, mm-scale, pumice-supported layer; pumices are coated in a fine ash matrix. The last unit in the sequence is 27 cm of medium-sorted, white ash, with a very minor component of lapilli sized pumices. This unit also contains brown, sub-mm scale, continuous laminations, where lithics appear to be concentrated. Towards the top of this layer, there is a greater abundance of pumice lapilli (on average ~2 mm in size). This unit grades into the top-soil. Pumices and ash within the two upper volcanic units contain quartz as ascertained via EPMA, in addition to plagioclase and pyroxene.

These localities on Sebuku and Kecil were not visited by Carey et al. (1996), however, they note a clay rich soil on the north of the island at the base of the sequence, similar to observations at locality U8 (Figure 4.6). Overlying this, they note two ash-rich units, followed by the top soil, which is again similar to observations made at locality U8.

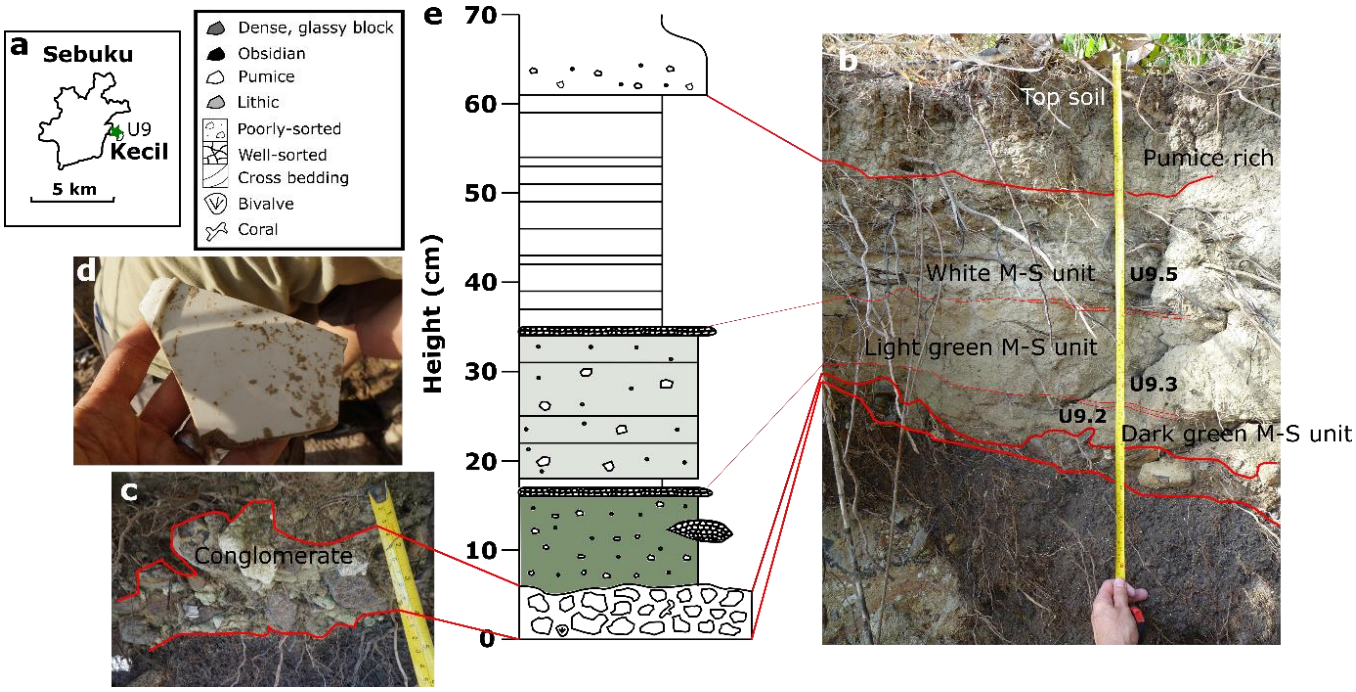

Figure 4.7: Insert (a) shows the location of locality U9 on the small island of Kecil, east of Sebuku (for the location of Sebuku and Kecil, see Figure 4.2). Field photograph (b) shows the pyroclastic deposits at this locality, tape measure for scale, with relevant sample numbers. Field photograph (c) is zoomed in on the basal conglomerate, whilst photo (d) shows the pottery fragment found within it. The field photograph is cross correlated in red with log (e). M-S = matrix-supported.

Locality U16 is located on the coast in Anjer, on mainland Java (Figure 4.8a), and was visited based on local understanding that the deposit could be related to the 1883 eruption of Krakatau. The outcrop is in total approximately 5 m thick and is well consolidated (Figure 4.8b). At the base of this outcrop is a poorly sorted, matrix-supported (~ 60 % ash) unit containing some coral clasts. The majority of clasts within this unit are pumices (~2 cm), with a smaller lithic component. Overlying this is a green, fine-grained, laminated ash unit (~15 cm thickness; Figure 4.8c), above which is 4 m of a massive, poorly sorted, matrix-supported unit, that is reverse graded towards the top. This matrix supported unit contains ~60 % ash matrix. Clasts (30 %) are predominantly pumice, however, there are lithics present, particularly in the larger size fractions. These volcanic units all contain plagioclase and pyroxene phenocrysts.

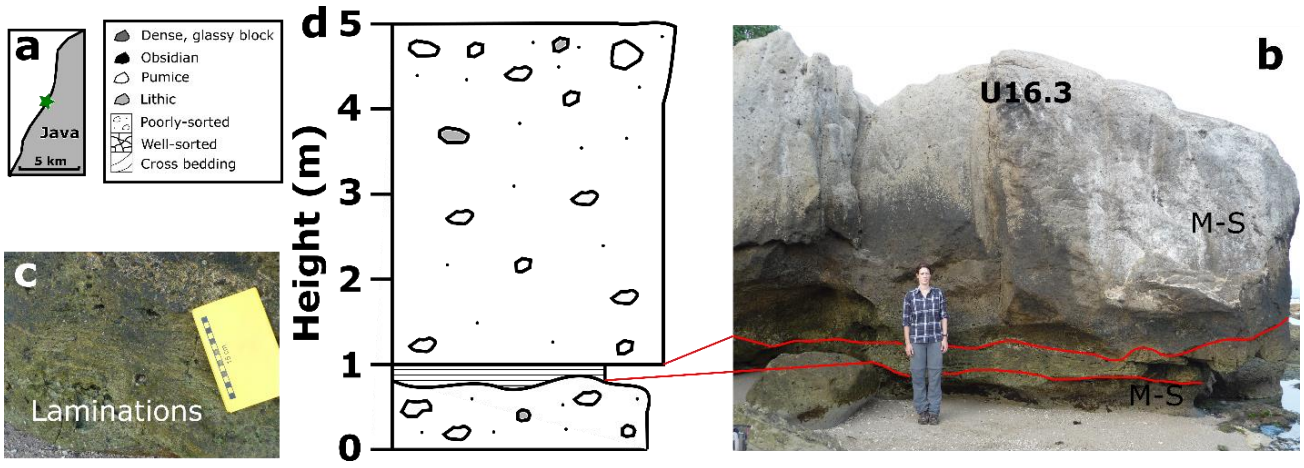

Figure 4.8: Insert (a) shows the location of locality U16 on mainland Java (for the location relative to other field localities, see Figure 4.2). Field photograph (b) shows the pyroclastic deposits at this locality, person for scale, and U16.3 indicating location in the sequence of relevant sample, with photo (c) showing the fine laminations in the unit below 1 m stratigraphic height. M-S = matrix supported. Field photograph (b) is cross correlated in red with log (c).

4.3.1.2 Pre-1883 volcanic deposits

Pre-1883 exposures were characterised as part of both field campaigns, and in particular for comparison with the activity in 1883. At locality, MS-Swim1 on southern Panjang (Figure 4.9a), a red, oxidised, continuous layer (lateral extent: 10s of meters) is shown in Figure 4.9b. This layer was also observed at the base of the 1883 sequence at a locality on south-east Rakata (U22), which was discussed in Chapter 2, and was laterally continuous over the m-scale outcrop (Madden-Nadeau et al., 2021). At both localities, this red layer is 2-5 cm thick, and is located directly beneath a cm-scale unit of green very fine ash. This unit is interpreted to be the 1883 palaeosol, which agrees with interpretations made by Beauregard (2001). The exposure directly below the 1883 palaeosol is accessible at field locality MS-Swim 1: at the base of the observable sequence, there is a massive, structureless, poorly sorted, matrix-supported unit containing large pumices (Figure 4.9b). This unit was sampled, and contains plagioclase, pyroxene, biotite and amphibole phenocrysts, followed by a thinner layer of a similar colour with improved sorting, that is pumice-supported (30 cm thick). This

unit has an erosional contact with the unit above: 2.5 m of an orange, poorly sorted, matrix-supported unit, containing pumice-supported lenses and cross stratification. Above this is a well-bedded, grey, poorly sorted, matrix-supported unit (~ 70 cm). Overlying this is another orange pumice-supported unit of 80 cm, of similar character to the one below. Above this is 3 m of a poorly sorted, matrix-supported unit containing large lithic blocks and pumices, showing normal grading, which has an erosional contact with the 1883 palaeosol above.

Locality U1 is located on western Panjang (Fiugre 4.10a), and was visited in 2019. At the base of the exposure there is an orange, poorly sorted, matrix-supported unit containing pumices (Figure 4.10b). Overlying this is 1.5 m of a dark, poorly sorted, matrix supported unit, containing scoria, with another 2 m of an orange unit, similar to the first, above. The sequence then becomes inaccessible, however overlying the second orange unit is a ~ 0.5 m pink unit, which appears to have an overall finer grain size. Above this is ~4.5 m of a very poorly sorted, matrix-supported unit containing large lithic blocks up to 50 cm in size. At the top of the sequence is another orange unit, broadly similar in character to the first two, before an unconformity with the distinctive white colour that characterises the 1883 pyroclastic sequence. The stratigraphy observed at localities MS-Swim1 and U1 agrees well with the pre-1883 stratigraphy presented in Beauregard (2001).

There is an accessible pre-1883 outcrop at the base of the cliff which bisects the old cone of Rakata on the north side of the island, referred to here as D2S1 (Figure 4.11a); this was visited in 2017. No contact was observed between the pre-1883 stratigraphy and the 1883 deposits, and units are likely much older as a result of being at the base of the Rakata cone. At the base of the outcrop, it is possible to observe a 2.9 m thick sequence comprising several poorly sorted, matrix-supported units of ash containing lapilli-sized scoria (Figure 4.11 b, c). These are interbedded with layers that are finer-grained and more consolidated, as well as with layers containing larger scoria clasts. A layer towards the top of this unit contains a bomb with accompanying bomb sag. These units grade into a red fine ash (25 cm thick). Overlying the red ash is 1 m of a crystal rich, likely andesitic lava flow with a brecciated contact. Above the lava are 1.5 m of deposits containing a series of layers similar to that at the base: poorly sorted, matrix-supported, with a similar overall grain size. At the base of this unit

there are clasts of the andesite lava from the unit below. Overlying this is a unit of 1.5 m thickness: finely laminated fine ash containing peletal layers of up to 1 cm thickness. Towards the top of this unit there appears to be slumping structures, as well as red ash clasts from the unit above. The unit above is 1.75 m of a red, poorly sorted, matrix supported, well consolidated pyroclastic material. Within this unit is a very fine-grained ash lens that is discontinuous, undulating and deformed, similar to the unit beneath. Overlying the red unit is a 20 cm thick fine ash layer, before a second layer similar in character to the red unit (Figure 4.11c). Above this is 75 cm of another red, poorly sorted, matrix supported unit containing pumices, with a maximum clast size of 20 cm. At the top of this outcrop it is possible to observe a second crystal-rich, likely andesitic lava flow with a brecciated base.

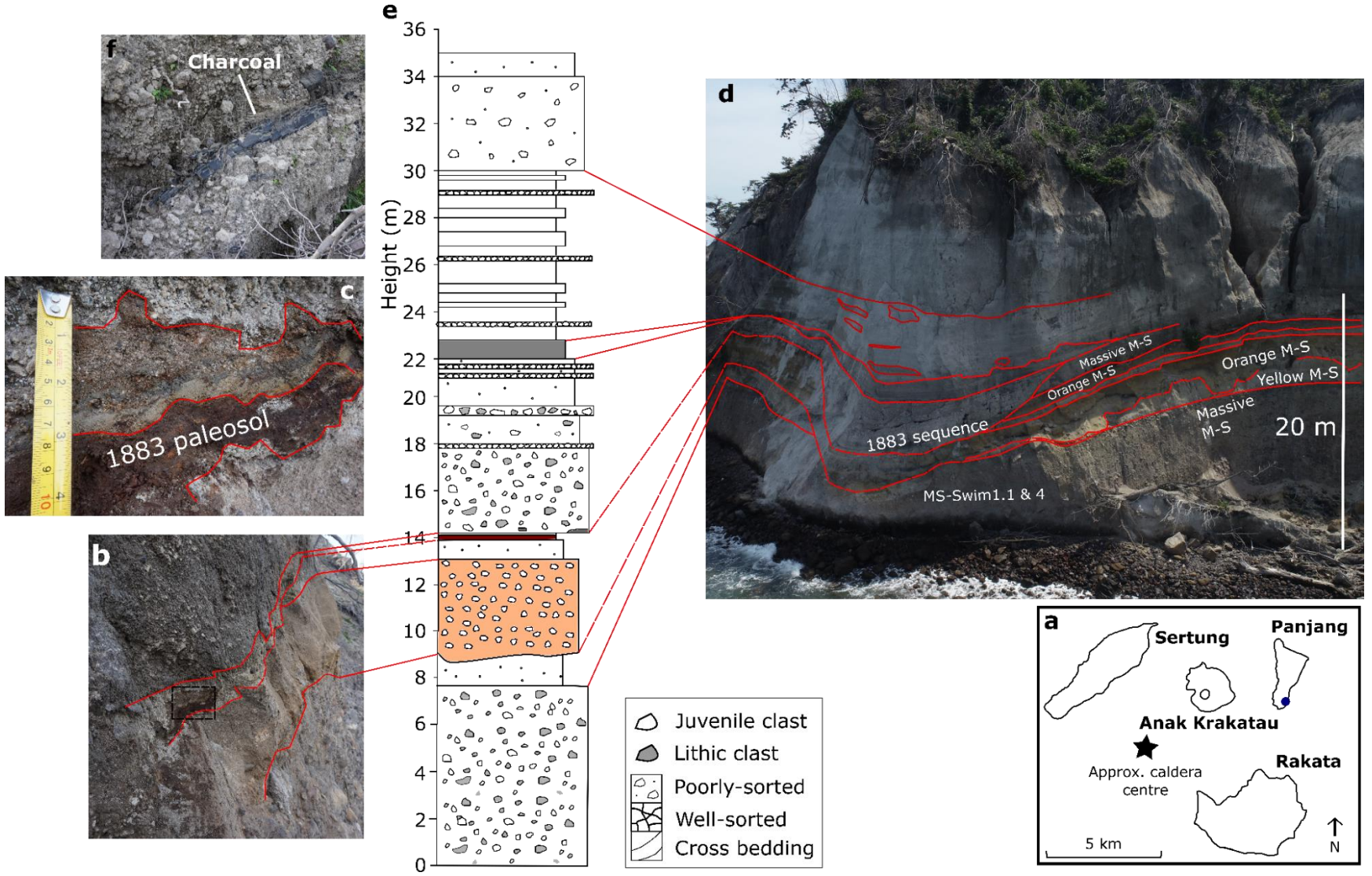

Figure 4.9: Map (a) shows the location of locality MS-Swim1 on southern Panjang (Figure 4.2), with photo (b) showing the 1883 palaeosol with dashed box giving area for close up shot (c). Drone image (d) shows the pre-1883 and 1883 sequence. Photo (b) and drone image (d) are cross correlated in red with log (e). M-S = matrix supported. Dashed lines represent erosional contacts. MS-Swim1.1 & 4 show the locations of samples relevant to this chapter. Photo (f) shows a close up of the charcoal in the first layer of the 1883 sequence at this locality.

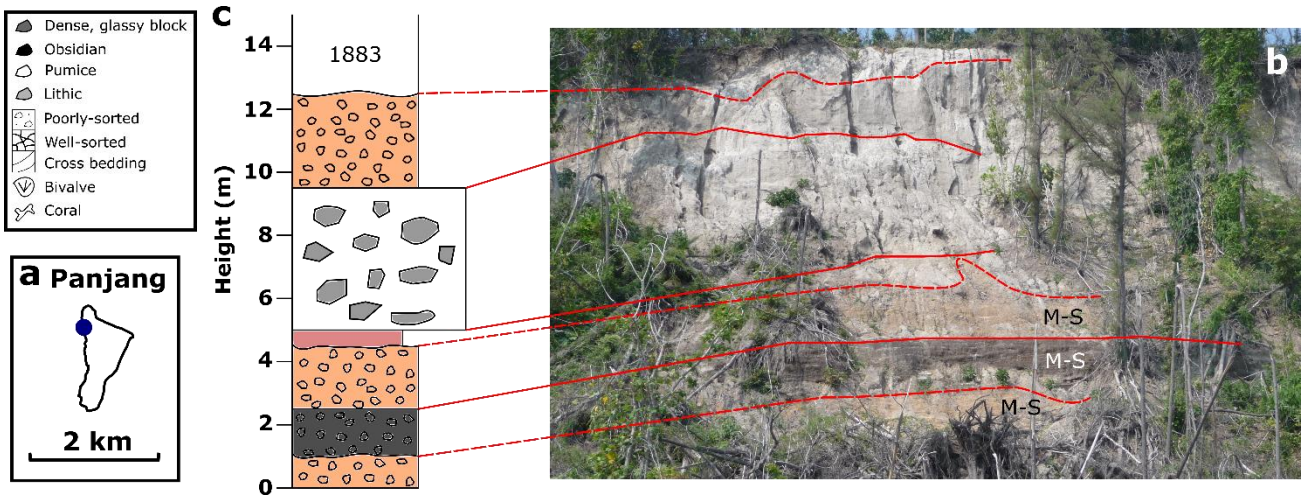

Figure 4.10: Insert (a) is a map showing Locality U1 on west Panjang (See Figure 4.2 for location of Panjang). Field photograph (b) is cross correlated in red with stratigraphic log (d). M-S = matrix-supported.

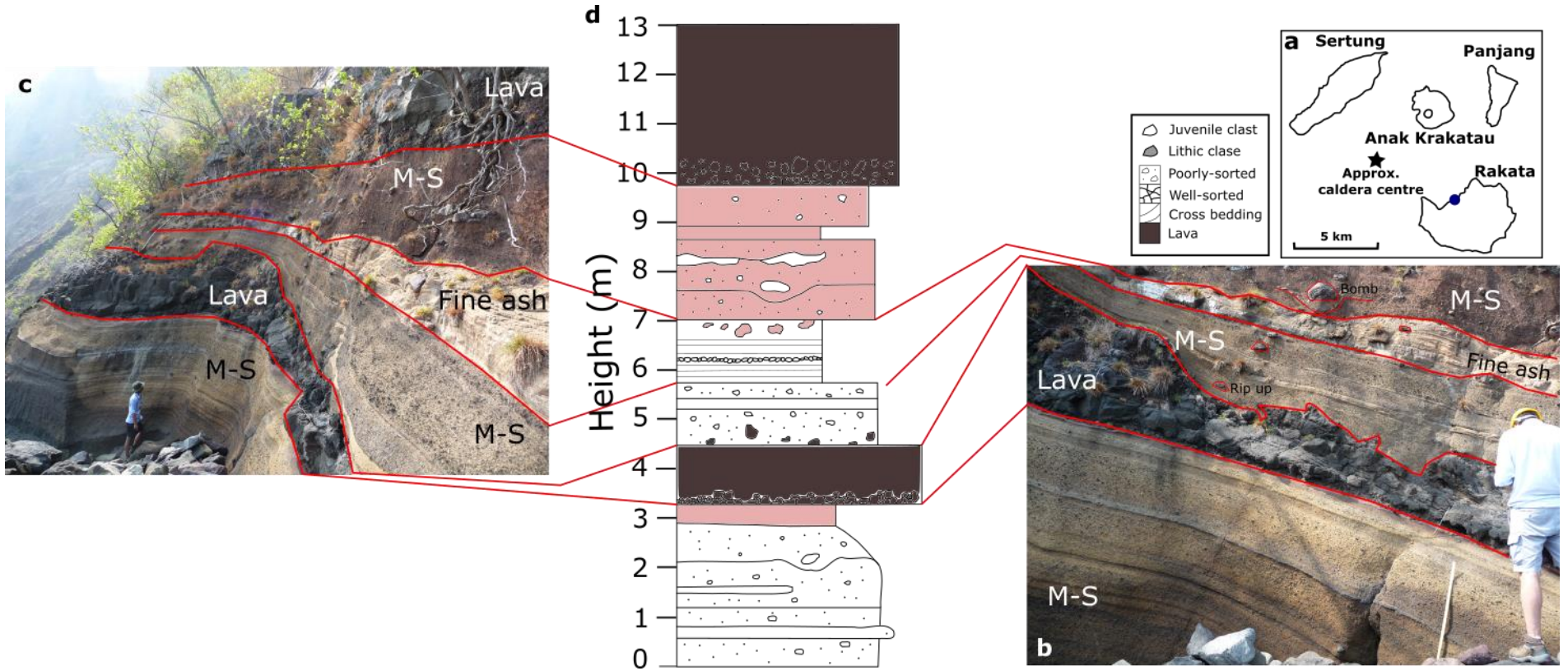

Figure 4.11: Map (a) shows the location of the pre-1883 outcrop at locality D2S1 on north Rakata (Figure 4.2). Field photos (b) and (c) are cross correlated in red with log (d). M-S = matrix-supported.

4.3.1.3 Pre-December 2018 Anak Krakatau

The volcanically active island of Anak Krakatau was visited in August 2017, prior to the subsequent collapse in December 2018 (Figure 4.2). Observations were made and samples collected, following guidance later detailed in Abdurrachman et al. (2018). Samples of lava flows from 1995 (D3S4; Figure 4.2), 2012 and 2017 (D3S6) were collected, as well as a volcanic bomb erupted in 2012 (up to 3 m, some with flow lines; D3S5).

Locality D3S3 was on NE Anak Krakatau (Figure 4.12a). The exposure consisted of a pyroclastic sequence, with a cliff exposure (Figure 4.12b) and smaller outcrops protruding from the beach at the base of the sequence (Figure 4.12c). These smaller outcrops (~20 cm thick) on the beach were clast supported, with a fine ash matrix, and predominantly contained lapilli-sized rounded, concentric accretions (accretionary lapilli). The cliff sequence was ~ 4m in size, and at the base was ~ 1m of a matrix-supported, poorly sorted unit containing pumice clasts. This unit was finely laminated, and in places contained cross bedding. Above this was a series of matrix-supported, poorly sorted units containing pumices, interbedded with continuous moderately sorted pumice-supported layers (pumices on average 1 cm). There were also some pumice lenses in this unit. Above this, again was a very fine ash, matrix-supported, poorly sorted unit containing cross bedding.

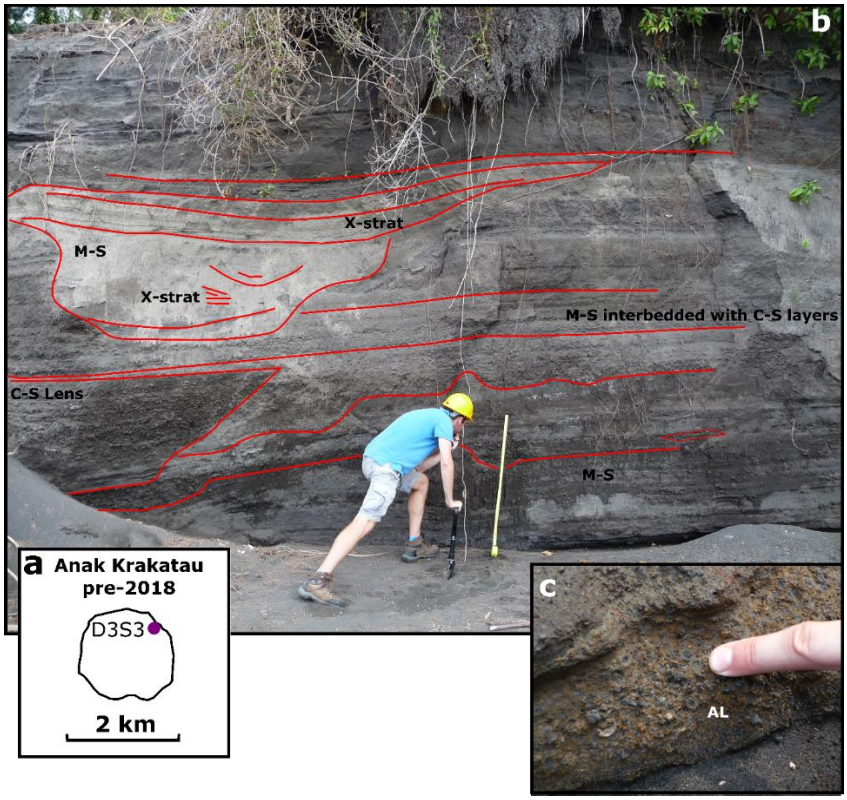

Figure 4.12: Insert (a) shows the location of locality D3S3 on Anak Krakatau prior to its collapse in 2018 (for the location of Anak Krakatau, see Figure 4.2). Field photograph (b) shows the pyroclastic deposits at this locality, tape measure for scale; C-S = clast-supported, M-S = matrix supported, X-strat = cross stratification, AL = accretionary lapilli. Photo (c) showing accretionary lapilli (AL) in protruding layers on the beach.

4.3.1.4 December 2018 – January 2019 Anak Krakatau Ash

July to October 2018 marked a period of elevated activity for Anak Krakatau, which culminated in the collapse of the southwestern portion of the island on December 22nd of that year. This generated a tsunami which greatly impacted the coast along the straits of Sunda, killing 453 people (EM-DAT, 2018). The stratigraphy of the volcanic deposits associated with this event may offer clues as to whether there was a direct magmatic trigger for the collapse event, or not.

A hole was dug on north Panjang at locality U10 (Figure 4.13a), which revealed a recent pyroclastic sequence which had not been present prior to December 2018. At the base of this sequence is a

structureless organic soil, rich in rootlets and ash (Figure 4.13b). Overlying the soil is a layer of variable thickness (4 – 11 cm) dominated by sub-rounded white pumice fragments, containing minor marine biogenic material, some of which is still intact. Scoriaceous fragments are also present (up to 3 mm in size), as well as minor angular lithics (up to 1mm) and plagioclase crystals. This unit has a planar top boundary with a relatively indurated, 5 mm thick, purple ash layer, with an oxidised crust; this layer has a high proportion of lithic grains, some of which are altered (Figure 4.12b). Above this is a reverse-graded, brown ash (35 mm thick) with planar bedding. This ash appears to contain dark juvenile clasts and some sparse rootlets. At the top of this there is a very fine mm-scale pale coloured layer. Overlying this are two very fine brown ash units of 25 mm and 28 mm thickness respectively, displaying weak low-angle cross stratification. Above this is 18 mm of a dark ash, followed by 7 mm of a fine ash. Overlying the fine ash is 4 mm of coarse ash, followed by a similar unit of variable in thickness (between 27-55 mm) containing 10 distinct layers, alternating between finer and coarser material. This unit contains low angle cross bedding. Above this is 2mm of fine ash, which truncates the unit below. The last unit contains four distinct layers alternating between coarser and finer material. Similar recent ash sequences were found further inland on northern Panjang, at localities NP2 and NP3 (Figure 4.2), however these were directly overlying the basal soil horizon, with the reworked white pumice layer containing bioclasts absent. A 1 cm thick ash deposit was also found on southern Sertung (locality U23.2; Figure 4.2).

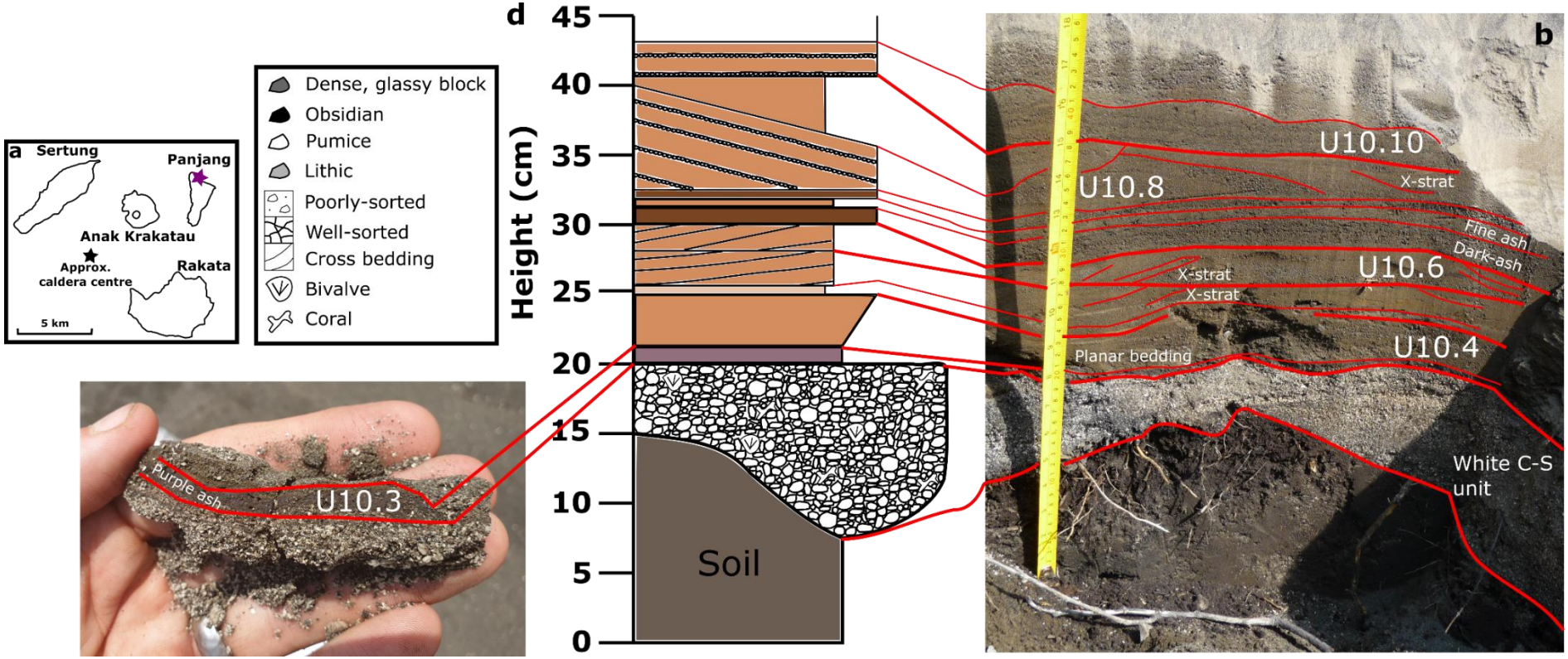

Figure 4.13: Insert (a) shows the location of locality U10 on north Panjang (Figure 4.2). Field photo (b) shows the 45 cm hole dug to reveal the recent 2018-2019 pyroclastic sequence, with (c) showing a close up of a distinct purple unit within the sequence. Numbers on field photos indicate samples relevant in this chapter. These photos are cross correlated with log (d) in red.

4.3.2 Matrix glass

4.3.2.1 Sebesi, Kecil (Sebuku), and Anjer, mainland Java

Matrix glass chemistry for the pyroclastic sequences found on Sebesi, Kecil (Sebuku) and Anjer, mainland Java are normalised to 100 % anhydrous compositions, with raw data available in Supplementary excel file for Chapter 4, Supplementary Data 2. Prior to normalisation, totals ranged from 96.0 to 101.4 wt %.

Matrix glass chemistry of the volcanic sequence found at locality U3 on Sebesi (Figure 4.2; 4.3) overlaps with matrix glass analysed from the proximal 1883 stratigraphy (Figure 4.14; Madden-Nadeau et al., 2021; Chapter 2). Samples U3.1, 2, 4 and most of U3.3 range from 70.8 to 72.5 wt% SiO_2. However, some analyses on U3.3, which was found above the road cutting, at the top of the stratigraphic sequence, appear to have compositions that overlap with the green ash aggregate layer (Unit A; Madden-Nadeau et al., 2021) at the base of the proximal 1883 stratigraphy, with SiO_2 ranging from 73.1 to 75.6 wt%.

Matrix glass chemistry for the pyroclastic sequence found at locality U9 on Kecil, off the East Coast of Sebuku (Figure 4.2; 4.7) is shown in Figure 4.15. Sample U9.2 was taken from the base of the volcanic stratigraphic sequence, has a range of 66.0 to 68.4 wt% SiO_2, and thus does not overlap with the proximal 1883 matrix glass chemistry. The compositional distribution for U9.3, the unit above, is bimodal, with SiO_2 ranging from 60.0 to 61.0 wt% and 72 to 72.7 wt%; the latter compositional range overlaps with the 1883 pyroclastic sequence. The compositions from 60.0 to 61.0 wt% SiO_2, however, were all measured from the same clast. At the top of the stratigraphic sequence, compositions of U9.5 overlap with the proximal 1883 matrix glass chemistry, with SiO_2 ranging from 71.2 to 73.1 wt%.

Matrix glass chemistry for a sample taken from the top of the volcanic sequence found at locality U16 on mainland Java (Figure 4.2;4.8), are shown in Figure 4.16. The matrix glass chemistry of the sample is more evolved than that in the proximal 1883 deposits, with SiO_2 ranging from 76.6 to 77.3 wt%.

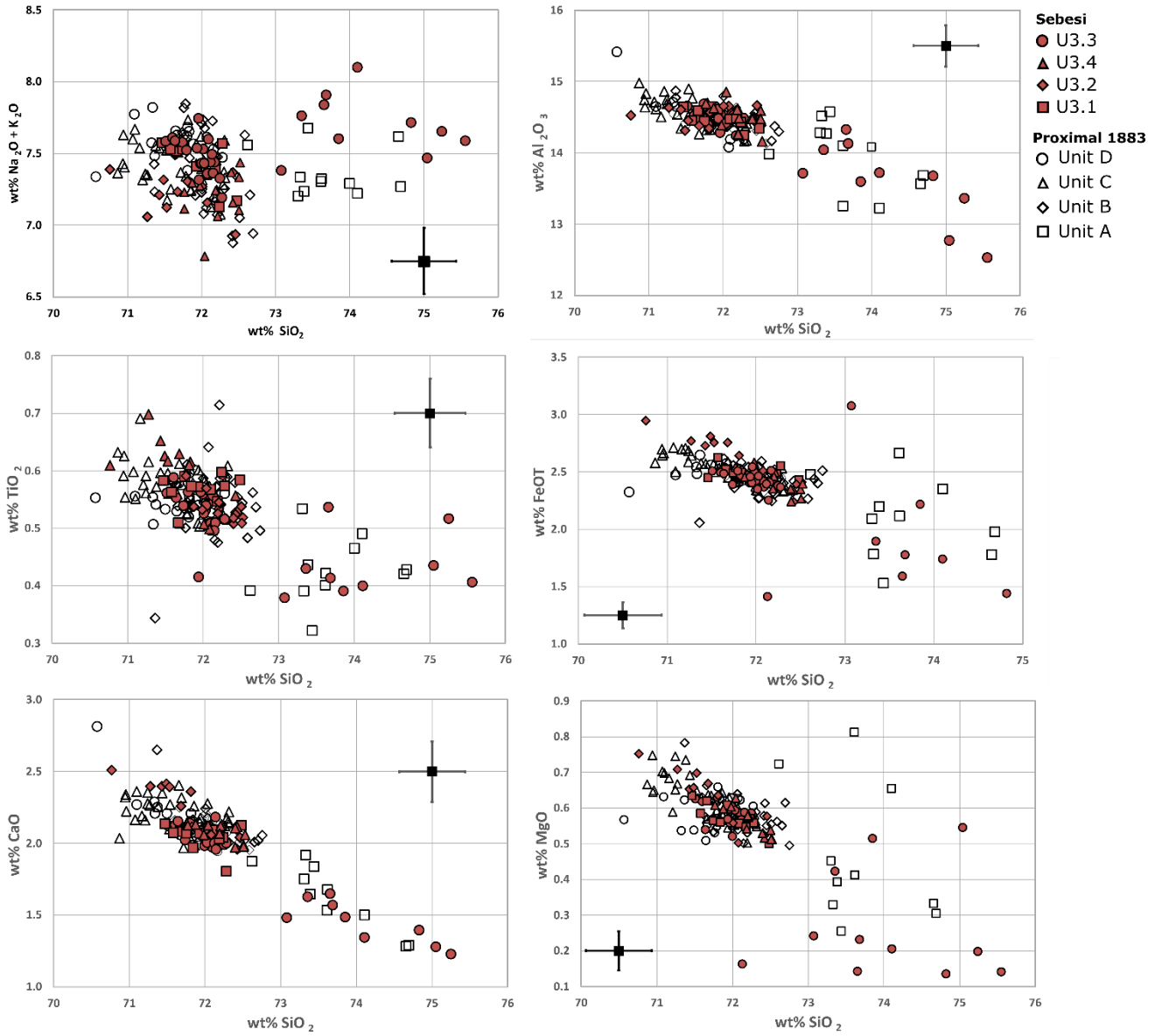

Figure 4.14: Harker diagrams showing the major element chemistry of the stratigraphy of the volcanic deposits found at locality U3 (Figure 4.2; 4.3) on Sebesi (red symbols), overlain on the proximal 1883 stratigraphy (colourless symbols). Keys in stratigraphic order. Black box error bars given to 1 σ.

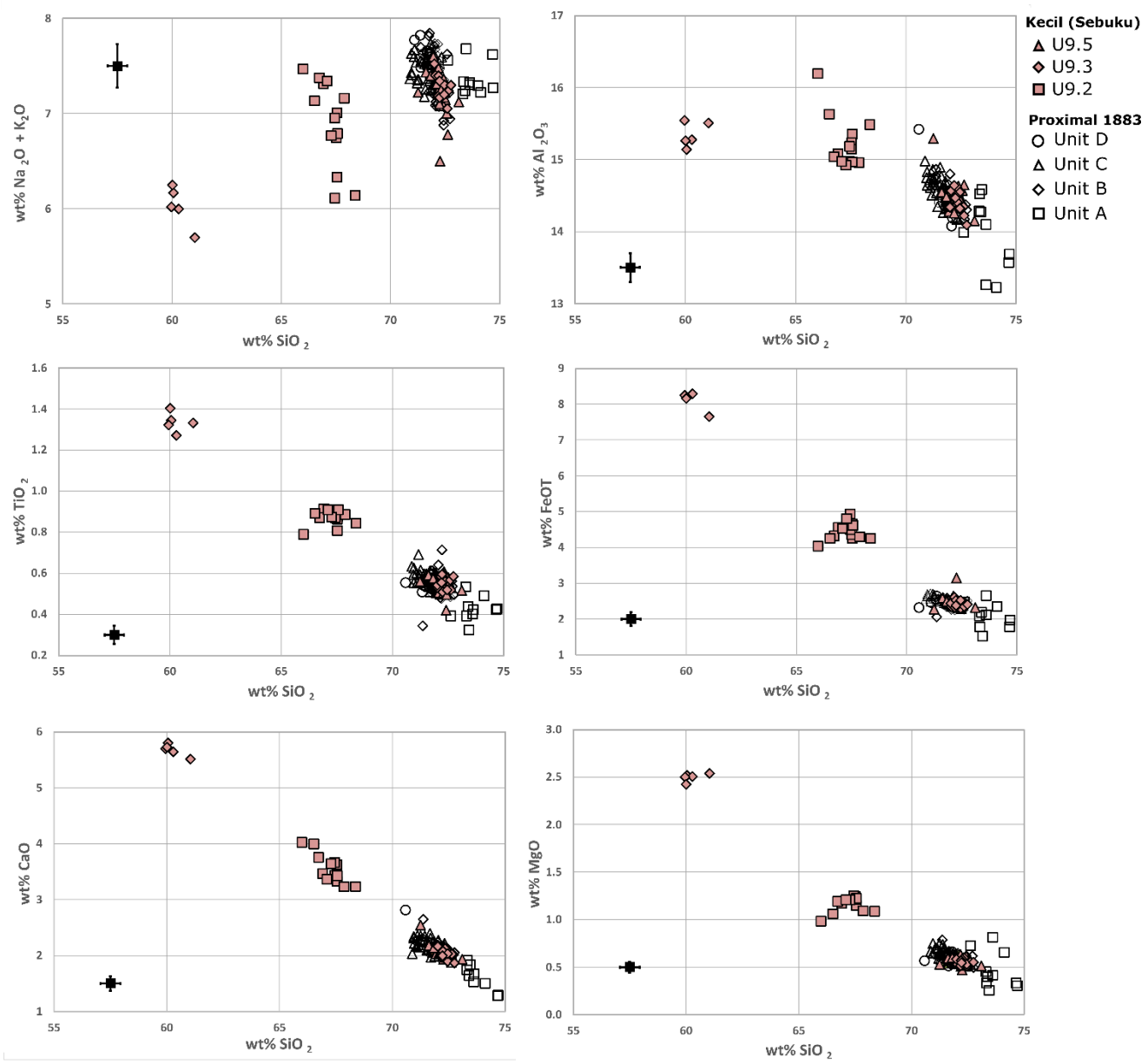

Figure 4.15: Harker diagrams showing the major element chemistry of the stratigraphy of the volcanic deposits found at locality U9 (Figure 4.2; 4.7) on Kecil, off the East coast of Sebuku (pink symbols), overlain on the proximal 1883 stratigraphy (colourless symbols). Keys in stratigraphic order. Black box error bars given to 1 σ.

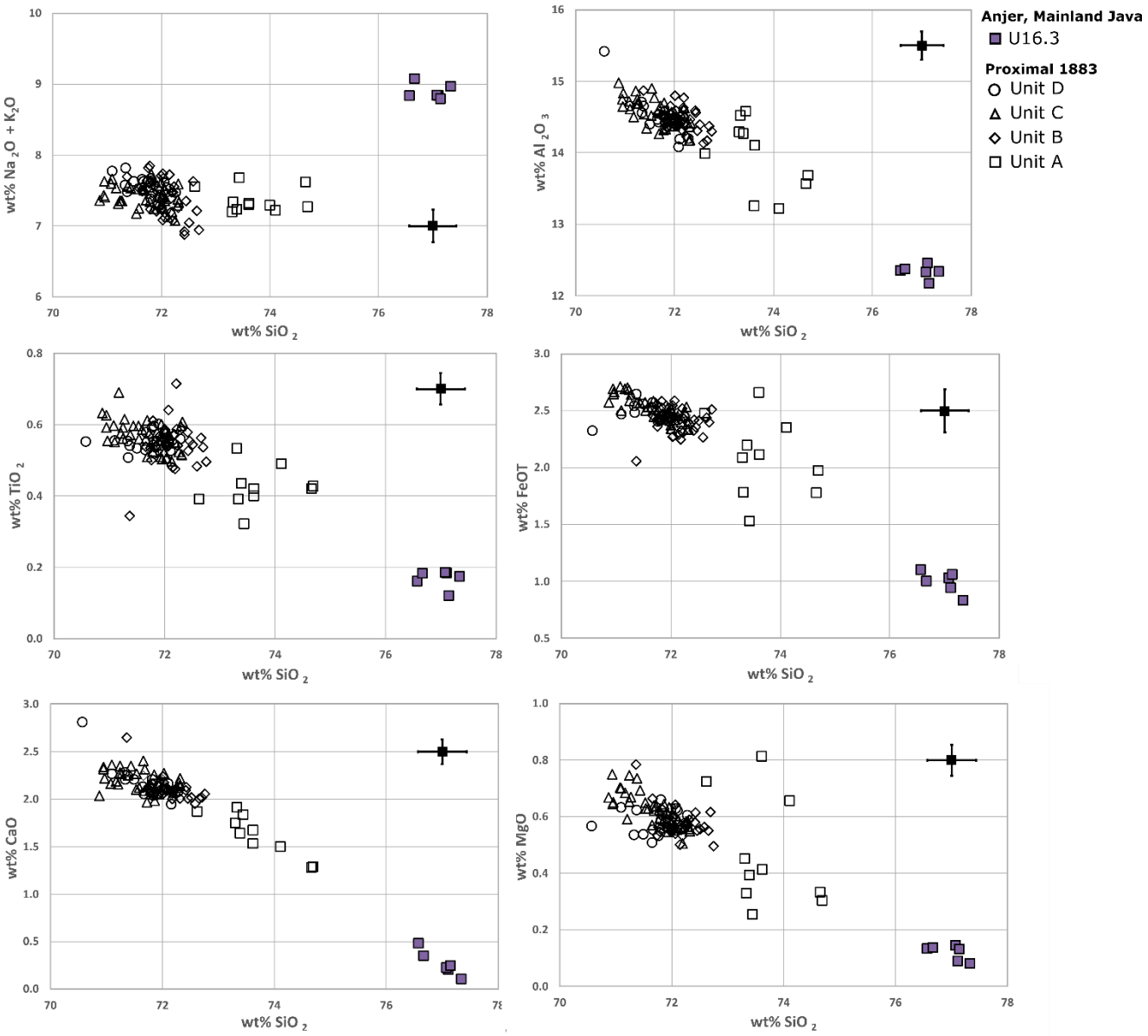

Figure 4.16: Harker diagrams showing the major element chemistry of the unit towards the top of the sequence found at locality U16 (Figure 4.2; 4.8) in Anjer on mainland Java (purple symbols), overlain on the proximal 1883 stratigraphy (colourless symbols). Keys in stratigraphic order. Black box error bars given to 1 σ.

4.3.2.2 Pre-1883 deposits

Matrix glass compositions of two units directly below the 1883 palaeosol at locality MS-Swim1 on South Panjang (Figure 4.2; 4.9) are shown in Figure 4.17, normalised to 100 % anhydrous compositions, with raw data available in Supplementary excel file for Chapter 4, Supplementary Data 3. Compositions of these pre-1883 samples overlap with matrix glass analysed from the proximal 1883 stratigraphy, with SiO_2 ranging from 71.2 to 72.7 wt%.

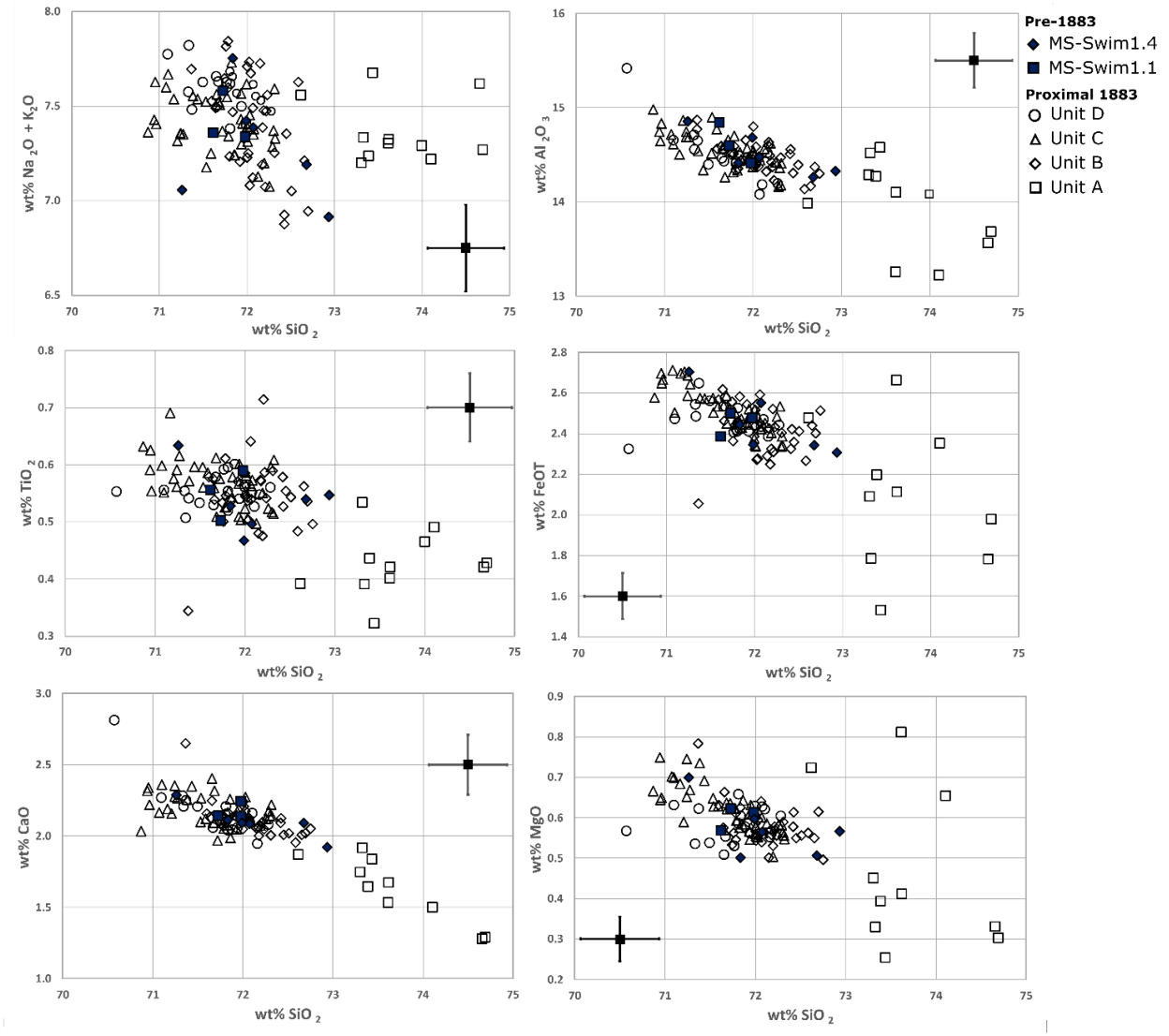

Figure 4.17: Harker diagrams showing the major element chemistry of the two units below the 1883 palaeosol at locality MS-SWIM1 (Figure 4.2; 4.9) on south Panjang (blue symbols), overlain on the proximal 1883 stratigraphy (colourless symbols). Keys in stratigraphic order. Black box represents error given to 1 σ.

4.3.2.3 2018-2019 Anak Krakatau ash

Matrix glass chemistry of the sequence of ash related to the December 2018 collapse of Anak Krakatau at locality U10 on Panjang (Figure 4.2; 4.13) is shown in Figure 4.18 (data in Supplementary excel file for Chapter 4, Supplementary Data 4). Compositions overlap with matrix glass data of other Anak Krakatau products (e.g., Darhen et al., 2012). There is a trend towards a more evolved composition up the sequence. The purple ash at the bottom of the volcanic sequence is the least evolved, with SiO_2 contents ranging from 58.3 to 59.3 wt%. The SiO_2 contents of the units next in the sequence, U10.4 and U10.6, range from 58.3 to 60.0 wt%, and the units towards the top of the sequence, U10.8 and U10.10, range from 58.9 to 60.8 wt%.

In addition, the U10.3 purple ash at the base is chemically distinct from the overlying units. The Al_2O_3 content of U10.3 is lower at 12.7 – 14.0 wt%, compared with 14.2 – 15.9 wt% for the overlying sequence. FeO contents are elevated for U10.3, at 9.65 – 10.81 wt%, compared with 8.14 – 9.07 wt% for the overlying sequence. TiO_2 contents are also elevated at 1.81 – 1.96 wt%, compared with 1.34 – 1.69 wt% for the overlying sequence. All matrix glass data within this chapter is shown again on a single Total Alkali and Silica diagram, in Figure 4.18.

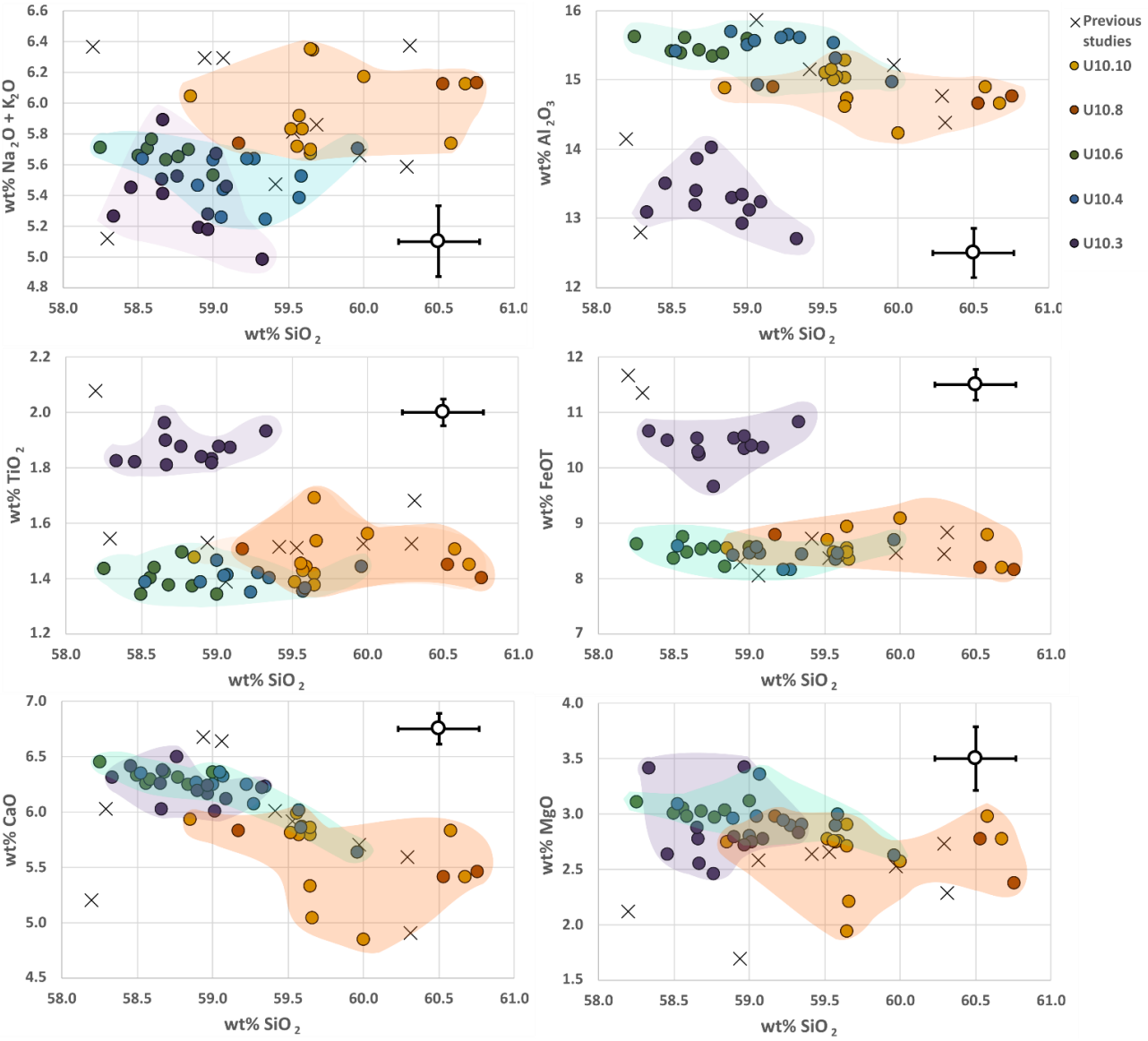

Figure 4.18: Harker diagrams showing the major element chemistry of the 2018 – 2019 ash sequence at locality U10 (Figure 4.2; 4.13) on Panjang, overlain on matrix glass chemistry for other Anak Krakatau products from Darhen et al., (2012). Keys in stratigraphic order. Colourless box represents error given to 1 σ.

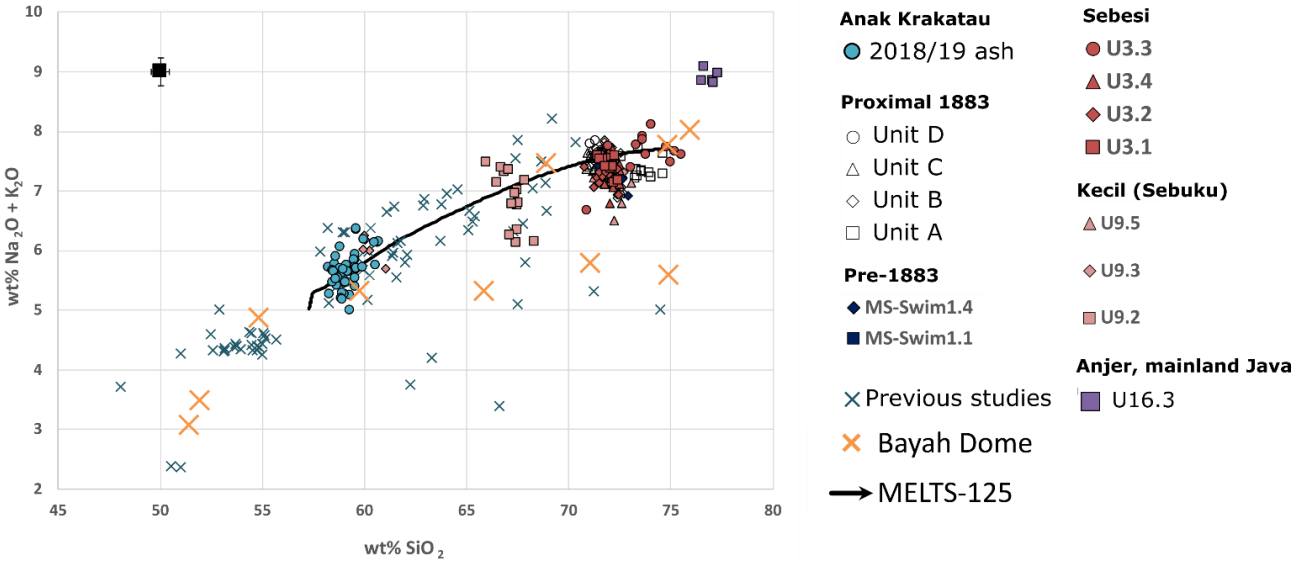

Figure 4.19: Total alkali and silica diagram (Le Bas et al., 1989), showing all matrix glass collected, overlain on previous matrix glass and whole rock chemical analyses for Krakatau and Anak Krakatau (Gardner et al., 2013; Darhen et al., 2021; Konig et al., 2011; Woodhead et al., 2001; Mandeville et al., 1996; Oba et al., 1992; Self 1992; Camus et al., 1987; Zen et al., 1964). Black line shows the modelled isobaric liquid line of descent from an Anak Krakatau basaltic andesite starting composition, at an initial water content of 1.5 wt%, and pressure at 125 MPa, modelled vis Rhyolite-MELTS (Gualda et al., 2012). Whole-rock analyses from Bayah Dome, west Java, also overlap with the liquid line of descent at Krakatau (orange crosses; Alves et al., 1999). All keys in stratigraphic order.

4.4 Discussion

4.4.1 Origins of the deposits on Sebesi, Sebuku and Anjer, mainland Java

Constraining the extent, thickness and nature of pyroclastic density current (PDC) deposits is important both for PDC modelling (e.g., Marti et al., 2016), and for tsunami-generation models (e.g., Choi et al., 2003), which will allow for these hazards to be better assessed. Carey et al. (1996) attributed the volcanic deposits on the islands of Sebesi and Sebuku to the 1883 eruption, predominantly based on observations of 1 – 1.5 m of ash deposits immediately after the eruption,

made by Verbeek (1884). In addition, deposits on mainland Java are also hypothesised to have been deposited during this eruption. Here we will compare matrix glass analyses from Sebesi, Sebuku and Anjer, mainland Java, to matrix glass analysed from the proximal 1883 deposits (Chapter 2; Madden-Nadeau et al., 2021). All analysed samples from deposits at these locations lie on a similar liquid line of decent, which overlaps with liquid lines of descent modelled isobarically via Rhyolite-MELTS (Gualda et al., 2012) for 1.5 wt% initial water contents, and 125-250 MPa (Madden-Nadeau et al., 2021; Figure 4.19). The compositions and the deposits' proximity to the volcano, means it is possible that all of these deposits were at some point erupted from Krakatau. However, it is not uncommon for volcanoes within the same region, undergoing similar local tectonic and crustal processes, to have overlapping matrix glass chemistry. For example, the Bayah Dome is a volcanic complex in western Java and the closest volcano to Krakatau with existing data (of which the current active edifice, Salak Volcano, lies on the northeast edge, 160 km from Krakatau). Volcanic deposits associated with the Bayah Dome have whole-rock compositions that overlap along Krakatau's liquid line of descent (Alves et al., 1999). In addition, there are other volcanoes even more proximal to these deposits, such as Mt. Rajabasa, which lies 42 km south of Krakatau, which do not have any existing chemical datasets, and may have overlapping geochemistry with Krakatau. This means the deposits on Sebesi, Sebuku and Anjer deposits cannot be definitively attributed to Krakatau, on this basis. Some samples from these localities directly overlap with the proximal 1883 tephra, however so does the pre-1883 matrix glass collected from MS-Swim1 on northern Panjang (Figure 4.17). Deposits with matrix glass chemistry that overlaps with the proximal 1883 stratigraphy may therefore not necessarily have been erupted during in 1883, but could be older and/or from another volcano entirely. Further work, therefore, would be to obtain further chemical analyses (e.g., trace element analyses; Pearce et al., 2020) of all samples to ascertain whether they can be attributed to Krakatau, and for those with a similar matrix glass chemistry, specifically to the 1883 eruption.

The volcanic deposits on Sebesi island comprise two poorly sorted, matrix-supported units containing rounded pumices (U2/3 and 4; Figures 4.3; 4.4), which are characteristic features of deposition via flow, and therefore are likely to have been deposited by pyroclastic density currents

(PDCs; Branney and Kokelaar, 2002). The major element matrix glass chemistry from the first three samples analysed in the sequence (U3.1, 2 and 4) overlaps with the bulk of the proximal 1883 sequence (Madden-Nadeau et al., 2021; Figure 4.14), making it possible that they were deposited in the same eruption. However, matrix glass chemistry of the units below the 1883 palaeosol also overlap with the proximal 1883 sequence (Figure 4.17), thus they may have also been deposited as a result of an older eruption. It should be noted that quartz was present in the first 3 samples in the Sebesi sequence (Figure 4.3; U3.1, 2 and 4), whereas there is no quartz within the proximal 1883 tephra. The subaerial volcanic deposits on Sebesi are also green, in contrast to the characteristic white of the 1883 proximal PDC deposits. The sample at the top of the sequence at locality U3 (U3.3) has more evolved matrix glass chemistry than the units below, overlapping with Unit A, the green ash aggregates at the base of the proximal 1883 stratigraphy (Figure 4.14). We undertook preliminary carbon dating of a piece of charcoal, which yielded post-1950 ages; there are no reports of post-1950 PDCs reaching Sebesi, and the thicknesses of these deposits indicates that they are older, so further dating and/or chemical analyses is needed to constrain the timing of these deposits. If these deposits do pertain to pre-1883 eruptions, this once again illustrates the hyper-mobility of PDCs from Krakatau that are able to travel over ~16 km over water. It is unlikely that these deposits would pertain to eruptions of Krakatau in 1680 and 1681 detailed by Vogel (1690) and Hesse (1690; 1694), as Sebesi is described as “densely covered in high trees” in November 1681 (Figure 4.1). However, it is possible that these eruptive units, if pertaining to Krakatau, could have been deposited in the 416 AD eruption detailed in the Book of Kings (Judd, 1889).

The volcanic deposits on Sebuku and Kecil are, again, mostly poorly sorted, matrix-supported units containing rounded pumices, and thus are likely PDC deposits (Branney and Kokelaar, 2002). There are three distinct units on Kecil at locality U9 (Figure 4.7). Sample U9.2 was collected at the bottom of the volcanic sequence, and has a less evolved matrix glass chemistry than the 1883 proximal sequence (Figure 4.15). The next unit in the sequence has bimodal glass chemistry: one similar to the 1883 proximal glass, and one less evolved, although the latter was only measured on one clast, making it possible this was an extraneous lithic fragment. Further geochemical analyses on the

matrix glass from this unit would therefore need to be conducted to clarify this. The unit towards the top of the sequence has a matrix glass composition that overlaps with the 1883 sequence. However, as discussed previously, units below the 1883 palaeosol also have compositions that overlap with the proximal 1883 matrix glass chemistry (Figure 4.17), and so a match in major elements is not diagnostic. In addition, both upper units contain quartz, which is not present in the proximal 1883 tephra. The lower two units are also green in colour, in contrast to the white proximal 1883 deposits. The fact that the basal unit has a different geochemistry, and that the volcanic deposits appear continuous stratigraphically, with no evidence of erosional surfaces or palaeosols between the units, means that it is possible that the deposits on Kecil were not erupted in 1883. The conglomerate at the base of this sequence was likely deposited in a high energy event, and contains marine fossils, meaning may have been deposited as a result of a tsunami older than those produced in 1883. In addition, the presence of the pottery fragment within the conglomerate, means it is possible that the eruption responsible for these deposits is historical (China has been exporting white pottery flatware since 900 AD; Zhiyan et al., 2010). A large tsunami is documented to have occurred, as a result of Krakatau erupting in 416 AD, in the Book of Kings (Judd, 1889), however there is no written evidence of any other tsunamis occurring until 1883 (Figure 4.1). Further work would include dating this pottery fragment to further investigate the age of this unit, and to ascertain that it is not a more recent contaminant.

The volcanic deposit in Anjer, on the coast of mainland Java (Figure 4.2) has lower and upper units which are massive, poorly sorted and matrix-supported, containing rounded pumices (Figure 4.8), which are characteristic features of PDC deposits (Branney and Kokelaar, 2002). The matrix glass chemistry of the upper PDC deposit is more evolved that the 1883 proximal matrix glass (Figure 4.16), and so was not erupted from Krakatau in 1883. However, it is not possible to rule out this unit being erupted from Krakatau prior to 1883 based solely on major element matrix glass chemistry, as it lies close to the general magma evolution trend for Krakatau on the Total Alkali and Silica Diagram (Figure 4.19). If voluminous PDCs (~ 5 m high deposits) are able to travel up to 50 km from Krakatau, this poses a major hazard for all those living on the coast around the Sunda Straits. The

only pre-1883 eruption that may have been sufficiently explosive to produce such PDCs is the 416 AD eruption documented in the Book of Kings (Judd 1889; Figure 4.1). However, it is also possible that this deposit was the result of an eruption from another volcano within the region (Figure 4.19).

4.4.2 Anak Krakatau

Since Anak Krakatau's vent stopped interacting with seawater in the 1960s, the volcano has predominantly erupted effusively, punctuated with Vulcanian and Strombolian explosions. In 2017 we found deposits at locality D3S3 on Anak Krakatau that contained cross bedding (Figure 4.12) which are characteristic features of deposition via flow. In addition, the matrix was comprised of fine ash and contained accretionary lapilli, which suggests that the deposits underwent magma-water interaction, and thus are likely recording the pre-1960s phreatomagmatic activity.

Intense phreatomagmatic activity at Anak Krakatau also occurred in the wake of the December 2018 collapse of island. Our objective when investigating the stratigraphy of the post-collapse deposits of 2018-2019 is to determine whether they represent pre- or post-collapse volcanic deposits, as this is crucial to investigating whether there was a magmatic contribution to the flank collapse of Anak Krakatau, which would be important in the consideration of precursors to such events (e.g., Watt 2019).

The base of stratigraphy at site U10 is a pumice-rich layer mixed with sparse marine shells, deposited on top of an organic soil (Figure 4.13). The white pumice fragments are rounded and appear to be reworked from the 1883 stratigraphy, based on appearance and the abundance of white pumice within the area. Based on the presence of reworked 1883 pumice with marine shells, as well as an absence of this layer at more elevated sites (NP2, 3 and U23b; Figure 4.2), this unit is interpreted to be a tsunami deposit, likely generated by the flank collapse of Anak Krakatau on 22nd December 2018. Overlying this unit is a series of well-bedded, well sorted, fine ash layers (Figure 4.13), likely to be fall deposits. Collectively, the thickness of U10 sequence of fine ash layers, and the fact that the tsunami deposit is not contaminated by the darker ash sequence above, is most consistent with

deposition from observed pulsatory post-collapse Surtseyan eruptions, which generated weak lower tropospheric ash-rich plumes between 22 December and early January 2019 (PVMBG, 2018; Prata et al., 2020). This phreatomagmatic activity was likely as a result of the vent being located below sea-level post-collapse (Novellino et al., 2020).

The matrix glass chemistry of the 2018/2019 ash does not differ significantly from previous Anak Krakatau tephra in composition, however there are subtle changes in matrix glass chemistry moving through the U10 sequence (Figure 4.18). Directly above the tsunami deposit is a ~0.5 cm thick purple ash layer (U10.3), which is distinct from the overlying sequence in colour and matrix glass chemistry, with lower Al_2O_3, and higher FeO and TiO_2 contents. This suggests that this layer may have undergone slightly less Fe-Ti oxide crystallisation prior to eruption, which may be as a result of less Fe-Ti oxide microlite formation. Microlites generally form as a result of decompression on ascent and increasing Fe-Ti oxide microlite formation throughout the sequence may therefore be reflective of the decompression rate initially being very high in the instantaneous aftermath of flank collapse, before decreasing and allowing time for more microlite formation (e.g., Szramek et al., 2006; Watt, 2019). The stratigraphy overlying the purple ash also trends towards slightly more evolved compositions over time, suggesting more time for degassing-induced crystallisation as the eruption progressed. The fact that this sequence was deposited post-collapse, and is potentially decompression driven, means that it provides no evidence for a direct magmatic trigger for the flank collapse of Anak Krakatau on 22nd December 2018.

4.5 Conclusions

The deposits, originally attributed to the 1883 eruption, on the islands of Sebesi and Sebuku, and in Anjer, mainland Java (16, 25 and 40 km away, respectively), have matrix glass chemistry consistent with products erupted from Krakatau volcano. However, at least one other volcano in the region (Bayah Dome) has tephra with major element compositions that overlap with Krakatau's liquid line of descent, which mean the most distal deposits in Anjer, Java were not necessarily erupted from

this volcano. The majority of tephra analysed from Sebesi (U3) and Sebuku (U9.5) have major element matrix glass chemistry consistent with the 1883 eruption, however these rhyodacitic compositions have been erupted by Krakatau prior to 1883. Therefore, these deposits cannot be definitively attributed to the 1883 eruption on the basis of major element composition alone. In addition, changes in matrix glass chemistry through the stratigraphic sequence are inconsistent with proximal 1883 tephra at one locality on Sebesi (U3), and all deposits are green colour and with inconsistent phenocryst contents which casts further doubt as to whether or not they were erupted in 1883. In any case, these deposits require further chemical analysis (e.g., dating, trace element chemistry) to be placed within the context of Krakatau's eruptive history. At least one deposit on Kecil, Sebuku (U9.2) has major element matrix glass chemistry inconsistent with proximal 1883 tephra. A plate fragment found within the likely tsunami deposit directly below this volcanic unit (U9.2) means it is possible that this tephra was erupted historically. If these eruptive deposits do not pertain to the 1883 eruption of Krakatau, this has important implications for modelling the 1883 pyroclastic density currents, and subsequent tsunamis. If they were erupted in 1883, then this has important implications for using major element matrix glass chemistry to correlate volcanic sequences, particularly where PDCs have travelled over large bodies of water and may have segregated and/or undergone chemical alteration.

The sequence of 2018-2019 ash deposits associated with flank collapse on Anak Krakatau overlies a likely tsunami deposit. This sequence of thin, fine ash units is consistent with observed pulsatory Surtseyan activity after the tsunamigenic flank collapse of Anak Krakatau on 22nd December 2018. The phreatomagmatic activity is likely to have occurred as a result of the vent being truncated below sea level as a result of the collapse (Novellino et al., 2020). The first unit erupted immediately post-collapse has lower Al_2O_3 and higher TiO_2 and FeO than the overlying sequence, likely reflecting less Fe/Ti oxide microlite formation, which may be as a result of high decompression rates in the immediate aftermath, which then decreased over time. The 2018-2019 ash found on the Krakatau islands is thus representative of post-collapse volcanic activity that appears decompression driven,

and thus provide no evidence for a direct magmatic trigger for the collapse of Anak Krakatau in 2018.

5. Conclusions and future work

This thesis set out to investigate how the 1883 silicic caldera-forming eruption of Krakatau progressed through time, both in terms of eruptive behaviour and magma reservoir conditions and processes. This has been achieved through the establishment of the proximal eruptive stratigraphy (Chapter 2), petrological and geochemical investigation of the magma reservoir and the processes and conditions therein, the integration of these datasets with the eruptive timeline (Chapters 2 and 3), and re-evaluation of more distal deposits attributed to the 1883 eruption (Chapter 4). The secondary aim of this thesis was to investigate explosive activity produced by Anak Krakatau, to improve the understanding of this system through time (Chapter 4). The following sections summarise the conclusions drawn from this work, and relate to objectives one to five as set out in the introduction.

5.1 1883 proximal eruptive stratigraphy

In Chapter 2, this thesis presents field observations from outcrops with significantly better exposure of the 1883 eruptive deposits of Krakatau than have been documented previously, revealed as a result of the removal of vegetation by the 2018 tsunami, generated by flank collapse of Anak Krakatau. These field observations have allowed for the volcanic stratigraphy to be considerably better constrained. A generalised stratigraphy is shown in Figure 5.1.

There is a thin, green, ash-aggregate layer overlying a red palaeosol at the very base of the sequence, delineating Unit A (Figure 2.4a). Overlying this is a sequence of pumice fallout units interbedded with PDC and dilute-PDC deposits, with some of these units containing charcoal (Unit B; Figure 2.4b, c), followed by a lithic lag breccia (Unit C; Figure 2.5a, b). Unit D consists of massive PDC deposits containing obsidian (Figure 2.5b, c). A second lithic lag breccia is observed at the top of Unit D at one location (D3S2/NP4; Figure 2.5b), and glassy blocks up to 8 m in size are present at another (D2S2/U23; Figure 2.5c), which are reported within this sequence for the first time. The shapes of these large glassy blocks suggest that they underwent ductile deformation during hot

emplacement. The directionality of the pyroclastic density currents changes after the deposition of the lithic lag breccia occupying a distinct horizon (Unit C; Figure 5.1). The lithic lag breccia is thus attributed to partial collapse of the island, and the removal of a topographic barrier. The second lithic lag breccia may have been deposited during the final stages of caldera collapse.

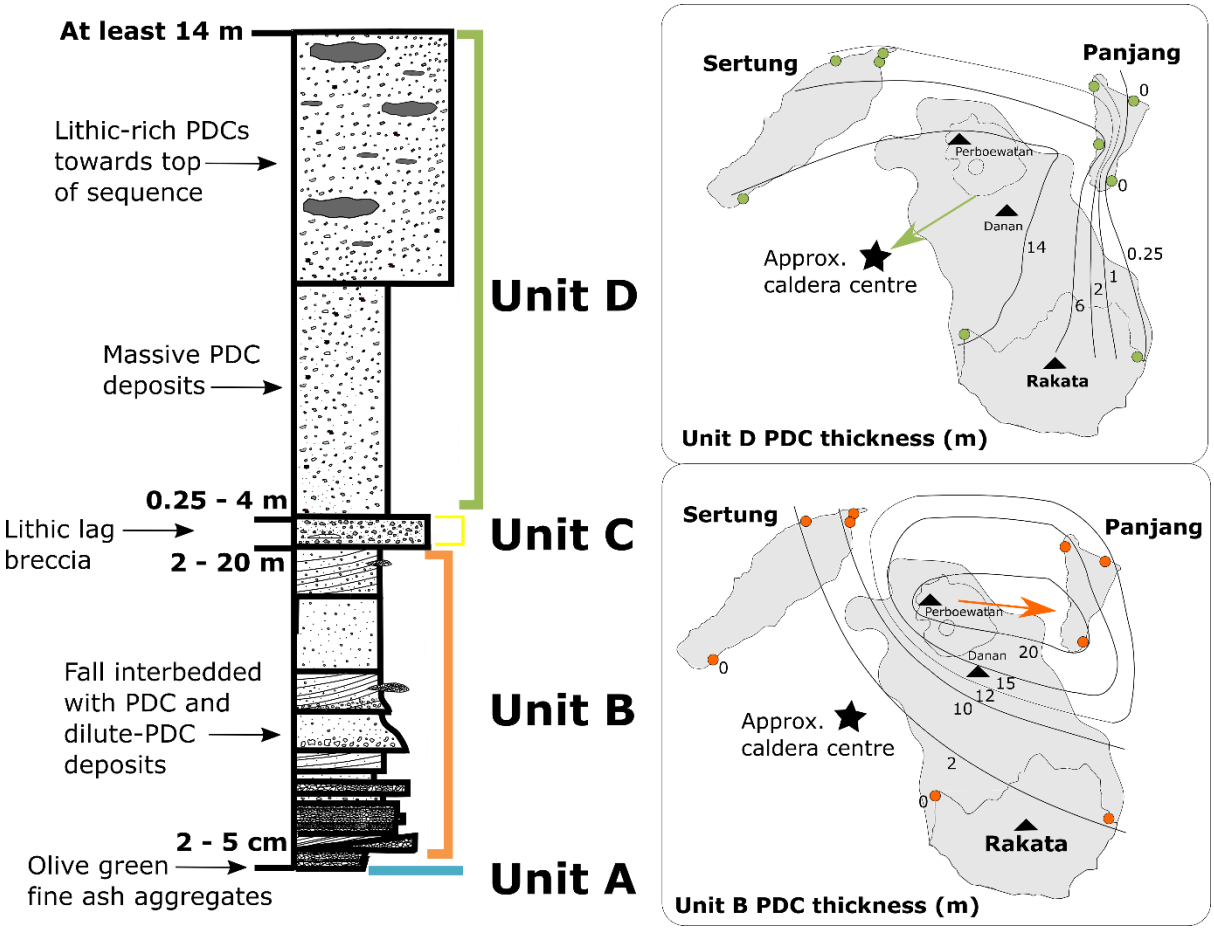

Figure 5.1: Synthesis figure showing composite 1883 proximal stratigraphy, along with isopach maps for PDC deposits of Unit B and D on the Krakatau islands as they were prior to 1883 (present-day arrangement given by the dotted lines), as derived in Chapter 2. Triangles show previously active cones, and arrow shows inferred PDC directionality.

5.2 Integration of the 1883 stratigraphy with the eruptive timeline

Integration of the eruptive timeline, as derived from written accounts, with the stratigraphic sequence is predominantly achieved in Chapter 2. The existence of distinct, green, basal ash aggregates (Unit A) at the base of the stratigraphy is consistent with reported observations of a maximum of 50 cm of green ash at the coast in June 1883 (Symons et al., 1888; Figure 2.2). Therefore, it is likely that Unit A was erupted during the precursory sub-Plinian activity observed in May 1883 (Symons et al., 1888), as hypothesised by Mandeville et al. (1996a). Units B to D therefore represent the climatic phase of the eruption on 26th and 27th August 1883 (Figure 2.2). The stress field associated with the subterranean system was potentially disrupted by the precursory eruption in May, leading to the paroxysm. These stress changes may have occurred simply as a result of gradual emptying of the initial silicic reservoir, however the loss of mass reported from the summits of Perboewatan and/or Danan may also have played a role (Figure 2.2). The change in PDC directionality (Figure 5.1) which coincides with the deposition of the first lithic lag breccia is attributed to partial collapse of the island. The 1883 eruption culminated in total caldera collapse, which, together with the PDC production at this stage, was a potential cause of the largest tsunami at 10 am on 27th August (e.g., Francis, 1985). This final caldera collapse is recorded in the stratigraphy as a second lithic lag breccia, observed at one locality (D3S2/NP4; Figure 2.5b). The identification of at least two lag breccias may indicate piecemeal caldera formation, where the first stage of collapse is the driving force behind the most energetic and explosive, climactic part of the eruption.

5.3 The thermochemical architecture of, and conditions and processes within, the 1883 pre-eruption magmatic system

Analyses of the geochemistry presented in the context of the refined eruptive stratigraphy in Chapters 2 and 3 does not support previous studies (e.g., Mandeville et al., 1996a) that have proposed that the eruption emanated from a chemically zoned magma reservoir (See summary diagrams in Figure 5.2).

An updated model for the magmatic system is proposed, accounting for the chemical variations in context with the stratigraphic sequence (Figures 5.2 and 3.14).

The matrix glass chemistry of the thin layer of basal ash aggregates (Unit A) shows that they are more silicic than the overlying sequence (Figure 2.12). In addition, phase equilibria experiments show that Unit A was likely erupted from a deeper magma storage region than the subsequent stratigraphy, at 100 - 150 MPa (~4 - 6 km) and 850 +/- 25 °C, in comparison with 50 - 100 MPa (~ 2 – 4 km) and 850 - 900 °C for Units B to D (Figures 3.2 and 3.3). This temperature constraint agrees with estimates generated using Fe-Ti oxide thermometry of 890 – 935 °C for Units B to D, discussed in Chapter 2. The deeper location of the reservoir from which the precursory activity in May was derived has important implications for the interpretation of geophysical monitoring data, and in particular volcano seismicity data, for systems with the potential to produce caldera-forming eruptions.

Modelling of isobaric fractional crystallisation of an Anak Krakatau basaltic andesite shows that simple melt evolution of this starting composition can generate a similar major element chemistry to the 1883 rhyodacites, under certain conditions (Figure 2.13). The modelled trends of melt evolution that replicate Krakatau's matrix glass and whole rock chemistry is between 125 and 250 MPa, which corroborates the estimates generated by phase equilibria experiments. The models also fit best with natural Krakatau data for an initial H_2O content of 1.5 wt%. Plagioclase-melt hygrometry estimates pre-eruptive H_2O contents at 3.4 – 3.6 wt%, which overlaps with the best-match liquid lines of decent modelled through Rhyolite-MELTS (Figure 2.13f). In addition, a high proportion of phenocrysts have normally zoned rims, which likely resulted from melt evolution. Modelling melt chemistry using partition coefficients and trace elements in plagioclase from Units B to D also show strong trends indicative of melt evolution (Figures 3.12 and 3.13). These trends overlap with matrix glass chemistry of products of phase equilibrium experiments, designed to simulateconditions within the pre-eruptive, shallow system. This makes it likely that fractional crystallisation was the dominant process in the shallow system prior to the 1883 eruption of Krakatau. Within Units B to D,

plagioclase of $An_{<67}$ is therefore most likely to have crystallised within chemically similar melts, under similar pressure and temperature conditions.

However, plagioclase phenocrysts have complex zoning profiles and textures (Figure 2.10), with a wide range in euhedral rim compositions (Figure 2.11), which would not be expected if fractional crystallisation was the only process ongoing in the shallow system. This could be explained if plagioclase crystallised in more diverse melts deeper within the system before being transported to shallower depths. Some crystals may also have settled out and become isolated from the melt phase, which would mean rim compositions generated over a period of time would be unable to re-equilibrate. Plagioclase of $An_{>67}$ in Units B to D show no evidence of melt evolution trends for modelled melt compositions, and are not replicated by experiments at shallow depths (Figure 3.13), and thus also support the hypothesis that there is greater melt diversity, which cannot be explained by fractional crystallisation, within the deeper magmatic system.

The large glassy blocks within Unit D have matrix glass chemistry similar to the rest of the 1883 tephra (Figure 2.12b). The matrix glass chemistry, along with signs of ductile deformation, suggest that the obsidians are likely juvenile, and may have been incorporated into PDCs from small, cooler (<800 °C), stagnant bodies of melt during final caldera collapse. Another possible mode of formation for the obsidians is fragmented 1883 melt sticking and sintering to sides of the conduit walls, before being erupted (e.g., Wadsworth et al., 2020).

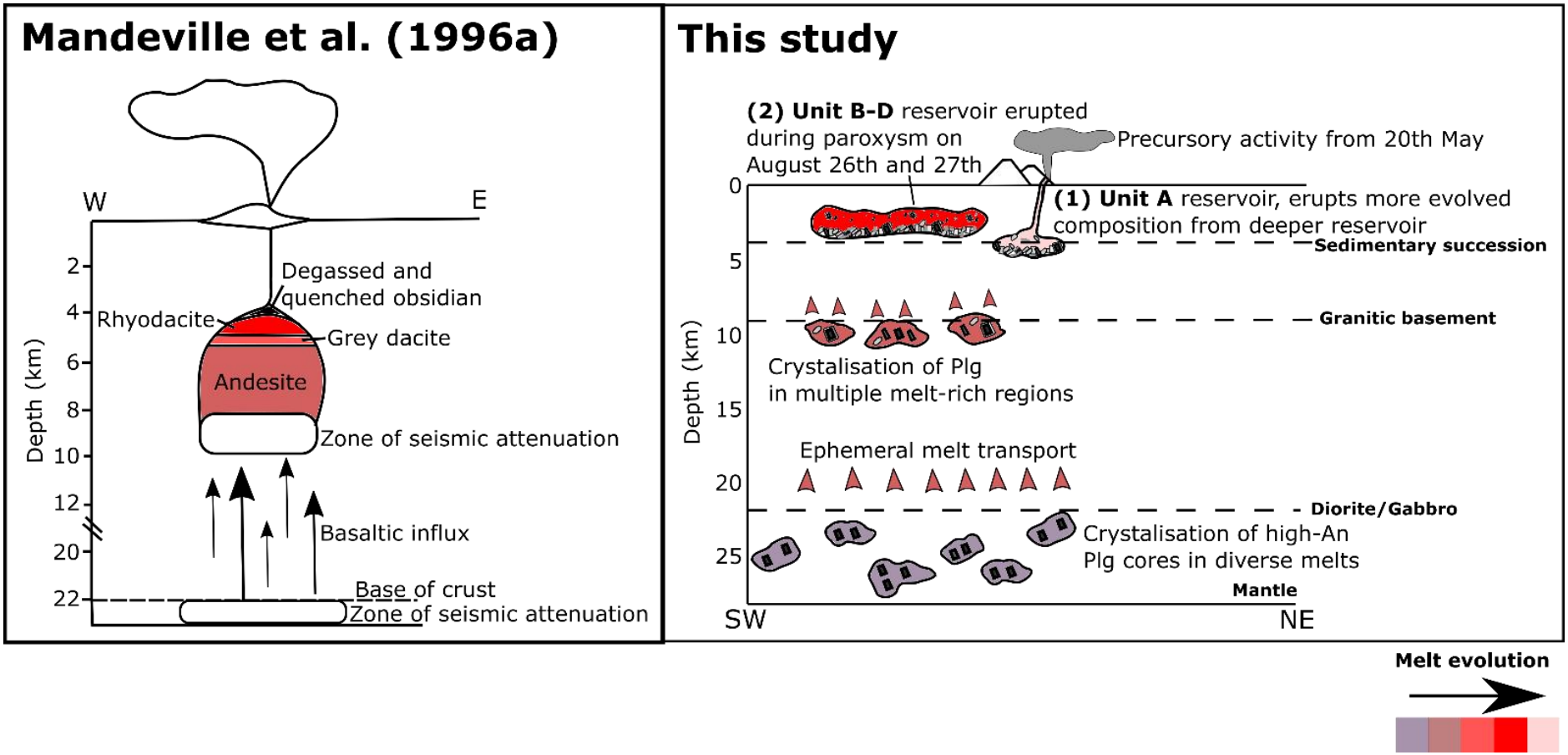

Figure 5.2: Schematic diagram showing the potential hypothesis for the architecture of the magmatic system during the 1883 eruption of Krakatau, modified from Chapter 3, Figure 3.14 (modified from Madden-Nadeau et al., 2021; lithological structure and crystallisation depths from Darhen et al., 2012; Mandeville et al., 1996a) next to the previous model for the system proposed by Mandeville et al. (1996a). Mandeville et al. (1996a) shows the system as a zoned magma reservoir based on volumetrically minor andesitic and grey dacite components (~6 %), however there is no evidence that their frequency varies with stratigraphic height. The model presented in this diagram shows two separate magma reservoirs within the shallow magmatic system: a more evolved reservoir responsible for the deposition of Unit A (Figure 3.1), evidenced from historical accounts, stratigraphic observations and matrix glass analyses (Chapter 3; Madden-Nadeau et al., 2021). Phase equilibria experiments constrain the depth of this reservoir to 4 - 6 km (Figures 3.2 and 3.4). The reservoir at 2 – 4 km depth is evidenced by matrix glass chemistry and phase proportions of phase equilibria experiments (Figures 3.2 and 3.4), and is the source of the paroxysmal phase of the eruption, as determined by stratigraphic and historical observations (Chapter 2; Madden-Nadeau et al., 2021).

5.4 Explosive deposits further afield

The stratigraphy and matrix glass chemistry of deposits previously attributed by Carey et al. (1996) to the 1883 eruption of Krakatau are discussed in Chapter 4. The deposits from Sebesi, Sebuku, Kecil and Anjer, Java (locations in Figure 4.2) have matrix glass chemistry consistent with Krakatau's liquid line of decent (Figure 4.19). However, the matrix glass chemistry of at least one other volcano within the region (Bayah Dome), also overlaps with Krakatau's magma evolution trend, meaning that the deposits cannot be definitively attributed to Krakatau on this basis. This is particularly important when assessing the more distal outcrops, such as in Anjer, Java, which is approximately 40 km away from Krakatau. Volcanic deposits found on Sebesi and Sebuku have matrix glass chemistry that directly overlaps with the proximal 1883 tephra (U3; Figure 4.14 and U9.5; Figure 4.15). However, tephra from pre-1883 explosive eruptions also has matrix glass chemistry that overlaps with the proximal 1883 sequence (Figure 4.17). Therefore, these deposits cannot be definitively attributed to the eruption in 1883 on this basis, although were likely derived from Krakatau volcano. In addition, locality U3, on Sebesi, has its most evolved matrix glass chemistry at the top of the sequence, which is not commensurate with the 1883 proximal stratigraphy (Figure 4.14). The deposits are also green in colour and often contain quartz. At least one volcanic unit (U9.2), found at the base of an outcrop on Sebuku, Kecil and overlying a likely tsunami deposit, has matrix glass chemistry that is distinct from the 1883 proximal stratigraphy (Figure 4.15). Therefore, more distal volcanic deposits on Sebesi, Sebuku and Kecil and Anjer, Java need to be reassessed in more detail (via dating/other geochemical correlations, such as trace element chemistry) to be placed within the context of Krakatau's eruptive history (Figure 4.1). If these deposits are from older Krakatau eruptions, this highlights the possibility that events that can generate PDCs which travel >25 km over the sea surface, are not uncommon for this volcano. The presence of a plate fragment found within a likely tsunami deposit (locality U9, Kecil) potentially provides evidence for the overlying pyroclastic density current (PDC) deposits being historical (Figure 4.7d). If these deposits were erupted in 1883, then this work has important implications for using major element matrix glass

chemistry as a correlating tool for volcanic sequences where PDCs have travelled large distances over bodies of water, where physical segregation and/or chemical alteration may have occurred.

5.5 2018/2019 eruptive stratigraphy of deposits associated with tsunamigenic flank collapse of Anak Krakatau

Assessment of the 2018/2019 volcanic deposits associated with the tsunamigenic flank collapse of Anak Krakatau was completed in Chapter 4. These 2018-2019 ash deposits overlie a likely tsunami deposit (Figure 4.13); the boundary between the two units is sharp, indicating that the volcanic stratigraphy is recording post-collapse activity. In addition, this sequence of thin, fine ash units is consistent with observed pulsatory Surtseyan activity after the tsunamigenic flank collapse of Anak Krakatau on 22nd December 2018 (Prata et al., 2020). This phreatomagmatic activity is likely to have occurred as a result of the vent being truncated below sea level as a result of the collapse (Novellino et al., 2020). Overall, the chemistry of this sequence does not differ significantly from other products of Anak Krakatau, and is basaltic andesite in composition (Figures 4.18 and 4.19). However, the first unit erupted immediately post-collapse has lower Al_2O_3 and higher TiO_2 and FeO than the overlying sequence (Figure 4.18), likely reflecting less Fe/Ti oxide microlite formation, which may be as a result of high decompression rates in the immediate aftermath, which then decreased over time. The 2018-2019 ash found on the Krakatau islands is thus representative of post-collapse volcanic activity that appears decompression driven, and thus provide no evidence for a direct magmatic trigger for the collapse of Anak Krakatau in 2018. This makes it more likely that the collapse occurred as a result of gravitational instabilities linked with long-term edifice building, which was potentially exacerbated by the high eruptive flux from June 2018 (Walter et al., 2019).

5.6 Implications

Achieving the objectives set out in the introduction has led to the conclusions detailed in the preceding sections (5.1 – 5.5). The overarching aim of the thesis set out in the introduction, to

investigate how the 1883 silicic caldera-forming eruption of Krakatau progressed through time, both in terms of eruptive behaviour and magma reservoir conditions and processes, has been achieved through the establishment of the proximal eruptive stratigraphy (Chapter 2), petrological and geochemical investigation of the magma reservoir and the processes and conditions therein, integration of these datasets with the eruptive timeline (Chapters 2 and 3), and re-evaluation of more distal deposits attributed to the 1883 eruption (Chapter 4). Achievement of these aims and objectives has important implications for Anak Krakatau, and other analogous systems.

Stratigraphic constraints paired with historical accounts of this eruption provides important information regarding the eruptive progression and associated hazards of potential future eruptions. For example, precursory Plinian activity is a useful phenomenon to be aware of for the future monitoring of volcanoes with a history of producing silicic caldera-forming eruptions. The 1883 eruption of Krakatau provides an example of an event where relatively moderate explosive eruptions may potentially have run-away effects culminating in cataclysmic caldera-collapse several months later. This study also highlights that it is important not to assume that the more silicic composition of magmas associated with precursory activity, are derived from shallower in the magmatic system, in comparison to the paroxysm-fed magmas, which is often done.

Additionally, better constraints on the 1883 stratigraphy have important implications for modelling the 1883 pyroclastic density currents, and subsequent tsunamis, which will not only help to understand these events better, but also help in forecasting the magnitude of future events and the areas they might affect. Improved stratigraphic constraints, integrated with the eruption timeline and geochemical data has led to the development of a model for the 1883 magmatic system (Figure 3.14); this has important implications for monitoring of Anak Krakatau, and other similar systems with the potential to produce caldera-forming eruptions. This is particularly the case for systems that are hypothesised to have a similar subterranean structure prior to these large eruptions, such as the Youngest Toba Tuff (Pearce et al., 2019). For example, seismic and deformation data collected during contemporary volcanic unrest can provide depths of magma storage (Saccorotti et al., 2015), therefore an improved understanding of the depths to these magma reservoirs for past explosive

eruptions is important, as it may help forecast nature and magnitude of possible eruptions associated with this unrest focussed at these depths.

The secondary aim of this thesis was to investigate explosive activity produced by Anak Krakatau, to improve the understanding of this system through time (Chapter 4). This was predominantly achieved through the assessment of the 2018/2019 ash associated with flank collapse of Anak Krakatau. The deposits were likely erupted post-collapse, and provide no evidence for a magmatic trigger to the collapse event and tsunami. These post-collapse products showed subtle compositional changes, likely related to microlite formation and ascent rates, which is in line with work completed by Watt (2019) on the influences sector collapses exert on magmatic systems. However, no large compositional changes occurred post collapse, which suggests that large scale restructuring of the subterranean system did not occur as in previous examples studied. This may be as a result of the discrepancy in size between the 2018 flank collapse of Anak Krakatau (0.175 km^3; Hunt et al., 2021) and the much larger collapses investigated by Watt (2019) of >5 km^3. Regardless, it more likely that gravitational instabilities linked with long-term edifice building, potentially exacerbated by the high eruptive flux from June 2018 (Walter et al., 2019), was the trigger of the flank collapse in December 2018. This has important implications for hazard assessment, as long-term monitoring of deformation of rapidly growing islands will likely play a key role in monitoring for such events. In addition, this data, along with data obtained for eruptions that occurred prior to 1883, will lead to an improved understanding of intra-caldera explosive activity, which, helps to establish key markers for stages of its caldera cycle, which in turn provides important context for monitoring of the system (e.g., Maisonneuve et al., 2021).

The wider implications of this work, particularly for other caldera-forming systems, is to provide an example for comparison. Wilson et al. (2021) concluded that there is not a single model for subterranean magmatic systems with the potential to produce caldera-forming eruptions. However, there are similarities that can be drawn between some of these systems. The model proposed for Krakatau in this thesis of multiple, chemically distinct, individual reservoirs, within the shallow system, that are tapped sequentially, with a deeper system that is more chemically diverse, is similar

to models proposed for the Younger Toba Tuff (Pearce et al., 2020), and for several caldera-related explosive eruptions in the Taupo Volcanic Zone (e.g., Charlier et al., 2003; Gravley et al., 2007; Bégué et al., 2014), and has been linked to areas undergoing active extension (Cashman and Giordano, 2014). Although the Java trench is an area of subduction, the Sunda Strait, in which Krakatau sits, is extending, as Sumatra rotates relative to Java (e.g., Hall, 2012). Therefore, magmatism in the Sunda Strait is not only a function of subduction, but also of rifting and extension associated with slab-thinning and mantle upwelling beneath Krakatau (Abdurrachman et al., 2018). This is likely to enhance its productivity, both in terms of eruptive volume and periodicity, in contrast to other volcanoes within the region. Although Wilson et al. (2021) focuses on "super eruptions" and the 1883 eruption of Krakatau is smaller in scale, there are common features both in eruption style and inferred magma-system architecture across these caldera-forming systems. This suggests that there is nothing inherently unique about the magmatic systems that produce these large scale "super eruptions", and that instead they represent one endmember in terms of magnitude of silicic caldera-forming eruptions.

5.7 Future work

The work detailed in this thesis has created more questions which could serve as potential avenues for research in the future. The large, glassy blocks described for the first time in the 1883 stratigraphy in Chapter 2 (Figure 2.5c), have matrix glass compositions which overlap with the 1883 tephra, and are therefore most likely sourced from the same magma (Figure 2.12b). However, it is still unclear how they were physically incorporated into these deposits. Two leading hypotheses for their formation were: (1) small, stagnant, degassed melt-rich regions that were excavated during caldera formation or, (2) 1883 melt that stuck to the conduit walls and sintered, before being excavated and incorporated into PDCs during caldera collapse. It would thus be important to look for sintering textures, and water content variations, within samples of these blocks to attempt to identify the mechanism under which they formed (e.g., Gardner et al., 2017).

In addition, detailed petrological work was completed on plagioclase phenocrysts to better understand the pre-eruptive processes and conditions within the magmatic system in Chapter 2. One common point in the crystallisation histories of some of these phenocrysts was the presence of a high anorthite core (Figures 2.10 and 2.11), which has been attributed to crystallisation within the deeper magmatic system. It would therefore be possible to assess the timescales over which individual crystals were resident in the shallow magmatic system prior to eruption by conducting diffusion chronometry modelling over the boundary between the high anorthite core and lower anorthite mantle (e.g., Costa et al., 2020). How quickly eruptions occur after melt extraction from magma mushes is one of the big questions in volcanology and igneous petrology at the moment, as it provides important temporal context for volcano monitoring. Crystals that would be ideal for this analysis have already been identified (e.g., Figure 2.10a).

Experimental petrology was used to investigate the eruptive deposits of Krakatau for the first time in Chapter 3 of this thesis. Although phenocrysts were assumed to have a negligible impact on the composition of the starting powder as a result of the low phenocryst content (Figure 3.2), mass balance calculations accounting for the incorporation of plagioclase into the starting composition show that wt% Al_2O_3 was elevated beyond natural matrix glass concentrations by ~2 wt%. Thus, determining the ideal experimental set up for these volcanic products may require further investigation. Experiments conducted on coarsely crushed, rather than powdered, material could be conducted, to determine whether the incorporation of phenocrysts would significantly affect the results presented in Chapter 3 (e.g., Pichavant et al., 2007). In addition, it was assumed that the bulk composition of Unit A was similar to the rest of the stratigraphy, despite small variations in matrix glass chemistry. Fe-Ti oxide geothermometry could be conducted on Unit A samples to compare with experiments, and/or experiments specifically using a Unit A starting material could be conducted to compare with results presented here to verify that the starting composition used is appropriate.

Another line of enquiry would be to further investigate the volcanic stratigraphy on the more distal islands of Sebesi and Sebuku. This thesis has raised questions about the origins of these deposits,

and so the natural next step for this research would be further dating of samples, as well as obtaining further geochemical data, such as trace elements to more effectively correlate these deposits to establish their provenance. It would also be useful to conduct an archaeological investigation into the piece of broken pottery identified in the likely tsunami deposits at locality U9 (Figure 4.7d). In addition, further investigation of petrological data (e.g., major and trace element chemistry, H_2O contents, temperatures, crystallinity estimates etc.) through time of the intra-caldera explosive activity at Anak Krakatau, and prior to the 1883 eruption, would aid in characterising which stage of its caldera cycle Anak Krakatau is now in, which will in turn inform the monitoring of the volcano (e.g., Maisonneuve et al., 2021).

There are many routes that investigating silicic caldera systems might take in the future. However, an important question to answer is how these magmatic systems respond to mass wasting events, such as caldera formation and flank collapse. The Krakatau 1883 eruption, and 2018/2019 eruptive deposits would therefore also make for excellent case studies to investigate how different collapse events impact on the subterranean system. Barometry could be completed for volcanic material erupted before and after these collapse events to investigate how the architecture of the magmatic system is affected, and what implications this has for changes in eruptive activity.

A better understanding of accumulation rates of eruptible magma in the shallow system prior to silicic caldera-forming eruptions is also needed. These melt dominant bodies are likely transient, with some petrological studies estimating timescales in the order of years for magma accumulation. Better estimates of these timescales via diffusion chronometry, combined with an improved understanding of the factors which cause the unrest associated with magma accumulation, will aid in identifying relevant geophysical signals. The identification of geophysical signals of magma accumulation in these systems is paramount, because once in place, these bodies may generate an explosive eruption on timescales of days to months, which only provides limited time for the interpretation of geophysical signals associated with the triggering of an eruption (Wilson, 2017; Wilson et al., 2021).

Bibliography

Abdurrachman, M., Widiyantoro, S., Priadi, B. and Ismail, T. (2018). Geochemistry and Structure of Krakatoa Volcano in the Sunda Strait, Indonesia. Geosciences, 8(4), 111.

Algemeen Dagblad (1883). 20th and 26th June, 17th and 27th August, 3rd, 5th and 11th September.

Allan, A.S., Wilson, C.J., Millet, M.A. and Wysoczanski, R.J. (2012). The invisible hand: Tectonic triggering and modulation of a rhyolitic supereruption. Geology, 40(6), 563-566.

Anderson, D.J. and Lindsley, D.H. (1988). Internally consistent solution models for Fe-Mg-Mn-T: Oxides. Am. Mineral, 66, 416-420.

Anderson D.J., Lindsley D.H. and Davdison P.M. (1993). QUILF: a pascal program to assess equilibria among Fe-Mg-Mn-Ti oxides, pyroxenes, olivine, and quartz. Computational Geosciences, 19, 1333–1350.

Anderson, J.L., Barth, A.P., Wooden, J.L. and Mazdab, F. (2008). Thermometers and thermobarometers in granitic systems. Reviews in Mineralogy and Geochemistry, 69(1), 121-142.

Andrews, B.J., Gardner, J.E. and Housh, T.B. (2008). Repeated recharge, assimilation, and hybridization in magmas erupted from El Chichón as recorded by plagioclase and amphibole phenocrysts. Journal of Volcanology and Geothermal Research, 175(4), 415-426.

Andrews, B.J. and Manga, M. (2014). Thermal and rheological controls on the formation of mafic enclaves or banded pumice. Contributions to Mineralogy and Petrology, 167(1), 1-16.

Andújar, J. and Scaillet, B. (2012). Relationships between pre-eruptive conditions and eruptive styles of phonolite–trachyte magmas. Lithos, 152, 122-131.

Arce, J.L., Gardner, J.E. and Macías, J.L. (2013). Pre-eruptive conditions of dacitic magma erupted during the 21.7 ka Plinian event at Nevado de Toluca volcano, Central Mexico. Journal of Volcanology and Geothermal Research, 249, 49-65.

Arce, J.L., Macias, J.L., Gardner, J.E. and Layer, P.W. (2006). A 2.5 ka history of dacitic magmatism at Nevado de Toluca, Mexico: petrological, 40Ar/39Ar dating, and experimental constraints on petrogenesis. Journal of petrology, 47(3), pp.457-479.

Arculus, R.J. and Wills, K.J. (1980). The petrology of plutonic blocks and inclusions from the Lesser Antilles island arc. Journal of Petrology, 21(4), 743-799.

Ashdown, E. (1883). A Floating Lava Bed [Letter to the editor, reprinted from the London Times]. Nature, 28:532-533.

Bacon, C.R. (1983). Eruptive history of Mount Mazama and Crater Lake caldera, Cascade Range, USA. Journal of Volcanology and Geothermal Research, 18(1-4), 57-115.

Bacon, C. R. and Hirschmann, M. M. (1988). Mg/Mn partitioning as a test for equilibrium between coexisting Fe-Ti oxides. American Mineralogist, 73(1-2), 57-61.

Barker, S.J., Rowe, M.C., Wilson, C.J., Gamble, J.A., Rooyakkers, S.M., Wysoczanski, R.J., Illsley-Kemp, F. and Kenworthy, C.C. (2020). What lies beneath? Reconstructing the primitive magmas fueling voluminous silicic volcanism using olivine-hosted melt inclusions. Geology, 48(5), 504-508.

Bataviaasch Handelsblad (1883). 16th and 28th August, and 9th September.

Beauregard, J.L. (2001). Explosive Rhyodacitic volcanism: The evolution and frequency of pre-1883 eruptions at Krakatau Volcano, Indonesia. PhD thesis, University of Rhode Island, available at: https://digitalcommons.uri.edu/dissertations/AAI3025530/

Bégué, F., Deering, C.D., Gravley, D.M., Kennedy, B.M., Chambefort, I., Gualda, G.A. and Bachmann, O. (2014). Extraction, storage and eruption of multiple isolated magma batches in the paired Mamaku and Ohakuri eruption, Taupo Volcanic Zone, New Zealand. Journal of Petrology, 55(8), 1653-1684.

Bindeman, I.N., Davis, A.M. and Drake, M.J. (1998). Ion microprobe study of plagioclase-basalt partition experiments at natural concentration levels of trace elements. Geochimica et Cosmochimica Acta, 62(7), 1175-1193.

Blake, S. (1984). Volatile oversaturation during the evolution of silicic magma chambers as an eruption trigger. Journal of Geophysical Research: Solid Earth, 89(B10), 8237-8244

Blundy, J.D. and Cashman, K. (2001). Ascent-driven crystallisation of dacite magmas at Mount St Helens, 1980–1986. Contributions to Mineralogy and Petrology, 140(6), 631-650.

Blundy, J., Cashman, K.V., Rust, A. and Witham, F. (2010). A case for CO2-rich arc magmas. Earth and Planetary Science Letters, 290(3-4), 289-301.

Blundy, J.D. and Wood, B.J. (1991). Crystal-chemical controls on the partitioning of Sr and Ba between plagioclase feldspar, silicate melts, and hydrothermal solutions. Geochimica et Cosmochimica Acta, 55(1), 193-209.

Branney, M. J. and Kokelaar, B. P. (2002). Pyroclastic density currents and the sedimentation of ignimbrites. Geological Society of London. Brown, R.J., Branney, M.J., Maher, C. and Dávila-Harris, P. (2010). Origin of accretionary lapilli within ground-hugging density currents: evidence from pyroclastic couplets on Tenerife. Bulletin, 122(1-2), 305-320.

Brown, R.J., Branney, M.J., Maher, C. and Dávila-Harris, P. (2010). Origin of accretionary lapilli within ground-hugging density currents: evidence from pyroclastic couplets on Tenerife. Bulletin, 122(1-2), 305-320.

Brown, S.J.A., Wilson, C.J.N., Cole, J.W. and Wooden, J. (1998). The Whakamaru group ignimbrites, Taupo Volcanic Zone, New Zealand: evidence for reverse tapping of a zoned silicic magmatic system. Journal of Volcanology and Geothermal Research, 84(1-2), 1-37.

Burgisser, A., Poussineau, S., Arbaret, L., Druitt, T.H., Giachetti, T. and Bourdier, J.L. (2010). Pre-explosive conduit conditions of the 1997 Vulcanian explosions at Soufrière Hills Volcano, Montserrat: I. Pressure and vesicularity distributions. Journal of Volcanology and Geothermal Research, 194(1-3), 27-41.

Cadoux, A., Scaillet, B., Druitt, T.H. and Deloule, E. (2014). Magma storage conditions of large Plinian eruptions of Santorini Volcano (Greece). Journal of Petrology, 55(6), 1129-1171.

Camejo-Harry, M., Melekhova, E., Blundy, J., Attridge, W., Robertson, R. and Christopher, T. (2018). Magma evolution beneath Bequia, Lesser Antilles, deduced from petrology of lavas and plutonic xenoliths. Contributions to Mineralogy and Petrology, 173(10), 1-26.

Camus, G., Gourgaud, A. and Vincent, P. M. (1987). Petrologic evolution of Krakatau (Indonesia): implications for a future activity. Journal of Volcanology and Geothermal Research, 33(4), 299-316.

Cashman, K. V. and Giordano, G. (2014). Calderas and magma reservoirs. Journal of Volcanology and Geothermal Research, 288, 28-45.

Carey, S., Sigurdsson, H., Mandeville, C. and Bronto, S. (1996). Pyroclastic flows and surges over water: an example from the 1883 Krakatau eruption. Bulletin of Volcanology, 57(7), 493-511.

Cashman, K.V., Sparks, R.S.J. and Blundy, J.D. (2017). Vertically extensive and unstable magmatic systems: a unified view of igneous processes. Science, 355(6331)

Cassidy, M., Castro, J.M., Helo, C., Troll, V.R., Deegan, F.M., Muir, D., Neave, D.A. and Mueller, S.P. (2016). Volatile dilution during magma injections and implications for volcano explosivity. Geology, 44(12), 1027-1030.

Cassidy, M., Ebmeier, S.K., Helo, C., Watt, S.F.L., Caudron, C., Odell, A., Spaans, K., Kristianto, P., Triastuty, H., Gunawan, H. and Castro, J.M. (2019). Explosive eruptions with little warning: Experimental petrology and volcano monitoring observations from the 2014 eruption of Kelud, Indonesia. Geochemistry, Geophysics, Geosystems, 20(8), 4218-4247.

Cassidy, M., Edmonds, M., Watt, S.F.L., Palmer, M.R. and Gernon, T.M. (2015). Origin of basalts by hybridization in andesite-dominated arcs. Journal of Petrology, 56(2), 325-346.

Cassidy, M., Manga, M., Cashman, K. and Bachmann, O. (2018). Controls on explosive-effusive volcanic eruption styles. Nature communications, 9(1), 1-16.

Ceylon Observer (1883). The Volcanic Eruption in the Sunda Straits. 6 Sep.

Charlier, B.L., Peate, D.W., Wilson, C.J., Lowenstern, J.B., Storey, M. and Brown, S.J. (2003). Crystallisation ages in coeval silicic magma bodies: 238U–230Th disequilibrium evidence from the Rotoiti and Earthquake Flat eruption deposits, Taupo Volcanic Zone, New Zealand. Earth and Planetary Science Letters, 206(3-4), 441-457.

Cheng, L., Costa, F. and Carniel, R. (2017). Unraveling the presence of multiple plagioclase populations and identification of representative two-dimensional sections using a statistical and numerical approach. American Mineralogist, 102, 1894–1905

Christopher, T.E., Blundy, J., Cashman, K., Cole, P., Edmonds, M., Smith, P.J., Sparks, R.S.J., and Stinton, A. (2015). Crustal-scale degassing due to magma system destabilization and magma-gas decoupling at Soufrière Hills Volcano, Montserrat." Geochemistry, Geophysics, Geosystems, 16(9), 2797-2811.

Choi, B.H., Pelinovsky, E., Kim, K.O. and Lee, J.S. (2003). Simulation of the trans-oceanic tsunami propagation due to the 1883 Krakatau volcanic eruption. Natural Hazards and Earth System Sciences, 3, 321–332.

Cioni, R., Gurioli, L., Sbrana, A. and Vougioukalakis, G. (2000). Precursory phenomena and destructive events related to the Late Bronze Age Minoan (Thera, Greece) and AD 79 (Vesuvius, Italy) Plinian eruptions; inferences from the stratigraphy in the archaeological areas. Geological Society, London, Special Publications, 171(1), 123-141.

Cole, J.W., Milner, D.M. and Spinks, K.D. (2005). Calderas and caldera structures: a review. Earth-Science Reviews, 69(1-2), 1-26.

Coombs, M.L., Eichelberger, J.C. and Rutherford, M.J. (2000). Magma storage and mixing conditions for the 1953–1974 eruptions of Southwest Trident volcano, Katmai National Park, Alaska. Contributions to Mineralogy and Petrology, 140(1), 99-118.

Cooper, G.F., Blundy, J.D., Macpherson, C.G., Humphreys, M.C. and Davidson, J.P. (2019). Evidence from plutonic xenoliths for magma differentiation, mixing and storage in a volatile-rich

crystal mush beneath St. Eustatius, Lesser Antilles. Contributions to Mineralogy and Petrology, 174(5), 39.

Cooper, G.F., Davidson, J.P. and Blundy, J.D. (2016). Plutonic xenoliths from Martinique, Lesser Antilles: evidence for open system processes and reactive melt flow in island arc crust. Contributions to Mineralogy and Petrology, 171(10), 1-21.

Cooper, K.M. and Kent, A.J. (2014). Rapid remobilization of magmatic crystals kept in cold storage. Nature, 506(7489), 480-483.

Costa, F., Scaillet, B. and Pichavant, M. (2004). Petrological and experimental constraints on the pre-eruption conditions of Holocene dacite from Volcán San Pedro (36 S, Chilean Andes) and the importance of sulphur in silicic subduction-related magmas. Journal of Petrology, 45(4), 855-881.

Costa, F., Shea, T. and Ubide, T. (2020). Diffusion chronometry and the timescales of magmatic processes. Nature Reviews Earth & Environment, 1(4), 201-214.

Cottrell, E., Gardner, J.E. and Rutherford, M.J. (1999). Petrologic and experimental evidence for the movement and heating of the pre-eruptive Minoan rhyodacite (Santorini, Greece). Contributions to Mineralogy and Petrology, 135(4), 315-331.

Dahren, B., Troll, V. R., Andersson, U. B., Chadwick, J. P., Gardner, M. F., Jaxybulatov, K. and Koulakov, I. (2012). Magma plumbing beneath Anak Krakatau volcano, Indonesia: evidence for multiple magma storage regions. Contributions to Mineralogy and Petrology, 163(4), 631-651.

De Hoog, J. C. M., Taylor, B. E. and Van Bergen, M. J. (2001). Sulfer isotope systematics of basaltic lavas from Indonesia: Implications for the sulfer cycle in subduction zones. Earth and Planetary Science Letters, 189, 237-252.

De Hoog, J. C. M., Taylor B. E. and Van Bergen, M. J. (2009). Hydrogen-isotope systematics in degassing basaltic magma and application to Indonesian arc basalts. Chemical Geology, 266, 256-266.

Deplus, C., Bonvalot, S., Dahrin, D., Diament, M., Harjono, H. and Dubois, J. (1995). Inner structure of the Krakatau volcanic complex (Indonesia) from gravity and bathymetry data. Journal of Volcanology and Geothermal Research, 64(1-2), 23-52.

Di Genova, D., Kolzenburg, S., Wiesmaier, S., Dallanave, E., Neuville, D.R., Hess, K.U. and Dingwell, D.B. (2017). A compositional tipping point governing the mobilization and eruption style of rhyolitic magma. Nature, 552(7684), 235-238.

Dohmen, R. and Blundy, J. (2014). A predictive thermodynamic model for element partitioning between plagioclase and melt as a function of pressure, temperature and composition. American Journal of Science, 314(9), 1319-1372.

Drake, M.J. and Weill, D.F. (1975). Partition of Sr, Ba, Ca, Y, Eu2+, Eu3+, and other REE between plagioclase feldspar and magmatic liquid: an experimental study. Geochimica et Cosmochimica Acta, 39(5), 689-712.

Druitt, T. H., Costa, F., Deloule, E., Dungan, M. and Scaillet, B. (2012). Decadal to monthly timescales of magma transfer and reservoir growth at a caldera volcano. Nature, 482(7383), 77-80.

Druitt, T. H. and Francaviglia, V. (1992). Caldera formation on Santorini and the physiography of the islands in the late Bronze Age. Bulletin of Volcanology, 54(6), 484-493.

Druitt, T.H., Mercier, M., Florentin, L., Deloule, E., Cluzel, N., Flaherty, T., Médard, E. and Cadoux, A. (2016). Magma storage and extraction associated with plinian and interplinian activity at Santorini Caldera (Greece). Journal of Petrology, 57(3), 461-494.

Druitt, T. H. and Sparks, R. S. J. (1982). A proximal ignimbrite breccia facies on Santorini, Greece. Journal of Volcanology and Geothermal Research, 13(1-2), 147-171.

Druitt, T.H., Pyle, D.M. and Mather, T.A. (2019). Santorini volcano and its plumbing system. Elements 15, 177-184.

Dutton, E.G. and Christy, J.R. (1992). Solar radiative forcing at selected locations and evidence for global lower tropospheric cooling following the eruptions of El Chichón and Pinatubo. Geophysical research letters, 19(23), 2313-2316.

EM-DAT: The Emergency Events Database, event 2018-0458-IDN - Université catholique de Louvain (UCL) - CRED, D. Guha-Sapir - www.emdat.be, Brussels, Belgium.

Edmonds, M. (2008). New geochemical insights into volcanic degassing. Philosophical Transactions of the Royal Society A: Mathematical, Physical and Engineering Sciences, 366(1885), 4559-4579.

Ellis, B.S., Barry, T., Branney, M.J., Wolff, J.A., Bindeman, I., Wilson, R. and Bonnichsen, B., (2010). Petrologic constraints on the development of a large-volume, high temperature, silicic magma system: The Twin Falls eruptive centre, central Snake River Plain. Lithos, 120(3-4), 475-489.

Ellis, B.S. and Wolff, J.A., (2012). Complex storage of rhyolite in the central Snake River Plain. Journal of Volcanology and Geothermal Research, 211, 1-11.

Flinders, A.F., Shelly, D.R., Dawson, P.B., Hill, D.P., Tripoli, B. and Shen, Y. (2018). Seismic evidence for significant melt beneath the Long Valley Caldera, California, USA. Geology, 46(9), 799-802.

Forni, F., Degruyter, W., Bachmann, O., De Astis, G. and Mollo, S. (2018). Long-term magmatic evolution reveals the beginning of a new caldera cycle at Campi Flegrei. Science advances, 4(11).

Francis, P.W. (1985). The origin of the 1883 Krakatau tsunamis. Journal of volcanology and geothermal research, 25(3-4), 349-363.

Francis, P. and Self, S. (1983). The eruption of Krakatau. Scientific American, 249(5), 172-187.

Furneaux (1964). Krakatoa. New Jersey, Prentice Hall.

Gardner, J.E., Llewellin, E.W., Watkins, J.M. and Befus, K.S. (2017). Formation of obsidian pyroclasts by sintering of ash particles in the volcanic conduit. Earth and Planetary Science Letters, 459, 252-263.

Gardner, M.F., Troll, V.R., Gamble, J.A., Gertisser, R., Hart, G.L., Ellam, R.M., Harris, C. and Wolff, J.A. (2012). Crustal differentiation processes at Krakatau volcano, Indonesia. Journal of Petrology, 54(1), pp.149-182.

Geschwind, C. H. and Rutherford, M. J. (1992). Cummingtonite and the evolution of the Mount St. Helens (Washington) magma system: an experimental study. Geology, 20(11), 1011-1014.

Ghiorso, M. S. and Evans, B. W. (2008). Thermodynamics of rhombohedral oxide solid solutions and a revision of the Fe-Ti two-oxide geothermometer and oxygen-barometer. American Journal of Science, 308(9), 957-1039.

Global Volcanism Program, 2018. Report on Krakatau (Indonesia) (Crafford, A.E., and Venzke, E., eds.). Bulletin of the Global Volcanism Network, 43:10. Smithsonian Institution. https://doi.org/10.5479/si.GVP.BGVN201810-262000

Ginibre, C., Wörner, G. and Kronz, A. (2002). Minor-and trace-element zoning in plagioclase: implications for magma chamber processes at Parinacota volcano, northern Chile. Contributions to Mineralogy and Petrology, 143(3), 300-315.

Gorshkov, G. S. (1959). Gigantic eruption of the volcano Bezymianny. Bulletin Volcanologique, *20*(1), 77-109.

Gottsmann, J. and Marti, J. (eds) Caldera Volcanism: Analysis, Modelling and Response (Dev. Volcanol. 10, Elsevier, 2008)

Grainger (1883). Algemeen Dagblad, 23rd May.

Gravley, D.M., Wilson, C.J.N., Leonard, G.S. and Cole, J.W., (2007). Double trouble: Paired ignimbrite eruptions and collateral subsidence in the Taupo Volcanic Zone, New Zealand. Geological Society of America Bulletin, 119(1-2),18-30.

Grilli, S. T., Tappin, D. R., Carey, S., Watt, S. F., Ward, S. N., Grilli, A. R. and Muin, M. (2019). Modelling of the tsunami from the December 22, 2018 lateral collapse of Anak Krakatau volcano in the Sunda Straits, Indonesia. Scientific reports, 9(1), 1-13

Grilli, S.T., Zhang, C., Kirby, J.T., Grilli, A.R., Tappin, D.R., Watt, S.F.L., Hunt, J.E., Novellino, A., Engwell, S., Nurshal, M.E.M., Abdurrachman, M., Cassidy, M., Madden-Nadeau, A.L. and Day, S. (2021). Modeling of the Dec. 22nd 2018 Anak Krakatau volcano lateral collapse and tsunami based on recent field surveys: Comparison with observed tsunami impact. Marine Geology, 106566.

Gualda, G.A., Ghiorso, M.S., Lemons, R.V. and Carley, T.L. (2012). Rhyolite-MELTS: a modified calibration of MELTS optimized for silica-rich, fluid-bearing magmatic systems. Journal of Petrology, 53(5), 875-890.

Haase, K.M., Lima, S., Krumm, S. and Garbe-Schönberg, D. (2014). The magmatic evolution of young island arc crust observed in gabbroic to tonalitic xenoliths from Raoul Island, Kermadec Island Arc. Lithos, 210, 199-208.

Hall, R. (2012). Late Jurassic–Cenozoic reconstructions of the Indonesian region and the Indian Ocean. Tectonophysics, 570, 1-41.

Hall, R. and Spakman, W. (2002). Subducted slabs beneath eastern Indonesia–Tonga region: insights from tomography. Earth and Planetary Science Letters, 201(2), 321-336.

Hammer, J.E. and Rutherford, M.J. (2002). An experimental study of the kinetics of decompression-induced crystallization in silicic melt. Journal of Geophysical Research: Solid Earth, 107(B1), ECV-8.

Harjono, H., Diament, M., Nouaili, L. and Dubois, J. (1989). Detection of magma bodies beneath Krakatau volcano (Indonesia) from anomalous shear waves. Journal of volcanology and geothermal research, 39(4), 335-348.

Heise, W., Caldwell, T.G., Bibby, H.M. and Bennie, S.L. (2010). Three-dimensional electrical resistivity image of magma beneath an active continental rift, Taupo Volcanic Zone, New Zealand. Geophysical Research Letters, 37(10).

Hesse, E.D. (1690). Ost Indiamische Reise-Beschreibung oder Diariu, Leipzig.

Hesse, E.D. (1694). Drie Seer Aanmerkelyke Reysen na en door Verlerley Gewesten in Oost-Indien; gedaan door Christophorus Frikius, Chirugyn, Elias Hesse, Berghschryver, Christophorus Schweitzer, Boekhouder; Yeder Bysonder; van ‘t Jaer 1675 tot 1686. Translated from German to Dutch by Simon de Vries. Utrecht.

Hildreth, W. (1981). Gradients in silicic magma chambers: implications for lithospheric magmatism. Journal of Geophysical Research: Solid Earth, 86, 10153-10192.

Hildreth, W. and Wilson, C. J. (2007). Compositional zoning of the Bishop Tuff. Journal of Petrology, 48(5), 951-999.

Hogg, A.G., Wilson, C.J., Lowe, D.J., Turney, C.S., White, P., Lorrey, A.M., Manning, S.W., Palmer, J.G., Bury, S., Brown, J. and Southon, J. (2019). Wiggle-match radiocarbon dating of the Taupo eruption. Nature communications, 10(1), 1-3.

Housh, T.B. and Luhr, J.F. (1991). Plagioclase-melt equilibria in hydrous systems. American Mineralogist, 76(3-4), 477-492.

Huang, H.H., Lin, F.C., Schmandt, B., Farrell, J., Smith, R.B. and Tsai, V.C. (2015). The Yellowstone magmatic system from the mantle plume to the upper crust. Science, 348(6236), 773-776.

Huber, C., Bachmann, O. and Manga, M. (2009). Homogenization processes in silicic magma chambers by stirring and mushification (latent heat buffering). Earth and Planetary Science Letters, 283(1-4), 38-47

Hunt, J.E., Tappin, D.R., Watt, S.F.L., Susilohadi, S., Novellino, A., Ebmeier, S.K., Cassidy, M., Engwell, S.L., Grilli, S.T., Hanif, M. and Priyanto, W.S. (2021). Submarine landslide megablocks

show half of Anak Krakatau island failed on December 22nd, 2018. Nature communications, 12(1), 1-15.

Javasche Courant (1883). 20th July.

Jaxybulatov, K., Koulakov, I., Ibs-von Seht, M., Klinge, K., Reichert, C., Dahren, B. and Troll, V.R. (2011). Evidence for high fluid/melt content beneath Krakatau volcano (Indonesia) from local earthquake tomography. Journal of Volcanology and Geothermal Research, 206(3-4), 96-105.

Joly, J. (1885) Notes on the microscopical character of the volcanic ash from Krakatoa. Proceedings of the Royal Dublin Society, 4, 291-299.

Judd, J.W. (1889). The earlier eruptions of Krakatau. Nature, 40, 365-366.

Kamata, H., Suzuki-Kamata, K. and Bacon, C.R. (1993). Deformation of the Wineglass Welded Tuff and the timing of caldera collapse at Crater Lake, Oregon. Journal of Volcanology and Geothermal Research, 56(3), pp.253-265.

Knesel, K.M., Davidson, J.P. and Duffield, W.A. (1999). Evolution of silicic magma through assimilation and subsequent recharge: evidence from Sr isotopes in sanidine phenocrysts, Taylor Creek Rhyolite, NM. Journal of Petrology, 40(5), 773-786.

Koleszar, A.M., Kent, A.J., Wallace, P.J. and Scott, W.E. (2012). Controls on long-term low explosivity at andesitic arc volcanoes: Insights from Mount Hood, Oregon. Journal of Volcanology and Geothermal Research, 219, 1-14.

Konig, S., Munker, C., Hohl, S., Paulik, H., Barth, A. R., Lagos, M., Pfander, J. A. and Buchl, A. (2011). The earth's tungsten budget during mantle melting and crust formation. Geochim. Cosmochim. Acta., 75, 2119-2136.

Koulakov, I., Kasatkina, E., Shapiro, N.M., Jaupart, C., Vasilevsky, A., El Khrepy, S., Al-Arifi, N. and Smirnov, S. (2016). The feeder system of the Toba supervolcano from the slab to the shallow reservoir. Nature communications, 7(1), 1-12.

Kudo, A.M. and Weill, D.F. (1970). An igneous plagioclase thermometer. Contributions to Mineralogy and Petrology, 25(1), 52-65.

Larsen, J.F. (2006). Rhyodacite magma storage conditions prior to the 3430 yBP caldera-forming eruption of Aniakchak volcano, Alaska. Contributions to Mineralogy and Petrology, 152(4), 523-540.

LaTourrette, T. and Wasserburg, G.J. (1998). Mg diffusion in anorthite: implications for the formation of early solar system planetesimals. Earth and Planetary Science Letters, 158(3-4), 91-108.

Latter, J.H. (1981). Tsunamis of Volcanic Origin: Summary of Causes, with Particular Reference to Krakatau, 1883. Bulletin Volcanologique, 44:467-490.

Laumonier, M., Gaillard, F., Muir, D., Blundy, J. and Unsworth, M. (2017). Giant magmatic water reservoirs at mid-crustal depth inferred from electrical conductivity and the growth of the continental crust. Earth and Planetary Science Letters, 457, 173-180.

Le Bas, M.J., Le Maitre, R. W., Streckeisen, A., Zanettin, B. and IUGS Subcommission on the Systematics of Igneous Rocks. (1986). A chemical classification of volcanic rocks based on the total alkali-silica diagram. Journal of petrology, 27(3), 745-750.

Lewis, J.F. (1973). Petrology of the ejected plutonic blocks of the Soufriere volcano, St. Vincent, West Indies. Journal of Petrology, 14(1), 81-112.

Lindemann, T.H. (1884). Report from H.B.M Consol at Batavia, inclosing extracts relating to the volcanic outburst in the Sunda Strait, from the logbook of the steamship Governor-General Loudon. Proceedings of the Royal Society of London, 36, 199-203.

Lindsley, D. H. and Frost, B. R. (1992). Equilibria among Fe-Ti oxides, pyroxenes, olivine, and quartz: Part I. Theory. American Mineralogist, 77(9-10), 987-1003.

Lipman, P.W. (1984). The roots of ash flow calderas in western North America: windows into the tops of granitic batholiths. J. Geophysical Research, 89, 8801–8841.

Lipman, P.W. (2000). Calderas. In: Encyclopedia of Volcanoes, 643–662.

Lunt, P., Burgon, G., and Baky, A. (2009). The Pemali Formation of Central Java and equivalents: Indicators of sedimentation on an active plate margin. Journal of Asian Earth Sciences, 34(1), 100-113.

Lyell, C. (1830). Principles of Geology. London.

MacKenzie (1883). Java Bode, 30 May.

Macleod (1884). De Uitbarsting van de Krakatau. Tijdschift van het Koninklijk Nederlandsch Aardrijk-skundig Genootschap, 2, 1: 184-191

[dataset] Madden-Nadeau, A.L. (2020): Geochemical and petrological data pertaining to the eruptive deposits of 1883 caldera-forming eruption of Krakatau. British Geological Survey. (Dataset). https://doi.org/10.5285/ad2a4fa0-7b66-4ec5-a5cf-d78944716ec4.

Madden-Nadeau, A.L., Cassidy, M., Pyle, D., Mather, T.A., Watt, S.F.L., Engwell, S.L., Abdurrachman, M., Nurshal, M.E.M., Tappin, D. & Ismail, T. (2021). The magmatic and eruptive evolution of the 1883 caldera-forming eruption of Krakatau: integrating field- to crystal-scale observations. Journal of Volcanology and Geothermal Research, 411, 107176.

Maeno, F. and Imamura, FTsunami generation by a rapid entrance of pyroclastic flow into the sea during the 1883 Krakatau eruption, Indonesia. Journal of Geophysical Research: Solid Earth, 116(B9).

de Maisonneuve, C.B., Forni, F. and Bachmann, O. (2021). Magma reservoir evolution during the build up to and recovery from caldera-forming eruptions–A generalizable model? Earth-Science Reviews, 103684.

Mandeville, C.W., Carey, S. and Sigurdsson, H. (1996a). Magma mixing, fractional crystallization and volatile degassing during the 1883 eruption of Krakatau volcano, Indonesia. Journal of Volcanology and Geothermal Research, 74(3-4), 243-274.

Mandeville, C. W., Carey, S. and Sigurdsson, H. (1996b). Sedimentology of the Krakatau 1883 submarine pyroclastic deposits. Bulletin of Volcanology, 57(7), 512-529.

Marsh, B.D. (1981). On the crystallinity, probability of occurrence, and rheology of lava and magma. Contributions to Mineralogy and Petrology, 78(1), 85-98.

Martel, C., Pichavant, M., Holtz, F., Scaillet, B., Bourdier, J.L. and Traineau, H. (1999). Effects of f_{O2} and H_2O on andesite phase relations between 2 and 4 kbar. Journal of Geophysical Research: Solid Earth, 104(B12), 29453-29470.

Marti, A., Folch, A., Costa, A. and Engwell, S. (2016). Reconstructing the plinian and co-ignimbrite sources of large volcanic eruptions: A novel approach for the Campanian Ignimbrite. Scientific reports, 6, 1-11.

McGuire, W.J. 2003. Volcano instability and lateral collapse. Revista, 1, 33-45.

Metrich, N. and Rutherford, M.J. (1992). Experimental study of chlorine behaviour in hydrous silicic melts. Geochimica et Cosmochimica Acta, 56(2), 607-616.

Metzger, E. (1884). Gleanings from Reports Concerning the Eruption of Krakatoa. Nature, 29:240-244.

Miller, C.F. and Wark, D.A. (2008). Supervolcanoes and their explosive supereruptions. Elements, 4(1), 11-15.

Mollo, S., Putirka, K., Iezzi, G., Del Gaudio, P. and Scarlato, P. (2011). Plagioclase–melt (dis) equilibrium due to cooling dynamics: implications for thermometry, barometry and hygrometry. Lithos, 125(1-2), 221-235.

Nelson, S.T. and Montana, A. (1992). Sieve-textured plagioclase in volcanic rocks produced by rapid decompression. American Mineralogist, 77(11-12), 1242-1249.

Newhall, C.G. and Dzurisin, D. (1988) Historical Unrest at Large Calderas of the World Vols 1 and 2, Bull. US Geol. Surv. 1855, USGS.

Newhall, C.G. and Pallister, J.S. (2015). Using multiple data sets to populate probabilistic volcanic event trees. In: Volcanic Hazards, risks and disasters, Elsevier, 203-232.

Newhall, C.G. and Self, S. (1982) The volcanic explosivity index (VEI) an estimate of explosive magnitude for historical volcanism. Journal of Geophysical Research: Oceans, 87, 1231-1238.

Newhall, C.G., Self, S. and Robock, A. (2018). Anticipating future Volcanic Explosivity Index (VEI) 7 eruptions and their chilling impacts. Geosphere, 14(2), 572-603.

Newman, S. and Lowenstern, J.B. (2002). VolatileCalc: a silicate melt–H_2O–CO_2 solution model written in Visual Basic for excel. Computers and Geosciences, 28, 597-604.

Nielsen, R.L., Ustunisik, G., Weinsteiger, A.B., Tepley III, F.J., Johnston, A.D. and Kent, A.J. (2017). Trace element partitioning between plagioclase and melt: An investigation of the impact of experimental and analytical procedures. Geochemistry, Geophysics, Geosystems, 18(9), 3359-3384.

Ninkovich, D. (1976). Late Cenozoic clockwise rotation of Sumatra. Earth and Planetary Science Letters, 29(2), 269-275.

Ninkovich, D. (1979). Distribution, age and chemical composition of tephra layers in deep-sea sediments off western Indonesia. Journal of Volcanology and Geothermal Research, 5(1-2), 67-86.

Nishimura, S., Harjono, H. and Suparka, S. (1992). The Krakatau Islands: the geotectonic setting. GeoJournal, 28(2), 87-98.

Nomanbhoy, N. and Satake, K. (1995). Generation mechanism of tsunamis from the 1883 Krakatau eruption. Geophysical Research Letters, 22(4), 509-512.

Nomikou, P., Hübscher, C., Mather, T.A., Paulatto, M., Kalnins, L.M., Kelfoun, K., Papanikolaou, D., Bejelou, K., Lampridou, D., Pyle, D.M., Carey, S., Watts, A.B., Weiß, B. and Parks, M.M. (2016). Post-eruptive flooding of Santorini caldera and implications for tsunami generation. Nature communications, 7(1), 1-10.

Novellino, A., Engwell, S.L., Grebby, S., Day, S., Cassidy, M., Madden-Nadeau, A.L., Watt, S., Pyle, D., Abdurrachman, M., Edo Marshal Nurshal, M. and Tappin, D.R. (2020). Mapping recent shoreline changes spanning the lateral collapse of Anak Krakatau Volcano, Indonesia. Applied Sciences, 10(2), 536.

Oba, N., Tomita, K., Yamamoto, M., Istidjab, M. and Badruddin, M. (1982). Geochemical study of lava flows, ejecta and pyroclastic flow from the Krakatau Group, Indonesia. Kagoshima Daigaku Rigakubu kiyō. Chigaku seibutsugaku, 15, 41-76.

Papale, P. (2018). Global time-size distribution of volcanic eruptions on Earth. Scientific reports, 8(1), 1-11.

Papale, P. and Marzocchi, W. (2019). Volcanic threats to global society. Science, 363(6433), 1275-1276.

Pearce, N.J., Westgate, J.A., Gualda, G.A., Gatti, E. and Muhammad, R.F. (2020). Tephra glass chemistry provides storage and discharge details of five magma reservoirs which fed the 75 ka Youngest Toba Tuff eruption, northern Sumatra. Journal of Quaternary Science, 35(1-2), 256-271.

Pichavant, M., Costa, F., Burgisser, A., Scaillet, B., Martel, C. and Poussineau, S. (2007). Equilibration scales in silicic to intermediate magmas—implications for experimental studies. Journal of Petrology, 48(10), 1955-1972.

Powell, R. and Powell, M. (1977). Geothermometry and oxygen barometry using coexisting iron-titanium oxides: a reappraisal. Mineralogical Magazine, 41(318), 257-263.

Prata, A.T., Folch, A., Prata, A.J., Biondi, R., Brenot, H., Cimarelli, C., Corradini, S., Lapierre, J. and Costa, A. (2020). Anak Krakatau triggers volcanic freezer in the upper troposphere. Scientific reports, 10, 1-13.

Probst, L.C., Sheldrake, T.E., Gander, M.J., Wallace, G., Simpson, G. and Caricchi, L. (2018). A cross correlation method for chemical profiles in minerals, with an application to zircons of the Kilgore Tuff (USA*).* Contributions to Mineralogy and Petrology, 173(3), 23.

Putirka, K.D. (2008). Thermometers and barometers for volcanic systems. Reviews in mineralogy and geochemistry, 69(1), 61-120.

Putirka, K.D., Mikaelian, H., Ryerson, F. and Shaw, H. (2003). New clinopyroxene-liquid thermobarometers for mafic, evolved, and volatile-bearing lava compositions, with applications to lavas from Tibet and the Snake River Plain, Idaho. American Mineralogist, 88(10), 1542-1554.

Pyle, D.M. and Barclay, J. (2020). Historical records of volcanic eruptions deserve more attention. Nature Reviews Earth and Environment 1, 183–184.

Reid, M.E. (2004). Massive collapse of volcano edifices triggered by hydrothermal pressurization. Geology, 32(5), 373-376.

Rossi, S., Petrelli, M., Morgavi, D., Vetere, F.P., Almeev, R.R., Astbury, R.L. and Perugini, D. (2019). Role of magma mixing in the pre-eruptive dynamics of the Aeolian Islands volcanoes (Southern Tyrrhenian Sea, Italy). Lithos, 324, 165-179.

Rougier, J., Sparks, R.S.J., Cashman, K.V. and Brown, S.K. (2018). The global magnitude–frequency relationship for large explosive volcanic eruptions. Earth and Planetary Science Letters, 482, 621-629.

Ruprecht, P. and Bachmann, O. (2010). Pre-eruptive reheating during magma mixing at Quizapu volcano and the implications for the explosiveness of silicic arc volcanoes. Geology, 38(10), 919-922.

Ruprecht, P., Bergantz, G.W., Cooper, K.M. and Hildreth, W. (2012). The crustal magma storage system of Volcán Quizapu, Chile, and the effects of magma mixing on magma diversity. Journal of Petrology, 53(4), 801-840.

Rust, A.C., Cashman, K.V. and Wallace, P.J. (2004). Magma degassing buffered by vapor flow through brecciated conduit margins. Geology, 32, 349–352.

Rutherford, M. J. and Devine, J. D. (1988). The May 18, 1980, eruption of Mount St. Helens: 3. Stability and chemistry of amphibole in the magma chamber. Journal of Geophysical Research: Solid Earth, *93*(B10), 11949-11959.

Saccorotti, G., Iguchi, M. and Aiuppa, A. (2015). In situ Volcano Monitoring: present and future. In: Volcanic Hazards, Risks, and Disasters, Elsevier, 169–202.

Scaillet, B. and Evans, B.W. (1999). The 15 June 1991 eruption of Mount Pinatubo. I. Phase equilibria and pre-eruption P–T–fO_2–fH_2O conditions of the dacite magma. Journal of Petrology, 40(3), 381-411.

Schlüter, H.U., Gaedicke, C., Roeser, H.A., Schreckenberger, B., Meyer, H., Reichert, C., Djajadihardja, Y. and Prexl, A. (2002). Tectonic features of the southern Sumatra-western Java forearc of Indonesia. Tectonics, 21(5), pp.11-1.

Schwandt, C.S., Cygan, R.T. and Westrich, H.R. (1998). Magnesium self-diffusion in orthoenstatite. Contributions to Mineralogy and Petrology, 130(3-4), 390-396.

Self, S. (1992). Krakatau revisited: the course of events and interpretation of the 1883 eruption. GeoJournal, 28(2), 109-121.

Self, S. (2006). The effects and consequences of very large explosive volcanic eruptions. Philosophical Transactions of the Royal Society A: Mathematical, Physical and Engineering Sciences, 364(1845), 2073-2097.

Self, S. and Rampino, M. R. (1981). The 1883 eruption of Krakatau. Nature, 294(5843), 699-704.

Self, S. and Wohletz, K. H. (1983). A new look at initiation and timing of the Krakatau 1883 eruption sequence. Eos, 64, 872.

Shields, J. K., Mader, H. M., Caricchi, L., Tuffen, H., Mueller, S., Pistone, M. and Baumgartner, L. (2016). Unravelling textural heterogeneity in obsidian: Shear-induced outgassing in the Rocche Rosse flow. Journal of Volcanology and Geothermal Research, 310, 137-158.

Sides, I.R., Edmonds, M., Maclennan, J., Swanson, D.A. and Houghton, B.F. (2014). Eruption style at Kīlauea Volcano in Hawai ‘i linked to primary melt composition. Nature Geoscience, 7(6), 464-469.

Sigurdsson, H., Cashdollar, S. and Sparks, S.R.J. (1982). The eruption of Vesuvius in A.D. 79 A.D.: reconstruction from historical and volcanological evidence. American Journal of Archaeology 86, 39-51.

de Silva, S.L. and Gosnold, W.D. (2007). Episodic construction of batholiths: Insights from the spatiotemporal development of an ignimbrite flare-up. Journal of Volcanology and Geothermal Research, 167, 320-335.

Simkin, T. and Fiske, R.S. (1983) Krakatau 1883: the volcanic eruption and its effects. Smithsonian Institution Press, Washington D.C., 464.

Smith, R.L. and Bailey, R.A. (1968). Resurgent cauldrons. Memoir of the Geological Society of America, 116, 613-662.

Sparks, R.S.J., Rymer, H., Self, S., Grattan, J., Oppenheimer, C. and Pyle, D. (2005). Super-eruptions: global effects and future threats. Geological Society of London.

Sparks, R.S.J., Sigurdsson, H. and Wilson, L. (1977). Magma mixing: a mechanism for triggering acid explosive eruptions. Nature, 267(5609), 315-318.

Sparks, R.S.J. and Wilson, C. J. N. (1990). The Minoan deposits: a review of their characteristics and interpretation. Thera and the Aegean world III, *2*, 89-99.

Stehn, C. E. (1929). The geology and volcanism of the Krakatau group. Fourth Pacific Science Congress, 1-54.

Sturdy, E.W. (1884). The volcanic eruption of Krakatau. Atlantic Monthly, 54, 385-391.

Sulzer (1883). Java Bode, 30th May.

Susilohadi, S., Gaedicke, C. and Djajadihardja, Y. (2009). Structures and sedimentary deposition in the Sunda Strait, Indonesia. Tectonophysics, *467*(1-4), 55-71.

Symons, G.J., Judd, J.W., Strachey, S.R., Wharton, W.J.L., Evans, F.J., Russell, F.A.R., Archibald, D. and Whipple, G.M. (1888). The eruption of Krakatoa and subsequent phenomena. Trübner & Company.

Szramek, L., Gardner, J.E. and Larsen, J. (2006). Degassing and microlite crystallisation of basaltic andesite magma erupting at Arenal Volcano, Costa Rica. Journal of Volcanology and Geothermal Research, 157, 182-201.

Tagliche Rundchau (1883). Berlin, 255-256.

Tarasewicz, J., White, R.S., Woods, A.W., Brandsdóttir, B. and Gudmundsson, M.T. (2012). Magma mobilization by downward-propagating decompression of the Eyjafjallajökull volcanic plumbing system. Geophysical Research Letters, 39(19).

Tennison-Woods, J.E. (1884). The Earthquake in the Straits of Sunda. Sydney Morning Herald, 16-18 Jan.

Times of London (1883). 3 July:10, column f, and 8 October.

Tollan, P.M.E., Bindeman, I. and Blundy, J.D. (2012). Cumulate xenoliths from St. Vincent, Lesser Antilles Island Arc: a window into upper crustal differentiation of mantle-derived basalts. Contributions to Mineralogy and Petrology, 163(2), 189-208.

Tramontano, S., Gualda, G.A. and Ghiorso, M.S. (2017). Internal triggering of volcanic eruptions: Tracking overpressure regimes for giant magma bodies. Earth and Planetary Science Letters, 472, 142-151.

Turner, S. P., Black, S. and Berlo, K. (2004). 210Pb – 226Ra and 228Ra – 232Th systematics in young arc lavas: Implications for magma degassing and ascent rates. Earth and Planetary Science Letters, 227, 1-16.

Turner, S. and Foden, J. (2001). U, Th and Ra disequilibria, Sr, Nd and Pb isotope and trace element variations in Sunda arc lavas: predominance of a subducted sediment component. Contributions to Mineralogy and Petrology, 142(1), 43-57.

United Nations Office for Disaster and Risk Reduction. (2015). Making Development Sustainable: The Future of Disaster Risk Management. Global Assessment Report on Disaster Risk Reduction (United Nations Office for Disaster Risk Reduction, Geneva, Switzerland, 2015).

Van den Berg, N.P. (1884). Vroegere Berichten Omtrent Krakatau. De uitbarsting van 1680. Tijdschrift voor Indische Taal-, Land-, en Volkenkunde, Batavia, 29, 208-228.

Van Heerdt, P.T. (1884?) Report of Captain Visman of the Prinses Wilhelmina. Letter to Symons, G.J. at the Royal Society, London.

Verbeek, R.D.M. (1884). The Krakatoa Eruption 1. Nature, 30,10–15.

Verbeek, R.D.M. (1885). Krakatau. Govt Press, Batavia, 1-495.

Viccaro, M., Giacomoni, P.P., Ferlito, C. and Cristofolini, R. (2010). Dynamics of magma supply at Mt. Etna volcano (Southern Italy) as revealed by textural and compositional features of plagioclase phenocrysts. Lithos, 116(1-2), 77-91.

Vogel, J.W. (1690). Journal einer Reise aus Holland nach Ost-In-dien. Frankfurt and Leipzig.

Wadsworth, F.B., Llewellin, E.W., Vasseur, J., Gardner, J.E. and Tuffen, H. (2020). Explosive-effusive volcanic eruption transitions caused by sintering. Science Advances, 6(39), 7940.

Wadsworth, F.B., Vasseur, J., Casas, A.S., Delmelle, P., Hess, K-U., Aryis, P.M. and Dingwell, D.B. (2021). A model for the kinetics of high temperature reactions between polydisperse volcanic ash and SO_2 gas. American Mineralogist, in press.

Walker (1884). Extracts from log of The Actea (May 20, 1883). Nature, 30.

Walter, T.R., Haghighi, M.H., Schneider, F.M., Coppola, D., Motagh, M., Saul, J., Babeyko, A., Dahm, T., Troll, V.R., Tilmann, F. and Heimann, S. 2019. Complex hazard cascade culminating in the Anak Krakatau sector collapse. Nature communications, 10(1), 1-11.

Waters, L.E. and Lange, R.A. (2015). An updated calibration of the plagioclase-liquid hygrometer-thermometer applicable to basalts through rhyolites. American Mineralogist, 100(10), 2172-2184.

Watt, S.F.L. (2019). The evolution of volcanic systems following sector collapse. Journal of Volcanology and Geothermal Research, 384, 280-303.

Williams, R., Branney, M. J. and Barry, T. L. (2014). Temporal and spatial evolution of a waxing then waning catastrophic density current revealed by chemical mapping. Geology, 42(2), 107-110.

Wilson, C.J.N. (2017). Volcanoes: characteristics, tipping points and those pesky unknown unknowns. Elements 13, 41–46.

Wilson, C.J.N., Cooper, G.F., Chamberlain, K.J., Barker, S.J., Myers, M.L., Illsley-Kemp, F. and Farrell, J. (2021). No single model for supersized eruptions and their magma bodies. Nature Reviews Earth & Environment, *in press.*

Wilson, C.J.N. and Walker, G.P.L. (1985). The Taupo eruption, New Zealand I. General aspects. Philosophical Transactions of the Royal Society of London. Series A, Mathematical and Physical Sciences, 314(1529), 199-228.

Wood, B.J. and Banno, S. (1973). Garnet-orthopyroxene and orthopyroxene-clinopyroxene relationships in simple and complex systems. Contributions to Mineralogy and Petrology, 42(2), 109-124.

Woodhead, J. D., Hergt, J. M., Davidson, J. P. and Eggins S. M. (2001). Hafnium isotope evidence for conservative element mobility during subduction zone processes. Earth and Planetary Science Letters, 192, 331-346.

Zen, M. T. and Hadikusumo, D. (1964). Recent changes in the Anak-Krakatau Volcano. Bulletin of Volcanology, 27, 259-268.

Zhiyan, L., Bower, V.L., He, L., Sensabaugh, D.A., Penbo, D., Jixian, L., Kuishan, Q., Barnes L.E., Yoh, K. and Sargent, W.R. (2010) Chinese Ceramics, From the paleolithic period through the Qing dynasty. Yale University Press, New Haven & London; Foreign Language Press, Beijing.

Ziberna, L., Green, E.C. and Blundy, J.D. (2017). Multiple-reaction geobarometry for olivine-bearing igneous rocks. American Mineralogist: Journal of Earth and Planetary Materials, 102(12), 2349-2366.

Data availability

Datasets related to this thesis that are not included in the main body of the thesis or the appendices or supplementary files can be found at https://www.bgs.ac.uk/services/ngdc/accessions/index.html#item137445, hosted at National Geological Data Centre by the British Geological Survey (Madden-Nadeau, 2020).

Appendix 1

(a) Chapter 2 Supplementary Figures

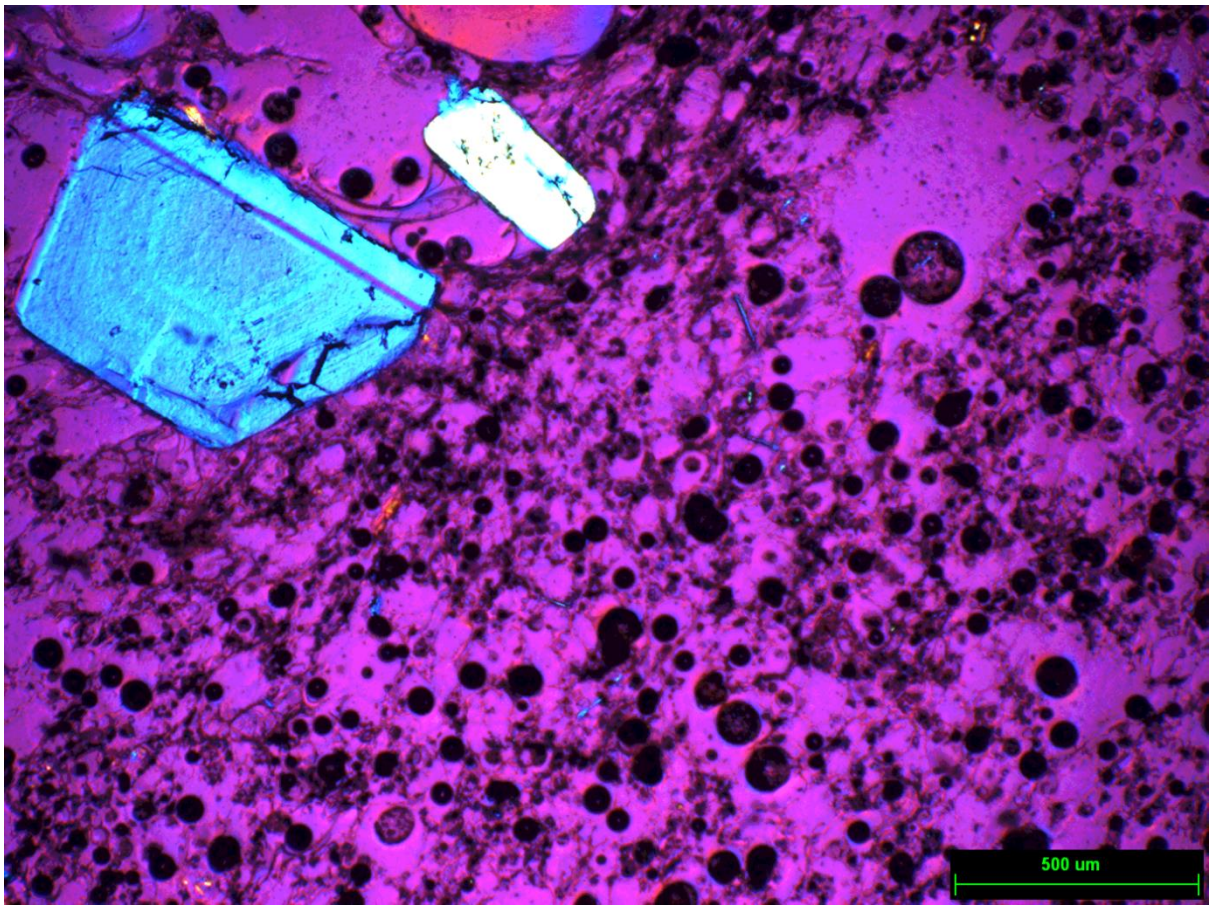

Supplementary Figure A: Example of a pictomicrograph image taken of a pumice thin section collected at D2S2 on South Sertung in 2017. This image was taken under crossed polars with the gypsum plate in, and crystals were subsequently drawn around by hand to estimate crystallinity. In supplementary material of Madden-Nadeau et al. (2021).

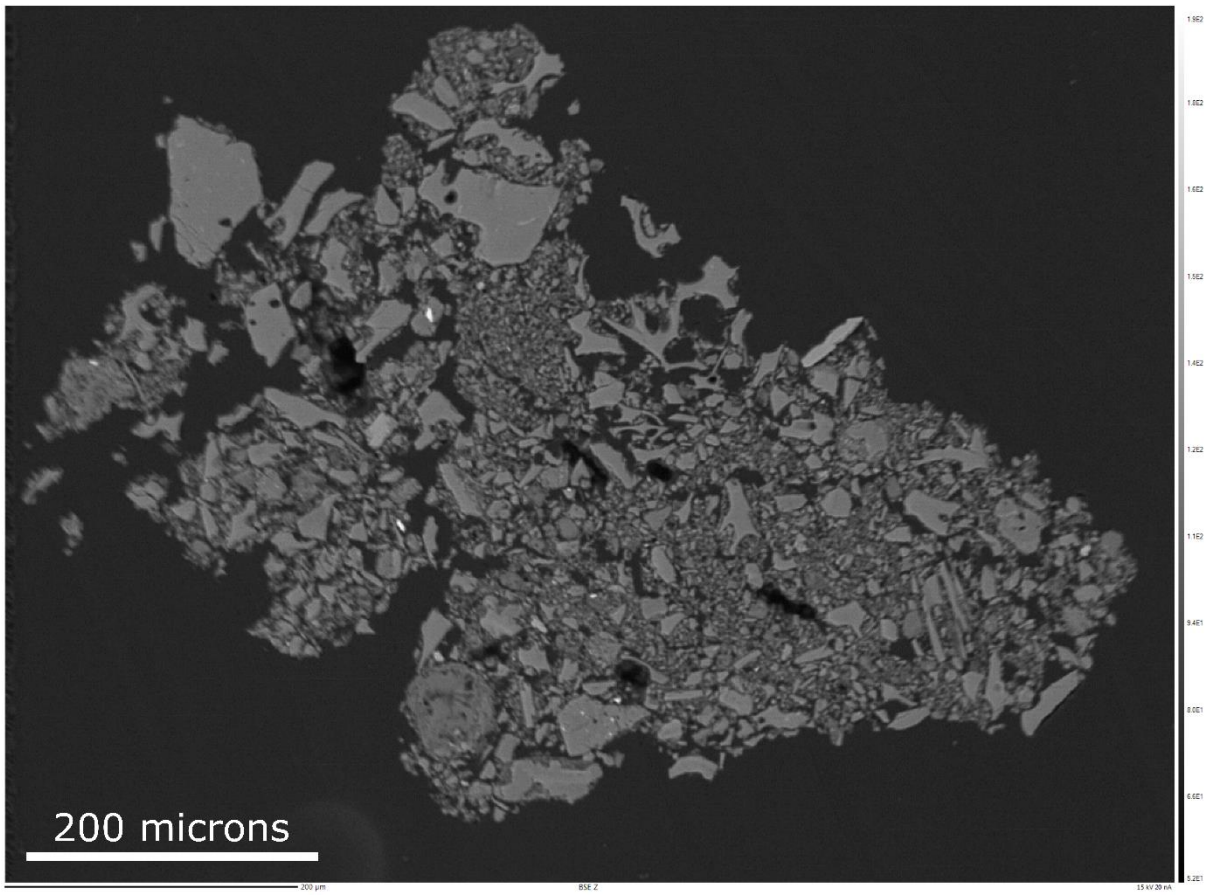

Supplementary Figure B: A backscatter electron image of an ash aggregate clast found in sample U22.2 (Rakata; Unit A). In supplementary material of Madden-Nadeau et al. (2021).

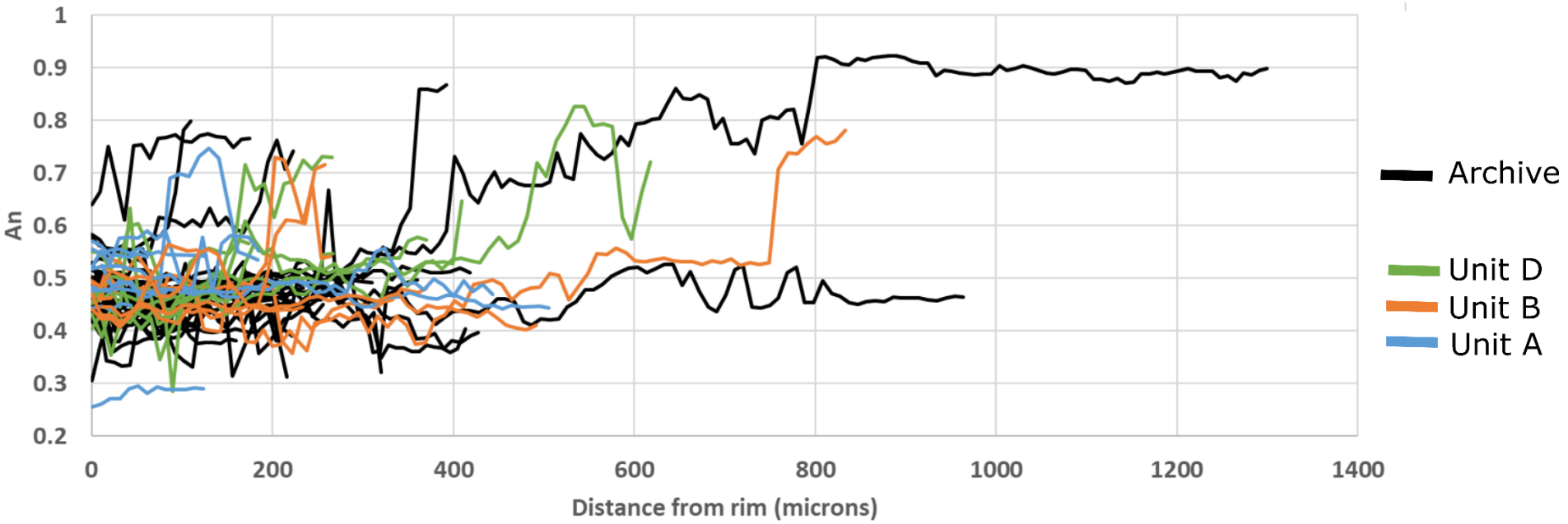

Supplementary Figure C: Complete anorthite transects (n = 51) across euhedral plagioclase phenocrysts, taken rim to core, for archive samples (black) and Unit A (blue), B (orange) and D (green). In supplementary material of Madden-Nadeau et al. (2021).

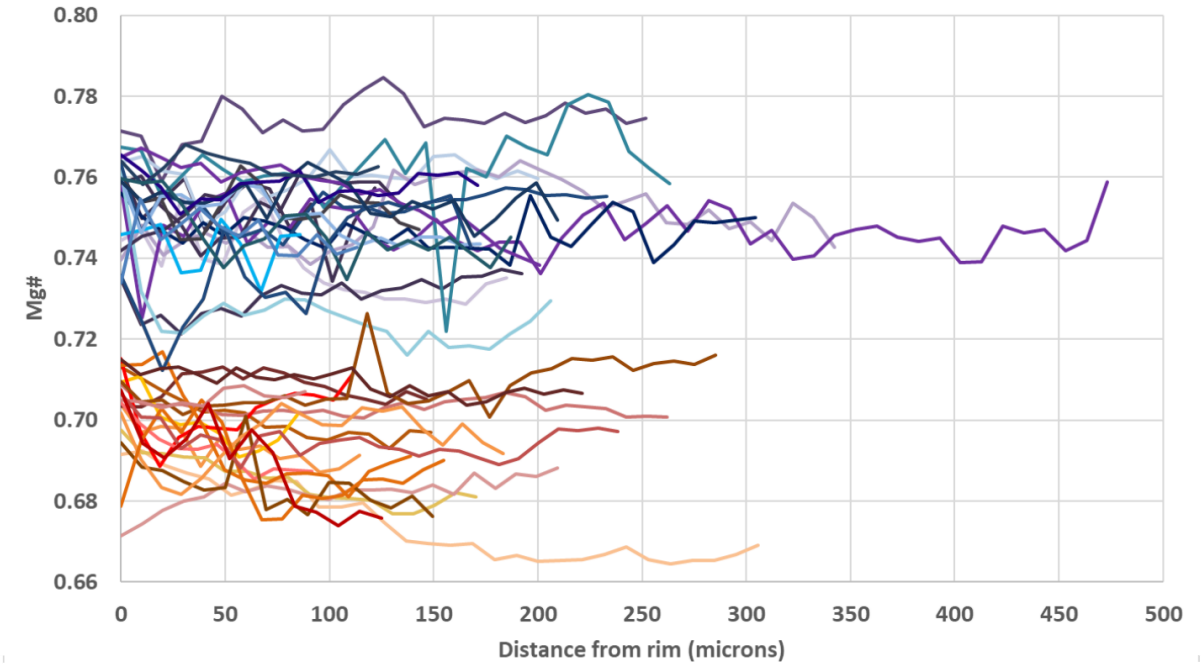

Supplementary Figure D: Complete Mg# traverses for pyroxene phenocrysts (n = 41). Orthopyroxene traverses are in blue, and clinopyroxene traverses in red. In supplementary material of Madden-Nadeau et al. (2021).

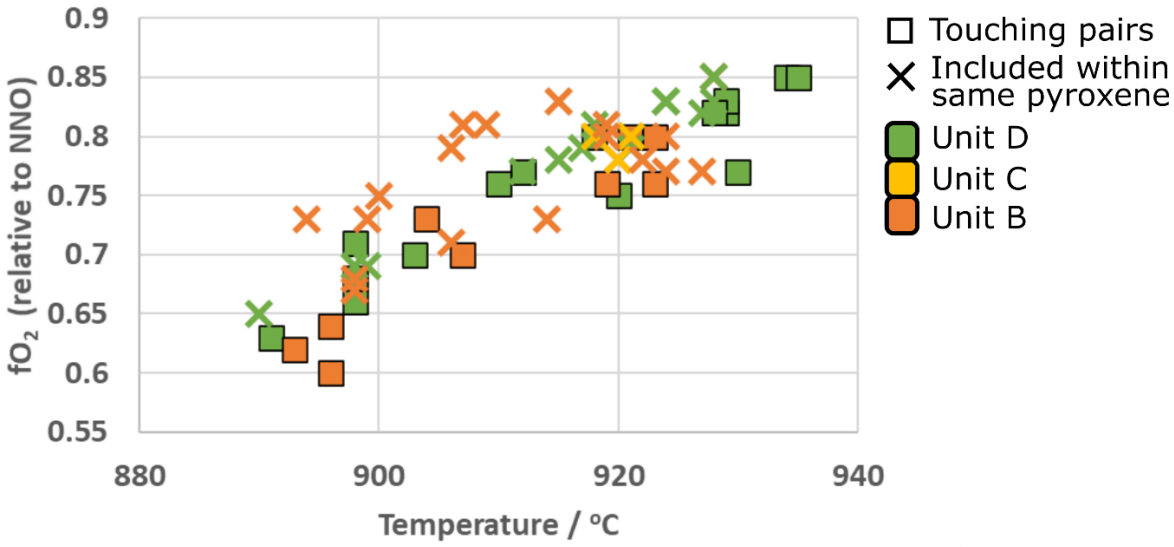

Supplementary Figure E: Plot showing results for Fe/Ti oxide thermometry using Ghiorso and Evans (2008), with temperature plotted against fO_2. Unit B is orange, Unit C is yellow and Unit D is green. Squares represent data derived from touching pairs, whereas crosses represent data from Fe/Ti oxides partially included within the same pyroxene rim, in contact with melt. In supplementary material of Madden-Nadeau et al. (2021).

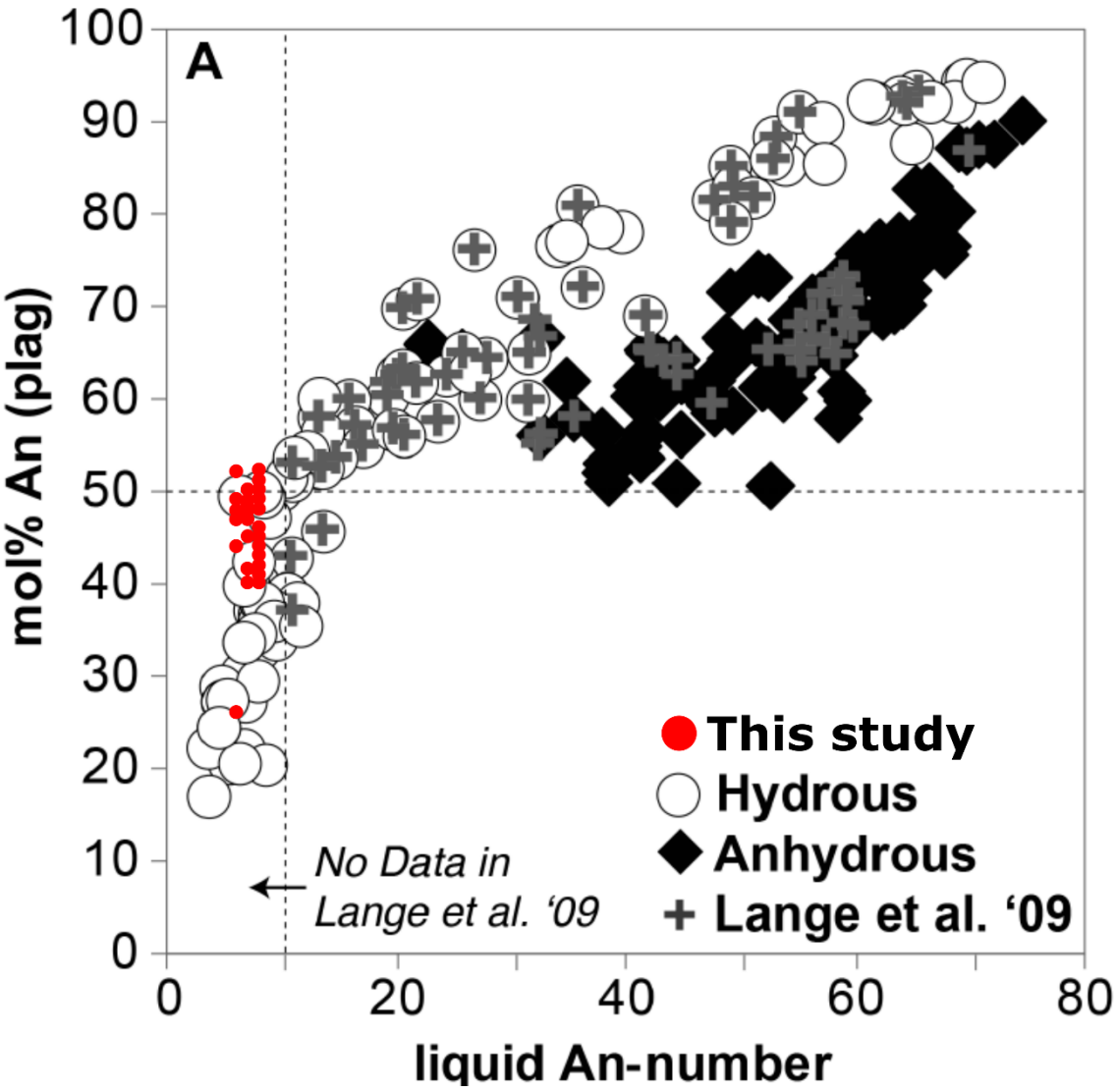

Supplementary Figure F: Plot taken from Waters and Lange (2015), showing mol% anorthite in plagioclase phenocrysts against melt anorthite content for the data they used to calibrate their plagioclase hygrometer (hydrous, anhydrous, Lange et al., 2009). This is compared with data for plagioclase analyses from this study plotted as red circles. Only those analyses that plotted within the data range used to calibrate the Waters and Lange (2015) hygrometer were used to generate estimates of water content using the hygrometer. In supplementary material of Madden-Nadeau et al. (2021).

(b) Chapter 2 Supplementary Table

Supplementary table 1: Table giving page numbers for historical sources used in recreating the timeline for the eruption.

Citation	Found	Page number	Date/Time of activity	Notes
Tennison-Woods (1884)	Simkin and Fiske (1983)	58	20th May	Original page numbers not known
Mackenzie (1883)	Simkin and Fiske (1983)	197	20th May	Printed in Java Bode on 30th May, reprinted in Verbeek (1885). Report by Commander of the Dutch Steamer Zeeland.
Tagliche Rundchau (1883)	Verbeek (1885)	85	20th-22nd May	Report by Captain Hollmann from German warship Elisabeth
	Simkin and Fiske (1983)	59		
Grainger (1883)	Simkin and Fiske (1983)	196	20th -23rd May	Printed in Algemeen Dagblad 23rd May, reprinted by Verbeek (1885)
Symons et al. (1888)	Symons et al. (1888)	11	20th-23rd May	
Walker (1883)	Simkin and Fiske (1983)	60	20th-23rd May	Report by Captain Walker of the ship Actaea (6 degrees 50 'S, 104 degrees 2'E)
Furneaux (1964)	Furneaux (1964)	13	21st-22nd May	Account by Mrs. Beyernick, wife of Dutch controller at Ketimbang. "they ran to the beach… the earth burst open at their feet" told by inhabitants of Sebesi visiting the island and the next day Controller of Kalimbang and The Resident of Lampong district report that "the fishermans story was true".
	Simkin and Fiske (1983)	61		
Sulzer (1883)	Simkin and Fiske (1983)	197	22nd May	Report by medical doctor aboard Dutch Steamer Soenda (name mistakenly printed as Lubzer) Printed in Java Bode 30th May and Locomotief 1st June, reprinted by Verbeek (1885).

Citation	Found	Page number	Date/Time of activity	Notes
Times of London, 03/06/1883	Simkin and Fiske (1983)	61	23rd May	
Symons et al., (1888)	Symons et al., (1888)	11	24th-26th May	"the eruption… became of a more moderate character… so much so that the residents in Batavia… ceased to pay much attention to the subject".
Symons et al., (1888)	Symons et al., (1888)	12	May 27th	Report from excursion party to island, Perboewatan in activity.
Symons et al., (1888)	Symons et al., (1888)	13	May 28th - June 19th	"although there was no intermission in the eruption, there appeared to be a decline in the volcanic activity, as far as can be judged from reports obtained from the lighthouses of the Strait, and from the captains of passing vessels."
Javasche Courant, 20/07/1883	Simkin and Fiske (1983)	199	June	Controller of Ketimbang's monthly report, "Krakatau continuously expelled smoke" and reports the loudest explosions on 28th and 30th, reprinted in Verbeek (1885)
Algemeen Dagblad, 20/06/1883	Simkin and Fiske (1983)	199	June 19th	Report from Anjer: "Krakatau smoked heavily"
Algemeen Dagblad, 26/06/1883	Simkin and Fiske (1983)	199	June 24th	Dense cloud over island dissipates, "two thick columns of smoke… rising majestically"
Symons et al., (1888)	Symons et al., (1888)	13	June 24th	"At Ketimbang… it was noticed that the appearance of the summit of Perboewatan had entirely changed; the conspicuous summit had disappeared"
Verbeek (1885)	Simkin and Fiske (1983)	199	June 24th	"The appearance of Perboewatan had completely changed": Printed in Javasche Courant 21st August.

Citation	Found	Page number	Date/Time of activity	Notes
Tennison-Woods (1884)	Simkin and Fiske (1983)	66	June 24th	"16th June… another outburst was heard at Anjer": attributed to June 19th by Algemeen Dagblad 20/06/1883. "Two dense columns of smoke" on 24th June.
Verbeek (1885)	Simkin and Fiske (1983)	199	July 3rd	Verbeek's own observations from Dutch vessel Prinses Marie which passed Krakatau from the east side: "through a dense haze, only a red glimmer was seen; no ash was noticed"
Ashdown (1883)	Simkin and Fiske (1983)	201	August 1st	Ship Siam sails through floating pumice
Verbeek (1885)	Verbeek (1885)	26	August 11th-12th	Letter and map sent from Ferzenaar to Verbeek, detailing his excursion to the island
	Simkin and Fiske (1983)	67		
	Symons et al., (1888)	13		
Symons et al., (1888)	Symons et al., (1888)	14	August 11th - 25th	"The vessels that passed close to Krakatau between the 11th of August and the time of the great catastrophe reported a heavy rain of pumice and dust and constant loud explosions"
Macleod (1884)	Macleod (1884)	185	August 13th	"the opening of the new crater was… a small hole, maybe 100 ft in diameter, only a few meters above sea level"; this account conflicts with Ferzenaars, and is not mentioned by Verbeek (1885) or by Symons et al., (1888).
	Simkin and Fiske (1983)	68		
Bataviaasch Handelsblad, 16/08/1883	Simkin and Fiske (1983)	200	August 14th	Report from Dutch Steamship Madura
Algemeen Dagblad, 17/08/1883	Simkin and Fiske (1983)	200	August 16th	Report from ship The Loudon

Citation	Found	Page number	Date/Time of activity	Notes
Verbeek (1885)	Verbeek (1885), addenda	479	August 18th	Report from steamship Europa
	Simkin and Fiske (1983)	31		
Joly (1885)	Joly (1885)	298	August 22nd	Report from the Ship Medea
	Simkin and Fiske (1983)	96		
Van Heerdt (1884?)	Simkin and Fiske (1983)	68	August 23rd	Quoted from Captain Visman's log from Princes Wihelmenia; can be found in the Royal Society archives
Symons et al., (1888)	Symons et al., (1888)	14	August 25th	
Van Heerdt (1884?)	Simkin and Fiske (1983)	68	August 25th	Quoted from Captain Visman's log from Princes Wihelmenia; can be found in the Royal Society archives
Van Heerdt (1884?)	Simkin and Fiske (1983)	112	August 26th, 10am	Quoted from Captain Visman's log from Princes Wihelmenia; can be found in the Royal Society archives
Symons et al., (1888)	Symons et al., (1888)	19	August 26th, 2pm	"a black mass rising up… no less than 17 miles"; Captain Thompson of Ship Medea
	Simkin and Fiske (1983)	96		
	Joly (1885)	298		
Sturdy (1884)	Simkin and Fiske (1983)	102	August 26th, 2pm	Report by Captain Watson, of the Ship Charles Bal.
Metzger (1884)	Simkin and Fiske (1983)	33	August 26th, 2pm	Berbice ship reports sky dark
Symons et al., (1888)	Symons et al., (1888)	19	August 26th, 5pm	
Sturdy (1884)	Simkin and Fiske (1983)	103	August 26th, 5pm	Report by Captain Watson, of the Ship Charles Bal.
Algemeen Dagblad, 11/09/1883	Simkin and Fiske (1983)	211	August 26th, 5pm	Report of first flooding by controller Le Sueur

Citation	Found	Page number	Date/Time of activity	Notes
Furneaux (1964)	Furneaux (1964)	60	August 26th, 7pm	Mr. Schint, a resident of Anjer, tells Rev. Tennison-Woods who sends the report to the Sydney Morning Herald; "smashing the boats and strewing the beach with wreckage".
Furneaux (1964)	Furneaux (1964)	67	August 26th, 7pm	"native proas… were dashed to pieces": account of Mr. Beyernick told my Mrs. Beyernick
	Simkin and Fiske (1983)	83		
Algemeen Dagblad, 05/09/1883	Simkin and Fiske (1983)	206	August 26th, 7pm	A report from Tjaringin from the Supervisor of the Department of Water Control, Mr. Gaston, printed in Verbeek (1885): "several houses were already destroyed"
Bataviaasch Handelsblad, 09/09/1883	Simkin and Fiske (1983)	72	August 26th, 9pm	New telegraph master at Anjer, Mr. Schruit's, report translated for the Ceylon Observer
Symons et al., (1888)	Symons et al., (1888)	84	August 26th, 10pm	Sounds heard in Australia; report by Mr. Kemp
	Simkin and Fiske (1983)	146		
Latter (1981)	Simkin and Fiske (1983)	388	August 26th - 27th	Origin time of waves
Tennison-Woods (1884)	Simkin and Fiske (1983)	102	August 27th, 12am	Report by Captain Logan, of the Ship Berbice; Original page numbers not known
Tennison-Woods (1884)	Simkin and Fiske (1983)	79	August 27th, 1am	Detonations heard in Singapore
Algemeen Dagblad, 27/08/1883	Simkin and Fiske (1983)	202	August 27th, 1am	Printed in Verbeek (1885); broken windows in Batavia
Symons et al., (1888)	Symons et al., (1888)	90	August 27th, 1am	Sirik on Java is partially submerged.
Sturdy (1884)	Simkin and Fiske (1983)	103	August 27th, 4am	Report by Captain Watson, of the Ship Charles Bal.

Citation	Found	Page number	Date/Time of activity	Notes
Symons et al., (1888)	Symons et al., (1888)	22	August 27th, 5.30 am	First major explosion; according to Verbeek
Verbeek (1885)	Simkin and Fiske (1983)	207	August 27th, 6am	"it did not become light"; observations from journal of lighthouse keeper M. van Mens
Verbeek (1885)	Simkin and Fiske (1983)	202	August 27th, 6am	
Metzger (1884)	Simkin and Fiske (1983)	88	August 27th, 6am	Several vessels were thrown on the beach; reports from the Loudon
Symons et al., (1888)	Symons et al., (1888)	22	August 27th, 6.44 am	Second major explosion; according to Verbeek
Sturdy (1884)	Simkin and Fiske (1983)	103	August 27th, 8 am	Report by Captain Watson, of the Ship Charles Bal.
Verbeek (1885)	Simkin and Fiske (1983)	202	August 27th, 8 am	Heaviest explosion in Batavia according to Dr. van der Stok of the Meteorological Observatory.
Symons et al., (1888)	Symons et al., (1888)	22, 69	August 27th, 10am	Largest major explosion
Symons et al., (1888)	Symons et al., (1888)	26	August 27th, 10am	Pumice the size of a pumpkin
Ceylon Observer 06/09/1883	Simkin and Fiske (1983)	146	August 27th, 10am	Explosions heard in Singapore
Algemeen Dagblad, 03/09/1883	Simkin and Fiske (1983)	205	August 27th, 10am	Printed in Verbeek (1885); lighthouse destroyed
Symons et al., (1888)	Symons et al., (1888)	93	August 27th, 10am	Immense wave inundates the coasts of Java and Sumatra; ship Berouw carried 1.8 miles inland
	Simkin and Fiske (1983)	39		
Symons et al., (1888)	Symons et al., (1888)	22	August 27th, 10.45am	Last major explosion

Citation	Found	Page number	Date/Time of activity	Notes
Times of London, 08/10/1883	Simkin and Fiske (1983)	133	August 27th, 12pm	150 human corpses observed by Bay of Naples Ship
Symons et al., (1888)	Symons et al., (1888)	26	August 27th, 11am - 3pm	"The dust fell in small rounded accretions" in Batavia
Symons et al., (1888)	Symons et al., (1888)	27	August 27th, 11pm	Explosions declined in violence

References in bibliography.

Appendix 2: Descriptions of individual outcrops associated with the proximal 1883 volcanic stratigraphy

Locality MS-Swim1 on southern Panjang (Supplementary Figure Ia) was visited for the first time during the 2019 field campaign. There is ~ 2 cm of olive-green, very fine ash aggregates at the base of the 1883 sequence here, interpreted as such because it is overlying ~ 4cm of red, oxidised palaeosol, defining an erosive boundary with pre-1883 volcanic rock below (Supplementary Figure Ib). Overlying the green ash aggregates is ~3 m of massive, light-grey, matrix-supported deposit (Supplementary Figure Ic). Clasts consist of ~80 % pumice, with ~20 % lithics, the latter up to 50 cm in size. Mandeville et al. (1996b) determined that the majority of lithics within the 1883 sequence are basalt and basaltic andesite. Charcoal is present towards the base of this layer (Supplementary Figure Ie). At the top of this unit there is up to ~10 cm of pumice supported layer. Above this there is ~60 cm of massive, poorly sorted, matrix-supported unit with a lower maximum clast size than below, and a lower proportion of lithics. Following this is another clast supported layer ~10 cm thick. Overlying this it is possible to observe ~2 m of a very matrix-rich unit, with pumice supported layers becoming more common towards the top. Above this unit there is a distinct, darker-grey, matrix-rich unit, which extends for ~1 m. Overlying this there is ~7 m of a light-grey, matrix-rich, stratified unit, interbedded with thin pumice-supported layers. Large lithics are completely absent from this section. Towards the top of this outcrop there is ~ 5 m of matrix-supported unit containing very coarse pumices, with the top metre having a lower maximum pumice size.

Locality U20/D4S1 on northern Panjang (Supplementary Figure IIa) was visited in both field campaigns, and is presented here for the first time. At the base of the sequence is ~3 m comprising predominantly bedded, pumice-supported units (Supplementary Figure IIb). The pumice in these units is light-grey and sub angular. The coarsest layers are found towards the base, the first three of which are internally reverse graded. Charcoal was observed in the coarsest of these pumice-supported layers (not graded; truncated by the unit overlying it). The unit overlying the charcoal is matrix-supported, and contains lapilli ~ 2 cm in size. This unit is also cross stratified with dark, fine

laminations. Sorting improves throughout the pumice-supported beds overlying this cross-stratified layer. These clast-supported layers are interbedded with matrix-supported layers predominantly composed of coarse ash, with some mm-scale pumice lapilli.

Moving west along the outcrop, and up in the stratigraphy, it is possible to observe m-scale units of matrix-supported deposits containing abundant low-angle cross stratification (Supplementary Figure IIc and d). These units contain sparse, pumice-supported lenses. At the very top of this outcrop it is possible to observe an ~50 cm thick, matrix-supported layer containing lithic blocks of up to 20 cm in size (Supplementary Figure IId). The boundary between this unit and the cross-stratified unit below appears to be gradational.

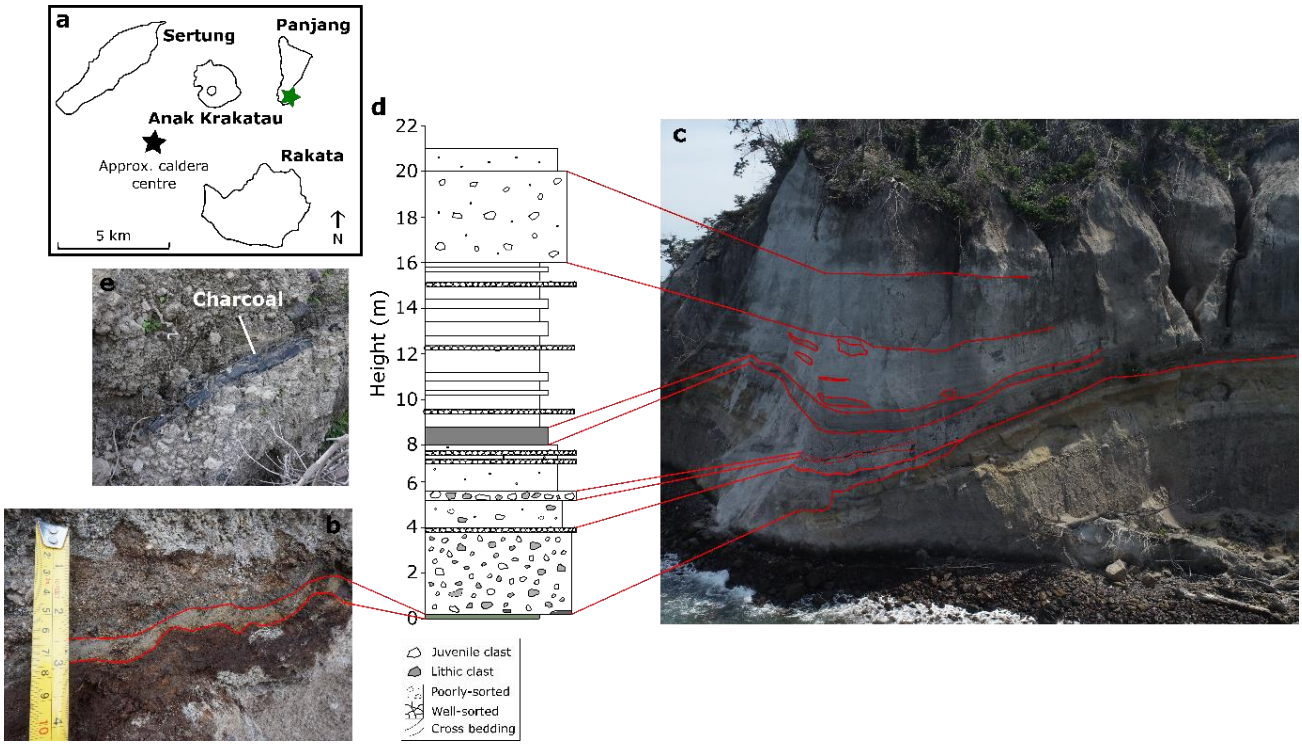

Supplementary Figure I: Insert (a) is a map showing the location of MS-Swim1 on south Panjang (green star), with field photo of the very base of the sequence (b) and drone image (c) cross correlated in red with a stratigraphic log (d). Tape measure for scale in (b). Field photo (e) shows the charcoal found in the unit below 4 m stratigraphic height.

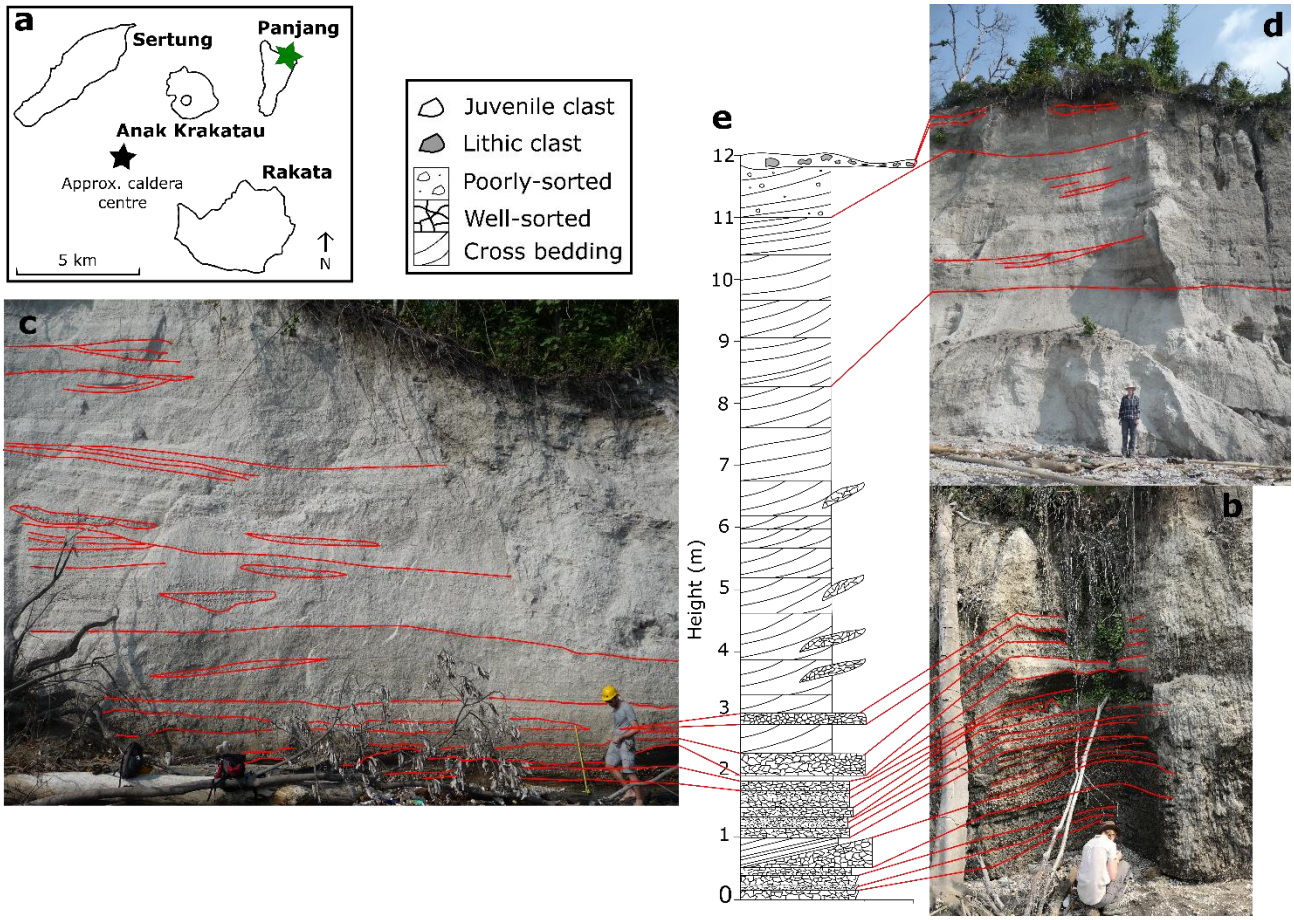

Supplementary Figure II: Insert (a) shows the location of sequence D4S1/U20 on north Panjang (green star), with field photos (b-d) cross correlated in red with a stratigraphic log (e).

At locality NP3/D3S1, northern Panjang (Supplementary Figure IIIa), visited in both field campaigns, there is a sequence of structureless, matrix-supported, poorly sorted units containing white pumice (~90 % of clasts), interbedded with similar units containing abundant, low-angle, cross stratification (Supplementary Figure IIIb to d). These units can be anywhere up to ~3.5 m in thickness, with pumices up to ~20 cm in size (average ~5 cm). The two units at the base are normally graded. The units containing cross stratification also contain pumice-supported lenses. Towards the top of this sequence, it is possible to observe ~ 50 cm of a matrix-supported unit containing lithic blocks up to 50 cm in size (Supplementary Figure IIId). Above this is another structureless, matrix-supported, poorly sorted unit.

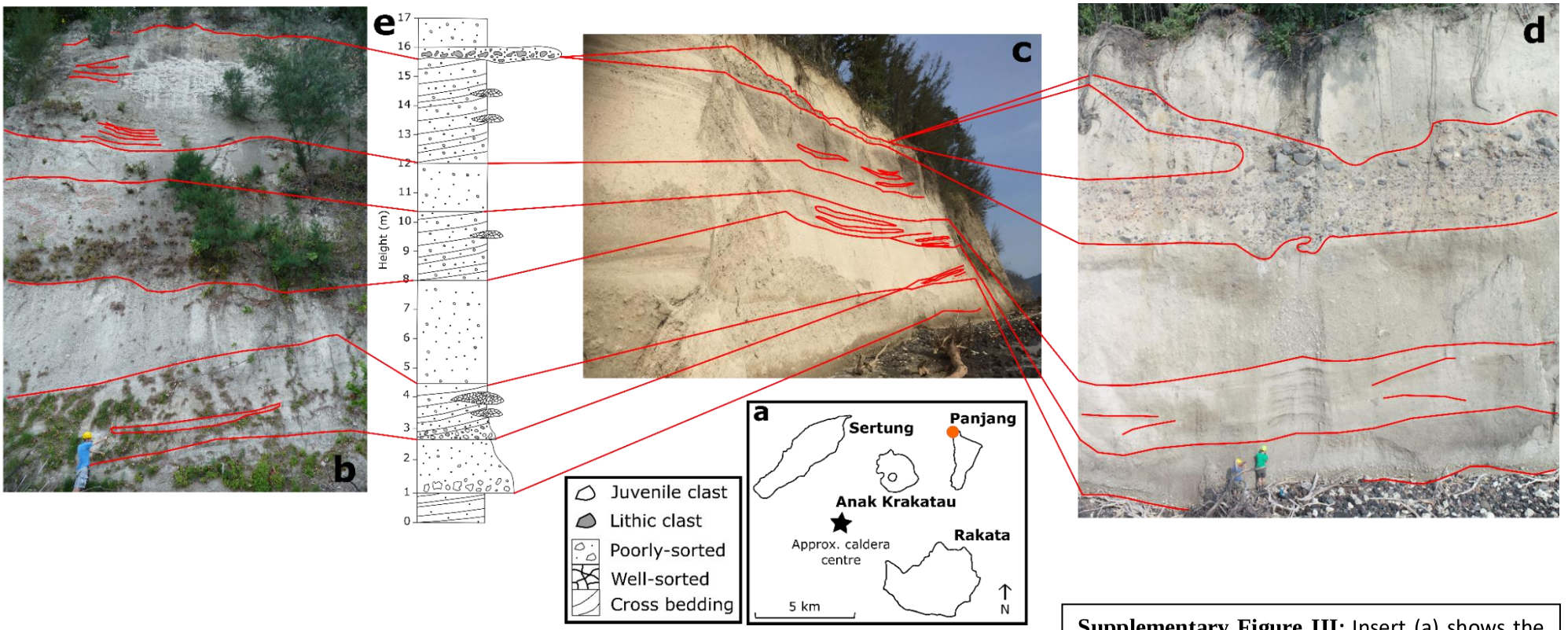

Supplementary Figure III: Insert (a) shows the location of sequence D3S1/NP3 on north Panjang, with field photos (b) and (c), and drone image (d) cross correlated in red with a stratigraphic log (e).

Localities U11 - U15/D2S3a are located on northern Sertung (Supplementary Figure IVa), and were visited in both field campaigns. In 2019 this outcrop was much more laterally extensive, thus being split into four separate localities. At the base of this outcrop there are clast-supported units containing predominantly pumice lapilli up to ~ 20 cm in size, interbedded with poorly sorted, matrix-supported units (Figure IVb - e). The poorly sorted layers contain discontinuous pumice lenses, in which the pumices are mostly well rounded. In the continuous pumice layers, pumices are often angular to sub-angular, and some of these units show reverse grading. Pumices found in the matrix supported units are rounded and on average ~ 1 cm in size. Towards the top of the sequence there is ~ 1 m of matrix-supported unit containing angular lithic blocks ~ 20 cm in size, with maximum size of ~60 cm (Figure IVc - e). The boundary with the units below and above this lithic-rich layer is gradational, and occasionally the layer bificates, with an absence of lithic blocks in between (Figure IV d and e). Above this is a massive, matrix-supported, poorly sorted unit, containing predominantly pumice, with a lower proportion of lithic clasts, of a smaller maximum and average size. Both the lithic-rich layer, and the unit above contain clasts of obsidian.

Locality D2S3b is located on western Sertung (Figure Va), and was only visited in 2017 as sea level was too high in 2019. At the base of this outcrop is a clast-supported unit predominantly containing angular lithic blocks ~ 20 cm in size (Figure V b). This gradually becomes matrix supported moving upwards in stratigraphic height. The maximum height of this lithic rich unit is 4 m however, it shows considerable lateral variation, and within 1 m tails off to 50 cm in height. Overlying this is a massive, matrix-supported unit containing predominantly pumice clasts.

Locality NP4/D3S2 on eastern Panjang (Figure VIa) was visited on both campaigns, however had considerably more exposure in 2019. At the base of the outcrop, it is possible to observe a matrix-supported ~ 2 m thick unit containing abundant lithic and obsidian blocks (maximum clast size ~ 30 cm; Figure VIb). There is a gradational boundary with the unit above, which itself is another, matrix supported, lithic-rich unit ~ 2 m in height, however the maximum clast size is larger at ~ 60 cm. Overlying this is a massive, structureless matrix supported unit ~ 6.5 m thick. 80 % of clasts in this

unit are pumice. At the top of this sequence it is possible to see another matrix-supported unit rich in lithic blocks, ~ 0.5 m thick. All units within this outcrop contain obsidian.

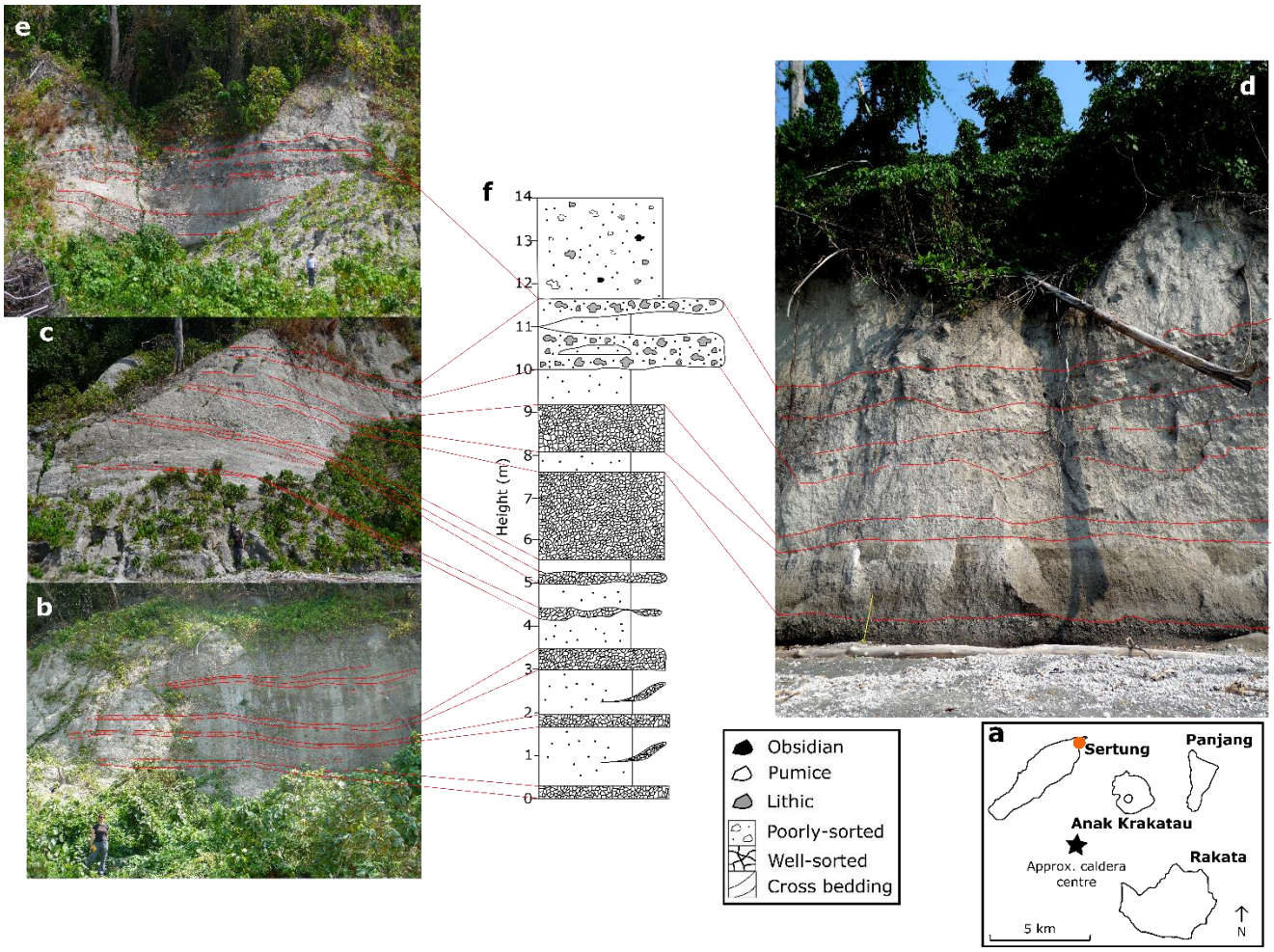

Figure IV: Insert (a) shows the location of sequence D2S3a/U11-15 on north Sertung, with field photos (b - e) cross correlated in red with a stratigraphic log (f). People for scale.

Locality U24/D1S1 is located on western Rakata (Figure VIIa) and was visited on both field campaigns. The outcrop is composed of ~ 14 m of massive, matrix-supported deposit (Figure VIIb). 80% of clasts are pumice, with 15 % dense, lava lithics. Both frothy, as well as glassy, obsidian is also present (~5 %) (e.g., Shields et al. 2016). The majority of pumice is white, however mixed pumice was also found at this locality, along with very small amount of dark coloured pumice. After the first 1.5 m of unit, the maximum clast size increases, and the deposit is normally graded moving up the sequence thereafter.

Locality U23/D2S2 located on southern Sertung (Figure VIIIa) was visited in both field campaigns, however the exposure in 2019 was far superior to 2017. This outcrop is composed of ~ 14 m of massive, poorly sorted, matrix-supported deposit, with two boundaries only denoted by crude colour changes at ~ 6 m and 12 m. It contains approximately 80 % pumice clasts (predominantly white), with 15 % dense lithics and 5% obsidian. It is possible to observe frothy, as well as glassy, obsidian clasts (e.g., Shields et al., 2016). This deposit also contains large, dense, glassy blocks of up to 8 m in size across their long axes, which are reported here for the first time. The blocks are internally coherent, but intensely fractured and have sub-rounded, irregular, in places "tear drop" shapes, aligned broadly horizontally, but not confined to a single horizon. Some of these fractured blocks look very similar to smaller glassy obsidian clasts, as they are vitreous with the same black colour and a similar phenocryst content, whereas other blocks are dull grey in colour with a higher phenocryst content. It should be noted that there were no sag structures associated with these large blocks. There are sparse mudstone clasts also incorporated in this deposit, that, when found close to the contact with the large glassy blocks, had irregular shapes that were aligned with the contact between the blocks and the matrix.

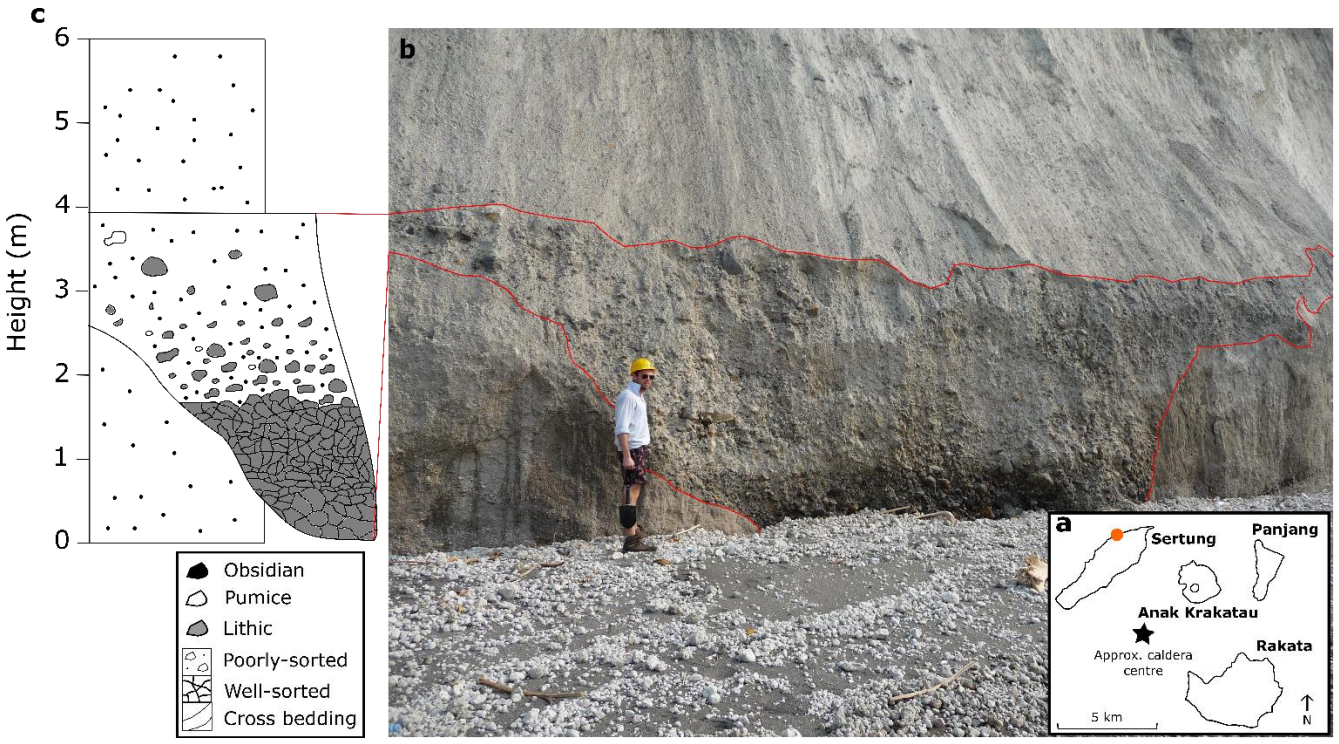

Figure V: Insert (a) shows the location of sequence D2S3b on east Sertung, with field photo (b) cross correlated in red with a stratigraphic log (c).

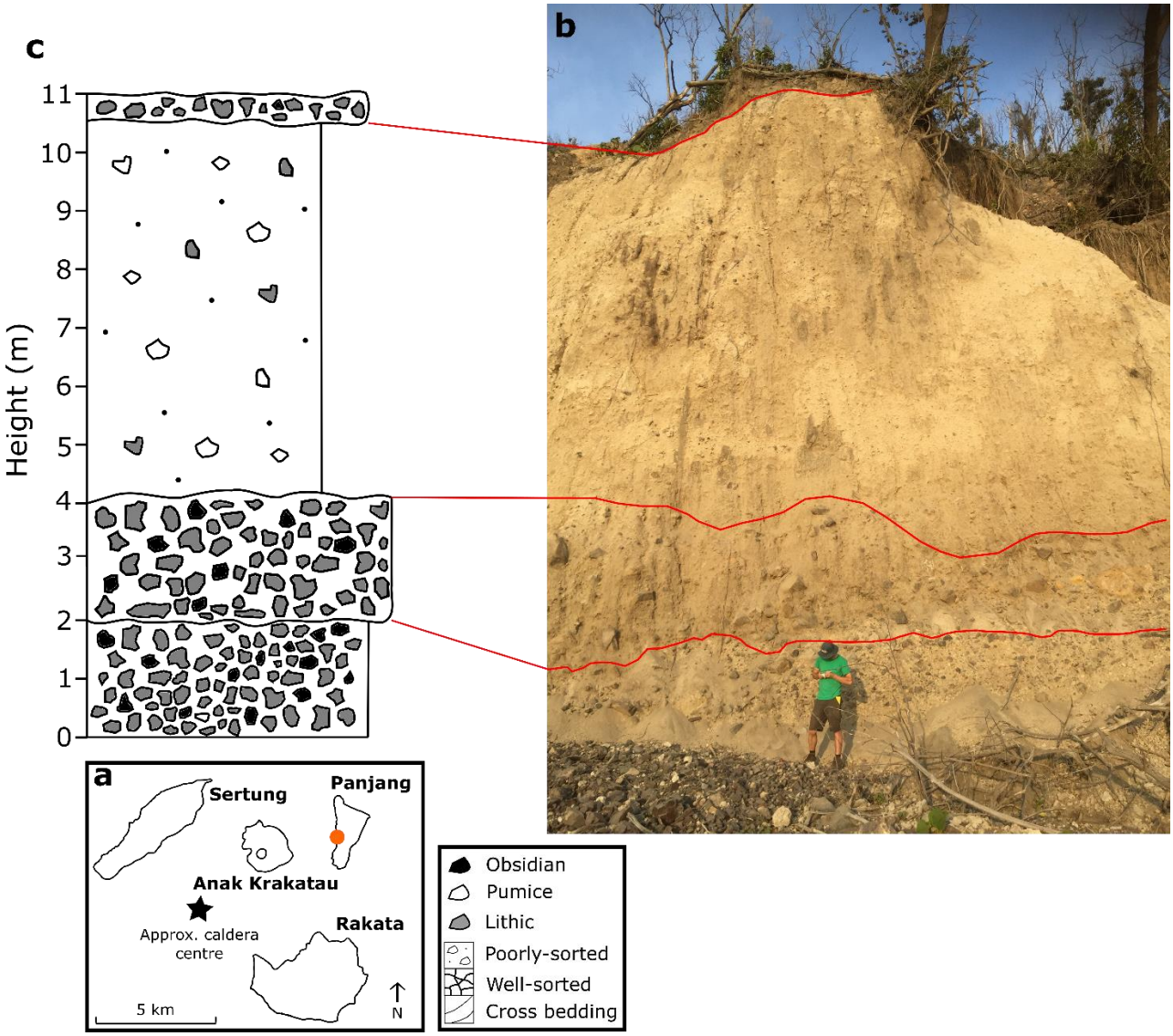

Figure VI: Insert **(a)** shows the location of sequence D3S2/NP4 on west Panjang, with field photo (b) cross correlated in red with a stratigraphic log (c). Person for scale.

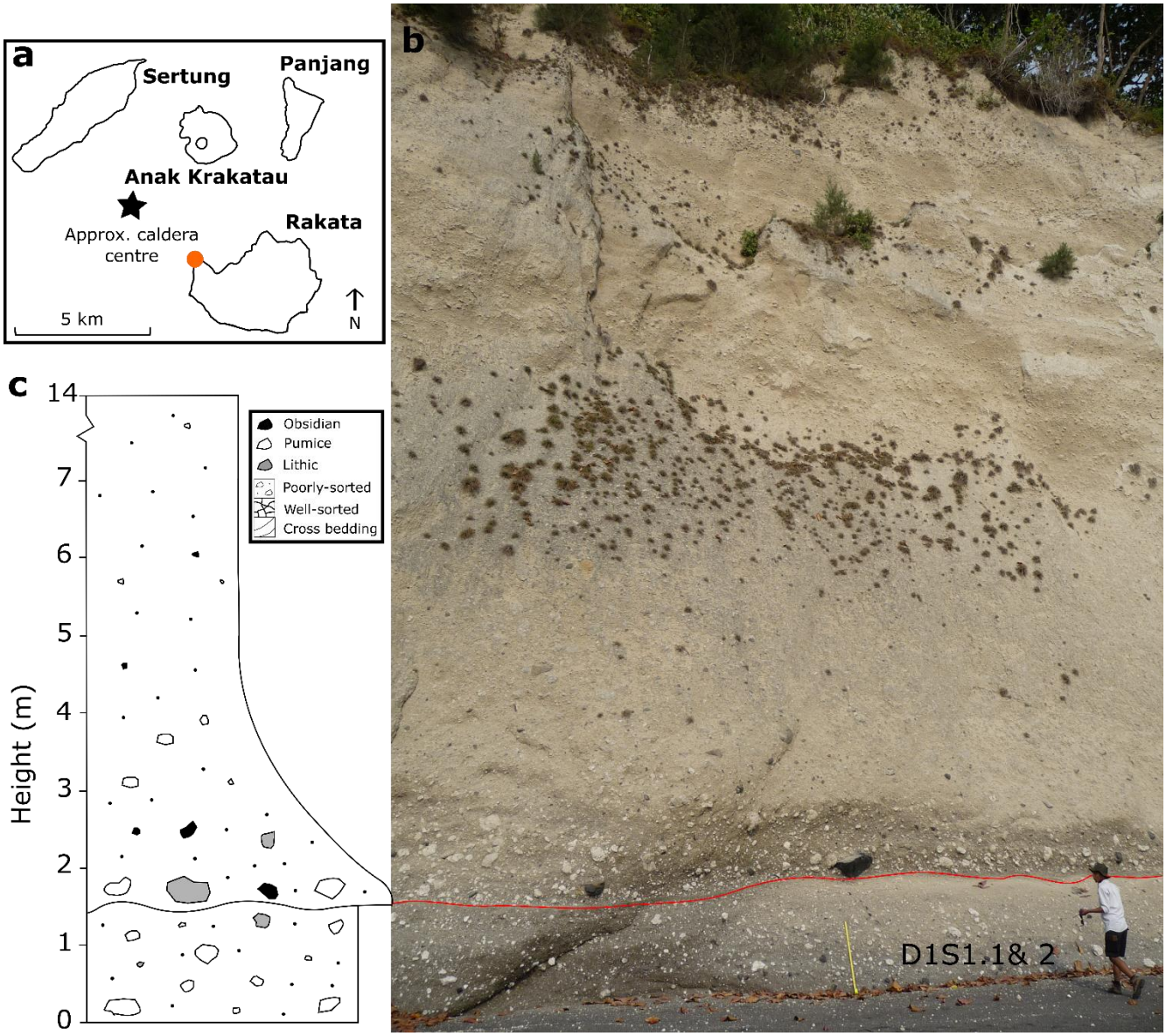

Figure VII: Insert (a) shows the location of sequence D1S1/U24 on west Rakata, with field photo (b) cross correlated in red with a stratigraphic log (c). Person for scale.

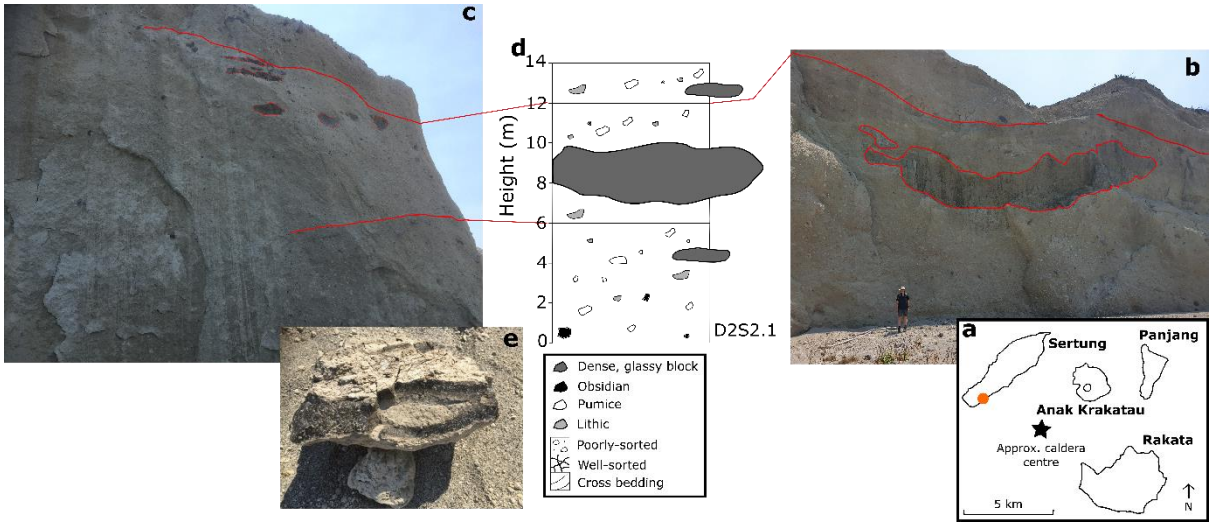

Figure VIII: Insert (a) shows the location of sequence D2S2/U23 on south Sertung, with field photos (b) and (c) cross correlated in red with a stratigraphic log (d), with relevant sample marked. Photo (c) is located around the corner from (b) on the southern tip of the locality. Field photo (e) shows a clast of frothy obsidian (e.g., Shields et al., 2016). Person for scale.

Appendix 3

(a) Chapter 3 Supplementary Figure A

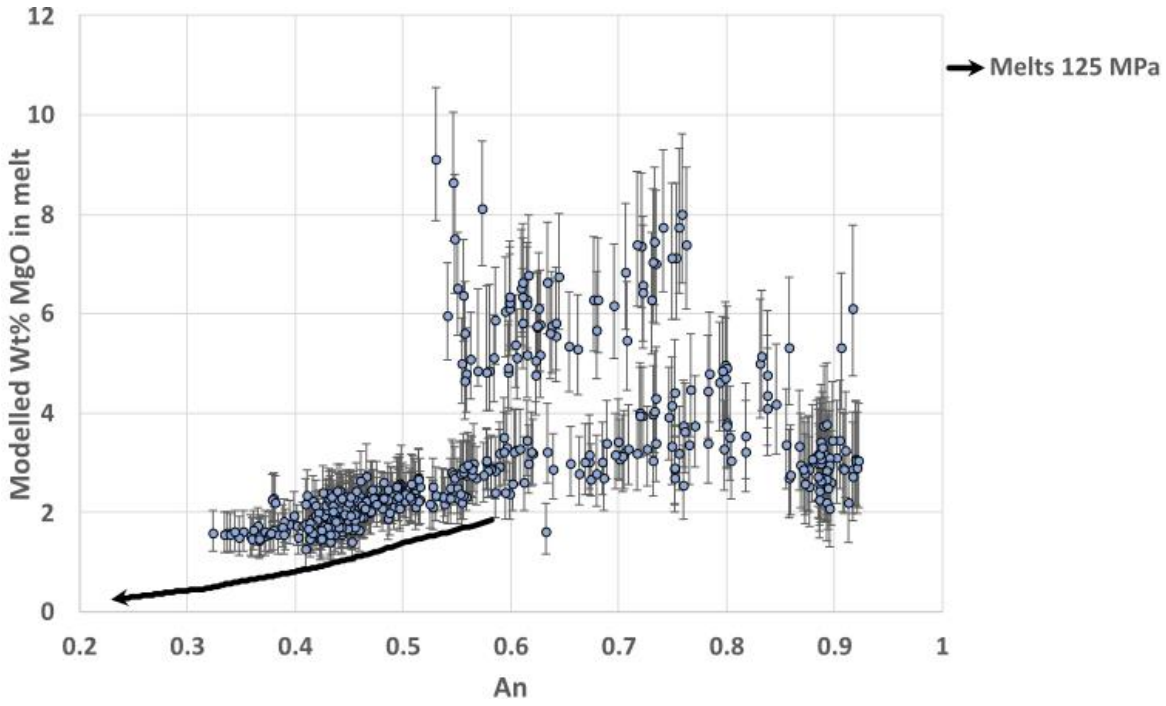

Supplementary Figure A: Modelled wt% MgO (blue circles) against the corresponding crystallised anorthite content, modelled using partition coefficients and plagioclase trace element data using the model Bindemann et al. (1998). Melt chemistry evolution estimated via Rhyolite-MELTS models at 125 MPa (Figure 3.9; Gualda et al., 2012; Madden-Nadeau et al., 2021) provided for comparison. Error bars are derived from estimated errors on empirically derived coefficients used to estimate the partition coefficients. This has then been added to the analytical error associated with the plagioclase analyses.

(b) Chapter 3 Supplementary Table A

Supplementary Table A: Phase proportions for experimental products on a vesicle-free basis.

Sample	Pressure (MPa)	Temperature (°C)	Gl (%)	Plg (%)	Cpx (%)	Opx (%)	Qtz (%)	Acc (%)
KK04	100	900	97.29	0.46	2.22	0	0	0.07
KK16	150	850	91.60	5.96	0.54	1.62	0	0.27
KK17	50	800	93.32	4.32	0.89	0.92	0	0.56
KK18	50	850	88.60	7.34	1.75	1.65	0	0.66
KK21	100	850	88.27	8.38	0.80	1.81	0	0.75
KK27	200	800	85.33	11.30	2.29	0	1.34	1.08
KK32	50	900	91.60	5.97	1.44	0.72	0	0.27
KK34	150	900	96.51	0	3.20	0	0	0.29
KK38	200	850	95.14	2.09	1.86	0.56	0	0.34
KK40	150	800	79.91	13.58	1.30	3.89	2.17	1.32
KK43	150	895	95.39	0.12	4.18	0	0	0.31
KK44	100	800	90.24	5.70	1.34	1.49	0	1.23

Gl= Glass, Plg = Plagioclase, Cpx = Clinopyroxene, Opx = orthopyroxene, Qtz = Quartz and Acc = Accessory minerals (Fe-Ti oxides and apatite).